## **New Front-End Separation Approaches for Top-Down Proteomics**

By

Eli J. Larson

A dissertation submitted in partial fulfillment

of the requirements for the degree of

Doctor of Philosophy

(Chemistry)

At the

UNIVERSITY OF WISCONSIN-MADISON

2023

Date of final oral examination: 7/7/2023

This dissertation has been approved by the following members of the Final Oral Committee:

Ying Ge, PhD, Professor, Cell & Regenerative Biology and Chemistry

Lloyd M. Smith, PhD, Professor, Chemistry

Lingjun Li, PhD, Professor, Pharmaceutical Sciences and Chemistry

Wei Guo, PhD, Assistant Professor, Meat Science & Muscle Biology

#### Acknowledgements

As I reflect on my time in Madison while sitting at the same desk I've occupied for five years, I feel a deep sense of both nostalgia and gratitude. Surrounded by picturesque views of the shimmering Lake Mendota to my right, and the 8<sup>th</sup> floor instrument room just to my left, I thank God for the many amazing people who've worked in this environment alongside me. First, I must acknowledge my PhD advisor, Prof. Ying Ge. Thank you to Ying for visiting Gustavus Adolphus College in November of 2017, showing me a new and exciting area of proteomics research and inspiring my application to UW-Madsion. You have given me so many incredible opportunities and I am fortunate to come from your group. I will always remember the hours spent in "walk talks" fondly, whether doing laps of the WIMR west wedge, finding turtles on Picnic Point, or being forced to retreat onto the 80 bus by hail. To my mentoring committee, Profs. Ying Ge, Lloyd Smith, Josh Coon, Lingjun Li, and Wei Guo, thank you for your scientific guidance and support throughout my graduate career. To Wei specifically, it's been a pleasure to work with you and your group in an exciting collaboration.

Thank you to all past and present members of the Ge group including Dr. Bifan Chen, Dr. Yutong Jin, Dr. Kyle Brown, Dr. Trisha Tucholski, Dr. Abe Wu, Dr. Tim Tiambang, Dr. Sam Knott, Dr. David Roberts, Dr. Jake Melby, Ben Wancewicz, Austin Carr, Elizabeth Bayne, Morgan Mann, Emily Reasoner, Timothy Aballo, David Moreno, Emily Chapman, Kevin Buck, Kalina Rossler, Holden Rogers, Jãán Andrews, Scott Price, Matthew Fischer, Ruby Chan, Mallory Wilson, Anna-Grace Towler, Yareslie Cruz Rivera, Zhuoxin Shi, Bridget Knight, Brad Li, Kent Wenger, Dr. Sean McIlwain, Dr. Yanlong Zhu, Dr. Melissa Pergande, Dr. Boris Krichel, Dr. Zhan Gao, and Dr. Mandi Wang. Specific thanks to Bifan for helping me begin my time in the Ge lab. Thank you as well to Yanlong, the sheriff of FTICR, a mass spectrometrist of highest quality, and an excellent scientific

sounding board. I've greatly enjoyed working and learning with you and being your FTICR deputy these past few years. Thank you to Kyle for your scientific alacrity and seemingly endless patience to field questions. Thank you to Tim for being an ever-cheerful presence and an excellent desk mate. To Ben, it's been wonderful to get to know you, but also to move away from our shirt matching ways. In Emily Reasoner resides a keen scientific mind...right next to the ability to absolutely destroy a slow-pitched softball. Thanks to Reasoner, Chappy, and Timothy for the fun and the laughs. To Timothy, thank you for keeping me biologically honest. To my mentees Holden, Matthew, Zhuoxin, and Bridget, you have bright futures ahead of you and I can't wait to see the amazing things you'll do. Thank you to David Roberts, a friend whose excitement for science is contagious and who's bound for an amazing career at any institution he chooses. Thanks also to David's wife, Jenny, for letting me steal him away from making you dinner on time to do lab work or hangout. Last but certainly not least, thank you to my dear friend Jake. Going through the experience of graduate school together has been a pleasure, and your curiosity and creativity inspire me. For no one else has the phrase "academic brother" rung truer.

I must also thank two key mentors from my undergraduate career at Gustavus Adolphus College, Profs. Dwight Stoll and Brian O'Brien. Dwight has been instrumental (pun fully intended) in launching my career as an analytical chemist and has given me an abiding love for separation science and 2DLC. My deepest thanks for your patience in instruction and dedication to investigating fundamental challenges in the field of HPLC. Thank you as well to previous Stoll lab members and collaborators who've helped and guided me including Dr. Chris Harmes, Dr. Claudia Seidl, Dr. Gabriel Leme, Dr. Steve Groskreutz, Prof. Kevin Clark, Dr. Brian Voigt, Prof. Sarah Rutan, Tyler Brau, and Ray Sajulga. Thank you to Prof. O'Brien for showing me life as a scientist outside of the lab and teaching me that true voracious learning goes beyond a formal

education. I thoroughly enjoyed our conversations about all things botanical and visits to local prairies and the calcareous fen. From my time at Genentech, I need to thank Drs. Mohammad Al-Sayah and C. J. Venkatramani as well as Dr. Wing Huang. To Mo, your patience, support and encouragement gave me the confidence to pursue a career in science. To C.J. your quick wit, constant energy, and scientific creativity are a joy to be around. In Wing I found a friend and curious investigator, and I'm glad that we can be "cousins" in the McLafferty scientific lineage.

To my friends in Madison, Jake, Sid, Trent, Autin, keep it real loafers. Thank you to the Blackhawk church community, and specifically the Allens for opening their home for our community group. Thanks to the UW Nordic ski club for the fun and laughs, specifically to Carl, Ian, Sid, and Paul.

To my brother Alex, whether it's terrible puns, traveling for races together, or deep conversations, thanks for all the fun and support. Thanks for the visits, support, faith, and your well-articulated insights over the years. I'm so glad to call you my brother, and I'm looking forward to many more races with you to come. To my girlfriend, Hannah, your sense of humor, smile, and care for those around you make you such a joy to be around, even in the Texas heat. Thanks for all the late-night calls, support, and encouraging Bible verses you've sent to help me through difficult experiments and lab marathons. I can't wait to see where God takes us in the coming years. To my parents Jan and Lib, thank you for your support and encouragement, without which I would not be here. Thank you for your advice over the years, Proverbs 1:8-9 says "Listen, my son, to your father's instructions and do not forsake your mother's teaching. They are a garland to grace your head and a chain to adorn your neck.". I am truly grateful that you are my parents. Thank you for starting me on this path, guiding me along the way, and everything else I can't find the words for. I love you both very much.

## **Table of Contents**

Table of contentsiv
Abstractvii
List of Figures and Tablesix-xvi
Chapter 1 – Top-Down Proteomics: Challenges, Opportunities, and Applications
1.1 Introduction to Top-Down Proteomics2
1.2 Recent Progress in Development of Separations for Top-Down Proteomics3
1.3 Data Analysis Challenges in Top-Down Proteomics13
1.4 Applications of Top-Down: Antibody-Based Therapeutics
Chapter 2 – Rapid Analysis of Reduced Antibody Drug Conjugate by Online LC-MS/MS with
Fourier Transform Ion Cyclotron Resonance Mass Spectrometry
2.1 Abstract19
2.2 Introduction20
2.3 Methods22
2.4 Results and Discussion24
2.5 Conclusions32
2.6 Figures34
2.7 Supplemental Information40

Chapter 3 – High-Throughput Multi-Attribute Analysis of Antibody Drug Conjugates Enabled	l by
Trapped Ion Mobility Spectrometry and Native Top-Down Mass Spectrometry	

Ĵ	8.1 Abstract62
Ĵ	3.2 Introduction63
Ĵ	3.3 Methods65
Ĵ	3.4 Results and Discussion68
Ĵ	3.5 Conclusions77
Ĵ	8.6 Figures79
Ĵ	8.7 Supplemental Information85
Chapter	• 4 – MASH Native: A Unified Solution for Native Top-Down Proteomics Data Processing
4	1.1 Abstract121
4	1.2 Introduction
4	1.3 Methods123
4	4.4 Results and Discussion124
4	1.5 Conclusions
4	1.6 Figures129
4	1.7 Supplemental Information

**Chapter 5** – Expanding Global Top-Down Proteomics Coverage by Sequential Protein Extraction and Online Two-Dimensional Liquid Chromatography

5.1 Abstract144
5.2 Introduction14:
5.3 Methods14
5.4 Results and Discussion15
5.5 Conclusions15
5.6 Figures158
5.7 Supplemental Information164
Chapter 6 – Conclusions and Future Perspectives
<b>Appendix I</b> – Rbm20 ablation is associated with changes in the expression of titin-interacting and
metabolic proteins
AI.1 Abstract
AI.2 Introduction
AI.3 Methods193
AI.4 Results and Discussion194
AI.5 Conclusions199
AI.6 Figures201
AI.7 Supplemental Information206

#### **Abstract**

Top-down mass spectrometry (MS) and top-down proteomics have become indispensable tools to characterize and identify unique proteoforms. Proteoforms are defined as all protein products of a single gene, including splicing variants, mutants, and post-translationally modified forms. Although the development of new MS capabilities has exploded in recent years, the comparative underdevelopment of intact protein separations and data processing solutions has prevented full realization of the benefits of top-down. To address these challenges, I have developed new front-end separation approaches for top-down proteomics, beginning with targeted separations for multi-attribute analysis of antibody-drug conjugates (ADCs) and later developing an online two-dimensional liquid chromatography (2DLC) method to expand global proteome coverage by top-down proteomics.

Chapter 1 focuses on recent advances in front-end separations and data processing solutions for top-down proteomics and introduces top-down applications to antibody-based therapeutic analysis. Chapter 2 and chapter 3 detail new targeted separation approaches for monoclonal antibodies and ADCs. Chapter 2 reports reversed phase liquid chromatography (RPLC) coupled to high-resolution Fourier transform ion cyclotron resonance MS for top-down analysis of a reduced cysteine-linked ADC. Chapter 3 details the development of a native complex-down workflow using trapped ion mobility spectrometry-MS with a cysteine-linked ADC and parent mAb under non-denaturing conditions (Chapter 3). Chapter 4 reports a new software package designed to address the challenges associated with native top-down proteomics, MASH Native. Chapter 5 focuses on the development of a new online 2DLC method coupling serial size exclusion and RPLC to expand global top-down proteome coverage, with application to human heart extract. Appendix I reports a shotgun proteomic approach to characterize the impact of

splicing factor RNA binding motif 20 knockout on the rat heart proteome and identifies targets for follow-up analysis by top-down proteomics. The developed techniques detailed here will address key challenges to front-end separation in the field of top-down proteomics, expanding analytical capabilities for future targeted and discovery studies.

<u>List of Figures</u> <u>Page</u>
Figure 2.1 Workflow concurrent ADC reduction strategy and generated subunits34
Figure 2.2 RPLC-MS analysis of partially and fully reduced ADC35
Figure 2.3 Impact of intrachain disulfide bond removal on Lc and Hc charge state distribution36
Figure 2.4 RPLC-FTICR-MS1 spectra of partially and fully reduced subunits37
Figure 2.5 RPLC-FTICR-MS2 analysis of fully reduced Lc0 and Lc1 subunits by CID38
Figure 2.6 RPLC-FTICR-MS2 analysis of fully reduced Hc1 subunit by CID39
Figure 2.S1 Triplicate analysis of partially reduced subunits by RPLC-FTICR-MS42
Figure 2.S2 Triplicate analysis of partially fully subunits by RPLC-FTICR-MS43
Figure 2.S3 TIC overlay of partially and fully reduced subunit analysis by RPLC-FTICR-MS44
Figure 2.S4 HIC-UV analysis for average DAR determination
Figure 2.S5 Comparison of MS1 charge state distributions between fully and partially reduced
subunits
Figure 2.S6 BPCs of partially and fully reduced subunit analysis by RPLC-FTICR-MS47
Figure 2.S7 Impact of MS skimmer voltage on DFA adduct formation for partially reduced
subunits
Figure 2.S8 Observed CID fragmentation products of MMAE drug and linker49
Figure 2.S9 RPLC-FTICR-MS2 analysis of partially reduced Lc0 subunit by CID50
Figure 2.S10 RPLC-FTICR-MS2 analysis of partially reduced Lc1 subunit by CID51

<u>List of Figures</u> <u>Page</u>
Figure 2.S11 RPLC-FTICR-MS2 analysis of partially reduced Hc0 subunit by CID52
Figure 2.S12 RPLC-FTICR-MS2 analysis of fully reduced Hc0 subunit by CID53
Figure 2.S13 RPLC-FTICR-MS2 analysis of partially reduced Hc1 subunit by CID54
Figure 2.S14 RPLC-FTICR-MS2 analysis of partially reduced Hc2 subunit by CID55
Figure 2.S15 RPLC-FTICR-MS2 analysis of fully reduced Hc2 subunit by CID56
Figure 2.S16 RPLC-FTICR-MS2 analysis of partially reduced Hc3 subunit by CID57
Figure 2.S17 RPLC-FTICR-MS2 analysis of fully reduced Hc3 subunit by CID58
Figure 3.1 Direct injection native TIMS complex-down workflow for ADC analysis79
Figure 3.2 Impact of TIMS off vs TIMS on ADC MS1 spectra using a timsTOF Pro80
Figure 3.3 Comparison of 1/K <sub>0</sub> mobility vs m/z heatmaps for parent mAb and ADC81
Figure 3.4 Muti-attribute analysis by complex-down to generate MS1, MS2, and MS3 spectra for
a cysteine-linked ADC82
Figure 3.5 Proof of concept for CID fragmentation of Lc1 subunit by a segmented approach to use
multiple collision energies83
Figure 3.6 Full native TIMS complex-down workflow in a 3-minute segmented analysis84
Figure 3.S1 Location of voltages used to optimized TIMS performance for intact ADC92
Figure 3.S2 Intensity normalized MS1 spectra from TIMS Δ3 voltage optimization92
Figure 3.S3 Total ion mobilograms from TIMS Δ3 voltage optimization93

<u>List of Figures</u>
Figure 3.S4 Mobility (1/ $K_0$ ) vs m/z heat maps from TIMS $\Delta 3$ voltage optimization94
Figure 3.S5 Intensity normalized MS1 spectra from TIMS Δ6 voltage optimization95
Figure 3.S6 Total ion mobilograms from TIMS Δ6 voltage optimization96
Figure 3.S7 Mobility (1/ $K_0$ ) vs m/z heat maps from TIMS $\Delta 6$ voltage optimization
Figure 3.S8 Total ion mobilograms of TIMS RF and TIMS duty cycle optimization for AbbVie
starting mAb98
Figure 3.S9 Total ion mobilograms TIMS duty cycle optimization at 300, 275, and 250 Vpp TIMS
RF for AbbVie starting mAb99
Figure 3.S10 Total ion mobilograms of TIMS RF optimization for NISTmAb100
Figure 3.S11 Plots of calculated CCS for AbbVie starting mAb and NISTmAb using multiple
TIMS RF voltages
Figure 3.S12 Total ion mobilograms of TIMS RF and TIMS duty cycle optimization for AbbVie
ADC102
Figure 3.S13 Mobility $(1/K_0)$ vs m/z heat maps from isCID voltage optimization103
Figure 3.S14 Intensity normalized MS1 spectra from isCID voltage optimization
Figure 3.S15 Intensity normalized MS1 for Lc1 <sup>8+</sup> subunit from isCID voltage optimization105
Figure 3.S16 MS1 overlay of detector TOF voltage optimization
Figure 3.S17 Intensity normalized MS1 spectra from TIMS DC gradient voltage optimization .107

<u>List of Figures</u> <u>Page</u>
Figure 3.S18 Total ion mobilograms from TIMS DC gradient voltage optimization
Figure 3.S19 Mobility (1/K <sub>0</sub> ) vs m/z heat maps from TIMS DC gradient voltage optimization109
Figure 3.S20 Regionally divided EIMs and MS1 spectra for the AbbVie starting mAb110
Figure 3.S21 Drug conjugations products of "native" conjugation for an IgG type 1 antibody111
Figure 3.S22 Overlay of total ion mobilograms for AbbVie starting mAb and ADC as a function of TIMS RF voltage
Figure 3.S23 Charge deconvoluted MS1 spectra of AbbVie ADC across mobility regions113
Figure 3.S24 Plot of calculated CCS vs average DAR for all AbbVie ADC mobility regions114
Figure 3.S25 EIMs for AbbVie starting mAb and all AbbVie ADC DAR species
Figure 3.S26 Charge deconvoluted MS2 spectra for released subunits
Figure 3.S27 Targeted MS3 CID fragmentation of Lc1 combining multiple fragmentation
energies117
Figure 3.S28 MS3 bbCID fragmentation of Lc1 combining multiple fragmentation energies118
Figure 3.S29 Targeted MS3 CID fragmentation of Lc1 combining multiple fragmentation energies
from a segmented 90 second analysis
Figure 4.1 Scheme of possible workflows supported by the MASH Native software129
Figure 4.S1 Software GUI of MASH Native
Figure 4.S2 Scheme of spectral summing workflow in MASH Native

<u>List of Figures</u> Page
Figure 4.S3 Spectral summing tool panel in MASH Native
Figure 4.S4 UniDec deconvolution support in the MASH Native process wizard
Figure 4.S5 MASH Native configuration panel
Figure 4.S6 Discovery complex-down data processing using MASH Native
Figure 4.S7 Targeted native top-down data processing with MASH Native
Figure 4.S8 Targeted complex-down data processing using MASH Native
Figure 4.S9 Internal fragment matching in MASH Native
Figure 4.S10 MASH Native user downloads by geographic region
Figure 5.1 Workflow of online 2D sSEC-RPLC-MS for global top-down analysis of a three-step
sequential extraction
Figure 5.2 Impact of 2D sSEC-RPLC-MS on separation performance and MS1 spectral quality for
identified proteins by global top-down proteomics
Figure 5.3 Protein IDs from top-down proteomics analysis of human heart tissue using 2D sSEC-
RPLC-MS and three-stage sequential extraction
Figure 5.4 Subcellular location GO for cytosolic, sarcomeric, and membrane protein extracts161
Figure 5.5 Mitochondrial proteins identified by top-down 2D sSEC-RPLC-MS and three-stage
sequential extraction

<u>List of Figures</u> <u>Page</u>
Figure 5.6 Nucleosome components identified by top-down 2D sSEC-RPLC-MS and three-stage
sequential extraction
Figure 5.S1 Triplicate top-down 1D SEC-MS analysis of 8-protein standard mixture165
Figure 5.S2 Triplicate top-down 1D RPLC-MS analysis of 8-protein standard mixture166
Figure 5.S3 Online top-down 2D sSEC-RPLC-MS analysis of 8-protein standard mixture167
Figure 5.S4 MS1 spectra of 8-protein standard mixture generated by 1D RPLC-MS and online 2D
sSEC-RPLC-MS
Figure 5.S5 Comparison of theoretical peak capacities from 1D RPLC-MS and online 2D sSEC-
RPLC-MS169
Figure 5.S6 Top-down 1D sSEC-MS analysis of TFA extract from human heart tissue170
Figure 5.S7 Comparison of CID fragmentation performance between 1D-RPLC-MS and 2D sSEC-
RPLC-MS analysis of MLC-V2171
Figure 5.S8 Histogram of all MS1 features observed in at least one extraction step binned by
molecular weight
Figure 5.S9 Overlap of subcellular GO term proteins identified between extracts
Figure 5.S10 Fragmentation of MDH2 by CID using online top-down 2D sSEC-RPLC-MS174
Figure AI.1 One-step azo extraction workflow and extraction performance summary201
Figure AT 2 WT and Rhm20 KO rat protein ID overlap and PCA 202

<u>List of Figures</u> <u>Page</u>
Figure AI.3 Volcano plot of differentially expressed proteins between WT and Rbm20 KO and
Western blot confirmation of Msrb2 expression changes
Figure AI.4 GO analysis of differentially expressed proteins between WT and Rbm20 KO204
Figure AI.5 String interaction network of differentially expressed proteins between WT and
Rbm20 KO
Figure AI.S1 Overlay of RPLC-MS TICs for WT and Rbm20 KO biological replicates208
Figure AI.S2 Histograms of protein IDs binned by LFQ intensity for WT biological
replicates
Figure AI.S3 Histograms of protein IDs binned by LFQ intensity for Rbm20 KO biological
replicates
Figure AI.S4 Boxplot of WT and Rbm20 KO expression changes for differentially expressed
proteins with nine highest -log <sub>10</sub> P values

<u>List of Tables</u> <u>Page</u>
Table 2.ST1 RPLC retention factor for fully reduced and partially reduced ADC subunits59
Table 2.ST2 EIC peak areas for partially reduced ADC subunits
Table 2.ST3 EIC peak areas for fully reduced ADC subunits
Table 3.ST1 Definition of relevant TIMS voltage parameters and locations applied88
Table 3.ST2 Calculated CCS values of AbbVie starting mAb as a function of TIMS RF voltage88
Table 3.ST3 Calculated CCS values of NISTmAb as a function of TIMS RF voltage89
Table 3.ST4 Calculated CCS values of AbbVie ADC as a function of TIMS RF voltage89
Table 3.ST5 Calculated MS1 masses for all AbbVie ADC DAR species90
Table 3.ST6 Calculated CCS values for all regions of AbbVie starting mAb mobility90
Table 3.ST7 Calculated CCS values for all regions of AbbVie ADC mobility91
Table 3.ST8 Calculated average DAR for all regions of AbbVie ADC mobility91
Table 4.S1 Deconvolution algorithms included in MASH Native and supported functions131
Table 5.ST1 Subcellular GO terms observed across extracts with gene counts and -log <sub>10</sub> FDR175
Table AI.ST1 Protein IDs by biological replicate for WT rats
Table AI.ST2 Protein IDs by biological replicate for Rbm20 KO rats207

## Chapter 1



Portions of section 1.2 have been published and are adapted from:

Melby, J. A. †; Roberts, D. S.†; <u>Larson, E. J.</u>; Brown, K. A.; Bayne, E. F.; Jin, S.; Ge, Y. "Novel Strategies to Address the Challenges in Top-Down Proteomics". *J. Am. Soc. Mass Spectrom.* **2021**.

#### 1.1 Introduction to Top-Down Proteomics

Proteins are the molecular machines that drive cell function, and are responsible for activities ranging from signaling, <sup>1–3</sup> to enzyme catalysis, <sup>4,5</sup> and immune response. <sup>6,7</sup> Assembly of proteins occurs at the end of the "central dogma of biology", where genetic information from DNA is transcribed to RNA and then translated into protein sequences. Each subsequent step in the process introduces additional complexity and proteoforms - a term indicating any protein product of a single gene<sup>8</sup> - include splicing variants, mutations, and post-translational modifications (PTMs). <sup>9</sup> The complexity of the proteome caused by a high number of possible proteoforms <sup>10</sup> is compounded by the dynamic range of protein expression levels. <sup>11,12</sup> These factors challenge efforts to monitor relative proteoform expression, a feature of the proteome known to cause alterations in function, <sup>13</sup> mark disease onset, <sup>14</sup> or indicate stage of disease progression. <sup>15</sup> Currently, the most widely-used tool to monitor proteome-wide expression changes is bottom-up proteomics. <sup>16–18</sup>

Bottom-up proteomics simplifies detection of proteins through enzymatic digestion of proteins into peptides prior to detection by mass spectrometry (MS) and tandem MS (MS2) analysis. This approach is facilitated by a plethora of MS instruments designed for sensitive peptide detection, highly efficient front-end separations, and well-established, automated data processing workflows. This approach allows sensitive detection of expression changes and is compatible with multiplexing and other high-throughput strategies. However, bottom-up proteomics faces several critical challenges when analyzing proteoforms including possible alterations to PTMs, detection bias between modified and unmodified peptides, and peptide to protein inference problems. Alternatively to bottom-up proteomics, top-down proteomics can provide a "bird's eye view" of proteoform-level changes. Top-down proteomics forgoes enzymatic digestion and introduces intact proteins to the MS, relying on gas-phase dissociation to

sequence the protein and localize PTMs.<sup>29,31,32</sup> This provides an unbiased view of the proteoform landscape by preserving labile modifications and enabling facile determination of relative proteoform expression.<sup>30,33</sup> Additionally, top-down proteomics can be performed in either denaturing or native conditions to preserve non-covalent interactions and protein complex association.<sup>34–36</sup> While top-down proteomics can provide critical insight into proteome changes, the implementation of top-down has been challenged by factors including the decreasing MS signal-to-noise as protein size increases,<sup>37</sup> underdeveloped front-end separations for intact proteins (Chapter 5), and a paucity of available software options relative to bottom-up proteomics.<sup>38</sup> In this chapter, I will provide context for how the field of top-down proteomics can address these challenges. I will detail recent advances and available techniques in the field of intact protein separations (1.2) and data processing software for top-down proteomics (1.3). Finally, I will discuss the utility of top-down proteomics for quality control and characterization of a prominent class of biotherapeutics, antibody-based therapeutics (1.4).

#### 1.2 Recent Progress in Development of Separations for Top-Down Proteomics

The complexity of the proteome remains a significant challenge to top-down proteomics, which necessitates the separation of intact proteins prior to the MS analysis.<sup>39–42</sup> As MS instruments capable of top-down analysis have become more widely available, the demand for the further development of intact protein separations has grown.<sup>29</sup> Despite the central roles played by LC in the development of bottom-up proteomics,<sup>43</sup> chromatographic separation of intact proteins remains underdeveloped.<sup>29,41</sup> However, recent improvements to liquid chromatographs,<sup>44,45</sup> advances in coreshell and monolithic stationary phases,<sup>46,47</sup> and the development of new column chemistries and selectivities<sup>48</sup> have greatly improved the separation resolution and efficiency of intact protein mixtures. Here, I will summarize recent progress in intact protein separations for

several important approaches used in the field of top-down proteomics including: reversed phase liquid chromatography (RPLC), size-based separations, non-denaturing separations, ion mobility spectrometry, and multidimensional LC (MDLC).

#### Reversed Phase Liquid Chromatography

The liquid separation technique employed most often in top-down, RPLC separates analytes by relative hydrophobicity. The standard RPLC workflow follows a "trap-and-elute" model with analytes loaded onto the hydrophobic stationary phase in an aqueous mobile phase where they are absorbed then eluted by increasing the percentage of organic solvent in the mobile phase. This causes analytes to elute in order from least hydrophobic character to most hydrophobic character. Similar to other absorptive modes of separation, RPLC is a high-resolution chromatographic technique (peak capacities >450 possible)<sup>49</sup> that yields predictable, reproducible, and robust separations. However, unlike some high-resolution chromatographic techniques, such as ion exchange chromatography (IEX), RPLC solvents are directly MS-compatible as they are comprised of volatile organic solvents and low amounts (< 0.2%) of volatile organic acids.<sup>50</sup>

Typically, RPLC is performed using a packed bed column containing mesoporous polymer particles or functionalized silica particles with ligands such as C2<sup>49</sup>, C4<sup>51</sup>, C8<sup>46</sup>, or a polyphenyl ligand.<sup>52</sup> These ligands are selected to have a lower hydrophobic character than the C18 ligands used for BUP or small molecule RPLC, which provide poor recovery in top-down proteomics.<sup>53</sup> Polymeric phases such as poly(styrene-divinylbenzene), or PLRP-S, have some advantages over the historically used fully-porous silica particles including greater chemical stability and reduced secondary interactions.<sup>54</sup> These materials are inexpensive and easy to home-pack, however, a key disadvantage to the use of PLRP-S material is lower mechanical stability with the maximum operating pressure commonly under 300 bar, less than half the pressure limit of silica-based

stationary phases and well under the 1200 bar operating pressure limit of modern UPLC systems.<sup>55</sup> Therefore, the initial production and subsequent rediscovery of superficially porous silica materials for intact protein separation by Kirkland and coworkers<sup>56</sup> motived the further development due to faster mass transfer kinetics and lower overall backpressure than fully porous silica. Development of these materials culminated in the release of HALO C4 3.4 µm 400 Å fused-core superficially porous material<sup>57</sup> and subsequent efforts have produced greater pore size materials (1000 Å) for improved intact protein separation efficiency.<sup>58</sup> While both polymeric and superficially porous packed bed stationary phases have experienced widespread adoption for RPLC-MS in top-down proteomics; non-porous particles, monolithic materials, and ordered stationary phase materials have all shown great promise in recent years. Here, contributions of these stationary phase materials for intact proteins will be discussed, but interested readers are referred to the excellent review by Astefanei *et al*<sup>53</sup>.

Development of non-porous, or "pellicular", stationary phase materials began with Horvath and coworkers<sup>59,60</sup> as a faster mass transfer alternative to the prevailing fully porous particle of the day.<sup>56,61,62</sup> Later extension to intact protein separations for both RPLC and IEX demonstrated the potential utility of pellicular phases for rapid, high efficiency analyses<sup>63,64</sup>, with intact protein separations performed for a five-protein mixture in as little as eight seconds<sup>63</sup>. Despite the advantages of pellicular phases, practical limitations including the high backpressure associated with optimal flowrates<sup>64</sup>, a need for high column temperature, and the associated system modifications needed for liquid separations performed beyond the vapor point of solvents<sup>65</sup> have greatly hindered widespread adoption of these materials. However, as the capabilities of commercially available liquid chromatographs increase, these materials may play a larger role. Alternatively, monolithic columns also possess faster mass transfer than porous packed bed

columns, but with substantially lower backpressure than either porous or pellicular phases. 66,67 This has led to a broader adoption of monolithic materials for intact protein separations and development of monoliths for RPLC, 68,69 IEX, 70,71 and even hydrophilic interaction liquid chromatography. 72,73 Although experiencing moderate success, trouble generating reproducibly sized monolithic structures and lower overall separation efficiency than porous or pellicular materials have prevented the full acceptance of monolithic materials. 74,75 This issue has been addressed through the development of ordered stationary phases over the past decade, 76 with micromachined "pillar-array" columns receiving great interest both industrially 77 and academically. 78–80 While work to improve these columns has yielded reported theoretical peak capacities >1,000,000 previously, 81 current machining method are incapable of generating pillar spacings small enough for practical use with intact proteins due to their low diffusion coefficients compared to peptides or small molecules.

#### Size-Based Separations

The broad range of protein molecular weights within a proteome can exceed five orders of magnitude, <sup>11</sup> making global top-down coverage of the proteome difficult. This challenge is most acute for large proteins because as protein size increases, the signal-to-noise ratio decreases due to an increased number of charge states and isotopomers. <sup>37</sup> Size exclusion chromatography provides a means to address this issue, separating analytes by their hydrodynamic radii, where the largest molecular weight species elute first and smallest species elute last. This is achieved not through affinity-based separation but using a porous stationary phase containing a distribution of pore sizes tailored to the size of the desired analyte, where larger analytes will be unable to diffuse into most pores and smaller analytes can diffuse into nearly all pores. Upon diffusion into a pore, the analyte enters a stagnant region of solvent and forward motion stops until the analyte diffuses back out of

the pore into the flowing region of the mobile phase. Recently, the Ge lab has developed serial size exclusion chromatography (sSEC) to improve chromatographic resolution and size-based proteome fractionation. Following sSEC fractionation with online RPLC-MS enabled the detection of proteoforms up to 223 kDa using a Q-TOF mass spectrometer. In contrast to conventional SEC methods which use only one separation column, the sSEC method links multiple columns of differing porosity to more effectively separate smaller proteoforms from large proteoforms, facilitating the characterization of high molecular weight proteins. Proteins in excess of 100 kDa that were previously only detectable using ultrahigh resolution MS, such as cardiac myosin binding protein C (140 kDa)<sup>85</sup> and myosin heavy chain (223 kDa), 6 could be characterized using online RPLC-MS/MS using a Q-TOF mass spectrometer. This work was further extended to characterization of large cardiac proteoforms, such as swine aconitate hydratase (82.5 kDa), using a 12T FTICR-MS without front-end RPLC separation.

In addition to SEC-based size fractionation, several other size-based proteome fractionation techniques have been developed. Tran and Doucette developed gel-eluted liquid fraction entrapment electrophoresis (GELFrEE) as an offline technique to bin proteins into size-selected fractions. Another method, termed Passively Eluting Proteins from Polyacrylamide gels as Intact species for MS (PEPPI-MS), has been developed for size-based proteome fractionation prior to LC-MS/MS. He PEPPI-MS method enables recovery of separated protein bands from SDS-PAGE gels using equipment common to biological and biochemical labs. Unlike GELFrEE or PEPPI-MS, SEC-based separation can fractionate proteins in both offline and online modes due to MS-compatibility of the mobile phases used. This affords sSEC greater flexibility and allows much higher sample throughput than other size-based separations.

### Non-Denaturing Separations

As the field of native top-down proteomics continues to grow, the need for native separation methods also grows. 36,90 Mobile phase compatibility with ESI is essential to the development of new separation selectivities or adaptation of previously developed techniques.<sup>91</sup> One separation mode with great promise for native separations is HIC, 92 where analytes elute in order from least to most hydrophobic, analogous to RPLC. Unlike RPLC, HIC selects by analyte surface hydrophobicity, beginning the separations using a high salt concentration in the mobile phase to "salt out" and retain proteins, then lowering salt content to elute proteins in order of increasing hydrophobic character on the surface. 92 However, the conventional HIC buffers such as sulfate or phosphate salts are non-volatile and incompatible with online MS analysis. 93,94 Recent work has allowed online coupling of HIC with MS using the volatile buffer ammonium acetate.<sup>94</sup> In collaboration with the late Andy Alpert from PolyLC, the Ge lab developed a series of morehydrophobic HIC materials that can separate proteins using MS-compatible concentrations of ammonium acetate while preserving protein structure. The HIC approach developed in the Ge enabled non-denaturing analysis of E Coli cell lysate in only 25 minutes. 94 The stabilizing effect of the volatile salt and limited time on column resulted in native-like charge state distributions for proteins, aiding the detection of large protein species up to 206 kDa and demonstrating the potential of online HIC-MS for both qualitative and quantitative top-down proteomics. Further development of HIC-MS by Chen et al. separated two intact IgG species, offering great potential for HIC-MS as a biotherapeutic characterization technique. 95

There is also significant interest in the development of capillary electrophoresis-MS (CE-MS) as a non-denaturing separation technique. <sup>96–98</sup> CE is a highly efficient separation technique which selects analytes based on their size and charge by applying a voltage potential across a capillary filled with buffered electrolyte solution. <sup>99</sup> Proteins migrate in CE in order of their

isoelectric point, which can be altered by sequence variants or charge altering PTMs such as phosphorylation, <sup>100</sup> acetylation, <sup>101</sup> or deamidation. <sup>102</sup> The wide variety of CE techniques that display complementary separation selectivity to conventional LC-MS methods and low sample volume requirements have made CE-MS a very attractive technique for native separations. <sup>103,104</sup> Because solvent gradients are not used to drive CE separation, CE avoids time consuming solvent equilibration and requilibration steps that are essential to avoid sample carryover in many LC-based separations. <sup>105</sup> Similar to SEC, CE can be performed under both native and denaturing conditions depending on the electrolyte solution that is chosen. <sup>103,106</sup> As new commercial systems and discrete devices are developed, <sup>107–109</sup> CE-MS may help to address the dearth of native separation options for top-down proteomics.

#### *Ion Mobility Spectrometry*

Although liquid phase separations remain the dominant separation approach used in top-down proteomics, the development and capabilities of ion mobility spectrometry (IMS) have exploded in just the past decade. 110–112 Techniques including traveling wave ion mobility spectrometry (TWIMS), 113 field asymmetric waveform spectrometry (FAIMS), 114 trapped ion mobility spectrometry (TIMS), 115 and structures for lossless ion manipulation spectrometry (SLIMS) have all expanded the utility of IMS beyond the limitations of more classical approaches such as differential ion mobility spectrometry (DIMS) 117 or drift tube ion mobility spectrometry (DTIMS). 118 Similarly to the suite of liquid separations presented above, each IMS tool relies on different selection mechanisms and exhibits unique benefits and limitations. 119 Dissimilarly to liquid separations, IMS is performed in the gas phase, commonly at sub-ambient pressures in the low vacuum region of the MS instrument. Fundamentally, separation by IMS occurs when the motion of ions under the influence of an electric field is impeded by the presence

of a neutral buffer gas. The mobility of an ion through the buffer gas, depends on the rotationally averaged collision cross section (CCS) of the analyte, with more compact ions having shorter drift times through the IMS device and larger ions having longer drift times when charge is equal. This enables filtering of ions by size or determination of CCS in some techniques, which may be used to probe alterations in analyte structure. 121,122

A key advantage of IMS is the high speed, with separations occurring on the second to millisecond timescale for intact proteins; a substantial improvement compared to the minute or hour timescale of liquid separations. 123-125 The fast analysis time of IMS also allows easy integration of IMS into existing LC-MS workflows, providing an additional dimension of separation without the need to modify existing LC conditions. Alternatively, using IMS in the direct infusion mode can circumvent the need for conditions that are compatible with analyte peak widths generated by CE or LC. 126,127 Direct infusion IMS-MS for intact protein analysis has shown success with all of the techniques listed above, but TWIMS and TIMS have been used the most extensively for intact protein work. TWIMS functions by applying a repeating pattern of oscillating DC voltage potential along the length of a drift tube filled with static drift gas. 128 The forward motion of ions with large CCS is impeded by the buffer gas, and voltage waves "overtake" these ions. The smaller the CCS of an ion, the fewer waves overtake the ion and the faster it moves through the TWIMS cell. TWIMS has proven to be a useful technique for structural elucidation and monitoring conformational stability. 129-131 Specifically, under native conditions through collision-induced unfolding (CIU), the structures of intact antibodies can be investigated. 130,132,133 TWIMS CIU is compatible with native top-down workflows and has shown promise as a separation technique for native top-down analysis of protein complexes. 134

Departing from traditional IMS designs, TIMS causes analytes to elute in order from largest CCS to smallest CCS.<sup>119</sup> In TIMS, analytes are pushed into the TIMS cell with a flowing buffer gas at fixed pressure, then trapped by an increasing DC voltage gradient in the first region of the TIMS cell (or accumulation region).<sup>135</sup> Ions with larger CCS or higher charge migrate further into the accumulation region of the TIMS cell before their forward motion is stopped by the applied voltage. The DC potential in the TIMS cell is then lowered to release trapped ions in order from largest to smallest CCS. There are several unique advantages to TIMS, including a compact cell design enabling hybrid instrument design,<sup>136,137</sup> easy integration with ultrafast<sup>138</sup> or slow scanning applications,<sup>139</sup> and flexibility of TIMS cell control.<sup>140,141</sup> Recent work showcases the potential of TIMS for native separations,<sup>136,142,143</sup> and the flexibility of TIMS design will facilitate its use in future either as a standalone technique or as a part of hybrid workflows.

#### Multidimensional Separations

Unlike peptides, proteins have a much more diverse range of physiochemical properties, <sup>144</sup> therefore, MDLC by combining multiple orthogonal separation modalities can be a useful approach to address the complexity of the intact proteome. <sup>29,41,145</sup> Although extensively used in bottom-up separations, the use of two-dimensional (2D) LC coupled to MS in top-down proteomics has been more recent. <sup>146–148</sup> Much of the 2DLC-MS work for top-down proteomics has used an "offline" coupling strategy, collecting fractions across the first dimension of separation (<sup>1</sup>D), then analyzing all fractions using the second dimension of separation (<sup>2</sup>D) interfaced directly with the MS. Offline <sup>1</sup>D separation allows samples to be buffer-exchanged or concentrated between dimensions, enabling use of traditionally MS-incompatible separation techniques. The Ge lab developed an offline 2DLC strategy coupling HIC and RPLC. <sup>147</sup> The orthogonality of HIC and RPLC separations extended the range of separable protein polarities and can be used to eliminate

the need for offline desalting of non-volatile buffers in HIC fractions as demonstrated by E coli cell lysate analysis. Valeja *et al.*<sup>149</sup> extended this to a three-dimensional (3D) LC approach, coupling HIC-IEX-RPC with offline <sup>1</sup>D HIC and <sup>2</sup>D IEX separation before third dimension (<sup>3</sup>D) online RPLC-MS.<sup>149</sup> This achieved a 14-fold improvement in protein identifications from human embryonic kidney cell lysate using 3D HIC-IEX-RPLC-MS compared to 2D IEX-RPLC-MS.<sup>149</sup> Alternatively, to enable better characterization of large proteoforms, Cai and Tucholski *et al.*<sup>83</sup> used a 2DLC approach coupling sSEC to separate proteins by size prior to RPLC-MS to separate by hydrophobicity.<sup>83</sup>

Though the advantages of MDLC are clear, the process of offline MDLC is timeconsuming and labor-intensive. Online MDLC strategies can alleviate this problem through automation, using a valve interface to automate transfer of eluent from <sup>1</sup>D to <sup>2</sup>D. <sup>145</sup> Coupling of orthogonal phases has been facilitated through the use of modulation strategies such as active solvent modulation, 150 stationary-phase assisted modulation, 151 and multiple heart-cutting. 152 While many coupling techniques have been developed for online 2DLC, <sup>145</sup> comprehensive mode, which transfers all eluent from <sup>1</sup>D to <sup>2</sup>D, has the greatest potential to aid global top-down proteomics. Several groups have employed online 2DLC for top-down proteomic analyses, 153-156 including a comprehensive high pH low pH RPLCxRPLC-MS method from the Schug group. Beyond 2DLC, Moore and Jorgenson developed an online comprehensive 3DLC system for peptide separation, which has not yet been extended for use with intact proteins. 157 In the coming years, the power of MDLC and the attraction of automation will likely lead to new combinations of separation modalities and routine MDLC analysis. Further extension of MDLC approaches to non-denaturing separation techniques is primed for rapid growth as the interest in native top-down proteomics grows within the top-down community.

#### 1.3 Data Analysis Challenges in Top-Down Proteomics

While data processing in bottom-up proteomics follows well-established workflows with a wide variety of software options, 21,158,159 workflows in top-down proteomics require more flexibility and suffer from a paucity of software options compared to bottom-up.<sup>38</sup> Typically, data analysis workflows for top-down proteomics begin with a spectral deconvolution step to identify fragment ion isotopic clusters in the MS2 spectra. If the top-down experiment took a targeted approach, the results of deconvolution are then compared to the known protein sequence for characterization. For discovery mode workflows, the results of deconvolution are input into a database search algorithm along with a list of possible protein sequences, allowing identification of unknown proteoforms. To address these data processing needs the commercially available ProSight family of software 160-162 and the freely available solutions such as the MASH software series<sup>38,163–165</sup> or MetaMorpheus<sup>166</sup> have developed software that is easy to use and capable of supporting these workflows. Although efforts have been made to standardize data processing as well as data reporting for top-down, 167 a lack of consensus about best practices regarding data processing remains. Here, I will summarize some of the challenges associated with top-down proteomics data deconvolution and database searching as well as discuss recent strides to address these challenges.

The term "deconvolution" can be used to denote either MS1-level or MS2-level data processing in the field of top-down proteomics, although the reporting of deconvolution results differs.<sup>38</sup> Deconvolution at the MS1 level identifies specific charge states within a distribution of multiply charged species,<sup>168</sup> and is often accompanied by the calculation of a "zero-charge" mass spectrum to simplify interpretation.<sup>169</sup> At the MS2-level, deconvolution is used to identify isotopic clusters and determine their charge, calculating the uncharged mass to identify potential fragment

ions<sup>170</sup> but typically omitting generation of a zero-charge spectrum. Currently, two key challenges in top-down deconvolution are isotopically unresolved data and the speed of data processing. Isotopically unresolved spectra are most commonly associated with native top-down, and pose challenges to charge state determination during MS1 deconvolution.<sup>38,171,172</sup> The Marty lab has developed a number of tools to address this challenge, beginning with UniDec<sup>171</sup> and later extending the software series to MetaUniDec<sup>173</sup> for batch processing to improve throughput. To address the second challenge to deconvolution, the Kohlbacher lab developed FLASHDeconv,<sup>174</sup> which sets the benchmark for fastest average scan processing time (whether profile or centroided) of less than 20 milliseconds. The speed of this approach has been leveraged to generate a real-time instrument control software, FLASHIda, not only improving data processing speed, but quality of generated data as well.<sup>175</sup> The extension of this platform to new instruments and data processing workflows, perhaps with real time searching as well, will continue to positively impact the top-down community for some time to come.

Although a number of database search tools exist for top-down proteomics, including MSPathFinderT,<sup>176</sup> pTop,<sup>177</sup> MS-Align+,<sup>178</sup> and TopPIC,<sup>179</sup> a consensus has not been reached regarding scoring of identifications made. This represents the first of two major challenges to top-down database searching: filtering and validation of identified proteoforms, and low ID numbers when MS2 performance is inadequate. Filtering and validation of proteoform IDs occurs differently in nearly all top-down software which are currently available.<sup>176–179</sup> In an effort to simplify data validation and reporting, and improve user control over identification stringency, Martin and coworkers developed TopPICR,<sup>180</sup> allowing *post hoc* filtering and scoring well-beyond the single step E-value or FDR based scoring commonly used,<sup>181,182</sup> and improving confidence in reported results. To address the negative impact of poor MS2 performance on proteoform

identifications, the Smith group developed Proteoform Suite, <sup>183</sup> which uses MS1 mass to identify proteoforms with MS1 spectra alone or in combination with MS2-level top-down or bottom-up spectral identifications. <sup>166</sup> Application of proteoform suite substantially increased the number of proteoforms over 60 kDa which were identified from human heart extract, however, these identifications remain controversial without MS2 data support. <sup>184</sup> In future, it is possible that MS1-level identifications could play a larger role in proteoform searching, but the utility identifications may be limited to a filtering step used to reduce the size of databases prior to MS2 database searching at the present time.

#### 1.4 Applications of Top-Down: Antibody-Based Therapeutics

Antibodies, or immunoglobulins, are a class of proteins that are part of the body's adaptive immune response<sup>185</sup> and neutralize foreign pathogens through specific complementary binding.<sup>186</sup> Formed from two heavy chains (Hc) and two light chains (Lc), antibodies take on a globular form with a hinge region connecting the constant region and the variable region, called the complementary determining region (CDR).<sup>187</sup> Efforts to engineer antibody CDRs for specific antigen recognition began in the 1970's and were first realized with the release of the monoclonal antibody (mAb) therapeutic, Orthoclone in 1986.<sup>188</sup> Since the first commercial success, the development of antibody therapeutics has exploded, with 162 FDA approved antibody-based therapeutics as of June 2022.<sup>189</sup> Along with this boom in popularity came the development of hybrid antibody-based therapies such as antibody-drug conjugates (ADC),<sup>190</sup> bispecific and trispecific (bsAb and tsAbs) antibodies,<sup>191,192</sup> Fab fragments,<sup>193</sup> and Fc-fusion proteins.<sup>194</sup> Despite the prominence and success of this drug class, the complexity of antibody-based therapeutics and evolving understanding of drug product stability as well as changing critical quality attributes (CQA) for each novel therapeutic make quality assurance difficult.<sup>195–197</sup> Additionally, the size of

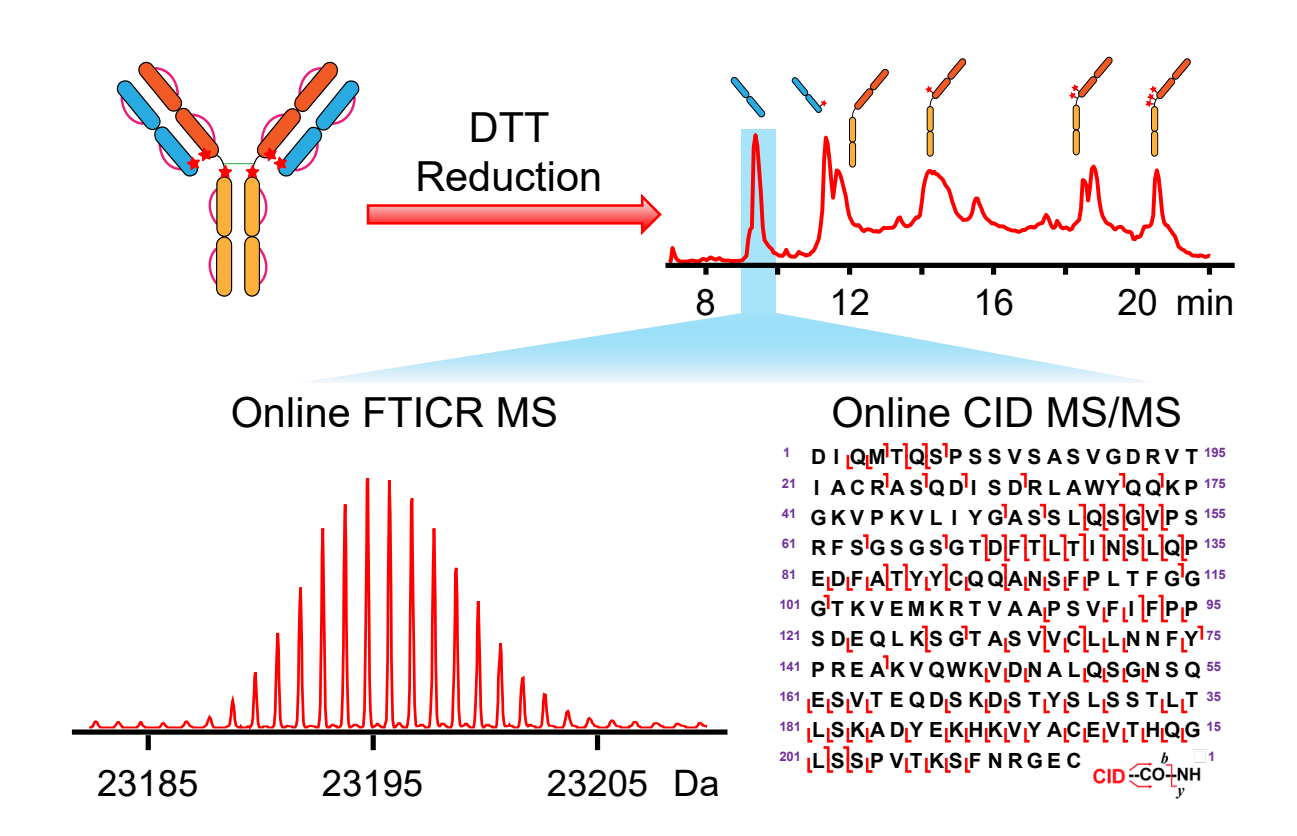
most antibodies (~150 kDa) can challenge characterization efforts. <sup>198</sup> Therefore, the need to revisit and reinvent previous quality control assays is a constant challenge to antibody-based therapeutic development.

Similar to discovery top-down experiments, bottom-up (termed "peptide mapping") remains the most commonly used MS characterization technique for mAbs and ADCs. 199 Though often used to determine the amount of deamidation<sup>200</sup> or oxidation<sup>201</sup> present in antibody-based therapeutics, a peptide mapping approach is known to alter these CQAs and induce additional artifactual modifications.<sup>202,203</sup> Additionally, determination of features such as relative glycoform expression or average drug-to-antibody ratios (DAR) of drug products is hindered in peptide mapping workflows due to differences in ionization efficiency of modified and unmodified peptides.<sup>27</sup> Middle-down digestion approaches<sup>204,205</sup> provide a useful alternative to peptide mapping that limit sample preparation time at elevated temperatures and enable determination of global features such as average DAR by producing ~25 kDa subunits after digestion. 198 This approach also allowed rapid determination of methionine oxidation in a forced degradation approach,<sup>206</sup> however, elevated temperature during digestion may still perturb oxidation levels. Alternatively, chemical reduction approaches forego digestion entirely, breaking disulfide bonds under ambient temperature using a reduction agent such as tris(2-carboxyethyl)phosphine (TCEP)<sup>207</sup> or dithiothreitol (DTT)<sup>208</sup> to generate two Lc (~25 kDa) and two Hc (~50 kDa) subunits from each antibody. 52,209 This approach is effective for determining CQAs, and is technically a top-down approach because it forgoes digestion. However, top-down approaches which eliminate steps to reduce the size of antibody-based therapeutics enable faster measurement duty cycle and provide the option to use non-denaturing conditions.

Top-down analysis of the NIST standard antibody, NISTmAb, on high-resolution Fourier transform ion cyclotron resonance MS enabled baseline isotopic resolution for determination of the monoisotopic mass of the 147 kDa intact antibody, and provided sequence characterization. <sup>210</sup> Another study using orbitrap MS with activated ion electron transfer dissociation for NISTmAb characterization enabled disulfide bond cleavage in the gas phase for deeper sequence coverage. <sup>211</sup> Recently, the inclusion in internal fragments for top-down sequence characterization of mAbs and ADCs on a UHMR orbitrap further improved sequence coverage to >75 % residue cleavage. <sup>212</sup> In addition to denaturing top-down opportunities, the use of non-denaturing conditions for antibody analysis creates a unique opportunity to not only preserve non-covalent interactors such as "native" cysteine-linked ADCs<sup>143</sup> or antigen binding, <sup>213</sup> but also probe changes in higher order structure of the antibodies. <sup>214</sup> Hybrid workflows such as complex-down analysis of non-covalently associated antibody drug products with TIMS demonstrate the potential of top-down proteomics to improve sample throughput and confidence in CQA measurements as both separations and MS instrumentation continue to improve.

# Rapid Analysis of Reduced Antibody Drug Conjugate by Online LC-MS/MS with Fourier Transform Ion Cyclotron Resonance Mass Spectrometry

Chapter 2



This chapter has been published and is adapted from:

Larson, E. J.; Zhu, Y.; Wu, Z.; Chen, B.; Zhang, Z.; Zhou, S.; Han, L.; Zhang, Q.; Ge. Y. Rapid Analysis of Reduced Antibody Drug Conjugate by Online LC-MS/MS with Fourier Transform Ion Cyclotron Resonance Mass Spectrometry. *Analytical Chemistry.* **2020**.

#### **Abstract**

Antibody drug conjugates (ADCs), which harness the high targeting specificity of monoclonal antibodies (mAb) with the potency of small molecule therapeutics, are one of the fastest growing pharmaceutical classes. Nevertheless, ADC conjugation techniques and processes may introduce intrinsic heterogeneity including primary sequence variants, varied drug-toantibody ratio (DAR) species, and drug positional isomers, which must be monitored to ensure the safety and efficacy of ADCs. Liquid chromatography coupled to mass spectrometry (LC-MS) is a powerful tool for characterization of ADCs. However, the conventional bottom-up MS analysis workflows require an enzymatic digestion step which can be time consuming and may introduce artifactual modifications. Herein we develop an online LC-MS/MS method for rapid analysis of reduced ADCs without digestion, enabling determination of DAR, characterization of primary sequence, and localization of drug conjugation site of the ADC using high-resolution Fourier transform ion cyclotron resonance (FTICR) MS. Specifically, a model cysteine-linked ADC was reduced to generate six unique subunits: light chain (Lc) without drug (Lc0), Lc with 1 drug (Lc1), heavy chain (Hc) without drug (Hc0), and Hc with 1-3 drugs (Hc1-3, respectively). A concurrent reduction strategy is applied to assess ADC subunits in both the partially reduced (intrachain disulfide bonds remain intact) and fully reduced (all disulfide bonds are cleaved) forms. The entire procedure including the sample preparation and LC-MS/MS takes less than 55 minutes enabling rapid multi-attribute analysis of ADCs.

#### Introduction

Development of antibody drug conjugates (ADCs) has become a focus of the pharmaceutical industry for the past two decades.<sup>215–217</sup> Coupling the targeting specificity of monoclonal antibodies (mAbs) with the cytotoxic small molecule drugs, ADCs are considered to be "magic bullets" which can kill the selected cell type and limit non-selective toxicity for normal cells.<sup>216,218,219</sup> This has generated considerable interest in ADC development, specifically for various types of cancer.<sup>215</sup> Small molecule drugs may be conjugated to the mAbs by 'native' cysteine conjugation, which breaks interchain disulfide bonds and attaches the cytotoxic drugs to the resulting free cysteines by stable chemical linkers. <sup>220</sup> This conjugation technique results in high heterogeneity for ADC products, causing drug positional isomers and a mixture of various drugto-antibody ratios (DAR) species. The average DAR is one of the essential quality attributes of ADC which may be associated with multiple properties such as pharmacokinetics, efficacy, safety and stability.<sup>220,221</sup> This necessitates the development of an efficient and accurate method for DAR determination. Additionally, modifications such as sequence truncation<sup>222</sup>, oxidation<sup>223</sup>, and glycosylation<sup>224</sup> which originate from the starting mAb and any following modification that occur to the mAb and drug linker components during the ADC manufacturing process may also impact ADC function, further convoluting ADC analysis. To ensure safe, stable, and efficacious use of ADCs, a robust assessment of multiple quality attributes is needed during both drug development and quality control stages.<sup>215</sup>

Among various analytical strategies that have been utilized to characterize ADCs, liquid chromatography with mass spectrometry (LC-MS) is a method of choice. <sup>225,226</sup> Typically, bottom—up MS with Trypsin or Lys-C digestion is used for analysis of ADC digestion. but it has intrinsic limitations for ADC characterization. <sup>26,198,227,229</sup> Moreover, bottom—up requires a lengthy sample

preparation procedure which may induce artifactual modifications to the ADCs.<sup>26</sup> Recently, intact MS has been utilized to analyze ADCs providing a broader view of ADC heterogeneity than bottom-up MS and has allowed determination of DAR value and detection of glycovariants. 230-232 However, it cannot effectively characterize the primary sequence variants of the ADC and conjugated drugs due to the lack of tandem MS (MS/MS) information. Top-down MS/MS strategies have been applied in characterization of intact therapeutic mAbs previously, but it has been challenging to perform efficient fragmentation or achieve baseline isotopic resolution due to the high molecular weight of the mAb.<sup>210</sup> Additionally, achieving isotopic resolution at the MSlevel was very time-consuming with one study needing >75 minutes to isotopically resolve the mAb. 210 Although ADCs are similar in size to mAbs, their analysis by intact top-down MS/MS is precluded by the extremely high heterogeneity. To overcome this, middle-down digestion<sup>233</sup> of ADCs can be performed where enzymes such as immunoglobulin gamma-degrading enzyme of Streptococcus pyogenes (IdeS)<sup>234</sup> or Gingipain K (KGP)<sup>235</sup> are able to produce the subunits of approximately 25 kDa in mass. Such a middle-down approach offers a comprehensive overview of the micro-variants associated with each subunits and facilitates greater MS/MS efficiency of the subunits than top-down MS/MS of an intact ADC. 198,236,237 Nevertheless, the process of digestion is still laborious, and the enzymes required are costly.

One technique that offers rapid generation of ADC subunits without the need of enzymatic digestion is chemical reduction, which breaks disulfide bonds to generate light chain (Lc) subunits (~25 kDa) and heavy chain (Hc) subunits (~50 kDa). This technique is particularly useful for molecules which are unstable in acidic, denaturing conditions such as cysteine-linked ADCs. Recently, Kelleher and coworkers reduced a model mAb and used front end high-field asymmetric wave form ion mobility coupled with an Orbitrap Eclipse<sup>TM</sup> Tribrid<sup>TM</sup> mass spectrometer (FAIMS-

MS/MS) to characterize Lc and Hc subunits by MS/MS.<sup>127</sup> Although the reduced mass strategy has also been applied to ADC analysis to monitor the intact mass of subunits,<sup>238,239</sup> the lack of MS/MS and high-accuracy MS data prevents confident subunit identification and assessment of quality attributes.

For the first time, we have developed a LC-MS/MS strategy for the rapid analysis of reduced ADCs using online reverse-phase (RP)LC coupled with ultrahigh-resolution Fourier transform ion cyclotron resonance (FTICR) MS. A concurrent reduction strategy was applied to assess subunits both in the partially reduced form (with interchain disulfide bonds cleaved but intrachain bonds intact) and the fully reduced form (with all disulfide bonds cleaved) (Figure 1). This method enables isotopic MS resolution and high-accuracy mass measurement for the reduced ADC subunits and allows us to monitor the light chain subunits (Lc) and heavy chain (Hc) subunits with various drug conjugations on a chromatographic timescale, for the first time. This integrated concurrent reduction with LC-MS/MS strategy offered rapid determination of multiple ADC quality attributes such as robust DAR quantitation, primary sequence characterization and drug conjugation region localization in less than 55 minutes.

#### **Materials and Methods**

## Reagents

HPLC grade water and acetonitrile (ACN) were purchased from Fisher Scientific (Fair Lawn, NJ). Difluoroacetic acid (DFA), 2-amino-2(hydroxymethyl)-1-3-propanediol hydrochloride (Tris-HCl), dithiothreitol (DTT), and guanidine hydrochloride (guanidine HCl) were purchased from Sigma-Aldrich (St. Louis, MO).

#### Sample Preparation

Model cysteine-linked ADC was provided by AbbVie (North Chicago, IL). For partial reduction, ADC was incubated in 20 mM DTT in 50 mM Tris buffer at pH 8.0 for 30 minutes at 25 °C in the absence of light. For full reduction, ADC was incubated in 20 mM DTT and 6 M guanidine HCl in 50 mM Tris buffer at pH 8.0 for 30 minutes at 25 °C in the absence of light. Prior to analysis, the fully reduced sample was desalted using a Pierce Protein Concentrator PES 10 kDa molecular weight cutoff filter (Thermo Fisher Scientific, Waltham, MA) by washing the sample five times with 0.1% DFA in water.

## LC-MS/(MS)

An ACQUITY UPLC M-class system (Waters, Milford, MA) was coupled to a solariX XR 12 Tesla FTICR mass spectrometer (Bruker Daltonics, Billerica, MA). A 150 x 1 mm BioResolve RP mAb polyphenyl column with 2.7 µm particles and 450 Å pore size (Waters, Milford, MA) was used for RPLC separation. For both the partially and fully reduced subunits, the same LC conditions were used: a 25 minute gradient with 60 °C column heating and a flow rate of 100 μL/min. Mobile phase A (MPA) was 0.1% DFA in water, and mobile phase B (MPB) was 0.1% DFA in ACN. The gradient began with a hold at 20 % MPB which lasted 5 minutes. The MPB was then increased to 40% MPB at 19 minutes, then 100% MPB at 21 minutes. Finally, the column was equilibrated at 20% MPB with a hold from 21.1 to 25 minutes. For the mass spectrometer, the endplate offset and capillary voltage were set to -500 V and 4500 V, respectively. The nebulizer gas pressure was set to 0.5 bar, with a dry gas flow rate of 4 L/min at 220 °C. The skimmer voltage, octopole RF amplitude, and collision cell RF were optimized at 60 V, 300 Vpp, and 1500 Vpp, respectively. For MS spectral collection, the quadrupole low mass was set to 500 m/z with a scan range of 500 to 3000 m/z. The ion accumulation time was optimized at 100 ms and the file size was 2,000,000 points. The collision cell voltage was set to 1.5 V. For MS/MS spectral collection the quadrupole low mass was set to 200 *m/z* with a scan range of 200 to 2500 *m/z*. The ion accumulation time was optimized at 400 ms and the file size was 1,000,000 points. Seven collisional energies were used for both the partially reduced and fully reduced ADC subunits. For the partially reduced ADC subunits 10, 15, 20, 22.5, 25, 27.5, and 30 V were used. For the fully reduced ADC subunits 10, 12.5, 15, 17.5, 20, 25, and 30 V were used.

# Data Analysis

All data were processed and analyzed using Compass DataAnalysis 4.3 (Bruker Daltonics, Billerica, MA) and MASH Explorer.<sup>240,241</sup> For DAR calculation, extracted ion chromatograms (EICs) were generated from the top five most abundant charge states with a window of 0.05 *m/z*. Subunit EICs were smoothed using the Gaussian smoothing algorithm in Compass DataAnalysis 4.3, smoothing to one data point per three seconds of data acquisition. The area under the curve (AUC) was integrated and DAR was calculated using the AUC values for individual subunits in the following equation (Equation 1):

$$DAR = 2\left[\left(\frac{Lc1}{Lc0 + Lc1}\right) + \left(\frac{Hc1}{Hc0 + Hc1 + Hc2 + Hc3}\right) + 2\left(\frac{Hc2}{Hc0 + Hc1 + Hc2 + Hc3}\right) + 3\left(\frac{Hc3}{Hc0 + Hc1 + Hc2 + Hc3}\right)\right]$$

Equation 1 was adapted from the previously published method for calculating DAR in a middle-down analysis of an ADC.<sup>225</sup> Maximum entropy was used for spectrum deconvolution with resolution set to 100,000 for high resolution spectra. All observed charge states were used for deconvolution. For peak picking, the SNAP algorithm was used with a quality threshold of 0.5 and an S/N lower threshold of 3. All fragment ions were manually validated using MASH Explorer.

#### **Results and Discussion**

Concurrent Reduction Strategy

Reduction of the model cysteine-linked ADC (partial or full) breaks interchain disulfide bonds and produces six distinct subunits (Figure 2.1); two light chain (Lc) and four heavy chain (Hc) variants. The Lc subunits can be conjugated to no drug (Lc0) or 1 drug (Lc1), and Hc subunits can be conjugated to no drug (Hc0) or 1–3 drugs (Hc1–3, respectively). Of the subunits generated during reduction, Hc1 and Hc2 have three possible drug positional isomers, whereas the rest of the subunits have only one possible form. The ADC can be analyzed both at the partial reduction level (intrachain disulfide bonds are intact) and at the full reduction level (all disulfide bonds are cleaved) (Figure 2.1). Partial reduction can be achieved by incubation with 20 mM DTT in 50 mM Tris buffer at pH 8.0 for 30 minutes at 25 °C, whereas full reduction requires both 20 mM DTT and 6M guanine HCl in 50 mM Tris buffer at pH 8.0 for 30 minutes at 25 °C during incubation.

## RPLC-FTICR MS

The six subunits in both the partially and fully reduced form can be effectively separated using RPLC-FTICR-MS (Figure 2.2). We have shown that the separation of both the partially and fully reduced subunits has been highly reproducible across replicate analyses (Figure 2.S1 and 2.S2). The separation of partially reduced ADC subunits yielded overall better separation performance in comparison to that of fully reduced ADC subunits. Each subunit was well separated in the chromatogram, with Lc0, Lc1, Hc0, and Hc3 subunits achieving baseline resolution (Figure 2.2A). For Hc1 and Hc2 subunits, three presumptive drug positional isomers can be detected, although baseline resolution of theses isomers was not achieved. Separation of fully reduced subunits showed stronger retention than partially reduced species (Figure 2.2B and Table 2.S1). An increase in retention factor (K') of fully reduced subunits relative to partially reduced subunits was detected (Table 2.S1). The observed difference in K' between the two reduction techniques indicates that retention time may be used as a qualitative metric to assess the reduction state of a

subunit peak based on the generated chromatogram alone. The separation of fully reduced subunits also displayed lower selectivity and broader peak widths than the partially reduced sample resulting in incomplete resolution of Lc1 and Hc0 (Figure 2.S3). This might be due to the higher denaturing level of subunits inducing more secondary interaction with the column. Additionally, only two presumptive positional isomers were observed for both Hc1 and Hc2.

This RPLC-MS method can effectively separate partially reduced and fully reduce ADC subunits, which enables the calculation of DAR, an important quality attribute for characterization of ADCs. To calculate the DAR, EICs were generated from the top five charge states for each subunit in both the partially reduced and fully reduced form and the AUC was utilized to calculate DAR (Figure 2.2). The Hc subunits elicit a lower instrumental response than Lc subunits. To account for this, Equation 1 calculates the drug-to-subunit ratio (DSR) for the Lc and Hc separately before it combines the DSR values to calculate the DAR value. An average DAR value of  $3.1 \pm 0.1$  was calculated for the three partially reduced replicates (Figure 2.S1) and  $3.0 \pm 0.1$  for the three fully reduced replicates (Figure 2.S2). Therefore, despite differences in separation performance, both fully reducing and partially reducing methods are reliable and reproducible for determining the average DAR (Table 2.S2 and 2.S3). These values are in good agreement with the value determined by hydrophobic interact chromatography coupled with ultraviolet detection (Figure 2.S4).

LC-MS analysis of fully and partially reduced subunits revealed noticeable differences between the charge state distribution and abundance (Figure 2.3 and 2.S5). For the Lc0 subunit, the number of charge states observed in the fully reduced form was more than twice that of the partially reduced form (Figure 2.3A). In addition to a shift in the charge state of the most abundant peak for the fully reduced subunit ( $Lc0^{22+}$  instead of  $Lc0^{14+}$  for the partially reduced subunit), the

intensity of the most abundant peak for the fully reduced subunit was less than one fifth of that for the partially reduced subunit (Figure 2.3A). These differences were even more pronounced for Hc1 (Figure 2.3B), with the intensity of the most abundant peak for the fully reduced Hc1 subunit at charge state 49<sup>+</sup> over an order of magnitude less than that of the most abundant peak for the partially reduced Hc1 subunit at charge state 33<sup>+</sup>. These trends were also observed for the Lc1, Hc0, Hc2, and Hc3 subunits (Figure 2.S5). We postulate that these differences are caused by the intrachain disulfide bonds in the partially reduced subunits shielding regions of the subunit during the ionization process<sup>242</sup>, limiting the number of charges which the partially reduced form will gain during ionization. The fully reduced form of the subunit has no such protection and takes on a greater number of charges during ionization as a result. While this difference in ionization behavior has no impact in the TIC (Figure 2.2), it greatly impacts detection using the base peak chromatogram profile, with reduced intensity and signal to noise (S/N) of fully reduced Hc chromatographic peaks most severely impacted (Figure 2.S6).

The deconvoluted mass spectra of the Lc and Hc subunits displayed the high resolving power of FTICR MS (Figure 2.4). All subunits are isotopically resolved with partially reduced subunits showing baseline resolution, despite the short elution time of each subunit peak in the RPLC separation. The chromatographic peak width (in seconds) determined the number of MS scans which could be collected and averaged for each subunit. Considering the free induction decay time of a single FTICR scan was 2.8 seconds using the specified conditions, isotopic resolution was achieved for peak widths as low as 12 seconds (partially reduced Hc3), or four MS scans. While the wider peaks of the fully reduced subunit separation allowed the collection of a greater number of MS scans, baseline isotopic resolution for fully reduced Hc subunits was not achieved. This is likely due to the decreased S/N value of fully reduced subunits caused by

spreading subunit signal over a greater number of charge states (Figure 2.3). The experimental mass spectra of fully reduced subunits were in better agreement with theoretical isotopic distributions than partially reduced experimental mass spectra (Figure 2.4), likely due to the greater MS scan number collected from the broader fully reduced chromatographic peaks (Figure 2.2). One factor which initially challenged the isotopic resolution of subunits was adduct formation between the subunits and DFA during the chromatograph process (Figure 2.S7). Such adduct formation decreased the intensity of the subunits as the signal intensity of the subunits distributed between subunits without DFA adducts and subunits with DFA adducts. As demonstrated, this problem was successfully addressed by increasing MS skimmer voltage from 30 V to 60 V, which eliminated DFA adducts and facilitated full isotopic resolution (Figure 2.S7).

By intact mass analysis, the identity of each subunit can be confirmed at the MS level. A mass shift of +1316.78 Da reflects a drug conjugation event. All Hc subunits displayed an additional shift of +1444.50 Da corresponding to G0F glycan attachment. None of the Hc subunits were observed without the glycan bound and no additional glycoforms were observed for this model ADC (Figure 2.4). The deconvoluted MS data of Hc subunits also displayed a –128.07 Da shift (Figure 2.4). This corresponds to C-terminal lysine clipping, a common modification for antibodies.<sup>204,243</sup> The ultrahigh resolution FTICR MS offers high mass accuracy, which helps unambiguously distinguish the small mass difference (0.35 Da) between a drug conjugation event (+1316.78 Da), and a bound glycan (+1444.50 Da) with C-terminal lysine clipping (-128.07 D). Conversely, the reported large MS mass error in the previous study<sup>239</sup> may be insufficient for confident MS-level subunit identification.

Deconvoluted MS spectra showed the reduction state of each subunit. Every intact intrachain disulfide bond in the subunit caused a -2 Da mass shift from the fully reduced subunit

mass. Therefore, reduction of two intrachain disulfide bonds in Lc subunits and four in Hc subunits resulted in a 4 Da and an 8 Da mass shift, respectively, between the partially and fully reduced forms. For the fully reduced subunits mass shifts of + 4 Da were observed for both Lc subunits and + 8 Da for all Hc subunits compared to the partially reduced subunits (Figure 2.4). This indicated that fully reduced species had no intact intrachain disulfide bonds, and all intrachain bonds were intact for the partially reduced subunits, confirming that reduction state is easily controllable by our concurrent reduction strategy. The reduced mass strategy allows facile determination of DAR, glycan identity, and primary modifications through ultrahigh resolution online LC-FTICR MS in less than 55 minutes. The ability to determine multiple critical quality attributes of ADC in a single LC-FTICR MS run makes this method ideal for pre-clinical studies.

## RPLC-FTICR MS/MS

Reduced ADC subunits were further characterized by online LC-MS/MS using collision-induced dissociation (CID) (Figure 2.5 and 2.6). We have shown that LC-MS/MS using CID yielded 34% residue cleavage of Lc0 when applying 25 V of collisional energy, and 13% residue cleavage of Lc1 when applying 17.5 V of collisional energy. While the percentage of residue cleavages for Lc1 is diminished compared Lc0, drug conjugation to the Lc1 subunit was confirmed through the presence of drug conjugated fragment ions ( $y_{96}^{8+}$  and  $y_{139}^{13+}$ , Figure 2.5B). Additionally, drug conjugation on Lc1 could be localized to C214 because  $b_{207}$  was not observed in the drug conjugated form. Since this is the first use of fragmentation for the reduced ADC analysis, no benchmark exists for LC-MS/MS or MS/MS performance in the previous literature. Nevertheless middle-down MS methods can provide reference LC-MS/MS data for Lc subunits. Our previous middle-down study yielded 35% residue cleavage for Lc0 when performing LC-MS/MS using

electron transfer dissociation (ETD) and 15% residue cleavage for the drug conjugated Lc1 subunit. 198

Decreased percentage of residue cleavages of the drug conjugated Lc is presumably due to the preferential fragmentation of the drug and linker, which generated several high abundance species during the CID process (Figure 2.S8).  $^{227}$  In addition to drug conjugation the presence of intrachain disulfide bonds was shown to negatively impact fragmentation efficiency. Partially reduced Lc subunits achieved only 4% and 2% residue cleavage for Lc0 and Lc1, respectively, due to the intrachain disulfide bonds (Figure 2.S9 and 2.S10), however drug-conjugated fragment ions were still observed ( $y_{96}^{6+}$  and  $y_{97}^{6+}$  in figure 2.S10). Although partially reduced subunits allow rapid MS-level quantitation, MS/MS analysis necessitates the use of fully reduced subunits to achieve maximum percentage of residue cleavages for subunit characterization.

Fragmentation of the fully reduced Lc0 subunit yielded 52% residue cleavage when combining the seven fragmentation energies listed in the methods section (Figure 2.5A). LC-MS/MS of fully reduced Lc1 displayed 21 % sequence using the same fragmentation energies (Figure 2.5B). Combining multiple CID energies for each subunit offered higher percentage of residue cleavages without compromising the speed of LC separation or the requirement of a specific instrument with various MS/MS techniques. A previous study reported 18% residue cleavage of the Lc0 subunit by CID and coverage of 62% when combining CID, ETD, and ultraviolet photodissociation.<sup>237</sup> Our LC-MS/MS method offered comparable fragmentation efficiency using a single commonly available fragmentation technique, CID, by combining fragments from multiple dissociation energies.

Similar to the results obtained for the Lc subunits, Hc subunits yielded greatly increased fragmentation efficiency in the fully reduced form compared to the partially reduced form (Figure

6 and Figures 2.S11 – 2.S17). The percentage of residue cleavages achieved for fully reduced Hc1 with one fragmentation energy (15 V) was 11%, increasing to 15% residue cleavage when combining the CID energies specified in the methods section. Although we are not aware of any literary precedent of LC-MS/MS analysis of drug conjugated Hc subunits, one study has investigated the fragmentation of a model mAb Hc subunit. This study achieved 11% residue cleavage of the fully reduced Hc using CID alone. To increase the coverage of the model mAb Hc, electron capture dissociation (ECD) fragmentation was also employed to yield 38% residue cleavage for the Hc when combining both CID and ECD. The lowered fragmentation efficiency observed in this study is likely due to a combination of two factors. First, in the case of the model mAb the total mass of Hc species is represented in one chromatographic peak. In our study, the total Hc mass is spread between four possible states of drug conjugation, lowering overall signal intensity for each species. Second, the previous model mAb study employed a 21 T FTICR 236, which offers a faster scan acquisition rate<sup>244</sup> than can be achieved with the 12 T FTICR used in this work and is capable of collecting a greater number of MS scans during online separations.

Sequence coverage of fully reduced Hc subunits was sufficient to confirm drug conjugation, localize conjugation region, monitor glycan state, and confirm C-terminal lysine clipping. Interestingly, MS/MS analysis of the fully reduced Hc0 did not show a marked difference from fully reduced Hc1 as was observed for Lc0 and Lc1. The achieved percentage of residue cleavages for Hc0 was 14%, comparable to the percent residue cleavage for Hc1 (Figure 2.S12). This is likely due to the location of drug conjugation in Hc subunits is in the middle of the sequence as opposed to drug attachment on the C-terminal residue for Lc1, which shows a paucity of y ions near the C-terminal. For drug conjugated Hc subunits, conjugated drugs do not impact

fragmentation dramatically because a pre-existing scarcity of labile bonds near the drug conjugation region limits fragmentation in that region even without drug conjugation.<sup>127</sup>

Conceivably, the MS/MS analysis of Hc subunits was hindered due to their large size, the decreased abundance of charge states relative to Lc subunit charge states and the lower S/N of Hc subunits relative to Lc subunits (Figure 2.3 and 2.6). Drug conjugation could, however, be localized to the region between C203 and A235 using  $b_{203}^{18+}$  and  $y_{215}^{19+}$ . Of the cysteine residues in this region (C203, C224, C230, and C233) it is highly unlikely that the drug is conjugated to C203. C203 is part of an intrachain disulfide bond and should not break under kinetically controlled reduction during the drug conjugation process which targets interchain disulfide bonds. Additionally, broken intrachain bonds during drug conjugation may lead to Hc species conjugated with more than 3 drugs, but none were observed in the MS spectra. Nevertheless, fragmentation near the hinge region was limited, thus preventing the determination of the drug conjugation site.

#### **Conclusion**

In summary, we have developed an LC-MS/MS method for the rapid analysis of reduced ADCs at the subunit level using concurrent reduction strategy for multi-attribute analysis of ADCs including determination of DAR value, detection of sequence variants and characterization of drug conjugation. The DAR value was determined using both partial and full reduction techniques to be  $3.1 \pm 0.1$  and  $3.0 \pm 0.1$  respectively, and subunit identity was confirmed by both the intact mass and MS/MS characterization using CID. The partial reduction technique offered better peak shape in RPLC and rapid MS characterization of subunits in the model cysteine ADC, with a total sample preparation and LC-MS analysis in less than 55 minutes but limited residue cleavages by online LC-MS/MS. Full reduction of the model ADC provided robust LC-MS/MS data with a greater number of residue cleavages, localization of drug conjugation region and confirmation of attributes

observed at the MS and MS/MS-level, but lower S/N at the MS-level than the partial reduction technique. Our method leverages the power of ultrahigh resolution FTICR to achieve MS and MS/MS characterization of a reduced mass ADC on a chromatographic timescale for the first time. We have shown that integration of concurrent reduction strategy with LC-MS/MS provides a rapid and robust tool for multi-attribute ADC analysis which can be added to the suite of techniques used to characterize novel antibody-based therapeutics.

# Acknowledgement

We would like to thank Xiaoli Liao from AbbVie Process Chemistry Department for providing us with the ADC sample used in this study. Financial support was kindly provided by AbbVie. Y.G would like to acknowledge NIH grants, GM125085 and high-end instrument grant S100D018475.

## **Figures**

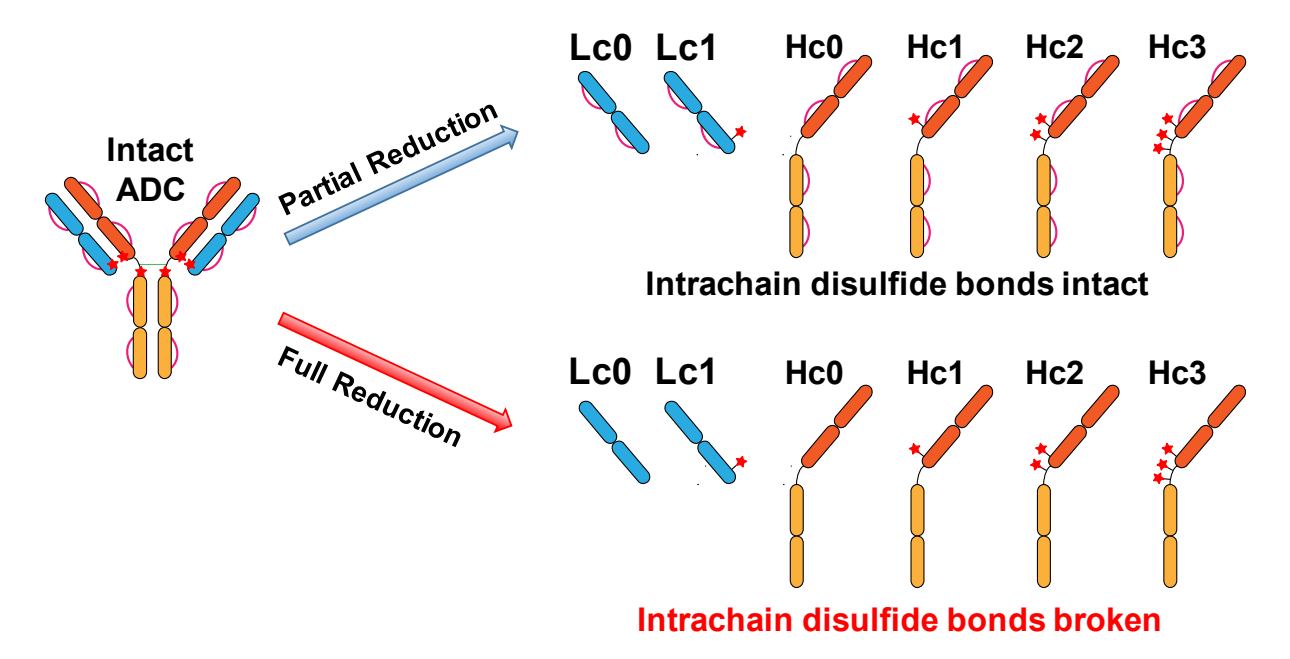


**Figure 2.1**: Schematic of potential products from a representative cysteine-linked antibody-drug conjugate (ADC) after full and partial reduction. This generates light chain subunits (Lc) with 0 or 1 conjugated drugs (Lc0 and Lc1 respectively) and heavy chain (Hc) subunits with 0, 1, 2, or 3 drugs (Hc0, Hc1, Hc2, and Hc3 respectively). Hc1 and Hc2 have three possible drug positional isomers. Positional isomers are not demonstrated in this figure. Partial reduction using DTT (20 mM) cleaves interchain disulfide bonds but preserves intrachain disulfide bonds (shown in pink arcs). In contrast, full reduction using DTT (20 mM) with the addition of guanidine HCl (6 M) during sample preparation cleaves both inter- and intrachain disulfide bonds in the ADC.

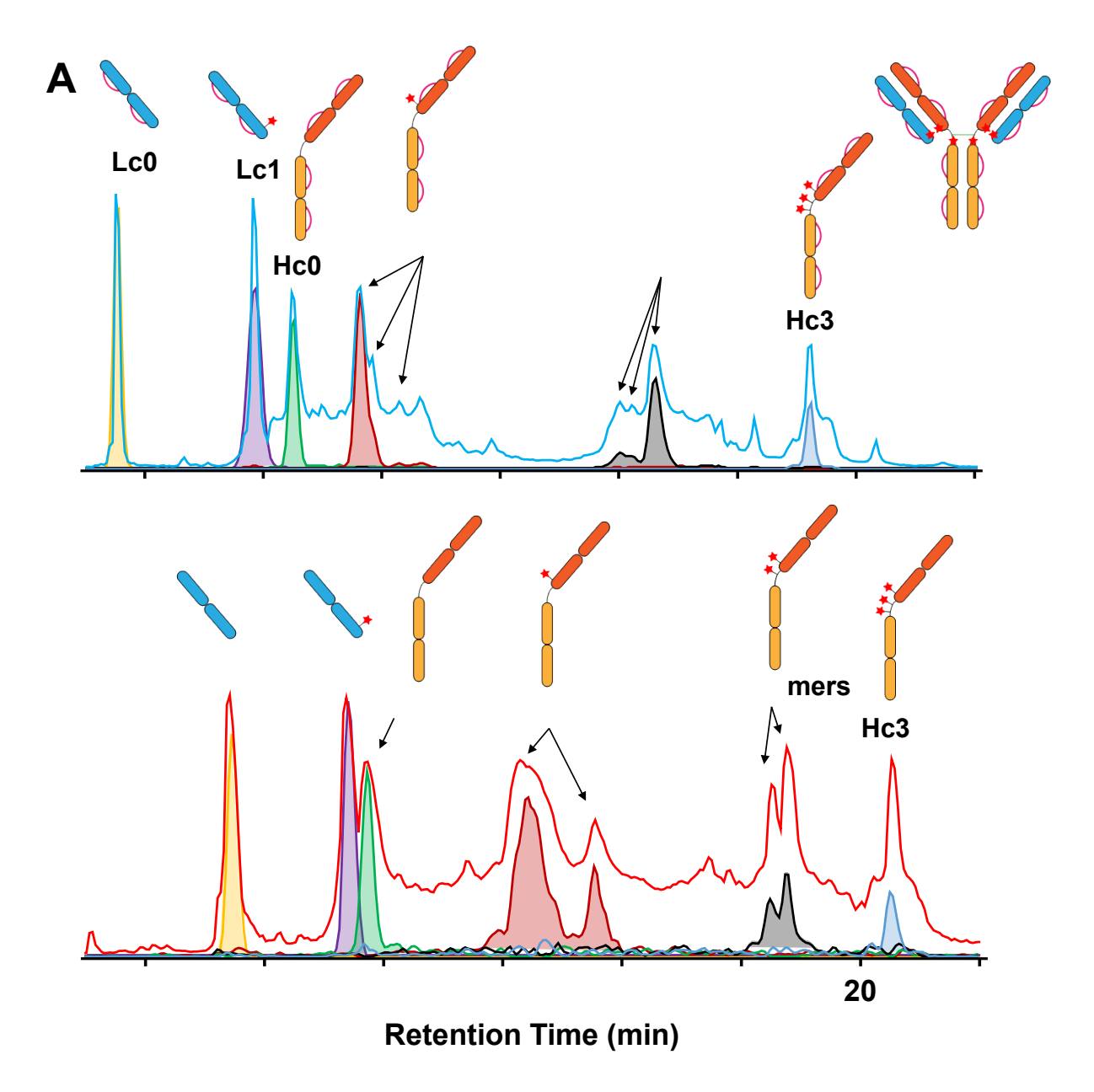


**Figure 2.2.** Online RPLC-MS of partially reduced ADC subunits (A) and fully reduced ADC subunits (B). The total ion chromatogram, shown in blue for panel A and red for panel B, is overlaid with the extracted ion chromatograms (EIC) for each subunit. The EICs shown were generated using the top-five most abundant charge states of each subunit as described in the methods section. The relative intensity of Lc EIC peaks is scaled to the intensity of the most abundant Lc peak and the relative intensity of Hc EIC peaks is scaled to the intensity of the most abundant Hc peak.

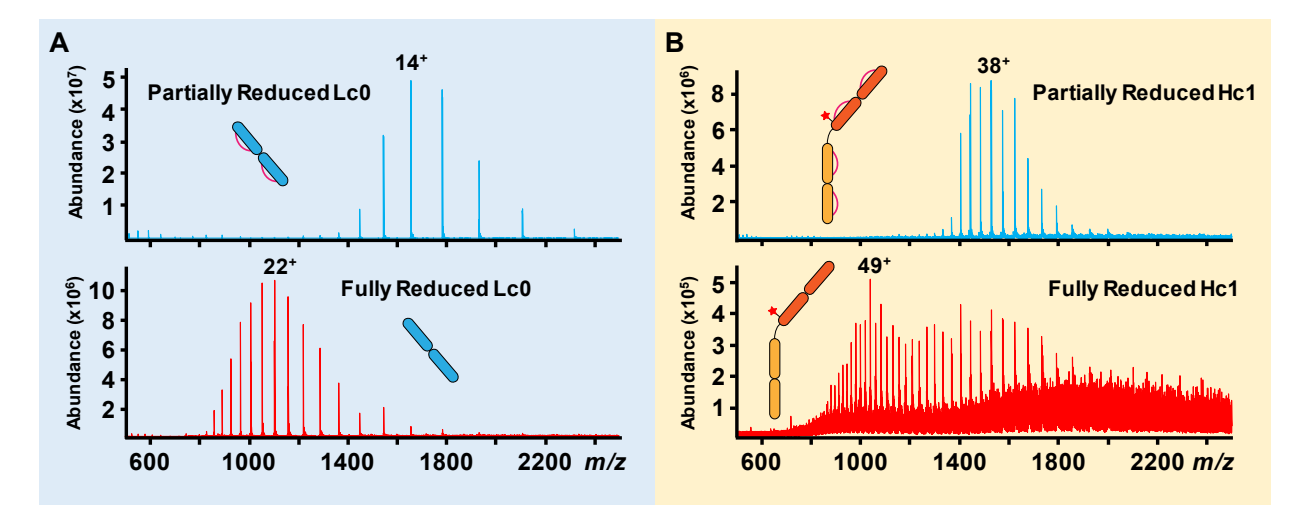


**Figure 2.3.** Full mass spectra of the partially and fully reduced Lc0 (A) and the most abundant conjugation isomer of Hc1 (B). The presence of intrachain disulfide bonds appears to limit the number of surface-exposed basic residues during ionization, resulting in a charge state distribution with higher m/z values and fewer charge states overall. This allows easier detection of Lc and Hc species in MS when using either base peak chromatograms or extracted ion chromatograms providing more robust MS quantitation than the fully reducing sample preparation procedure.

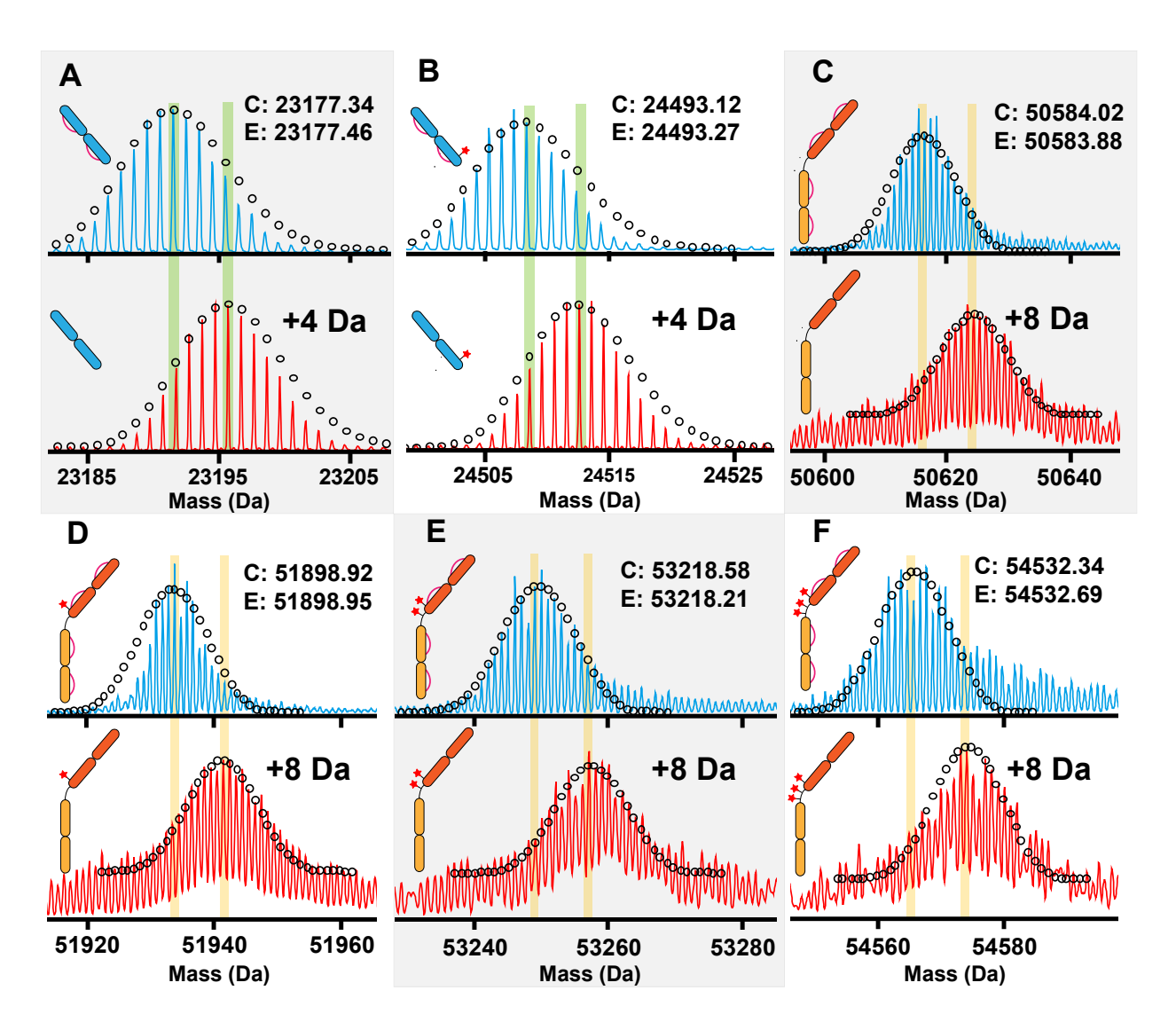


**Figure 2.4**. Isotopically resolved FTICR mass spectra of partially reduced subunits (shown in blue) and fully reduced subunits (shown in red). A) Lc0; B) Lc1; C) Hc0; D) Hc1; E) Hc2; and F) Hc3. A mass shift of 4 Da (corresponding to 2 disulfides) for the Lc subunits and 8 Da (corresponding to 4 disulfides) for the Hc subunits confirmed the cleavage of intrachain disulfide bonds during the fully reducing sample preparation. All Hc subunits in both the partially and fully reduced form displayed a +1316.43 Da mass addition, corresponding to bound G0F glycan (+1444.50 Da) and C-terminal lysine clipping (-128.07 Da). The ultrahigh resolution FTICR MS allowed isotopic resolution of subunits during online RPLC-MS.

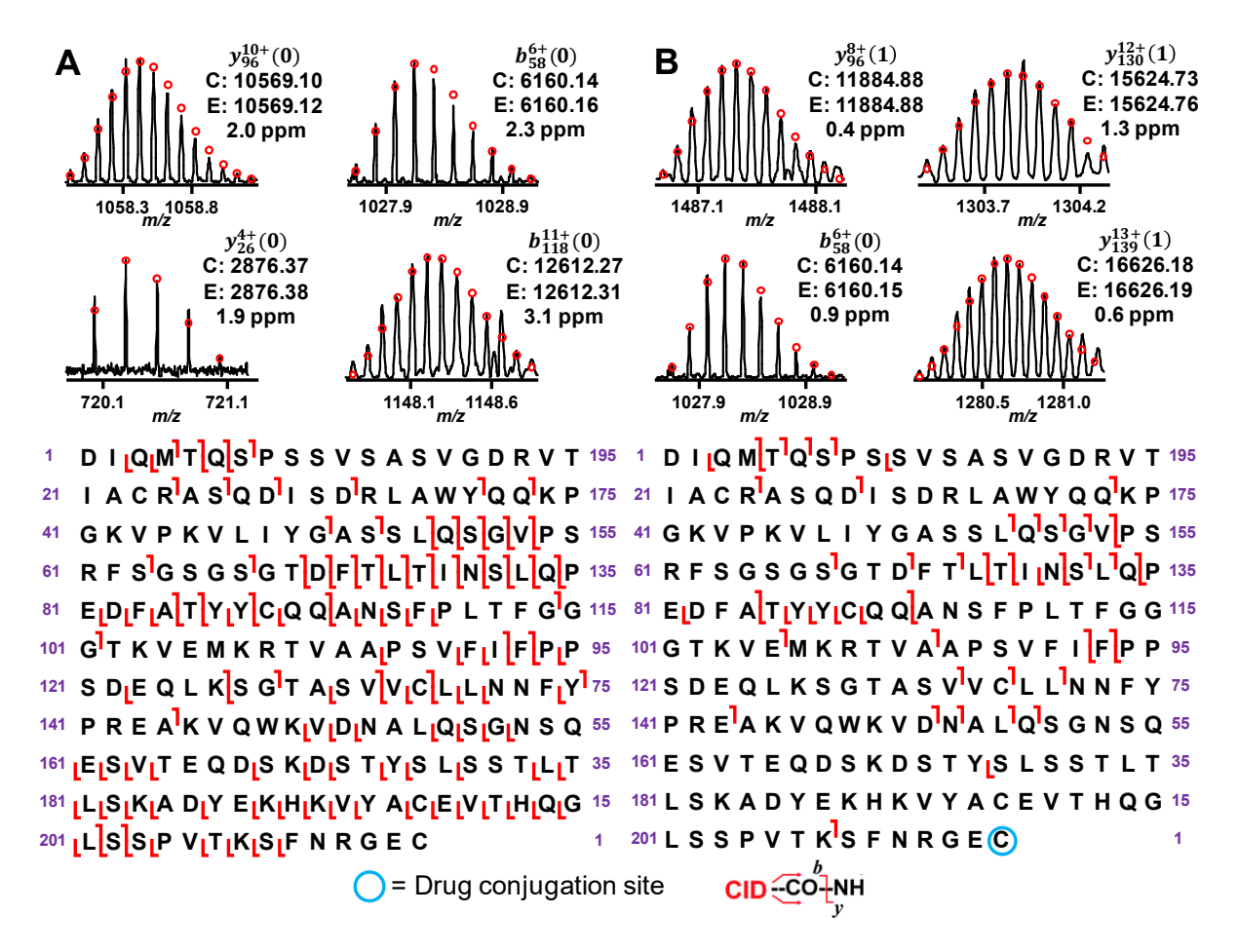


**Figure 2.5**: Online MS/MS of Lc0 (A) and Lc1 (B). Number of drugs bound to each fragment ion are indicated using (#) following each ion identifier. Fragmentation was performed using the seven CID collisional energies for fully reduced subunits specified in the methods section. For Lc0, online LC-MS/MS resulted in 110/214 bond cleavages, or 52% residue cleavage. For Lc1, the drug is fragmented preferentially over the subunit back bone, resulting in 45/214 bond cleavages with 21% residue cleavage.

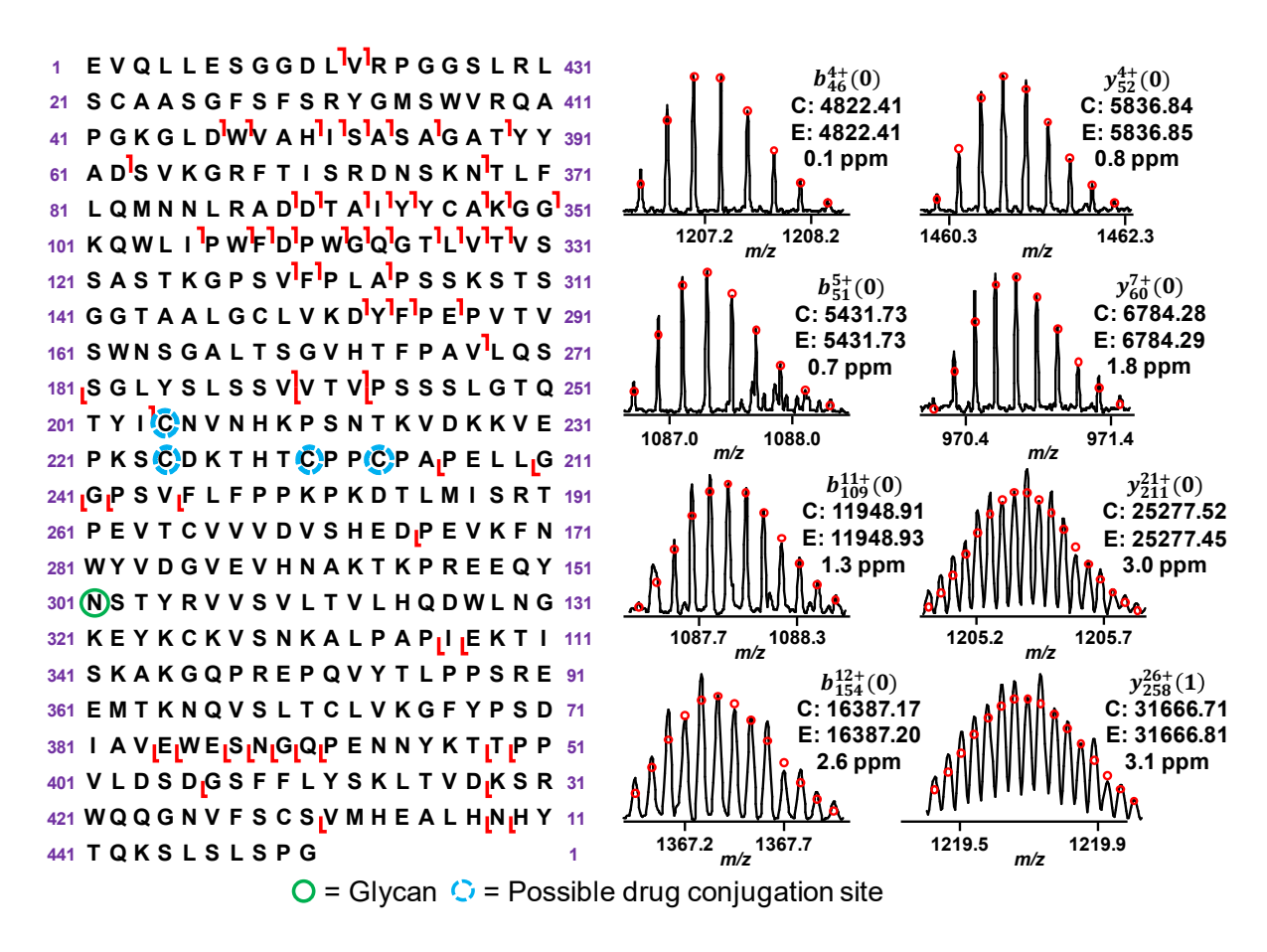


**Figure 2.6**: Online MS/MS of fully reduced Hc1 subunit. CID using the seven energies specified for fully reduced subunits in the methods section resulted in 66/450 bonds cleaved or 15% residue cleavage using online LC-MS/MS. Number of drugs bound to each fragment ion are indicated using (#) following each ion identifier. The drug conjugation was confirmed ( $y_{258}$ ) and localized to the region between Cys203 and Ala235.

# Chapter 2

# **Supporting Information**

# High-throughput Analysis of Reduced Antibody-Drug Conjugate by Online LC-MS/MS with Fourier Transform Ion Cyclotron Resonance Mass Spectrometry

Table of Contents Page
Supplemental Methods41
Figure 2.S1 Triplicate analysis of partially reduced subunits by RPLC-FTICR-MS42
Figure 2.S2 Triplicate analysis of partially fully subunits by RPLC-FTICR-MS43
Figure 2.S3 TIC overlay of partially and fully reduced subunit analysis by RPLC-FTICR-MS44
Figure 2.S4 HIC-UV analysis for average DAR determination
Figure 2.S5 Comparison of MS1 charge state distributions between fully and partially reduced subunits
Figure 2.S6 BPCs of partially and fully reduced subunit analysis by RPLC-FTICR-MS47
Figure 2.S7 Impact of MS skimmer voltage on DFA adduct formation for partially reduced subunits
Figure 2.S8 Observed CID fragmentation products of MMAE drug and linker49
Figure 2.S9 RPLC-FTICR-MS2 analysis of partially reduced Lc0 subunit by CID50
Figure 2.S10 RPLC-FTICR-MS2 analysis of partially reduced Lc1 subunit by CID51
Figure 2.S11 RPLC-FTICR-MS2 analysis of partially reduced Hc0 subunit by CID52
Figure 2.S12 RPLC-FTICR-MS2 analysis of fully reduced Hc0 subunit by CID53
Figure 2.S13 RPLC-FTICR-MS2 analysis of partially reduced Hc1 subunit by CID54
Figure 2.S14 RPLC-FTICR-MS2 analysis of partially reduced Hc2 subunit by CID55

Figure 2.S15 RPLC-FTICR-MS2 analysis of fully reduced Hc2 subunit by CID	.56
Figure 2.S16 RPLC-FTICR-MS2 analysis of partially reduced Hc3 subunit by CID	57
Figure 2.S17 RPLC-FTICR-MS2 analysis of fully reduced Hc3 subunit by CID	.58
Table 2.ST1 RPLC retention factor for fully reduced and partially reduced ADC subunits	59
Table 2.ST2 EIC peak areas for partially reduced ADC subunits	.59
Table 2.ST3 EIC peak areas for fully reduced ADC subunits	.60

## **Supplemental Methods**

HIC-UV method

Hydrophobic interaction chromatography coupled with ultraviolet detection (HIC-UV) analysis of the intact ADC was conducted on an Agilent 1260 HPLC system. There is minimal absorbance contributed by drug linker at 280 nm for this model ADC, therefore the UV signal acquired at 280nm was directly used for DAR calculation. Mobile phase A contains 25 mM disodium phosphate and 1.5 M ammonium sulfate. Mobile phase B contains 25 mM disodium phosphate with isopropanol (75/25 v/v). The pH values of both mobile phases are adjusted to 7.0 ± 0.1 with phosphoric acid. ADC sample was prepared by diluting the ADC to ~2 mg/mL with 0.9 M ammonium sulfate. HIC Butyl-NP (4.6×35 mm, 1.7 um) column was used for separation with the column temperature been set to 30 °C. A 20-minute gradient was utilized for the separation of different DAR species. The gradient starts with 10% B and increases to 35% B in 2 minutes. In the next 12 minutes the mobile phase B increases from 35% to 100%. After that the percentage of mobile phase B is brought down to 10% in 0.2 minute and kept until the end of gradient. The average DAR was calculated using the AUC values for individual DAR states in the following equation (Equation S1) as reported previously 225.245:

$$Average \ DAR = \left[ \left( \frac{(2*DAR2) + (4*DAR4) + (6*DAR6) + (8*DAR8)}{DAR0 + DAR2 + DAR4 + DAR6 + DAR8} \right) \right]$$

# **Supplemental Figures**

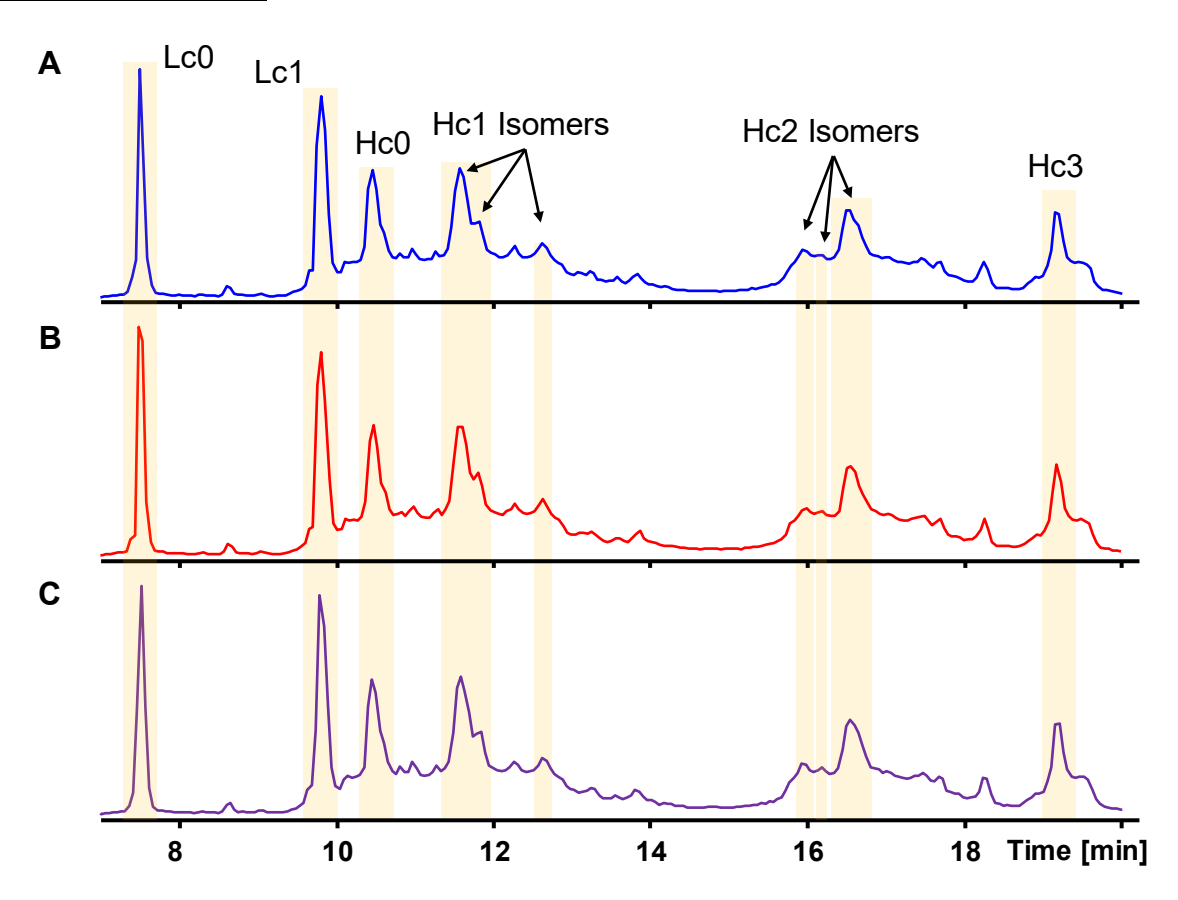


**Figure 2.S1**. Total ion chromatograms (TIC) of online reverse-phase liquid chromatography (RPLC) coupled with Fourier transform ion cyclotron resonance (FTICR) mass spectrometry (MS) analysis of partially reduced antibody-drug conjugate (ADC) using Waters BEH Bioresolve polyphenyl column. Three injection replicates (A, B, C) show excellent separation reproducibility. Separation method specified in the methods section.

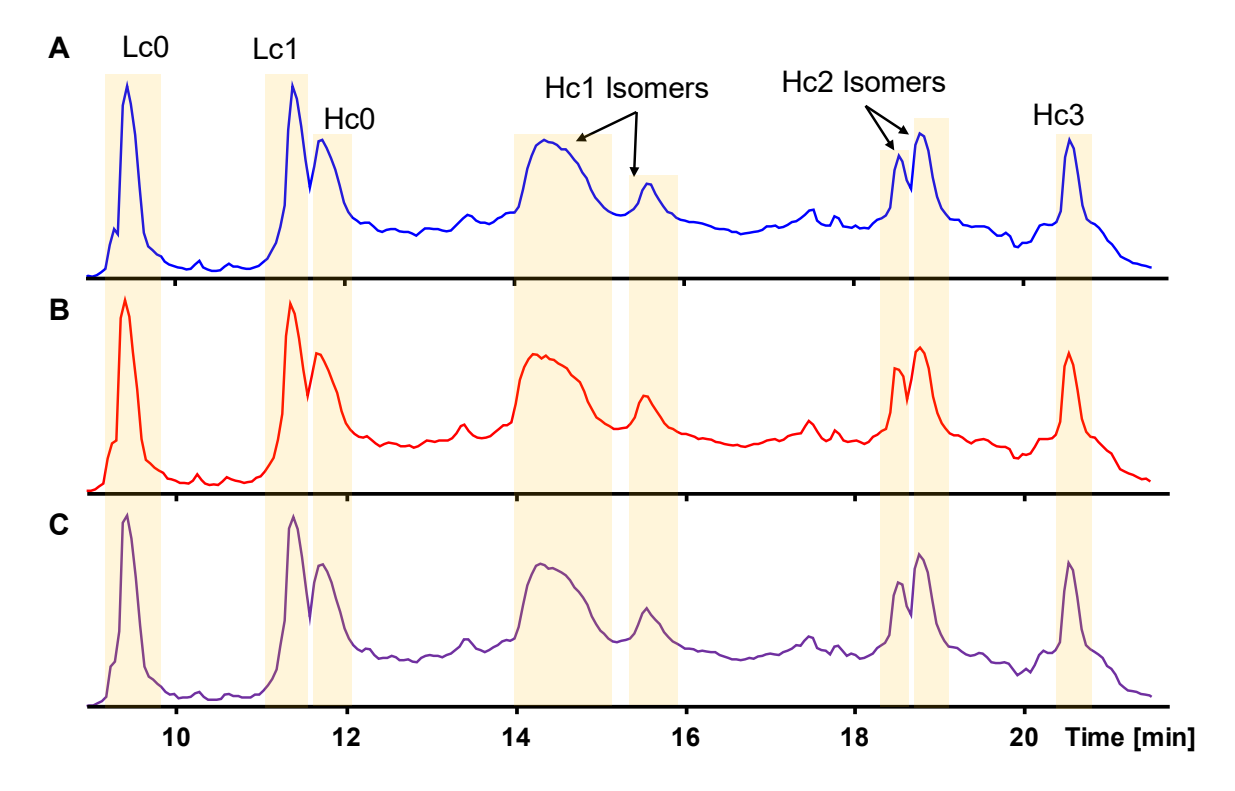


**Figure 2.S2**. TIC of online RPLC-FTICR MS analysis of fully reduced ADC using Waters BEH Bioresolve polyphenyl column. Three injection replicates (A, B, C) show excellent separation reproducibility. Separation method specified in the methods section.

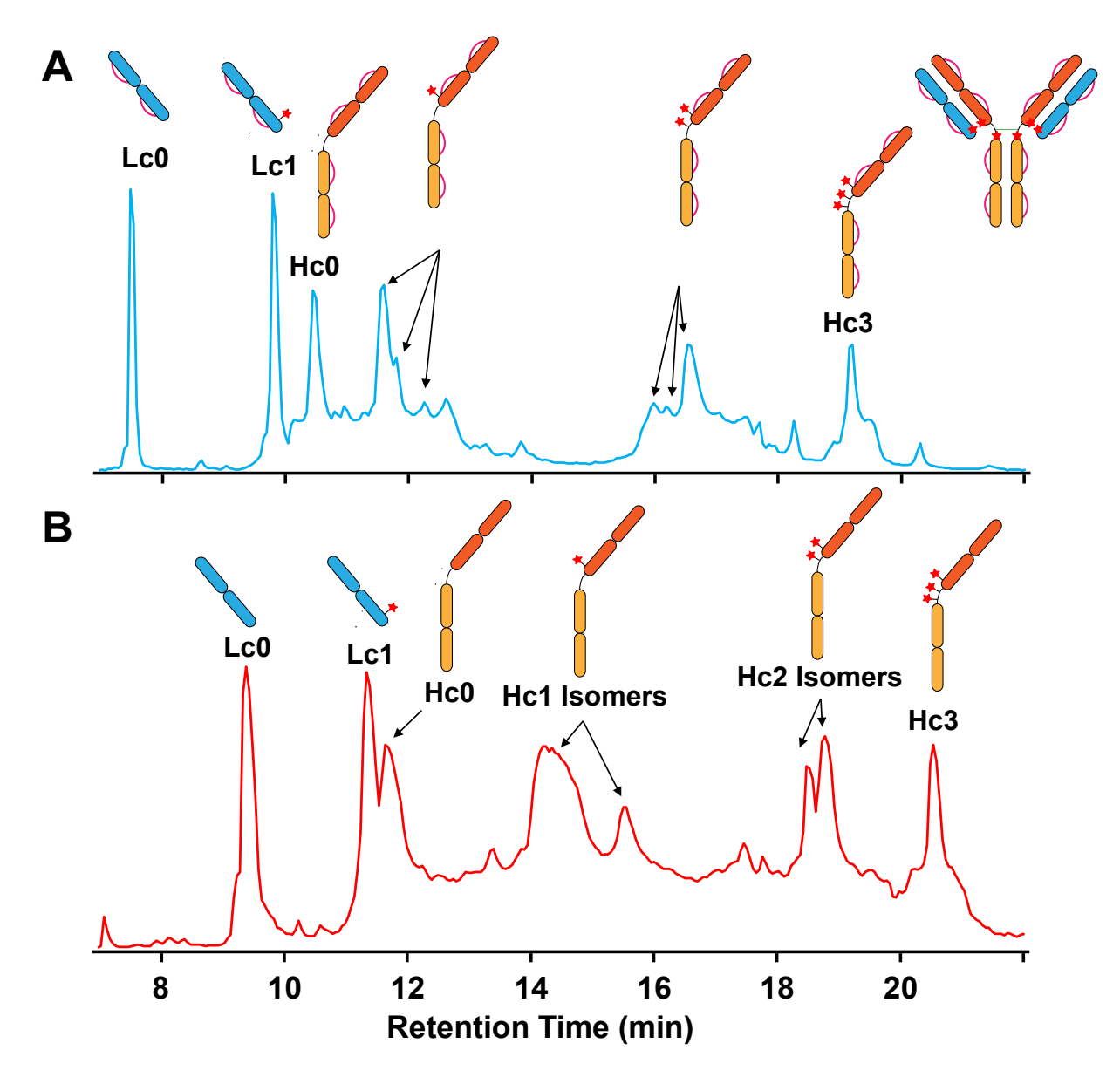


**Figure 2.S3.** Online RPLC-MS of partially reduced (A) and ADC fully reduced (B) subunits. Shown are total ion chromatogram (TIC). RPLC was performed using a Waters BioResolve RP mAb polyphenyl column (150 x 1 mm, 2.7 μm particles, 450 Å pore size).

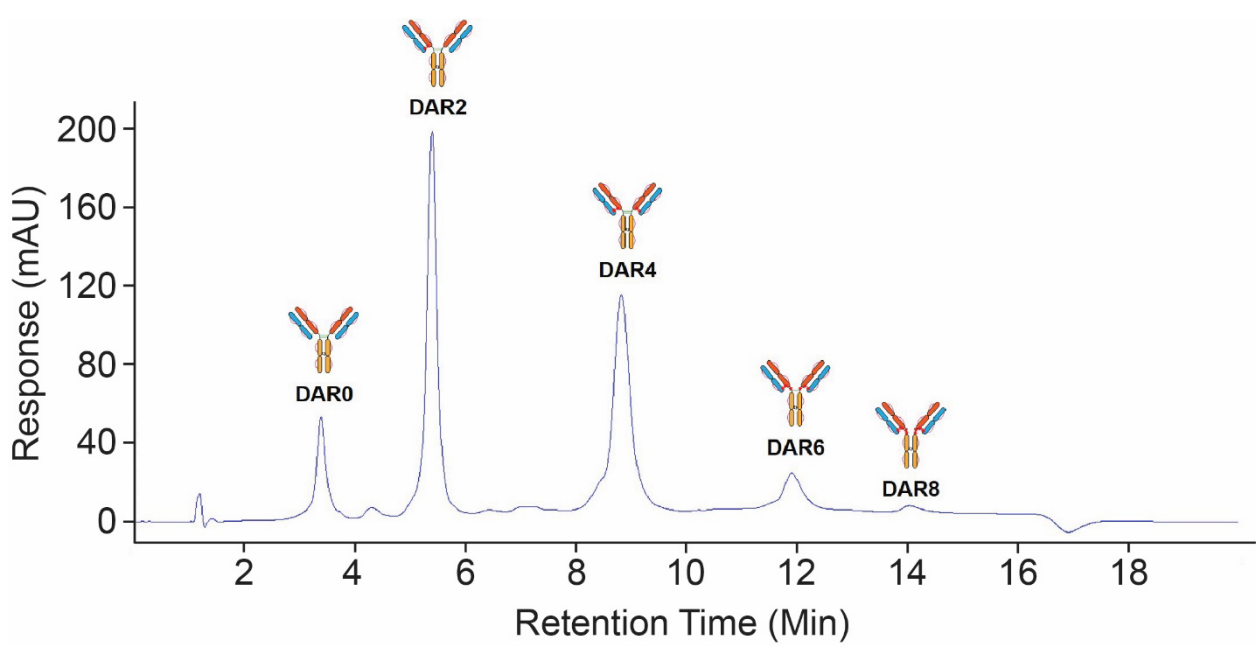


**Figure 2.S4.** Separation of native intact model ADC by HIC-UV at 280 nm. HIC-UV allowed the determination of the average DAR for the model ADC, which was found to be 3.1. This value is in good agreement with that determined by RPLC-FTICR-MS for both the fully reduced and partially reduced samples. Separation conditions for HIC-UV are specified in the supplemental methods section.

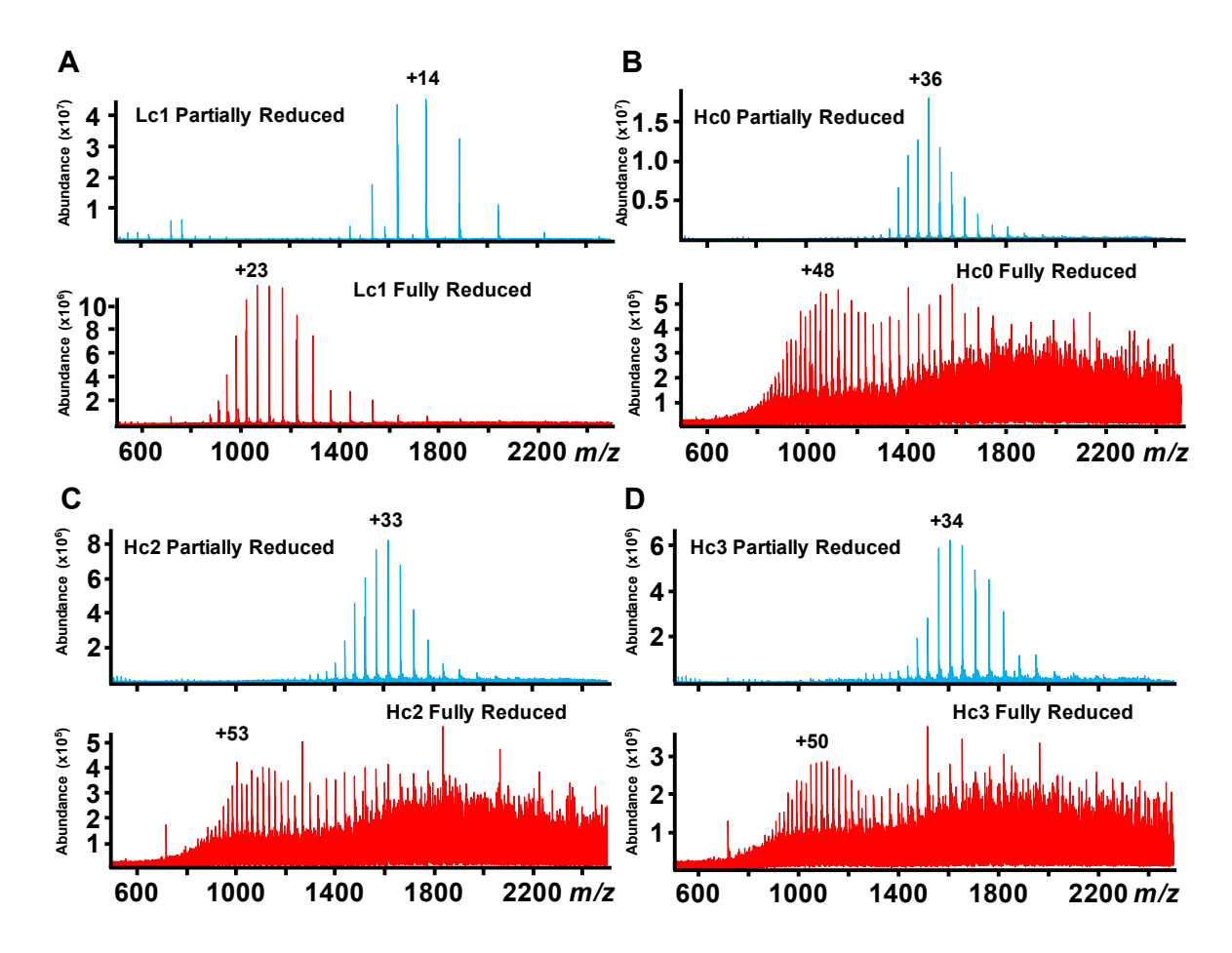


**Figure 2.S5**: Full mass spectral comparison of partially and fully reduced Lc1 (A), Hc0 (B), Hc2 (C), and Hc3 (D). Subunits shown here are complimentary to the subunits shown in figure 4. This figure illustrates that for all subunits the partially reduced form has a lower number of charge states in the distribution and a lower z value for the most abundant charge compared to the fully reduced form of the subunit.

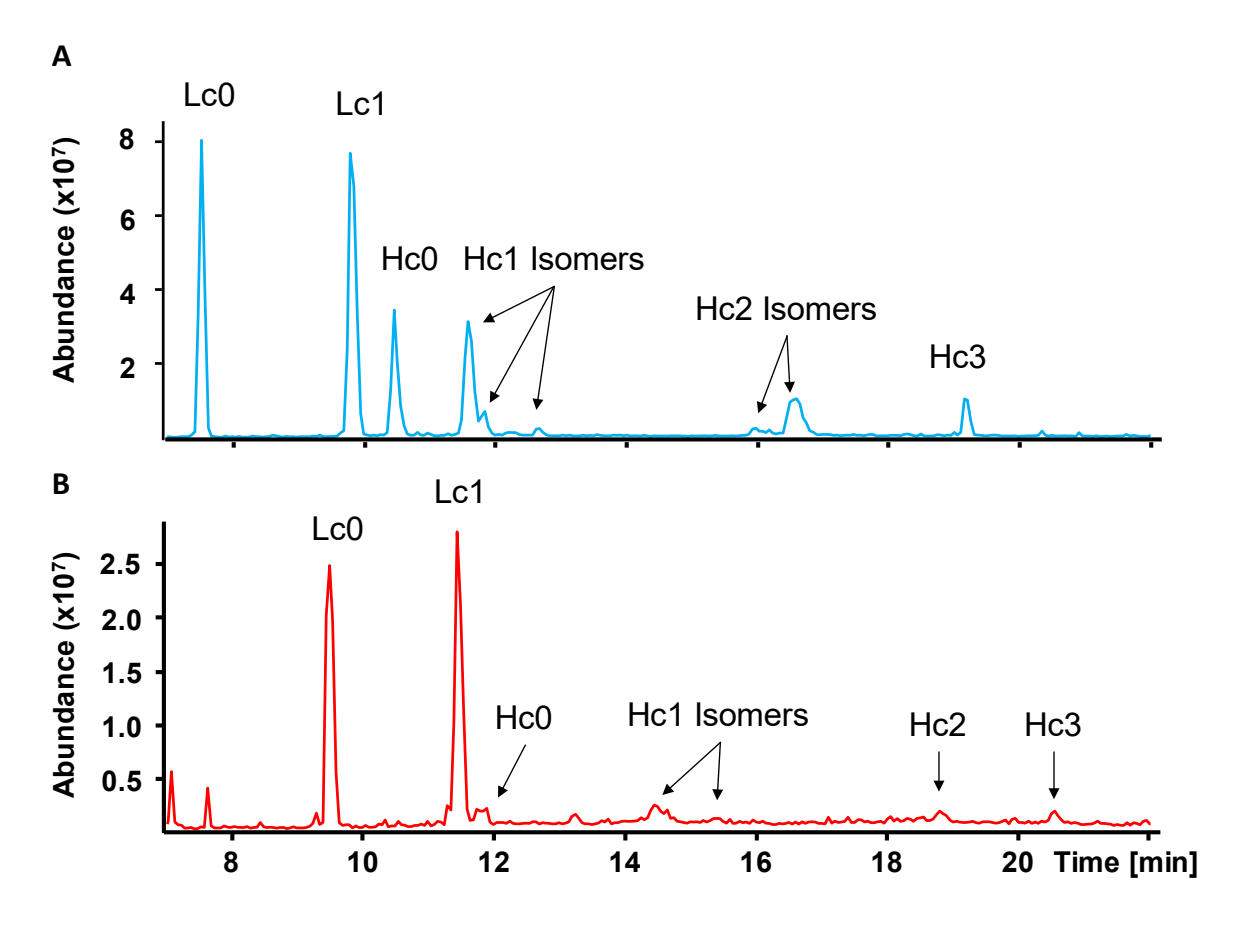


**Figure 2.S6.** Base peak chromatograms (BPC) for RPLC-FTICR MS separations of partially reduced ADC (A) and fully reduced ADC (B).

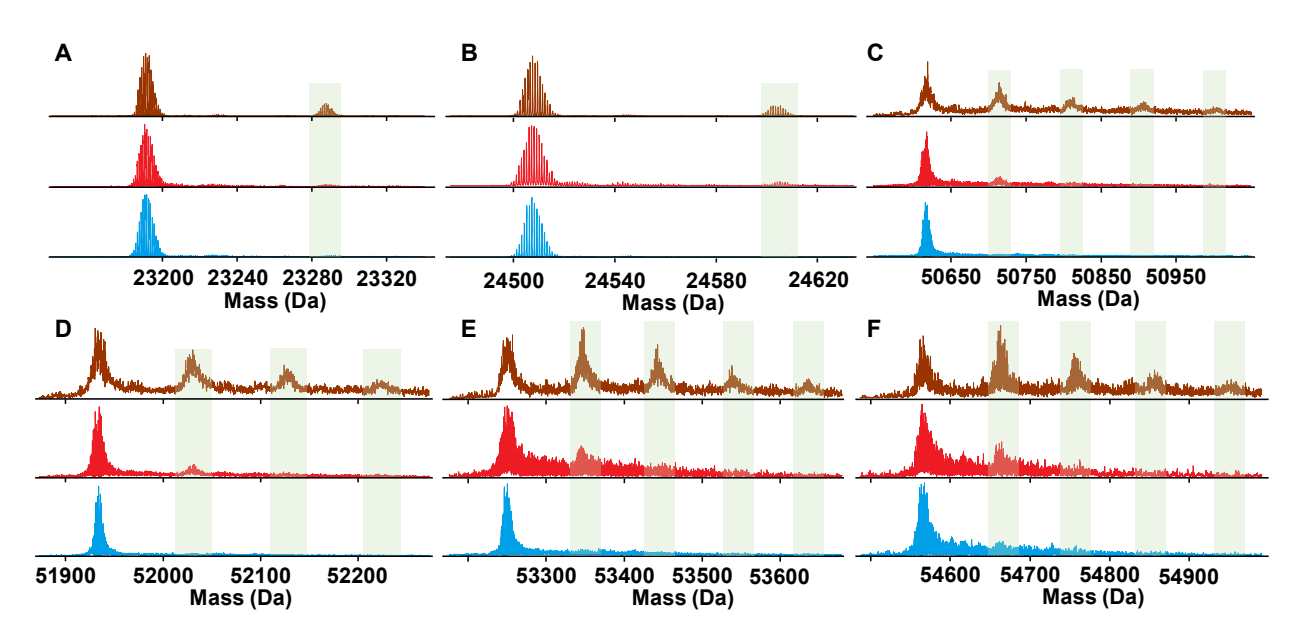


**Figure 2.S7.** Impact of skimmer voltage on DFA adduct formation and MS1 resolution of individual subunits for partially reduced form of the ADC, 30 V shown in brown, 40 V in red, and 60 V in blue. DFA adducts highlighted in green. A) Lc0, B) Lc1, C) Hc0, D) Hc1, E) Hc2, F) Hc3.

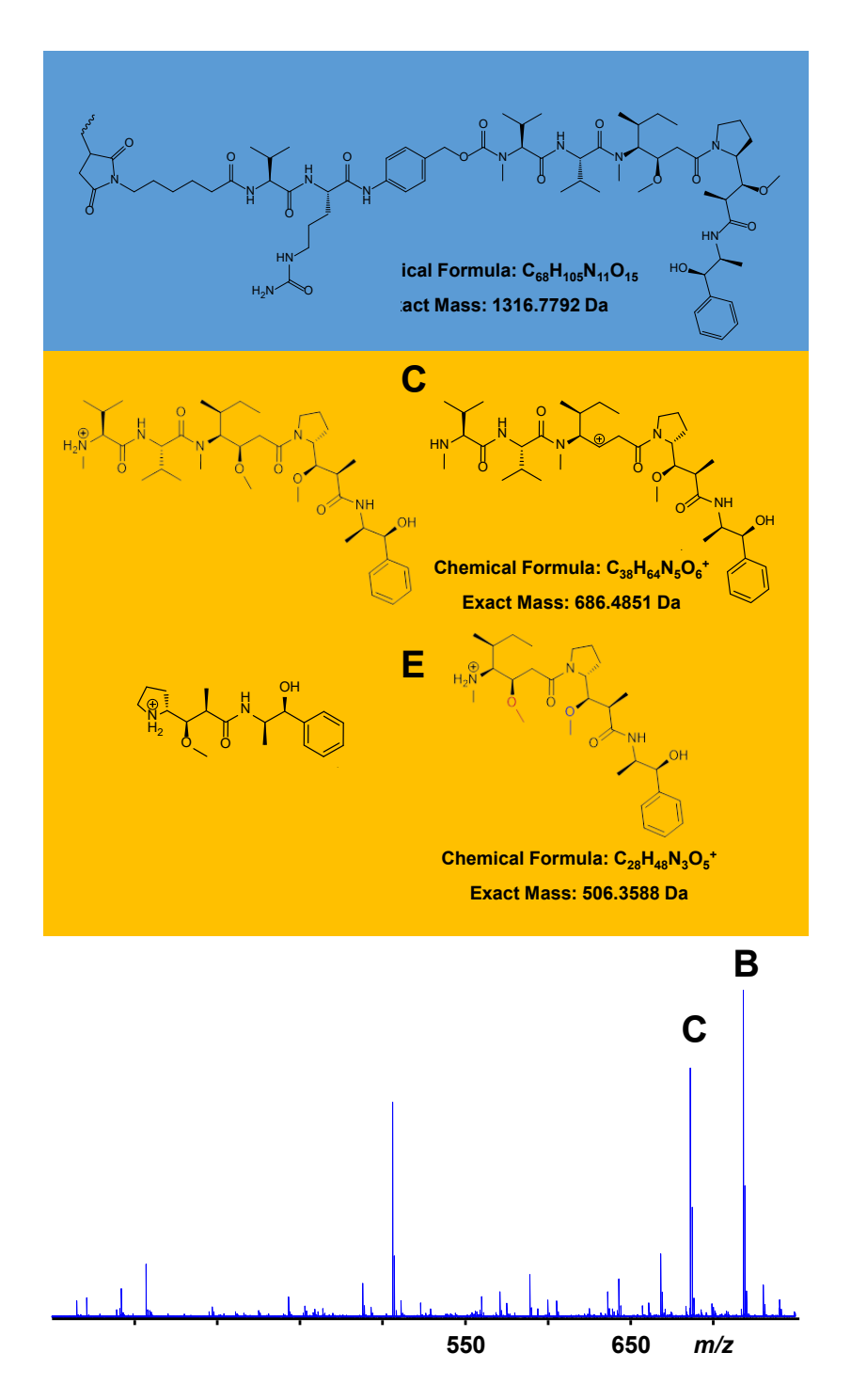


**Figure 2.S8.** Structure of drug and linker used with this model ADC. The linker is formed by connecting three moieties: a maleimidocapyrol (mc) moiety, a valine-citrulline moiety (vc), and a para-amino benzyl alcohol (pabc) moiety, which is cleaved proteolytically cleaved during endocytosis. The drug used is monomethyl auristatin E (MMAE). The full structure of the mc-vc-pabc-MMAE is shown in panel A. Panel B shows four fragments of mc-vc-pabc-MMAE after application of CID was applied to drug conjugated subunits in this study. A representative drug fragmentation spectrum is shown from using 25 V CID with the partially reduced Lc1 subunit.

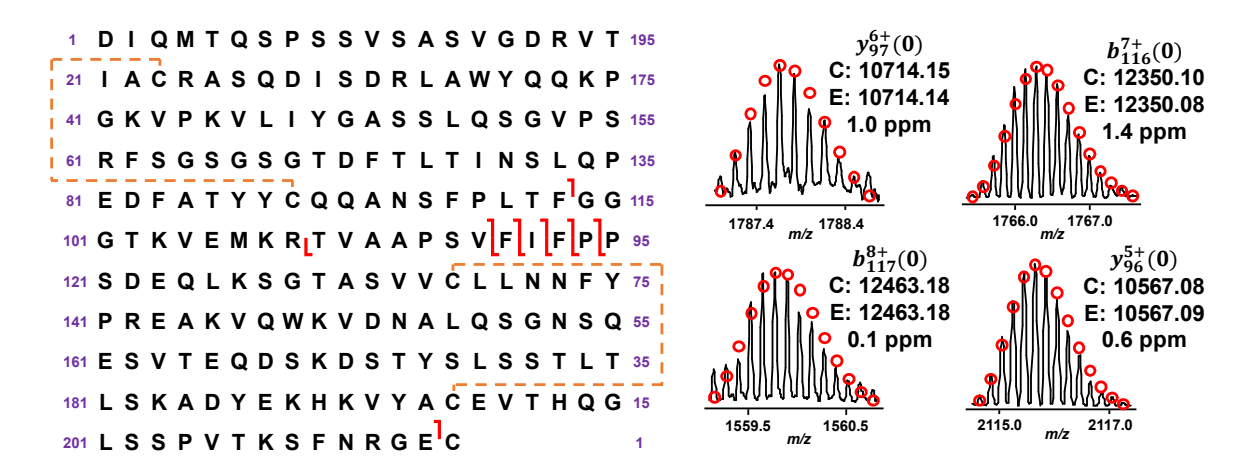


**Figure 2.S9.** Online LC-MS/MS fragmentation of partially reduced Lc0 using CID. Fragmentation yielded 8/214 bond cleavages (4% total residue cleavage) when combining the seven CID energies specified for partially reduced subunits in the methods section. Representative fragment ions shown. C, calculated molecular weight; E, Experimental molecular weight.

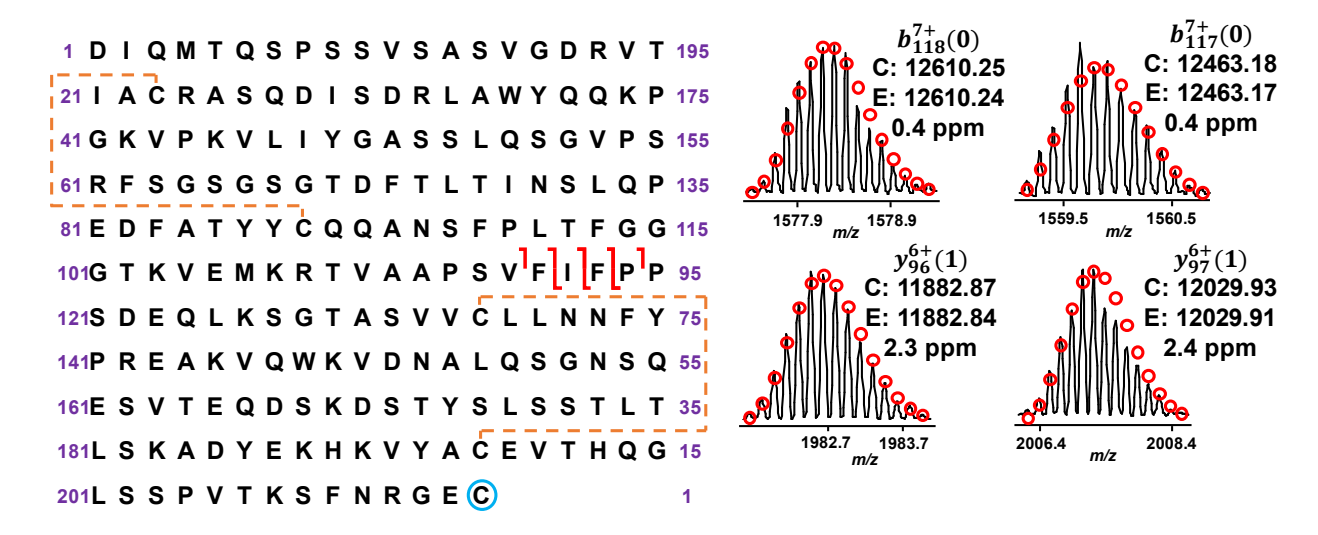


**Figure 2.S10**. Online LC-MS/MS fragmentation of partially reduced Lc1 using CID. Fragmentation yielded 5/214 bond cleavages (2% total residue cleavage) when combining the seven CID energies specified for partially reduced subunits in the methods section. Representative fragment ions shown. C, calculated molecular weight; E, Experimental molecular weight.

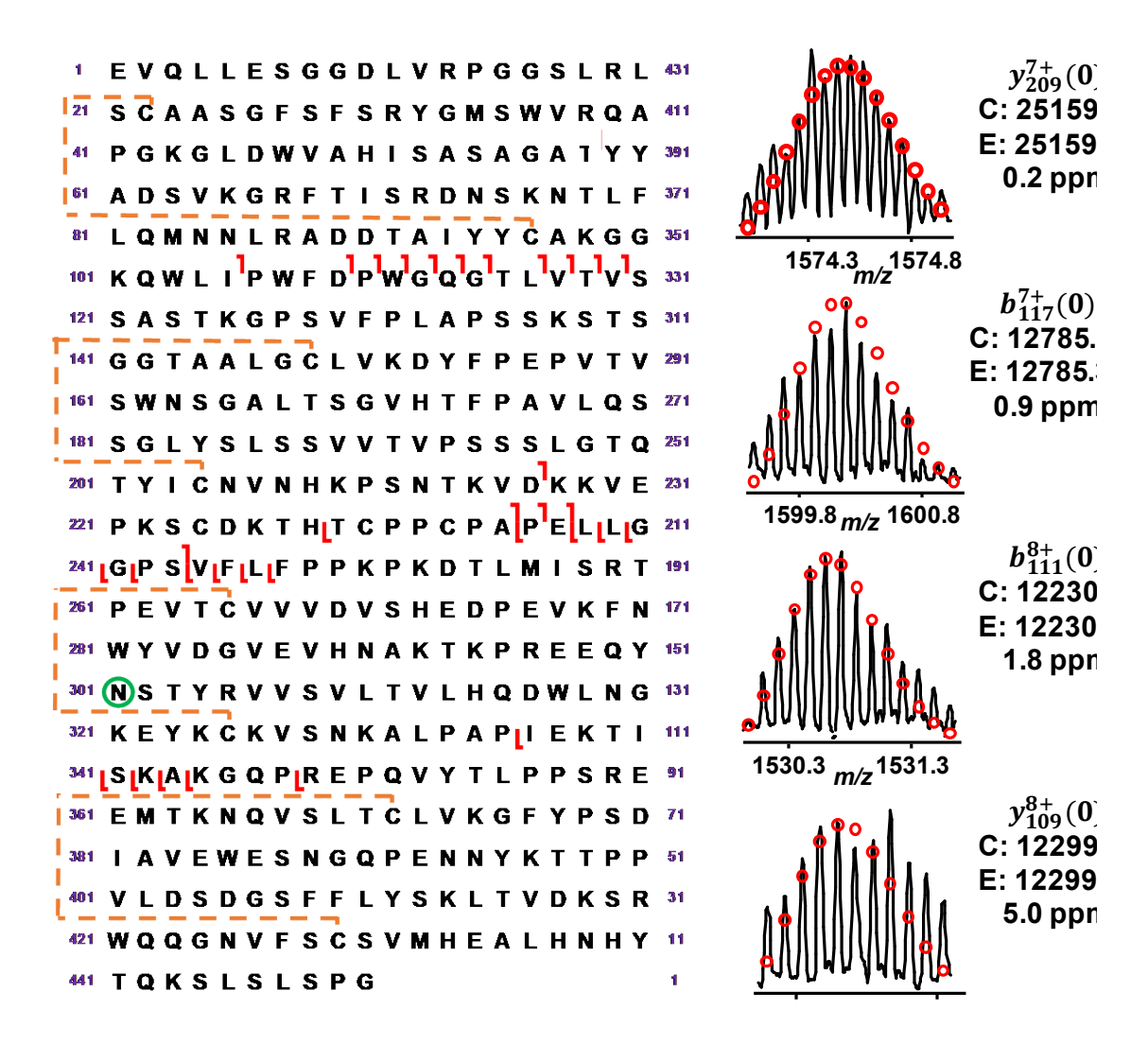


**Figure 2.S11**. Online LC-MS/MS fragmentation of partially reduced Hc0 using CID. Fragmentation yielded 31/450 bond cleavages (7% total residue cleavage) when combining the seven CID energies specified for partially reduced subunits in the methods section. Representative fragment ions shown. C, calculated molecular weight; E, Experimental molecular weight.

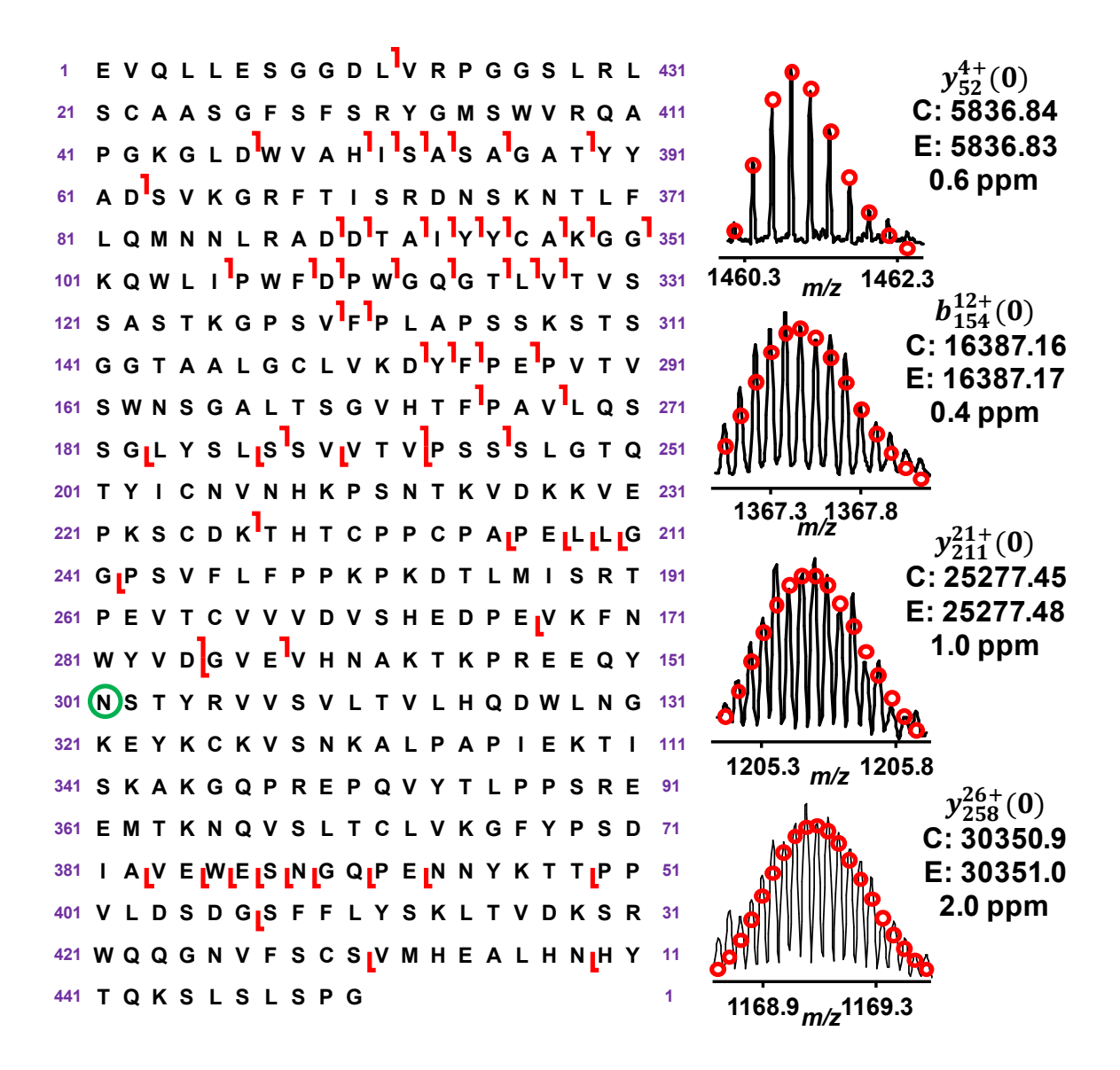


**Figure 2.S12**. Online LC-MS/MS fragmentation of fully reduced Hc0 using CID. Fragmentation yielded 61/450 bond cleavages (14% total residue cleavage) when combining the seven CID energies specified for fully reduced subunits in the methods section. Representative fragment ions shown.

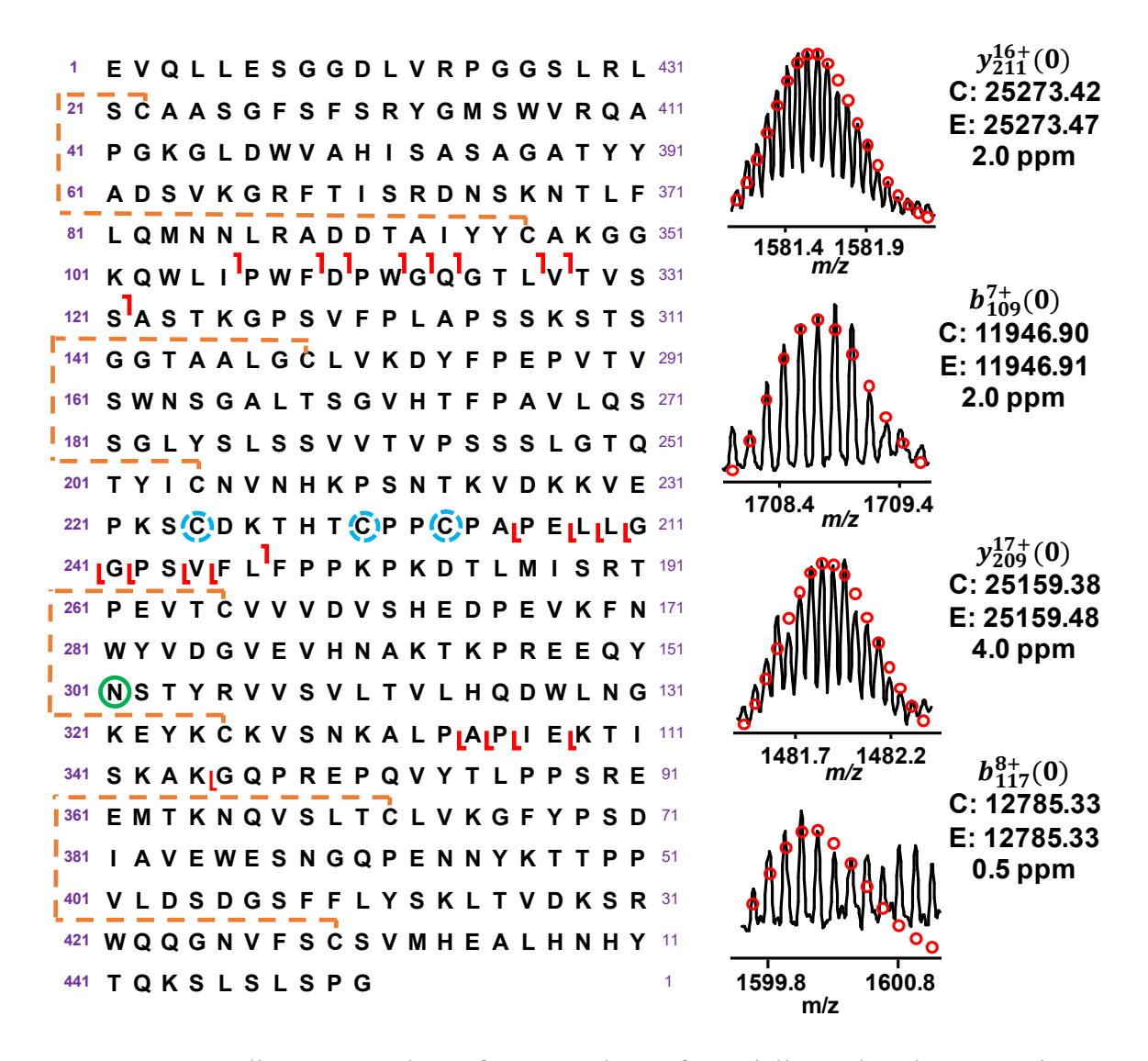


**Figure 2.S13**. Online LC-MS/MS fragmentation of partially reduced Hc1 using CID. Fragmentation yielded 24/450 bond cleavages (5% total residue cleavage) when combining the seven CID energies specified for partially reduced subunits in the methods section. Representative fragment ions shown.

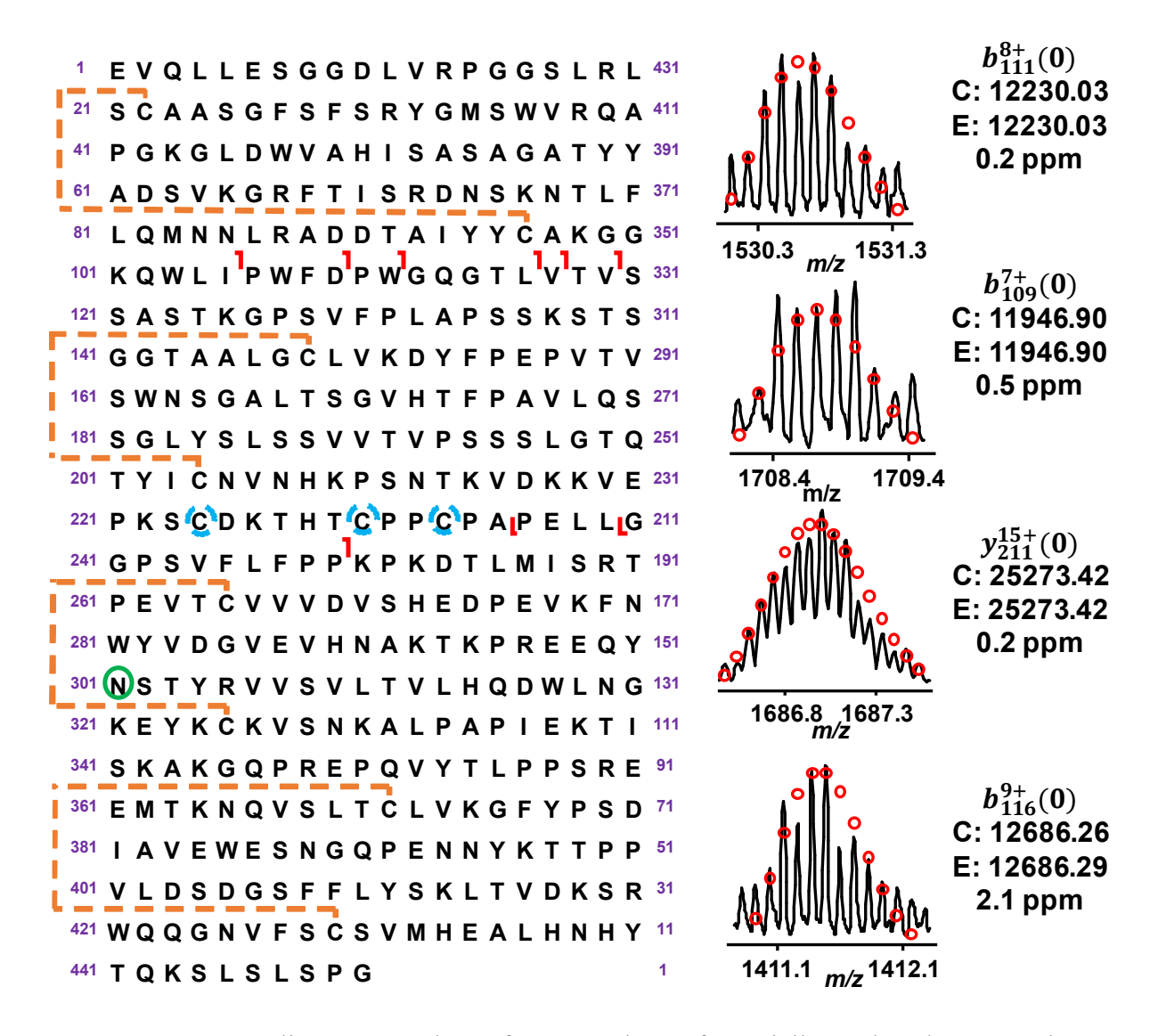


**Figure 2.S14**. Online LC-MS/MS fragmentation of partially reduced Hc2 using CID. Fragmentation yielded 9/450 bond cleavages (2% total residue cleavage) when combining the seven CID energies specified for partially reduced subunits in the methods section. Representative fragment ions shown.

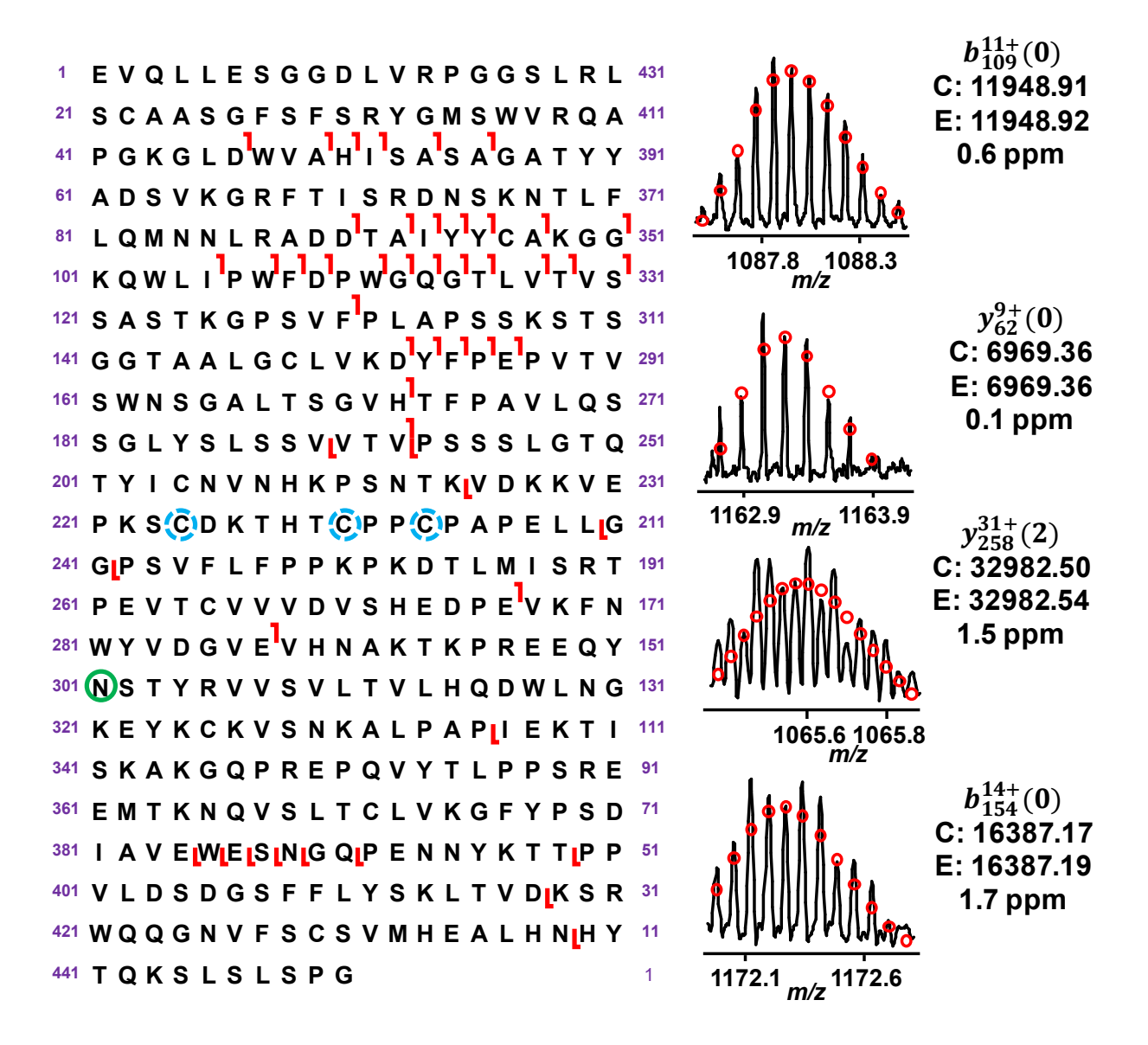


**Figure 2.S15**. Online LC-MS/MS fragmentation of partially fully reduced Hc2 using CID. Fragmentation yielded 49/450 bond cleavages (11% total residue cleavage) when combining the seven CID energies specified for fully reduced subunits in the methods section. Representative fragment ions shown.

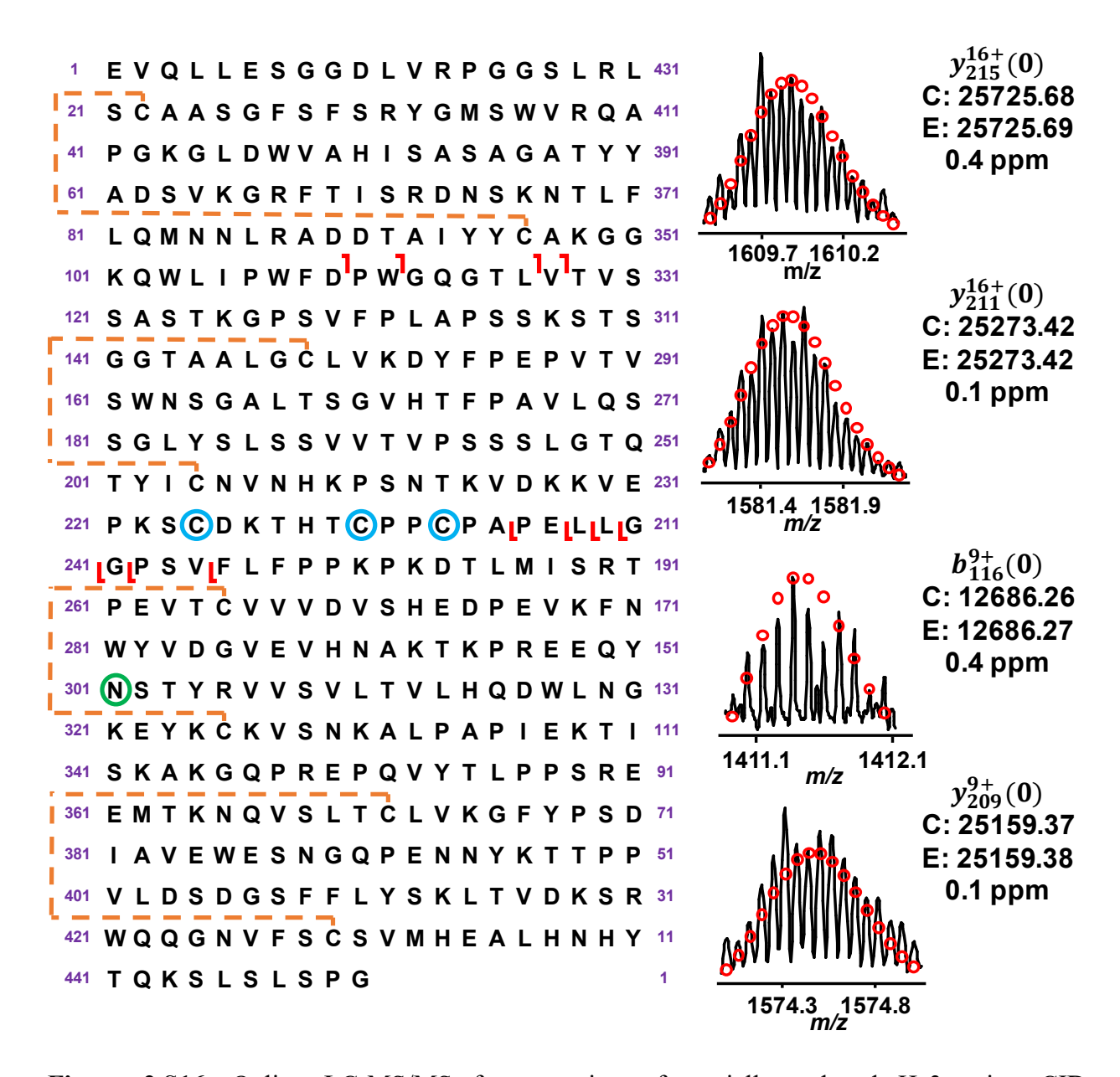


**Figure 2.S16**. Online LC-MS/MS fragmentation of partially reduced Hc3 using CID. Fragmentation yielded 11/450 bond cleavages (2% total residue cleavage) when combining the seven CID energies specified for partially reduced subunits in the methods section. Representative fragment ions shown.

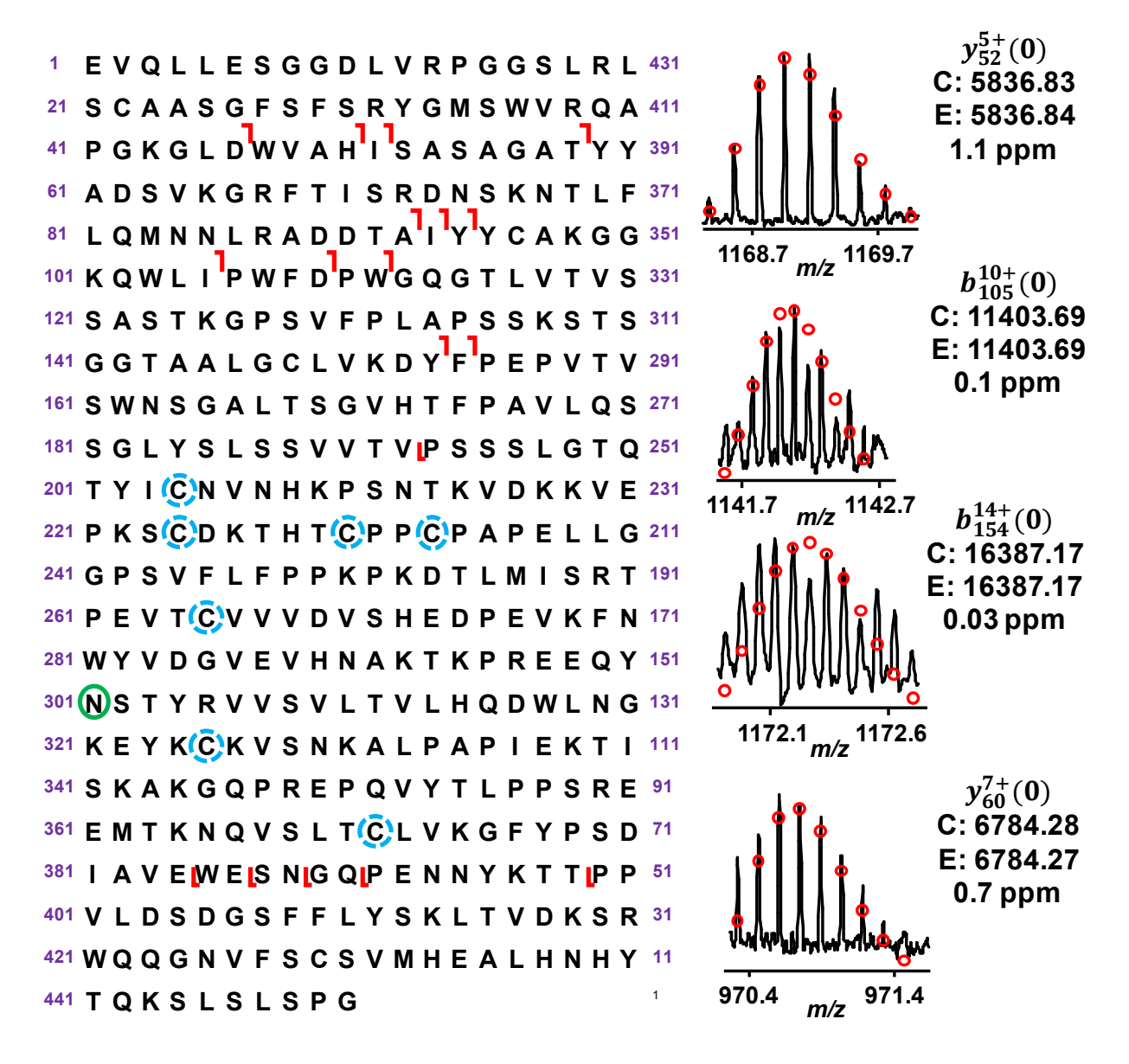


**Figure 2.S17**. Online LC-MS/MS fragmentation of fully reduced Hc3 using CID Fragmentation yielded 18/450 bond cleavages (4% total residue cleavage) when combining the seven CID energies specified for fully reduced subunits in the methods section. Representative fragment ions shown.

## **Supplemental Tables**

**Table2.ST1**. Retention factor (K') of subunits in both partially and fully reduced forms. K' is calculated using the following equation: K' = (Tr-Tv)/Tv

Where Tr is the retention time of the peak and Tv is the void volume elution time.

Subunit Partially Reduced K'		Fully Reduced K'
<b>Lc0</b> 5.25 ±0.01		6.83 ±0.03
Lc1	7.18 ±0.01	8.45 ±0.04
Hc0	7.71 ±0.01	8.71 ±0.03
Hc1 8.67 ±0.02		10.84 ±0.03
Hc2	12.78 ±0.01	14.64 ±0.02
Нс3	15.0 ±0.02	16.10 ±0.02

**Table 2.ST2.** Peak areas for individual subunits from three injection replicate RPLC-FTICR MS analyses of the partially reduced sample. The drug-to-subunit ratios (DSR) and drug-to-antibody ratios (DAR) for each run are shown along with average DSR values for Lc and Hc subunits, average DAR values for every run and calculated standard deviations.

	Run 1	Run 2	Run 3		
Lc0	1.39E+09	1.31E+09	1.58E+09		
Lc1	1.68E+09	1.50E+09	1.60E+09		
Hc0	4.53E+09	4.29E+09	4.66E+09		
Hc1	7.84E+09	7.23E+09	7.79E+09		
Hc2	3.00E+09	2.62E+09	2.77E+09		
Hc3	9.74E+08	8.74E+08	9.20E+08		
				Average	Standard Deviation
DSR Lc	0.55	0.53	0.50	0.53	± 0.02
DSR Hc	1.03	1.00	1.00	1.01	± 0.01
Average DAR	3.14	3.08	3.00	3.1	± 0.1

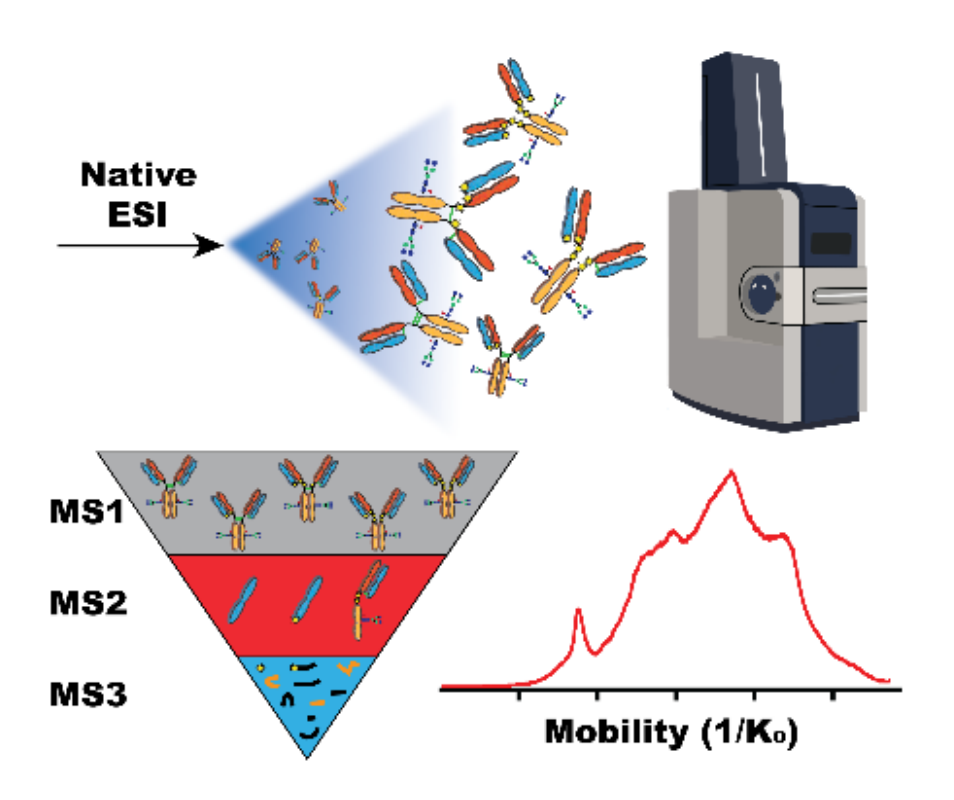
**Table 2.ST3.** Peak areas for individual subunits from three injection replicate RPLC-FTICR MS analyses of the fully reduced sample. The DSR and DAR values for each run are shown along with average DSR values for Lc and Hc subunits, average DAR values for every run and calculated standard deviations.

	Run 1	Run 2	Run 3		
Lc0	3.86E+09	3.38E+09	2.91E+09		
Lc1	4.08E+09	3.63E+09	3.44E+09		
Hc0	2.20E+08	1.69E+08	2.12E+08		
Hc1	7.54E+08	6.33E+08	6.35E+08		
Hc2	1.04E+08	1.07E+08	9.82E+07		
Hc3	5.26E+07	4.81E+07	4.34E+07		
				Average	<b>Standard Deviation</b>
DSR Lc	0.51	0.52	0.54	0.52	± 0.02
DSR Hc	0.99	1.04	0.97	1.00	± 0.03
Average DAR	3.01	3.11	3.03	3.0	± 0.1

## Chapter 3

High-Throughput Multi-Attribute Analysis of Antibody Drug Conjugates Enabled by

Trapped Ion Mobility Spectrometry and Native Top-Down Mass Spectrometry



This chapter has been published and is adapted from:

Larson, E. J.; Roberts, D. S.; Melby, J. A.; Buck, K. M.; Zhu, Y.; Zhou, S.; Han, L.; Zhang, Q.; Ge. Y. High-Throughput Multi-attribute Analysis of Antibody-Drug Conjugates Enabled by Trapped Ion Mobility Spectrometry and Top-Down Mass Spectrometry. *Analytical Chemistry*. 2021.

#### **Abstract**

Antibody drug conjugates (ADCs) are one of the fastest growing classes of anticancer therapies. Combining the high targeting specificity of monoclonal antibodies (mAbs) with cytotoxic small molecule drugs, ADCs are complex molecular entities that are intrinsically heterogeneous. Primary sequence variants, varied drug-to-antibody ratio (DAR) species, and conformational changes in starting mAb structure upon drug conjugation must be monitored to ensure the safety and efficacy of ADCs. Herein, we have developed a high-throughput method for the analysis of native cysteinelinked ADCs using trapped ion mobility spectrometry (TIMS) combined with native top-down mass spectrometry (MS) on the Bruker timsTOF Pro. This method is capable of analyzing ADCs by TIMS followed by a three-tiered native top-down MS characterization strategy for multiattribute analysis of a native ADC (~150 kDa). First, the charge state distribution of the native ADC is monitored (MS1). Second, the intact mass of subunits dissociated from the ADC by lowenergy collision induced dissociation (CID) is determined (MS2). Third, primary sequence for the dissociated subunits is characterized by CID fragmentation using elevated collisional energies (MS3). We further automate this workflow by directly injecting the native ADC using and using MS segmentation to obtain all three tiers of MS information in a single three-minute run. Overall, this work highlights a multi-attribute native top-down MS characterization method that possesses unparalleled speed for high-throughput characterization of ADCs.

#### Introduction

By conjugating the targeting efficacy of monoclonal antibodies (mAbs) with the cytotoxicity of small molecule drugs, antibody-drug conjugates (ADCs) have become a rapidly growing sector of pharmaceutical development with considerable focus on anti-cancer applications. <sup>215,246–248</sup> In many cases, a "native" cysteine conjugation approach is used to break interchain disulfide bonds and attach small molecule drugs to the resulting free cysteines via stable chemical linkers with fast conjugation reactions and minimal structural perturbation. <sup>220,246</sup> Products of cysteine conjugation include a mixture of varied drug-to-antibody ratios (DAR) species and drug conjugation positional isomers in most cases. The average DAR value, along with ADC primary sequence and conformational variants can markedly impact pharmacokinetics, stability, safety, and efficacy. <sup>221,223,249,250</sup> Therefore, a rapid and robust assessment of multiple quality attributes is beneficial for both pre-clinical development and quality control analyses.

A variety of methods for assessing ADC quality attributes have coupled liquid chromatography to mass spectrometry (LC-MS).<sup>225,239,251</sup> To assess the primary sequence of ADCs, a bottom-up MS approach using trypsin or Lys-C digestion prior to LC coupled to tandem mass spectrometry (LC-MS2) is commonly used.<sup>227,228</sup> However, bottom-up approaches suffer from lengthy sample preparation procedures and artifactual modifications,<sup>26</sup> and acquisition of integral information such as average DAR via bottom-up approaches may be difficult.<sup>227,229</sup> In recent years, middle-down and reduced mass analyses have allowed more comprehensive detection of molecular details than bottom-up MS.<sup>52,198,234</sup> Using specific digestion by enzymes such as immunoglobulin gamma-degrading enzyme of *Streptococcus pyogenes* (IdeS) followed by chemical reduction of disulfide bonds or simply chemical reduction alone, subunits between 25 and 50 kDa can be generated. This allows subunit-level MS analysis where quality attributes

including average DAR and glycoform distribution can be monitored. Additional sequence information can be probed at peptide level with high primary sequence coverage using MS2 analysis. 52,198,237,252,253 While a middle-level approach provides a more comprehensive analytical characterization than bottom-up MS, previously described techniques cannot directly probe native ADC quality attributes, such as conformational heterogeneity. To assess these quality attributes, native MS strategies have been developed for mAbs and ADCs. This strategy requires significantly less sample preparation than previously described techniques and often foregoes front-end separation, thus increasing sample throughput. While rapid characterization of average DAR and glycoform distribution can be achieved by intact native MS, 256 characterization of ADC conformation and localization of primary sequence variants and modifications are not possible with intact analysis alone.

One solution which can provide deeper insight into ADC conformations without compromising analysis speed is by incorporating ion mobility spectrometry (IMS). 119,257,258 Previous studies have used IMS to monitor DAR and assess conformational heterogeneity of intact native ADCs using techniques such as drift tube IMS (DTIMS) and traveling wave IMS (TWIMS). 258,259 Another IMS technique that has gained significant attention due to its compact design and utility for both selective and comprehensive separation modes is trapped ion mobility spectrometry (TIMS). 115,119,122,137,260,261 Previous studies have shown TIMS to be a useful technique for native protein and protein complex analysis. 136,137,142,261–265 Recently, Liu *et al.* used a custom tandem-TIMS instrument to characterize the avidin homotetramer (~64 kDa) by tandem-TIMS–MS. 137 However, the broader application of TIMS-MS in the proteomics community will require commercially available instrumentation that is generally accessible to a broad user base.

Herein, we have developed a high-throughput method to monitor multiple critical quality attributes of native cysteine–linked ADCs using the Bruker timsTOF Pro, for the first time. Our method couples direct injection with a TIMS separation and a three-tiered approach to MS characterization of a native protein complex using a commercially available and unmodified instrument. The three-tiered MS approach profiles the native intact ADC (MS1), dissociates intact subunits upon collisional activation (MS2), and fragments the released subunits at higher collisional energy (MS3). Characterization of the primary sequence by MS3 can be achieved using two fragmentation styles: either broadband collision induced dissociation (bbCID) or CID of an individual subunit. To increase the sample data throughput, segmentation of a single direct injection into 30 second windows enables multiple tiers of MS data to be rapidly collected. This method rapidly acquires TIMS, MS1, MS2, and MS3 data in only 3 minutes for the characterization of a ~150 kDa native protein complex, which represents a significant advance in both the speed of analysis and the depth of information attainable from a natively prepared ADC.

#### **Materials and Methods**

Reagents. HPLC grade water and ammonium acetate (AA) were purchased from Fisher Scientific (Fair Lawn, NJ, USA). Model cysteine-linked ADC (in 30 mM histidine buffer at pH 6.8) and its starting mAb (in 30 mM histidine buffer at pH 6.8 with 8% sucrose (w/v)) was provided by AbbVie (North Chicago, IL, USA). ESI-L Low Concentration Tuning Mix was purchased from Agilent Technologies (Santa Clara, CA, USA). NISTmAb humanized IgG1<sub>k</sub> monoclonal antibody was purchased from MilliporeSigma (Burlington, MA, USA).

Sample Preparation. The ADC sample was diluted to 15 μM in 150 mM AA solution prior to injection. Starting mAb and NISTmAb samples were buffer exchanged into 150 mM AA by washing the sample five times with a 10:1 ratio of initial volume to final volume using 30 kDa

Amicon® Ultra molecular weight cutoff filters (MilliporeSigma, Burlington, MA, USA). The mAb was then diluted to 15 μM in 150 mM AA solution prior to injection.

MS Analysis. A Bruker nanoElute LC system (Bruker Daltonics, Bremen, Germany) was coupled to a timsTOF Pro mass spectrometer (Bruker Daltonics, Bremen, Germany). Samples were directly injected using the nanoElute, injecting 5 µL of sample into 150 mM AA with a flow rate of 1 μL/min. To calibrate the MS and TIMS device, Agilent tune mix was directly infused to provide species of known mass and reduced mobility.<sup>266,267</sup> For MS calibration, the MS resolution for the most abundant calibrant signal, 1222 m/z, was 62,000. Calibrant points at 922, 1222, and 1522 m/z were used for TIMS calibration. Nitrogen was used as the TIMS drift gas for all TIMS measurements made in this work. For TIMS calibration, the TIMS resolution for the most abundant calibrant signal, 1222 m/z, was 77.6. For the MS inlet, the endplate offset and capillary voltage were set to -500 V and 3800 V, respectively. The nebulizer gas pressure was set to 1.5 bar, with a dry gas flow rate of 6 L/min at 160 °C. TIMS region voltages were optimized at -20 V, -120 V, 160 V, 200 V, 0 V and 100 V for  $\Delta 1 - \Delta 6$  respectively. TIMS RF was set to 350 Vpp, TIMS DC gradient to 200 V. A ramp time of 400 ms yielded the optimal TIMS separation performance. To facilitate high MS signal intensity, the TIMS accumulation time was locked to a 100% duty cycle, or 400 ms accumulation time. In the MS transfer optics the funnel 1 RF, funnel 2 RF, deflection delta, insource collision induced dissociation (isCID) energy and multipole RF were optimized at, 350 Vpp, 600 Vpp, 55 V, 140 eV, and 600 Vpp respectively. For MS1 spectral collection, the quadrupole low mass was set to 900 m/z with a scan range of 500 to 7000 m/z. Collision cell CID (ccCID) energy was set to 20 eV, with 3500 Vpp collision cell RF, a 170 µs transfer time, and a pre pulse storage time of 50 µs. For MS2 spectral collection the quadrupole low mass was set to 200 m/z with a scan range of 200 to 7000 m/z. The collision cell RF was set to 3500 Vpp, a 170  $\mu$ s transfer time, and a pre pulse storage time of 20 µs were used. For MS3 spectral collection, MS conditions were the same as the MS2 conditions with the exception of the isCID and ccCID voltages. The isCID energy was increased 180 eV and three ccCID energies were used for fragmentation of ADC species: 80, 90, and 100 eV. More detail about the voltages explored in this work can be found in Table S1 and Figure S1.

Data Analysis. All data were processed and analyzed using Compass DataAnalysis 5.3 and MASH Explorer. 165,240 For average DAR calculation, spectra were deconvoluted with the maximum entropy deconvolution algorithm using resolution set to 60,000. All observed charge states were used for deconvolution. This "natively" conjugated cysteine ADC displays five potential levels of drug conjugation: zero drugs conjugated (DAR 0), two drugs conjugated (DAR 2), four drugs conjugated (DAR 4), six drugs conjugated (DAR 6), and eight drugs conjugated (DAR 8). While DAR 0 and DAR 8 each generate only one conjugation isomer; DAR 2, DAR 4, and DAR 6 all generate multiple drug conjugation positional isomers which are isobaric at a given level of drug conjugation. In this work, we will refer to all products of drug conjugation to the mAb moiety as "DAR species", regardless of the level of conjugation of drug conjugation position. The area under the curve (AUC) for all DAR species were measured and average DAR was calculated using the AUC values for individual DAR species in the following equation (Equation 1):

Eq. 1 
$$Average DAR = \frac{(2*DAR2) + (4*DAR4) + (6*DAR6) + (8*DAR8)}{(DAR0 + DAR2 + DAR4 + DAR6 + DAR8)}$$

Equation 1 was adapted from previously published methods for calculating the average DAR of an intact ADC by MS1 analysis.  $^{225,268}$  To calculate the collisional cross section using TIMS with nitrogen drift gas ( $^{TIMS}CCS_{N2}$ ) $^{269}$  in Å<sup>2</sup> for species of interest, the Mason-Schamps equation was applied (Equation 2):

Eq. 2 
$$CCS = \frac{\frac{3}{16}\sqrt{\frac{2\pi}{\mu k_b T}}ze}{N_0 K_0}$$

Where  $\mu$  is the reduced mass of collision parameters,  $k_b$  is Boltzmann's constant, T is the drift region temperature, z is the ionic charge, e is the charge of an electron,  $N_\theta$  is the buffer gas density, and  $K_\theta$  is the reduced mobility. Equation 2 was selected to agree with previously published collisional cross section (CCS) calculations. For MS1 peak picking, the Sum Peak algorithm from Bruker DataAnalysis 5.3 was used with and absolute threshold of 50 and a relative intensity threshold of 0.1 %. For MS2 and MS3 peak picking, the sophisticated numerical annotation procedure (SNAP) algorithm was used with a quality threshold of 0.5 and an S/N lower threshold of 3. All fragment ions were manually validated using MASH Explorer 2.1 searching using the TopFD and eTHRASH deconvolution algorithms.  $^{165,179,271}$ 

#### **Results and Discussion**

Optimization of TIMS separation using the timsTOF Pro

Analysis of the model cysteine-linked ADC in the native state was performed by direct injection in 150 mM AA using the timsTOF Pro (Figure 3.1). A selective approach to TIMS optimization was used to facilitate IMS analysis of model ADC prior to MS analysis. The parameters found to have the greatest impact on the TIMS separation performance were the  $\Delta 3$  voltage, the  $\Delta 6$  voltage, the TIMS RF, and the TIMS cell collision energy (Table 3.S1, Figure 3.S1). The  $\Delta 3$  voltage, which applied in the TIMS funnel 1, is useful for desolvation and declustering of ions entering the TIMS device, but may fragment or unfold a native antibody if the voltage is too high (Table 3.S1).<sup>272</sup> This is similar to the impact that the TIMS DC gradient has on

TIMS separation performance (Figure 3.S1). While the  $\Delta 3$  voltage and TIMS cell collision energy largely affect desolvation, the  $\Delta 6$  voltage is applied at the end of the TIMS accumulation tunnel and affects the trapping and release efficiency of ions into the TIMS tunnel for separation (Table 3.S1).

Screening five different  $\Delta 3$  voltages found that the MS1 signal intensity (Figure 3.S2) and the TIMS separation performance (Figures 3.S3 and 3.S4) were maximized when using a  $\Delta 3$ voltage of 160 V. Similarly, Δ6 voltage conditions were also tested (Figure 3.S5-3.S7). Whereas comparison of MS1 spectra showed that a Δ6 voltage of 90 V provided the highest MS1 signal intensity (Figure 3.S5), it did not provide adequate sensitivity for low mobility species (Figure 3.S6 and 3.S7). Therefore, the selected  $\Delta 6$  voltage was 100 V, which provided high MS1 signal intensity and sensitive detection for all mobility regions (Figure 3.S6 and 3.S7). We examined the effects of TIMS RF on the TIMS separation performance using the AbbVie starting mAb, NISTmAb, and the AbbVie ADC (Figure 3.S8-3.S12). For all antibodies, we note that there is a slight shift toward lower 1/K<sub>0</sub>, and in turn lower TIMS CCS<sub>N2</sub>, as the TIMS RF decreases from 350 Vpp to 250 Vpp (Figure 3.S8, 3.S10, 3.S12; Table 3.S2-3.S4). The model IgG1 NISTmAb (Figure 3.S10) yielded TIMS separation profiles and TIMSCCS<sub>N2</sub> values similar to the AbbVie starting mAb in all tested conditions (Figure 3.S11). Moreover, the measured TIMSCCS<sub>N2</sub> and related error values for the NISTmAb were slightly higher than those of the AbbVie mAb (Table 3.S2 and 3.S3). Unlike the AbbVie mAb, which is glycoengineered to display only the G0F glycan,<sup>52</sup> the NISTmAb possesses multiple glycoforms, many of which are large than G0F, which can contribute to its larger TIMSCCS<sub>N2</sub> relative to the AbbVie mAb<sup>273</sup>. Similarly, the ADC showed a shift in mobility toward lower 1/K<sub>0</sub> values as the TIMS RF was lowered (Figure 3.S12). We note that while lowering the TIMS RF resulted in a more compact gas-phase structure, the signal intensity was significantly

attenuated when shifting from 350 Vpp TIMS RF to 250 Vpp for both the starting mAb (~15-fold decrease) and the ADC (~50-fold decrease) (Figure 3.S8A,B and 3.S12A,B). Although the current platform does not preserve the most compact gas-phase form of the mAb or ADC, a higher TIMS RF is practically useful for the high-throughput analysis of larger proteins such as the mAbs/ADCs due to higher ion transmission efficiency. Thus, we found that a TIMS RF of 350 Vpp offered suitable compromise between TIMS separation and MS intensity, which will later be shown to aid accurate DAR quantification through improved S/N. Finally, several TIMS accumulation times were screened for the starting mAb and the ADC (Figure 3.S8C,D and 3.S12C,D). While the measured TIMSCCS<sub>N2</sub> did not change at varying TIMS accumulation times for either the mAb or ADC, the relative intensity of the observed mobility regions did change. This effect should be considered in future applications whenever the concentration of sample varies by time, such as potential LC-TIMS-MS applications.

## MS1 Analysis of Cysteine-linked Model ADC and Starting mAb

After optimization of the TIMS separation parameters, MS1 conditions were optimized to facilitate desolvation and maximize signal intensity. First, seven different isCID energies were surveyed to optimize desolvation (Figure 3.S12-3.S14). All isCID conditions yielded similar mobility separation performance with the exception of 180 eV (Figure 3.S12A), which did not detect the lowest mobility region observed at other isCID energies (Figure 3.S12B-G). Higher isCID energies yielded higher MS1 signal intensity, with the greatest MS1 signal intensity found when using 160 eV isCID energy (Figure 3.S13B). Lower isCID energies resulted in lower MS1 signal intensity due to inadequate desolvation of analytes (Figure 3.S13D-G), 275,276 therefore higher isCID energies were preferred. However, higher isCID energies caused dissociation of the light chain with one conjugated drug (Lc1), which is non-covalently associated with the ADC

(Figure 3.S14). The optimal isCID was 140 eV, which facilitated good desolvation and MS1 signal intensity while minimizing dissociation of Lc1. Optimizing the detector TOF voltage showed that a modest increase in detector TOF voltage of ~10% yielded a greater than three-fold increase in MS1 signal intensity (Figure 3.S15). Next, the TIMS DC gradient, applied in the segmented collision cell, was observed to fragment ADC species and cause light chain dissociation and apparent collisional unfolding at higher voltages, as anticipated (Figure 3.S16-3.S18). However, lower TIMS DC gradient voltages resulted in lower signal for high mobility species (Figure 3.S17 and 3.S18). Therefore, a TIMS cell collision energy of 200 V was chosen to minimize fragmentation and maximize detection sensitivity across the whole mobility range.

Implementation of the TIMS technology for native intact ADC analysis offered clear advantage over conventional intact MS approaches. When direct injection of an ADC is performed without the use of front-end separation, overlap in the charge state distributions of different DAR species can inhibit MS1 detection of lower abundance species such as DAR 8 (Figure 3.2A), which can negatively impact calculation of average DAR. The TIMS separation of native model cysteine-linked ADC (Figure 3.2B, C) greatly increased the signal-to-noise ratio (S/N), thereby simplifying MS1 measurements (Figure 3.2D-I). In the case of DAR0<sup>28+</sup>, shown at 5270 m/z in Figure 2A, the calculated S/N was 4.5 with TIMS disabled. When TIMS was enabled, an increase in the S/N to 7.0 was observed with MS1 accuracy  $\leq$ 12 ppm for all DAR species (Figure 3.2D, Table 3.S2). Beyond MS1 improvements, TIMS also allows the partial separation of DAR species (Figure 3.2D-H).

To assess the impact of drug conjugation on the ADC conformation, the same optimized TIMS parameters used for the ADC were applied to the starting mAb by native direct injection (Figure 3.3A). Two distinct regions of mobility were observed for the starting mAb (Figure

3.S19A). This is potentially due to Fc wagging or Fab elbow bending, which have been reported for IgG1 model mAbs previously, $^{277,278}$  and may also be due to collisional activation due to the TIMS RF (Figures 3.S9). Calculation of average  $^{TIMS}CCS_{N2}$  values from three replicate injections yielded values of  $7735.1 \pm 16.4 \, \text{Å}^2$  of mAb $^{29+}$  for mobility region 1 and  $7802.4 \pm 23.2 \, \text{Å}^2$  of mAb $^{28+}$  for mobility region 2 (Figure 3.S19, Table 3.S3). These values are in close agreement with previously published values for the NIST standard IgG1 mAb by DTIMS (using nitrogen as the drift gas with a 0.1 % and 0.9 % difference, respectively).

Assessment of the model ADC by native TIMS analysis showed an increased number of mobility regions compared to the starting mAb (Figure 3.3B). Five mobility regions were observed for the ADC, referred to as region 1 (1.1-1.18  $1/K_0$ ), region 2 (1.18-1.26  $1/K_0$ ), region 3 (1.26-1.34  $1/K_0$ ), region 4 (1.34-1.42  $1/K_0$ ), and region 5 (1.42-1.5  $1/K_0$ ). While the mobility regions observed for the mAb between 1.3 and 1.5 1/K<sub>0</sub> were also observed for the ADC, three additional regions of mobility were observed between 1.1 and 1.3  $1/K_0$ , indicating the possible conformational changes induced by the "native" drug conjugation process (Figure 3.S21). Previous work comparing the dynamics of starting mAb and ADCs using hydrogen/deuterium (H/D) exchange has suggested that a change to the conformation state of the mAb may occur during drug conjugation. <sup>280</sup> TWIMS data has confirmed this finding for a site-specifically conjugated model ADC.<sup>238</sup> However, our current work represents the first native TIMS data showing that "native" drug conjugation may influence the gas-phase conformation of mAb moiety. Interestingly, the ADC shows mobility regions (regions 1-3) that represent more compact structures than those of the starting mAb, resulting in 1/K<sub>0</sub> values and TIMSCCS<sub>N2</sub> values (Figure 3.3 and 3.S22) lower than those observed for the starting mAb. Although some ADC mobility regions displayed lower TIMSCCS<sub>N2</sub> values than the starting mAb, other ADC mobility regions (regions 4 and 5, 1.34-1.5 1/K<sub>0</sub>, also shown in

Figure 3.S17 and 3.S22) generated higher <sup>TIMS</sup>CCS<sub>N2</sub> values than those of the mAb (Table 3.S4). The observed <sup>TIMS</sup>CCS<sub>N2</sub> values reveal the wide range of diverse changes that "native" drug conjugation may have on mAb conformation. While positional isomers of various DAR species (Fig. 3.S21) is a plausible explanation for the observed range of ADC mobility, the true influence of drug conjugation location on ADC mobility is yet to be fully determined.

After determining the TIMSCCS<sub>N2</sub> for each mobility region (Table 3.S4), the average DAR value across the whole ion mobilogram and the regional average DAR values were calculated based on the deconvoluted MS1 spectra using equation 1 (Figure 3.S23). The average DAR for all mobility regions was found to be  $3.01 \pm 0.01$ , which is in excellent agreement with previously established literary values for this specific model ADC.<sup>52</sup> The average DAR for the whole mobility space and regional average DAR were determined by triplicate analysis and displayed greater precision than previous studies owing to the greater sensitivity and S/N afforded by the timsTOF Pro. 52,198 A strong linear relationship was observed between the regional average DAR value and the regional TIMSCCS<sub>N2</sub> value calculated from the most abundant charge state in each mobility region, with an R<sup>2</sup> value of 0.95 (Figure 3.S24, Table 3.S5). Comparison of extracted ion mobilograms (EIMs) for each DAR species supports this finding and demonstrates that while individual DAR species exist in all observed mobility regions, the distribution of higher DAR values skews toward the larger mobility species (Figure 3.S25). Therefore, while drug conjugation can induce ADCs to form more compact structures than the starting mAb, an increase in the drug load still results in higher TIMSCCS<sub>N2</sub> values for ADCs.

Released Subunit Analysis by MS2

Following MS1 analysis of the model ADC, individual non-covalently linked subunits were dissociated for MS2 characterization by increasing the ccCID energy from 20 to 60 eV (Figure 3.4A and 3.4B). Collisional subunit dissociation for MS2 analysis was also achieved by increasing the isCID voltage from 140 to 180 eV. The most abundant of the observed dissociated subunits was the light chain conjugated to one drug molecule (Lc1) (Figure 3.4B and 3.S26). Because the Lc is attached to the heavy chain (Hc) of the antibody through a single interchain disulfide bond, drug conjugation to the Lc causes its association to the Hc to be entirely noncovalent in a cysteine ADC. The intact monoisotopic mass of this species was determined to be 24993.05 Da, which is in good agreement with the theoretical mass with an error of 8.8 ppm (Figure 3.S26C). The Lc species was also observed with only the linker bound to the Lc and no drug associated (Figure 3.S26B). This is likely caused by fragmentation of the drug and linker as a result of increased ccCID or isCID energy to promote subunit dissociation.<sup>227</sup> Intriguingly, the Lc subunit without a drug conjugation (Lc0) was also observed (Figure 3.S26A). The experimental mass found for Lc0 indicates that the C-terminal cysteine is protonated, indicating that this subunit was generated in-solution prior to MS analysis. While it is possible that this Lc0 may be generated by CID-induced cleavage of drug and linker, this observation has not previously been detected as a major fragmentation product of Lc1 when using CID.<sup>52</sup> Therefore, this Lc0 species is likely a result of odd numbered drug loading during the drug conjugation process.<sup>281–283</sup> The final dissociated subunit observed was the Lc bound through an interchain disulfide bond to an Hc bearing two conjugated drugs (Lc-Hc2) (Figure 3.S26D). Lc-Hc2 was observed at much lower intensity than other dissociated subunits, largely due to a relatively high monoisotopic mass of 76,389 Da and a lower probability of drug conjugation isomers that can produce this subunit. Of the 11 possible combinations of DAR state and drug positional isomers only two species can

produce Lc-Hc2 for observation by MS2 compared to eight species which can produce Lc1 by MS2 (Figure 3.S21). While Lc-Hc2 was observed, it was not sufficiently resolved to calculate the experimental monoisotopic mass. Interestingly, the observed average mass of 76435.0 Da does indicate that the G0F glycan is bound and the C-terminal lysine has been clipped, which is in good agreement with previous characterization of this ADC by reduced mass analysis.<sup>52</sup>

#### MS3 Characterization using CID

After assessing subunits using MS2, isCID was set to 180 eV and ccCID energy was further increased to allow MS3 characterization of the primary sequence using both CID and broadband (bbCID) (Figure 3.4C-F). CID was used to characterize the fragment Lc1 subunit after collisioninduced release from the native ADC complex and quadrupole isolation of the most abundant charge state (Lc1<sup>11+</sup>, m/z = 2229) (Figure 3.4C and 3.4D). Screening three CID energies facilitated greater sequence coverage of the Lc1 subunit, 8 % total residue cleavage over the course of 15 minutes of injection time (Figure 3.5A, 3.S27). Although this method yields limited sequence coverage, it can still confirm drug binding, and locate interchain disulfide bonds. Moreover, this method offered greater coverage than our previous LC-MS2 method to characterize denatured subunits with intrachain disulfide bonds intact using CID, which showed only 2.3% residue cleavage for the Lc1 subunit.<sup>52</sup> The observed increase over the previous characterization method is likely due to the combination of TIMS, which doubles the S/N, and the use of direct injection, which allowed a greater number of MS3 scans to be collected than the previous online LC-MS2 method. Although direct injection using the timsTOF Pro can increase the number of residue cleavages, the presence of intrachain disulfide bonds still limits the fragmentation for native Lc1. Despite the presence of intrachain disulfide bonds, this analysis still confirmed the presence and location of drug binding, and intrachain disulfide bonds (Figure 3.5A). Because the mass isolation

range of the timsTOF Pro's quadrupole cannot isolate species above 3000 *m/z*, larger subunits required bbCID to be used for primary sequence characterization (Figure 3.S27). These analyses yield a paucity of fragment ions, resulting no confidently identified cleavage in the Hc of the antibody and only three residue cleavages for the Lc1 subunits by bbCID. However, drug binding on Lc1 was still detected and could be localized using the presence of y<sub>96</sub>. The sequence coverage could be improved with further developments in TIMS technologies. For example, Liu *et al* recently described a native top-down method using a modified tandem TIMS device (not yet commercially available) which enabled improved sequence coverage for a glycoprotein homotetramer complex avidin. Additionally, equipping a TIMS front-end device on a system equipped with multiple fragmentation options such as a Solarix Fourier transform ion cyclotron resonance mass spectrometer (FTICR-MS) may be an attractive option to further improve protein sequence coverage.

## Segmentation for Rapid Multi-Attribute Characterization

To further increase the throughput of analysis, a MS segmentation strategy was applied to a single direct injection run (Figure 3.6). By dividing a single 10-minute direct injection run into 30 second increments, MS parameters could be switched every 30 seconds to provide unique quality attributes. In the span of only 3 minutes, three tiers of quality attributes of ADC were profiled from a single run. First, MS1 analysis of the native model ADC was performed along with TIMS separation (Figure 3.6A). Second, non-covalently linked subunits were released by CID to monitor intact subunit mass by MS2 (Figure 3.6B). Third, the primary sequence was characterized by CID, providing an isolation spectrum (Figure 3.6C) and screening three ccCID energies for MS3 characterization (Figure 3.5B and 3.6D-F). The total residue cleavage by MS3 using the 10-minute, multiple segmentation approach was 6.1%, which is comparable to the 8% achieved by

the 15 min method as detailed above (Figure 3.5, 3.S27 and 3.S29). This strategy has two significant advantages over previously developed techniques for IMS-MS and intact native MS characterization of ADCs. First, our method uses a single MS instrument to determine average DAR and perform IMS analysis, MS1, MS2, and MS3 characterization of an intact native ADC. Previous IMS-MS techniques, whether native or denatured, have not simultaneously utilized IMS analysis of intact ADCs and characterized the primary sequence of the ADC in a single method.<sup>284,285</sup> While Beck and coworkers have paired native IMS-MS analysis with a separate middle-down analysis, the process of using multiple analytical strategies is time-consuming and may require the use of multiple MS instruments.<sup>285</sup> In contrast, our method uses a single commercially available instrument to profile all quality attributes in a MS run. Second, the throughput of our method is much greater than previously established methods. <sup>18,53</sup> In our recently developed middle-down LC-MS2 method, sample preparation required 2.5 hours for a single analysis. 198 However, using this new direct injection method which couples TIMS and native topdown MS, we could perform 15 individual analyses in the same time. Since the sample preparation time of our current method is negligible, the time required for analysis is essentially equivalent to the MS method time (10 min). These factors make ADC analysis by direct injection using TIMS and native top-down MS a valuable and high-throughput tool for future characterization of antibody-based therapeutics in both pre- and post-clinical analyses.

#### **Conclusion**

In summary, we have developed a rapid and high-throughput method for the multi-attribute analysis of native cysteine ADCs by direct injection using the timsTOF Pro. Characterization of the ADC by TIMS, intact ADC mass analysis by MS1, intact subunit mass analysis by MS2, and primary sequence monitoring by MS3 can achieved in less than 3 minutes using a single MS

method and a commercially available and unmodified instrument. The analytical method described in this study represents a significant advance in both the fields of native top-down MS and ADC analysis and enables rapid analysis of multiple ADC critical quality attributes. Additionally, this strategy can be leveraged for preclinical studies to enable extremely rapid screening of antibody-based drug products using a robust and easily automated platform. We have shown that the combination of TIMS and native top-down MS using direct injection on the timsTOF Pro allows for high-throughput multi-attribute ADC analysis and represents a new analytical tool for the characterization of antibody-based therapeutics in both pre- and post-clinical quality control.

## Acknowledgements

The authors would like to thank Guillaume Tremintin, Yue Ju, Christian Albers, Conor Mullins, Michael Greig, and Gary Kruppa of Bruker Daltonics for their kind help and provision of the Bruker timsTOF Pro used in this work. The funding was provided by Abbvie, Inc. D.S.R. would like to acknowledge support from the American Heart Association Predoctoral Fellowship Grant #832615 / David S. Roberts / 2021. Y.G. would like to acknowledge NIH R01 GM125085 which provides funding support for the development of the MASH Explorer software for analysis of top-down MS data.

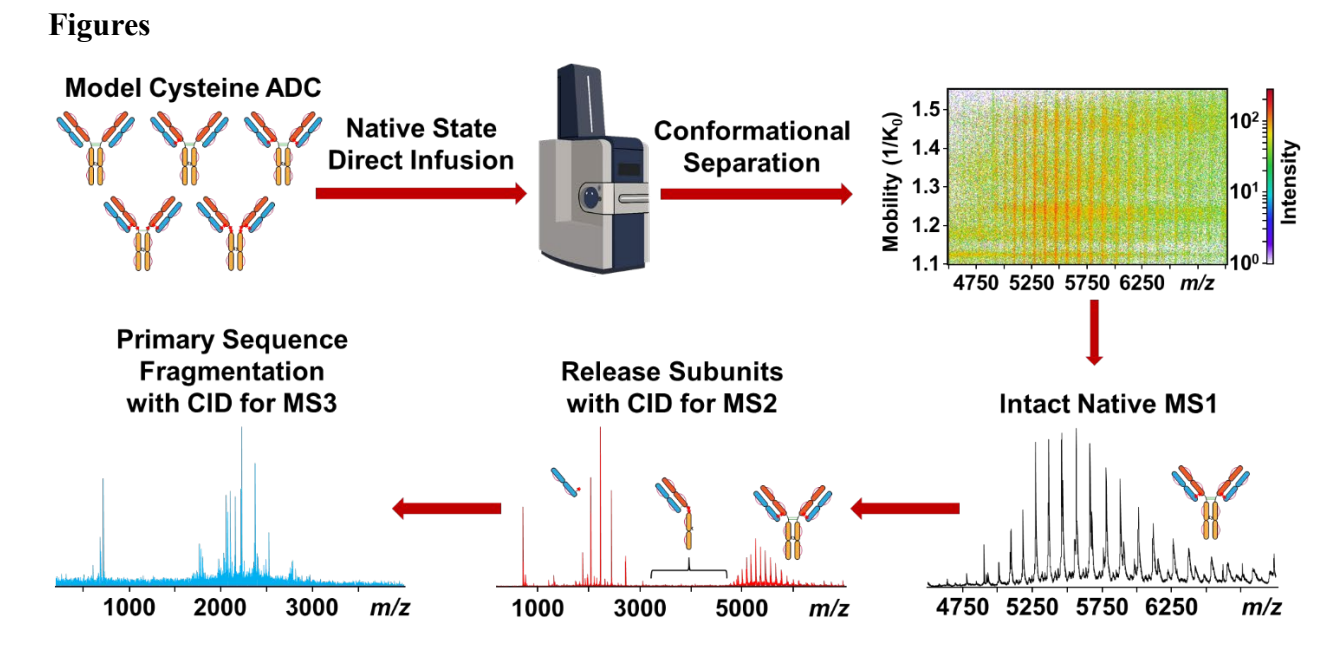


**Figure 3.1.** Workflow for the native direct injection of model cysteine-linked ADC. Direct injection using the Bruker nanoElute coupled with the timsTOF Pro allows gas-phase analysis of DAR species by TIMS followed by MS1 analysis of intact ADC, release of non-covalently bound subunits, and primary sequence fragmentation.

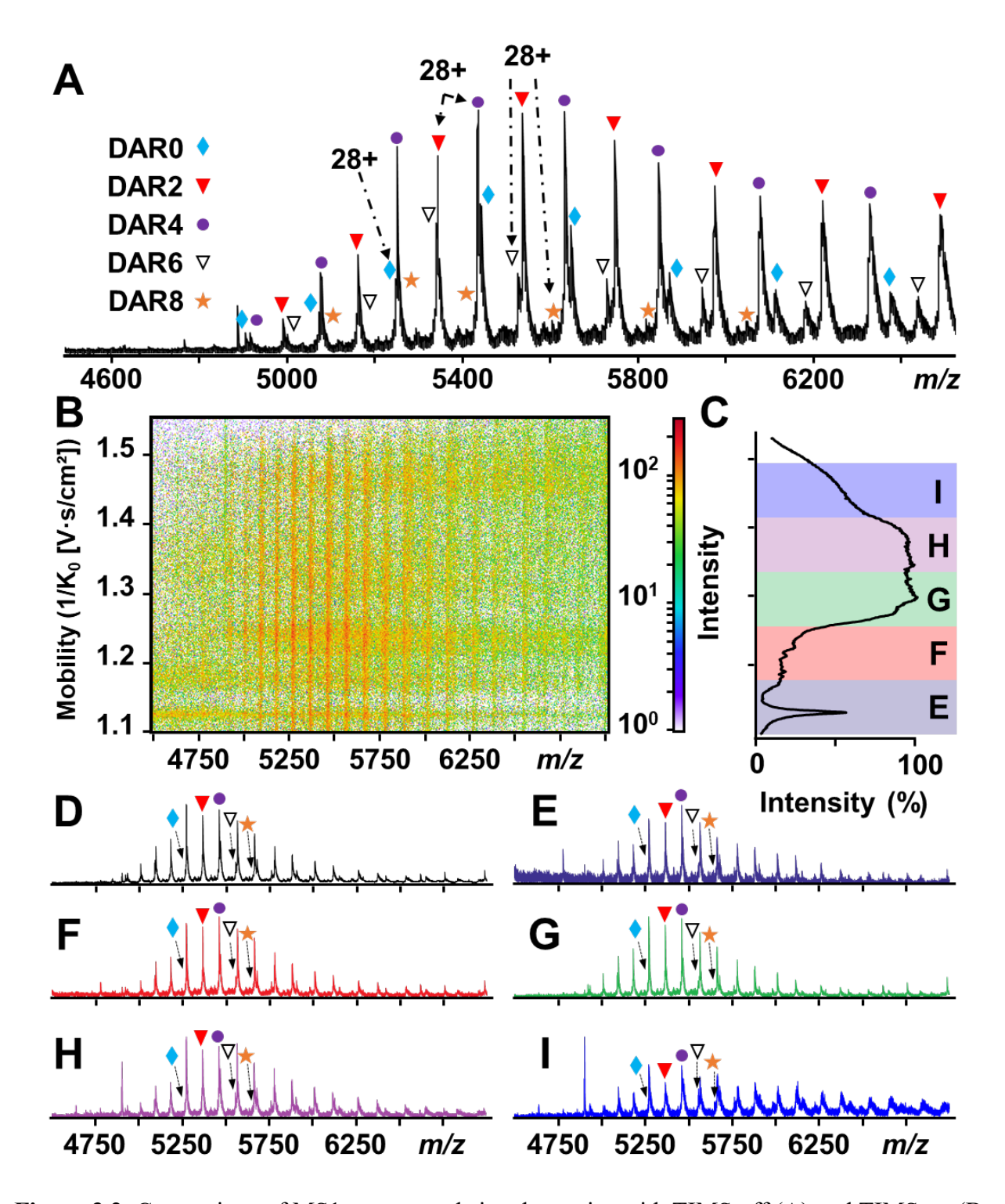
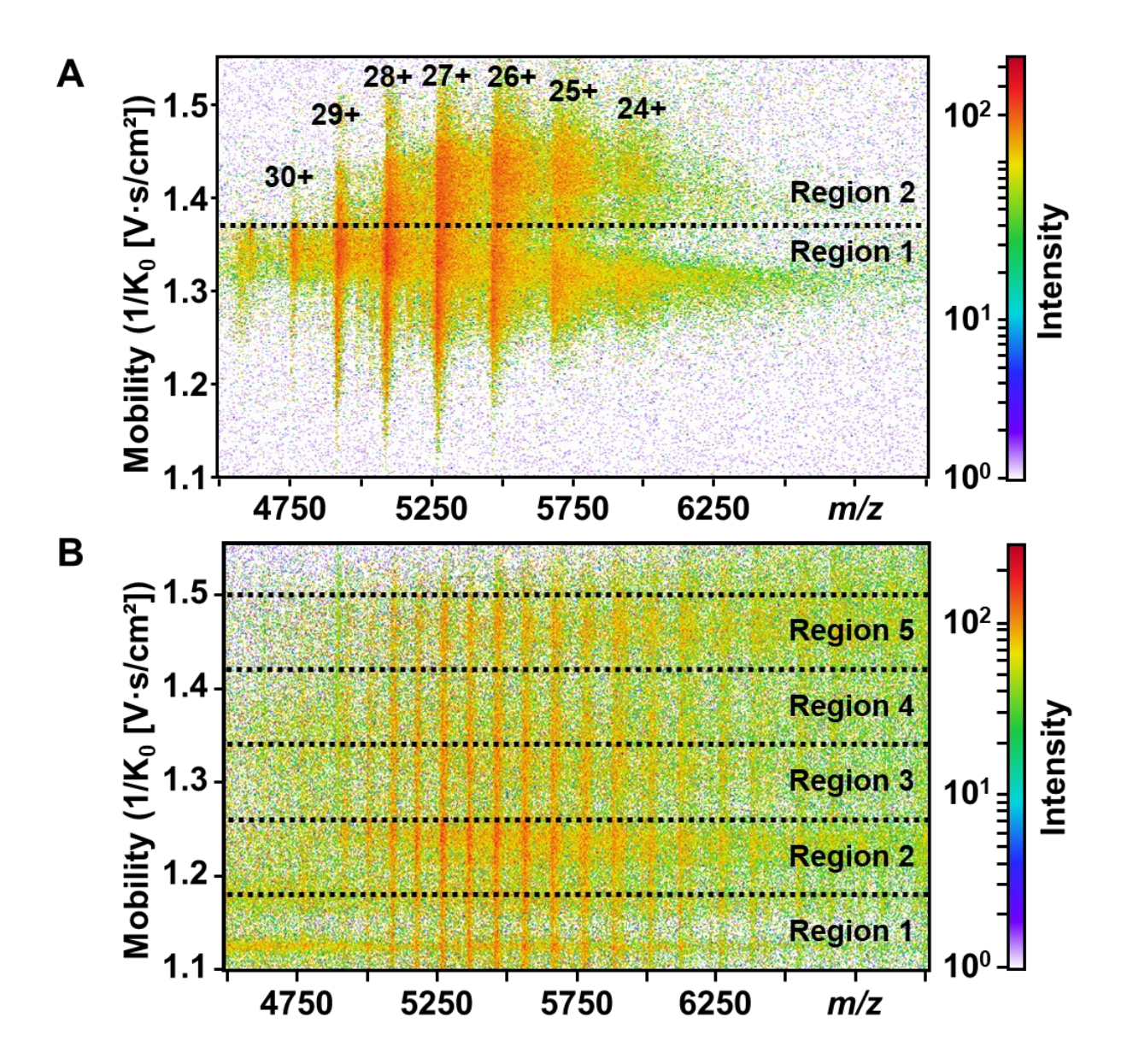
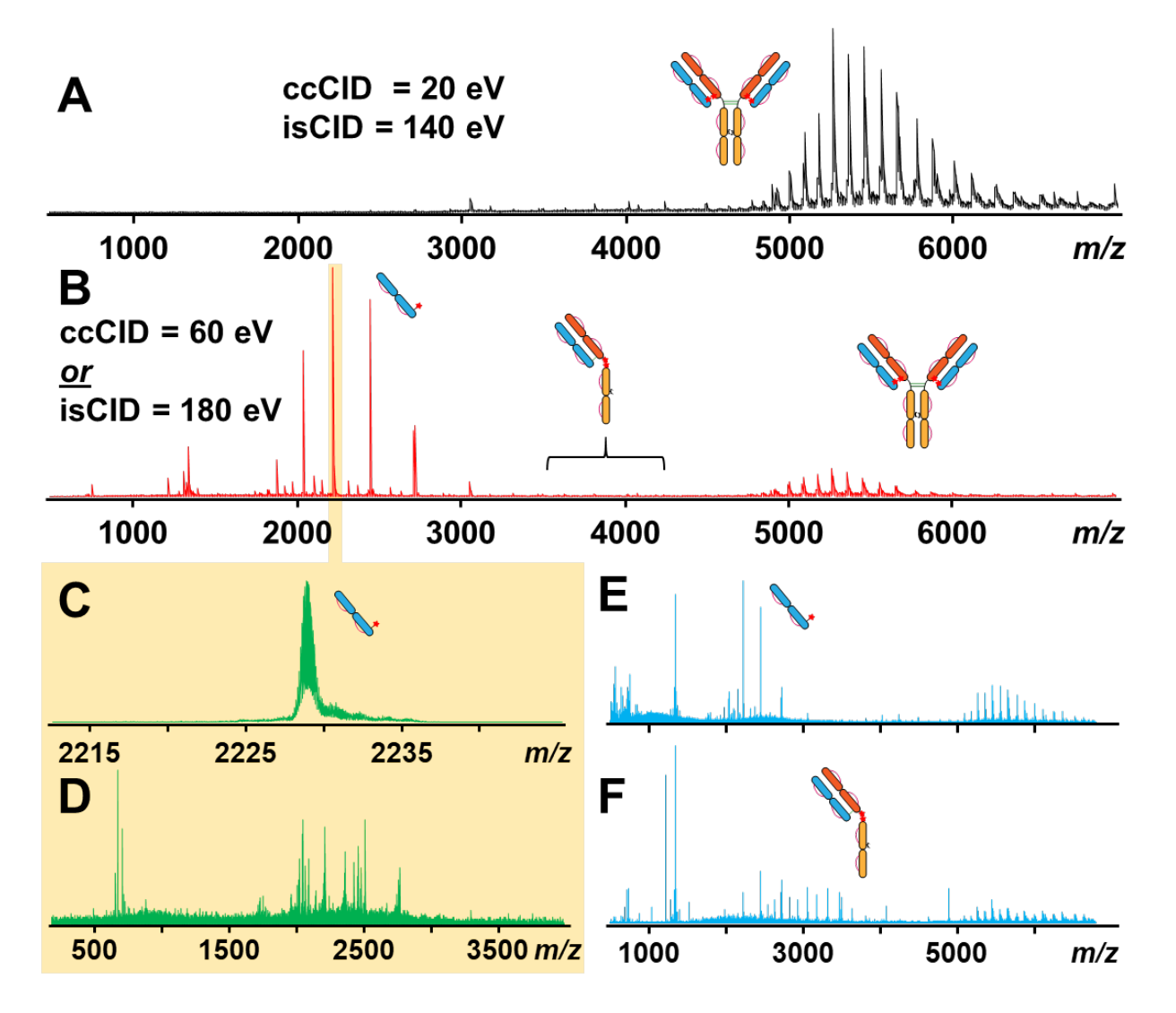


Figure 3.2. Comparison of MS1 spectra and signal to noise with TIMS off (A) and TIMS on (B-I). The 28+ charge is indicated for all DAR species in panel A, and panels D-I. The separation the ADC into mobility regions (B-C) using trapped ion mobility offers an additional benefit over traditional intact MS1 characterization techniques. The average MS1 spectra with TIMS on (D) show an increase in signal-to-noise ratio of the most abundant peak. Differences between MS1 spectra for each mobility regions 1-5 were shown in E-I respectively.



**Figure 3.3.** Comparison of mobility heat maps for starting mAb (A) and ADC (B). TIMS analysis of the starting mAb sample shows two distinct regions of mobility (A). The ADC shows five regions of mobility (B). Mobility differences demonstrate changes in DAR species relative to the starting mAb. This indicates that drug conjugation perturbs the conformational state of the mAb moiety in the ADC.



**Figure 3.4.** Multi-attribute analysis of native ADC using the Bruker timsTOF Pro. MS1 analysis (A), dissociation of subunits (B), and fragmentation of primary sequence (C-G). Two different fragmentation strategies were used: Isolation (C) and fragmentation with 80 eV collision energy for individual subunits by CID (D) and bbCID (E, F). bbCID offers additional advantage of profiling the subunits generated by MS2 across several mobility regions. The average bbCID spectra using 80 eV (E, F) may be compared to bbCID using 80 eV for regions of low 1/K<sub>0</sub> values (E) and high 1/K<sub>0</sub> values (F).

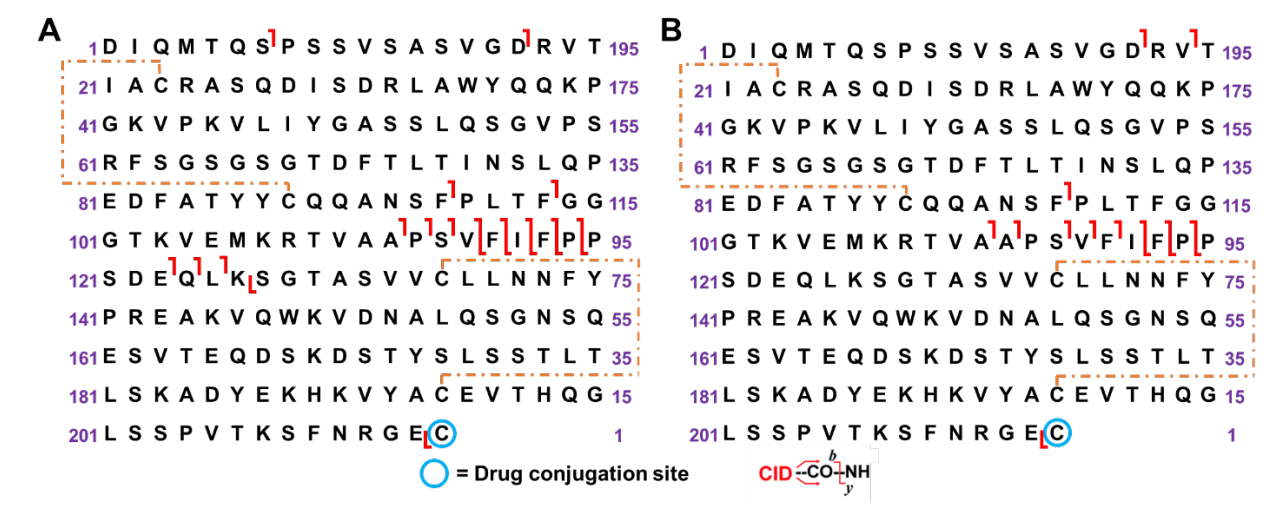


**Figure 3.5.** CID of dissociated Lc1 subunit combining three fragmentation energies, 80, 90, and 100 eV. Two fragmentation strategies were used: A) three 5-min MS3 analyses, one each of the fragmentation energies, which yielded 17 out of 213 possible bond cleavages and B) a single MS3 experiment, scanning all three fragmentation energies for 30 seconds each, yielding 13 out of 213 possible bond cleavages. Generated fragment ions confirmed the presence of intrachain disulfide bonds and localized drug conjugation.

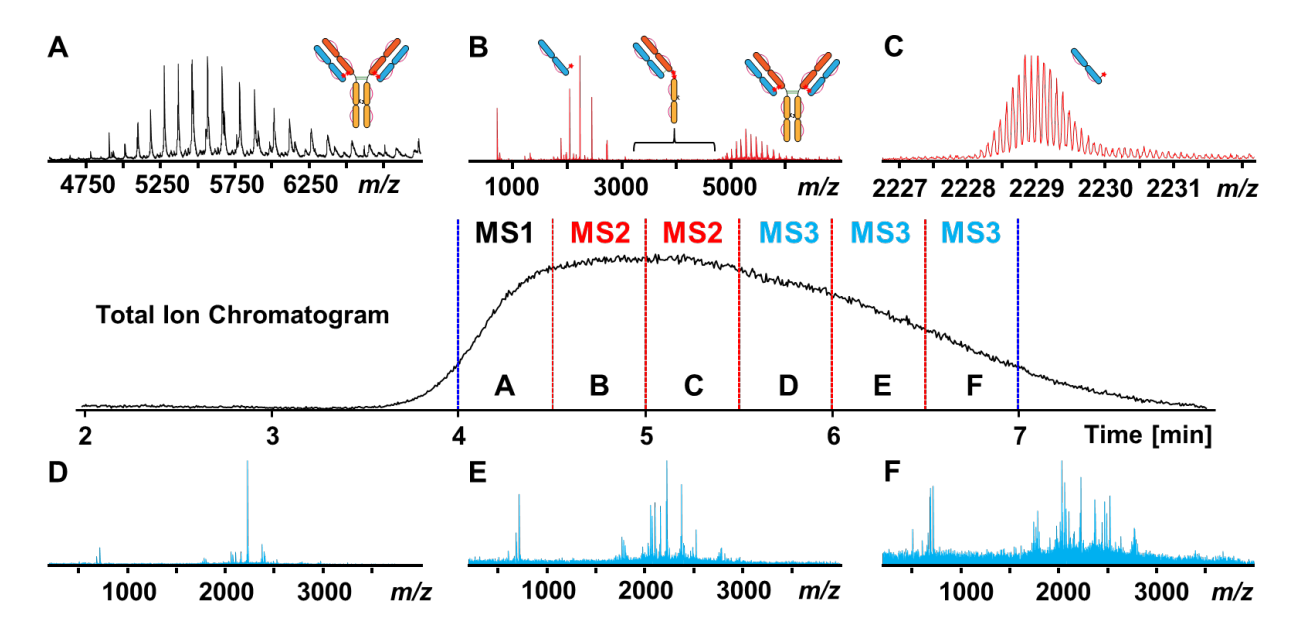


**Figure 3.6.** Segmentation for multi-attribute analysis in a single MS run. Direct injection total ion chromatogram was divided into 30 second increments, labeled A-F, respectively. The segments characterize the intact ADC by MS1 (A), intact subunits dissociated with 60 eV CID energy for MS2 analysis (B), the CID isolation spectra for the most abundant Lc1 subunit charge state (C), and fragmentation using CID with collision energies of 80 eV (D), 90 eV (E) and 100 eV (F) for MS3 characterization.

# Chapter 3

# **Supporting Information**

High-Throughput Multi-Attribute Analysis of Antibody Drug Conjugates Enabled by

Trapped Ion Mobility Spectrometry and Native Top-Down Mass Spectrometry

<u>Table of Contents</u> <u>Pages</u>
Table of Contents
Table S3.ST1 Definition of relevant TIMS voltage parameters and locations applied88
Table 3.ST2 Calculated CCS values of AbbVie starting mAb as a function of TIMS RF voltage88
Table 3. ST3 Calculated CCS values of NISTmAb as a function of TIMS RF voltage89
Table 3.ST4 ST4 Calculated CCS values of AbbVie ADC as a function of TIMS RF voltage89
Table 3.ST5 Calculated MS1 masses for all AbbVie ADC DAR species90
Table 3.ST6 Calculated CCS values for all regions of AbbVie starting mAb mobility90
Table 3.ST7 Calculated CCS values for all regions of AbbVie ADC mobility91
Table 3.ST8 Calculated average DAR for all regions of AbbVie ADC mobility91
Figure 3.S1 Location of voltages used to optimized TIMS performance for intact ADC92
Figure 3.S2 Intensity normalized MS1 spectra from TIMS Δ3 voltage optimization92
Figure 3.S3 Total ion mobilograms from TIMS Δ3 voltage optimization93
Figure 3.S4 Mobility $(1/K_0)$ vs m/z heat maps from TIMS $\Delta 3$ voltage optimization94
Figure 3.S5 Intensity normalized MS1 spectra from TIMS Δ6 voltage optimization95
Figure 3.S6 Total ion mobilograms from TIMS Δ6 voltage optimization96
Figure 3.S7 Mobility (1/ $K_0$ ) vs m/z heat maps from TIMS $\Delta 6$ voltage optimization
Figure 3.S8 Total ion mobilograms of TIMS RF and TIMS duty cycle optimization for AbbVie starting mAb
Figure 3.S9 Total ion mobilograms TIMS duty cycle optimization at 300, 275, and 250 Vpp TIMS RF for AbbVie starting mAb
Figure 3.S10 Total ion mobilograms of TIMS RF optimization for NISTmAb
Figure 3.S11 Plots of calculated CCS for AbbVie starting mAb and NISTmAb using multiple TIMS RF voltages
Figure 3.S12 Total ion mobilograms of TIMS RF and TIMS duty cycle optimization for AbbVie ADC
Figure 3.S13 Mobility (1/K <sub>0</sub> ) vs m/z heat maps from isCID voltage optimization103
Figure 3.S14 Intensity normalized MS1 spectra from isCID voltage optimization
Figure 3.S15 Intensity normalized MS1 for Lc1 <sup>8+</sup> subunit from isCID voltage optimization105
Figure 3.S16 MS1 overlay of detector TOF voltage optimization

Figure 3.S17 Intensity normalized MS1 spectra from TIMS DC gradient voltage optimization107
Figure 3.S18 Total ion mobilograms from TIMS DC gradient voltage optimization108
Figure 3.S19 Mobility $(1/K_0)$ vs m/z heat maps from TIMS DC gradient voltage optimization109
Figure 3.S20 Regionally divided EIMs and MS1 spectra for the AbbVie starting mAb110
Figure 3.S21 Drug conjugations products of "native" conjugation for an IgG type 1 antibody111
Figure 3.S22 Overlay of total ion mobilograms for AbbVie starting mAb and ADC as a function of TIMS RF voltage
Figure 3.S23 Charge deconvoluted MS1 spectra of AbbVie ADC across mobility regions113
Figure 3.S24 Plot of calculated CCS vs average DAR for all AbbVie ADC mobility regions114
Figure 3.S25 EIMs for AbbVie starting mAb and all AbbVie ADC DAR species
Figure 3.S26 Charge deconvoluted MS2 spectra for released subunits
Figure 3.S27 Targeted MS3 CID fragmentation of Lc1 combining multiple fragmentation energies
Figure 3.S28 bbCID fragmentation of Lc1 combining multiple fragmentation energies118
Figure 3.S29 Targeted MS3 CID fragmentation of Lc1 combining multiple fragmentation energies from a segmented 90 second analysis

Table 3.ST1. Definition and location of applied voltages optimized and referenced in the manuscript.

Voltage	Voltage definition and location
name	
isCID	The in-source collision induced dissociation (isCID) voltage is applied between exit funnel of the TIMS device and funnel 2; after TIMS separation, but before quadrupole isolation.
Δ3	The $\Delta 3$ voltage is applied between the deflection transfer plate and the inlet to TIMS funnel 1.
Δ6	The $\Delta 6$ voltage is applied between the exit of the accumulation region and the entrance of the analyzer region of the TIMS device.
ccCID	The collision cell collision induced dissociation (ccCID) is applied in the collision cell. The notation "ccCID" is used here to emphasize the location of voltage application.

**Table 3.ST2.** TIMS CCS<sub>N2</sub> for the AbbVie starting mAb at varied TIMS RF voltages. The calculated TIMS CCS<sub>N2</sub> and standard deviation from triplicate injection replicates is reported for the 29+ through 24+ charge states. All mobility regions observed at a given TIMS RF voltage are reported here.

Charge	29+	28+	27+	26+	25+	24+
350 vpp	7282.5 ± 3.4	7031.3 ± 3.2	6780.2 ± 3.1	6529.2 ± 3.0	6278.0 ± 2.9	6026.9 ± 2.8
Reg. 1						
350 vpp	7614.6 ± 3.7	7352.0 ± 3.5	7089.5 ± 3.4	6826.9 ± 3.3	6564.4 ± 3.2	6301.8 ± 3.0
Reg. 2						
300 vpp	7078.0 ± 10.4	6834.0 ± 10.1	6589.9 ± 9.7	6345.8 ± 9.3	6101.8 ± 9.0	5857.4 ± 8.1
Reg. 1						
300 vpp	7195.1 ± 14.4	6947.0 ± 14.0	6699.0 ± 13.4	6450.8 ± 12.9	6202.7 ± 12.4	5954.6 ± 12.0
Reg. 2						
275 Vpp	6909.7 ± 12.9	6671.4 ± 12.5	6433.2 ± 12.0	6194.9 ± 11.6	5956.7 ± 11.1	5718.4 ± 10.7
Reg. 1						
250 Vpp	6867.7 ± 2.7	6630.9 ± 2.6	6394.1 ± 2.5	6157.2 ± 2.4	5920.4 ± 2.3	5683.6 ± 2.3
Reg. 1						

**Table 3.ST3.** TIMS CCS<sub>N2</sub> for NISTmAb at varied TIMS RF voltages. The calculated TIMS CCS<sub>N2</sub> and standard deviation from triplicate injection replicates is reported for the 29+ through 24+ charge states. All mobility regions observed at a given TIMS RF voltage are reported here.

Charge	29+	28+	27+	26+	25+	24+
350 vpp	7376.6 ± 24.4	7122.2 ± 23.6	6867.8 ± 22.7	6613.5 ± 21.8	6359.1 ± 21.0	6104.8 ± 20.2
Reg. 1						
350 vpp	7786.7 ± 36.1	7518.1 ± 34.8	7249.7 ± 33.6	6981.1 ± 32.4	6712.6 ± 31.1	6444.1 ± 29.8
Reg. 2						
300 vpp	7219.6 ± 8.6	6970.6 ± 8.3	6721.6 ± 8.0	6472.7 ± 7.7	6223.7 ± 7.4	5974.8 ± 7.1
Reg. 1						
300 vpp	7452.9 ± 59.9	7196.0 ± 57.8	6938.9 ± 55.8	6682.0 ± 53.7	6425.0 ± 51.7	6168.0 ± 49.6
Reg. 2						
275 Vpp	7072.5 ± 6.2	6828.6 ± 6.0	6584.7 ± 5.8	6340.8 ± 5.5	6096.9 ± 5.4	5853.1 ± 5.2
Reg. 1						
250 Vpp	6904.9 ± 3.1	6666.8 ± 3.0	6428.7 ± 3.0	6190.6 ± 2.8	5952.5 ± 2.7	5714.4 ± 2.6
Reg. 1						

**Table 3.ST4.** TIMS CCS<sub>N2</sub> for the AbbVie ADC at varied TIMS RF voltages. The calculated TIMS CCS<sub>N2</sub> and standard deviation from triplicate injection replicates is reported for the 29+ through 24+ charge states. All mobility regions observed at a given TIMS RF voltage are reported here.

Charge	29+	28+	27+	26+	25+	24+
350 Vpp	6457.2 ± 4.3	6234.5 ± 4.1	6011.8 ± 4.0	5789.2 ± 3.8	5566.5 ± 3.7	5343.9 ± 3.5
Reg. 1						
350 Vpp	6744.6 ± 10.4	6512.1 ± 10.0	6279.5 ± 9.6	6046.9 ± 9.3	5814.3 ± 9.0	5581.8 ± 8.6
Reg. 2						
350 Vpp	7044.0 ± 9.9	6801.1 ± 9.6	6558.2 ± 9.2	6315.3 ± 8.9	6072.4 ± 8.6	5829.5 ± 8.2
Reg. 3						
300 Vpp	6342.0 ± 9.6	6123.2 ± 9.3	5904.6 ± 9.0	5685.9 ± 8.7	5467.2 ± 8.3	5238.5 ± 10.5
Reg. 1						
300 Vpp	6447.3 ± 9.8	6225.9 ± 9.9	6002.6 ± 9.1	5780.3 ± 8.8	5558.0 ± 8.5	5335.6 ± 8.1
Reg. 2						
300 Vpp	6771.8 ± 20.9	6538.3 ± 20.2	6304.8 ± 19.4	6071.2 ± 18.8	5837.7 ± 18.0	5604.2 ± 17.3
Reg. 3						
275 Vpp	6289.2 ± 15.0	6072.3 ± 14.5	5855.5 ± 13.9	5638.6 ± 13.4	5421.7 ± 12.9	5204.9 ± 12.4
Reg. 1						
275 Vpp	6424.3 ± 2.1	6202.8 ± 2.1	5981.2 ± 2.0	5759.7 ± 1.9	5538.2 ± 1.8	5316.6 ± 1.8
Reg.2						
250 Vpp	6343.4 ± 2.8	6124.7 ± 2.7	5905.9 ± 2.6	5687.2 ± 2.4	5468.5 ± 2.4	5249.7 ± 2.3
Reg. 1						

**Table 3.ST5.** MS1 experimental and calculated masses of all DAR species determined by direct injection MS analysis with optimized TIMS parameters.

DAR	Theoretical Average Mass (Da)	Experimental Average Mass (Da)	Error (ppm)
DAR 0	147616.1	147615.0	7.5
DAR 2	150247.6	150246.9	4.7
DAR 4	152879.1	152880.5	9.2
DAR 6	155510.7	155512.6	12.2
DAR 8	158142.2	158143.9	10.7

**Table 3.ST6.** Regional average  $^{TIMS}CCS_{N2}$  (Å<sup>2</sup>) of the two starting monoclonal antibody (mAb) mobility regions with standard deviations from three replicated analyses.

Charge	Region 1	Region 1 stdv	Region 2	Region 2 stdv
29+	7373.7	±14.8	7635.6	±27.4
28+	7119.4	±14.2	7372.3	±26.5
27+	6865.1	±13.8	7109.0	±25.5
26+	6610.9	±13.2	6845.7	±24.6
25+	6356.6	±12.7	6582.4	±23.6
24+	6102.3	±12.2	6319.1	±22.7

**Table 3.ST7.** Regional average  $^{TIMS}CCS_{N2}$  (Å<sup>2</sup>) of the five antibody-drug conjugate (ADC) mobility regions with standard deviations from three replicated analyses. The  $^{TIMS}CCS_{N2}$  was calculated using the charge states of DAR 2, the most abundant DAR species.

Charge		Region 1 stdv	Region 2	Region 2 stdv	Region 3	Region 3 stdv	Region 4	Region 4 stdv	Region 5	Region 5 stdv
29+	6645.7		7286.0	±15.9	7331.5	±6.3	7861.9		8336.3	±26.7
28+	6416.5	±11.3	7034.8	±15.4	7078.7	±6.1	7590.8	±25.3	8048.8	25.8
27+	6187.3	±10.9	6783.5	±14.8	6825.9	±5.9	7319.8	±24.4	7761.4	±24.9
26+	5958.2	±10.5	6532.3	±14.3	6573.1	±5.6	7048.6	±23.5	7473.9	±24.0
25+	5729.0	±10.1	6281.0	±13.7	6320.3	±5.5	6777.5	±22.6	7186.4	±23.1
24+	5499.9	9.7	6029.8	±13.2	6067.5	±5.2	6506.4	±21.7	6899.0	±22.2

**Table 3.ST8.** Calculated regional average drug-antibody ratio (DAR) and collisional cross section (TIMSCCS<sub>N2</sub>) calculated from the 29+ charge state for each mobility region of the ADC. These values were generated from three replicate infusions of the model cysteine ADC using optimized TIMS parameters specified in the methods section.

Region	DAR	TIMSCCS <sub>N2</sub> (Å <sup>2</sup> ) (29+)			
Avg	3.01 ± 0.01	N/A			
1	2.91 ± 0.05	6645.7 ± 11.7			
2	$2.99 \pm 0.02$	7286.0 ± 15.6			
3	$3.03 \pm 0.03$	7331.5 ± 6.3			
4	3.16 ± 0.08	7861.9 ± 26.1			
5	3.34± 0.05	8336.2 ± 26.7			

# **Supplemental Figures**

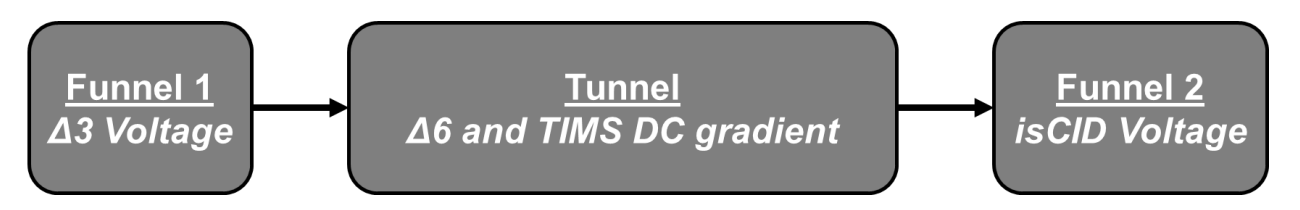


**Figure 3.S1**. Voltages used to optimize TIMS separation performance. Voltages shown in the region of the TIMS cell where each voltage is applied.

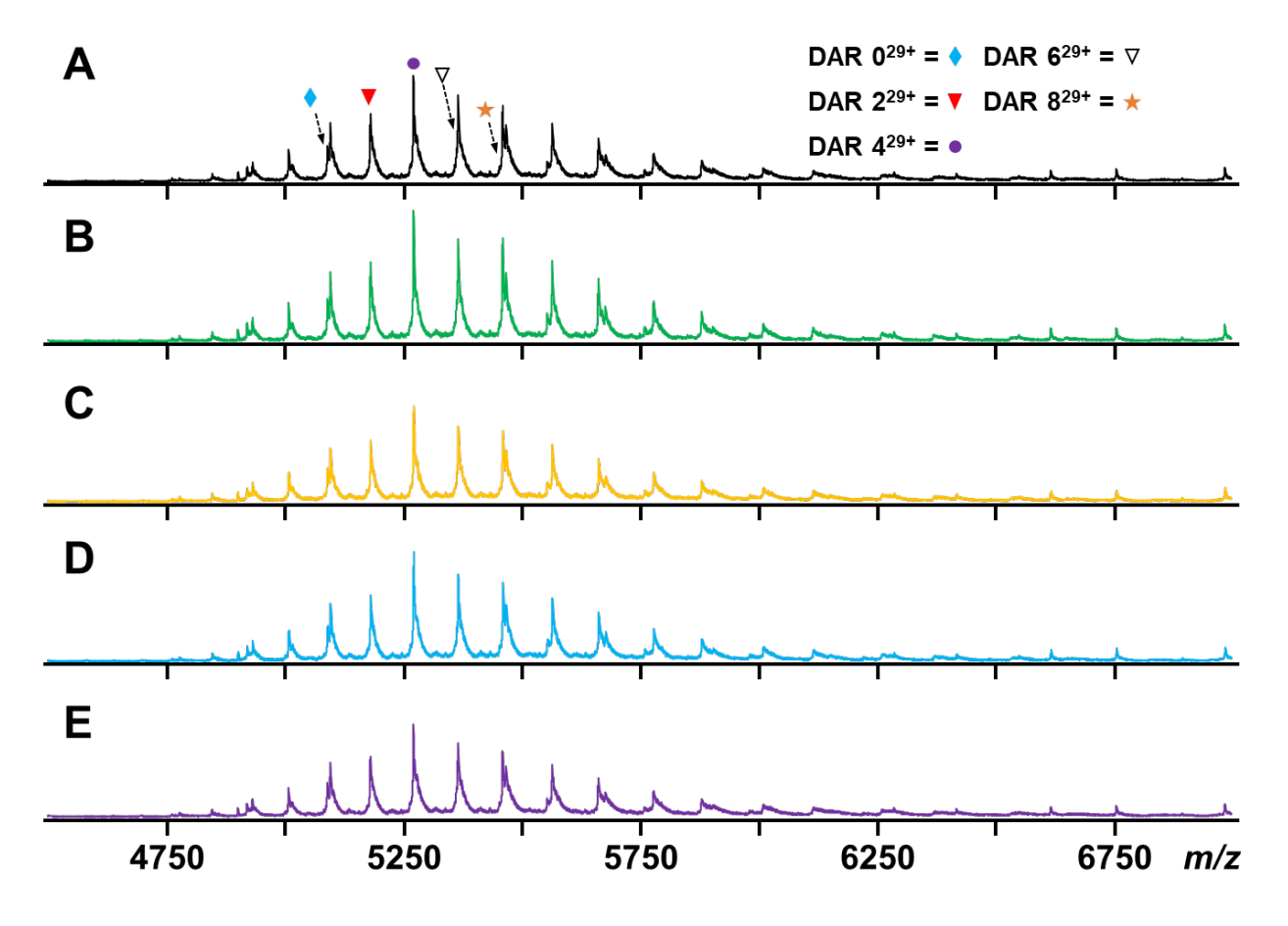


**Figure 3.S2.** TIMS  $\Delta 3$  voltage optimization. Normalized MS1 spectra of five conditions screened, 170 V (A), 160 V (B), 150 V (C), 140 V (D), and 130 V (E). 160 V provided the highest MS signal intensity.

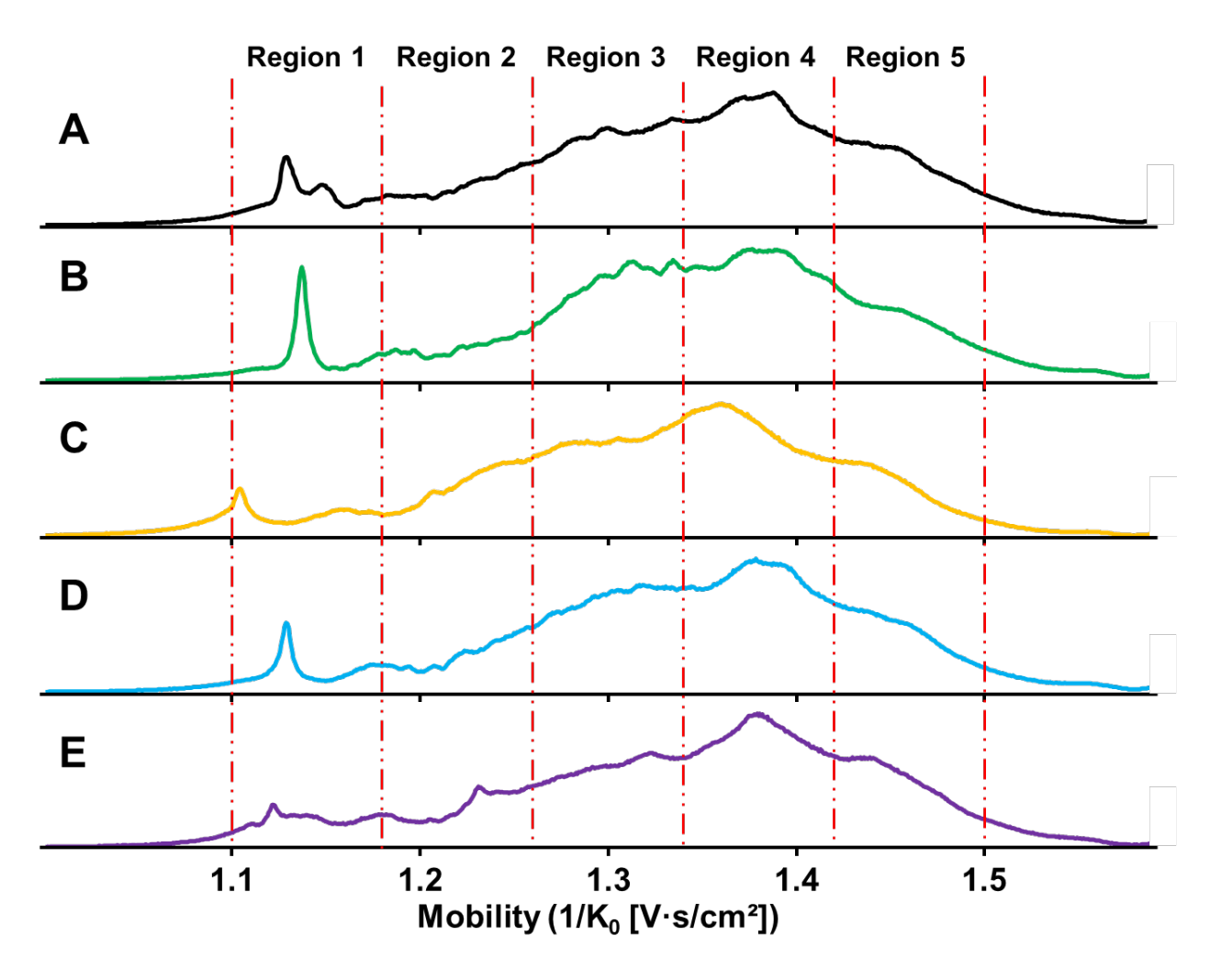


**Figure 3.S3.** TIMS  $\Delta 3$  voltage optimization. Total ion mobilograms (TIMs) of five conditions were screened, 170 V (A), 160 V (B), 150 V (C), 140 V (D), and 130 V (E). 160 V provided the most well-defined mobility separation for both the low mobility (1.1-1.26  $1/K_0$ ) and high mobility (1.34-1.5  $1/K_0$ ) regions

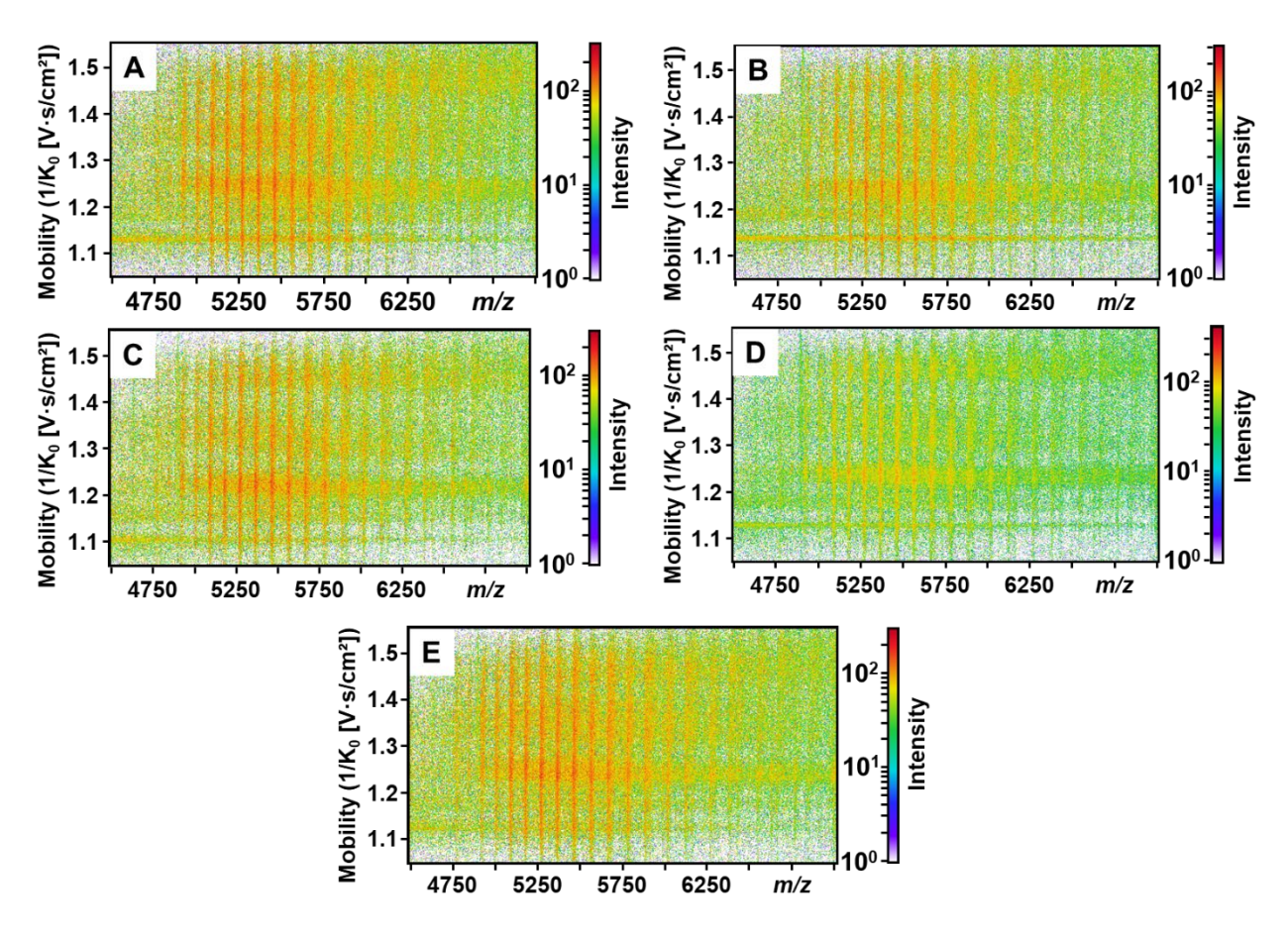


**Figure 3.S4.** TIMS  $\Delta 3$  voltage optimization. Five conditions were screened, 170 V (A), 160 V (B), 150 V (C), 140 V (D), and 130 V (E). 160 V provided the most well-defined mobility separation for both the low mobility (1.1-1.3 1/K<sub>0</sub>) and high mobility (1.3-1.5 1/K<sub>0</sub>) regions.

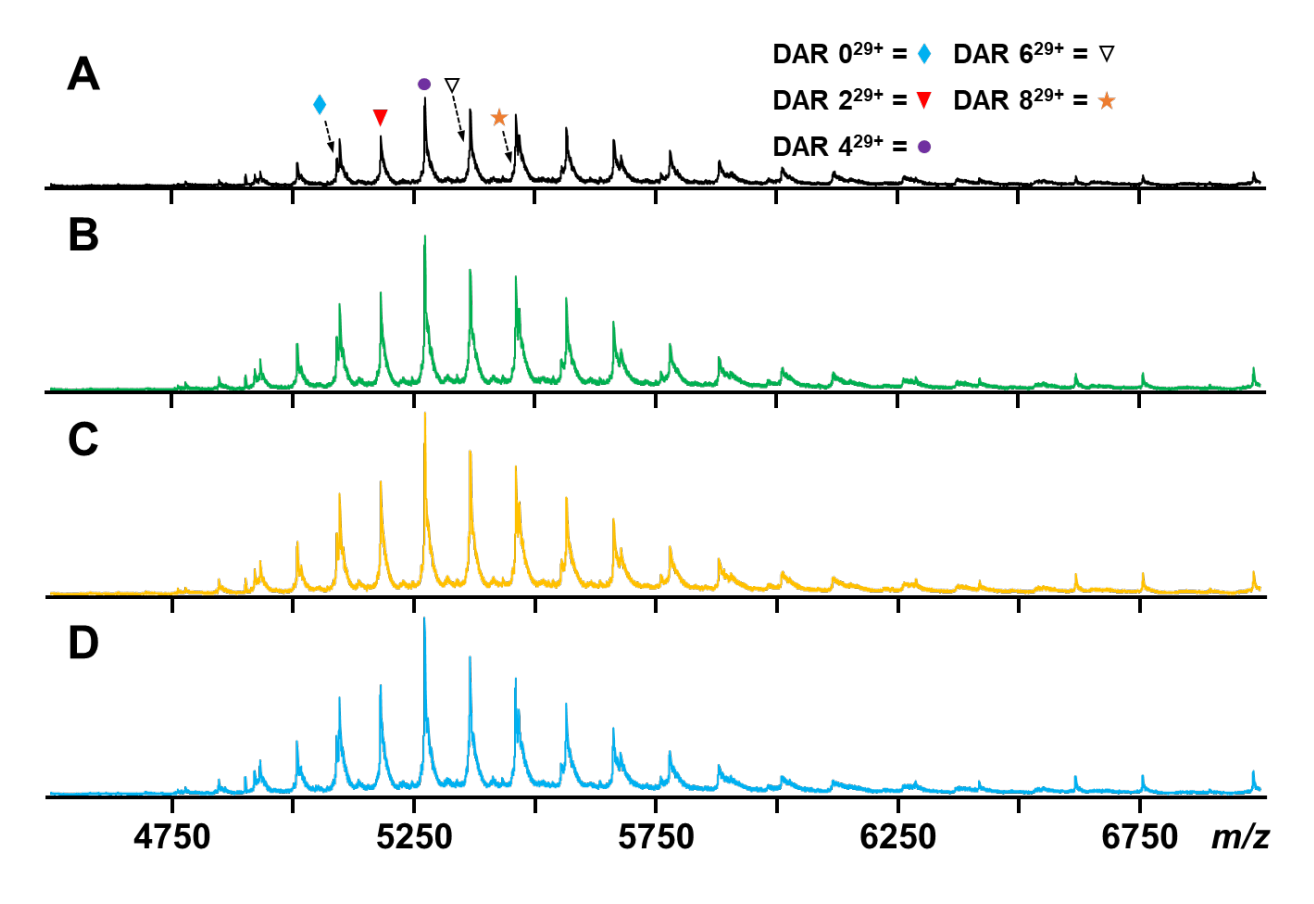


**Figure 3.S5.** TIMS  $\Delta6$  voltage optimization. Normalized MS1 of four conditions screened, 110 V (A), 100 V (B), 90 V (C), and 80 V (D). 90 V provided the most intense MS1 signal, with 100 V providing a similar, but slightly lower signal intensity.

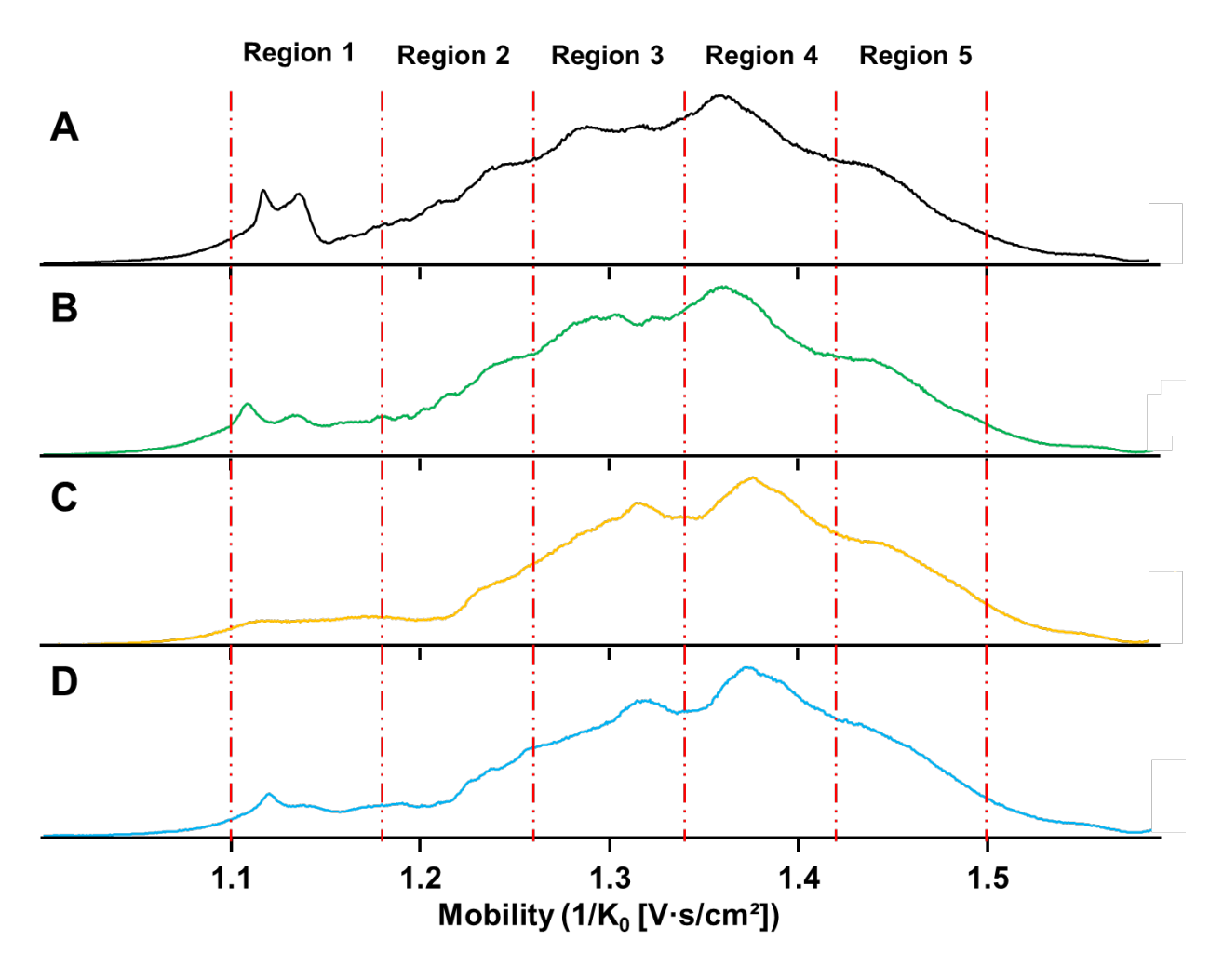


**Figure 3.S6.** TIMS  $\Delta 6$  voltage optimization. TIMs of four conditions screened, 110 V (A), 100 V (B), 90 V (C), and 80 V (D). 100 V provided the most intense signal from the low mobility regions (1.1-1.3  $1/K_0$ ).

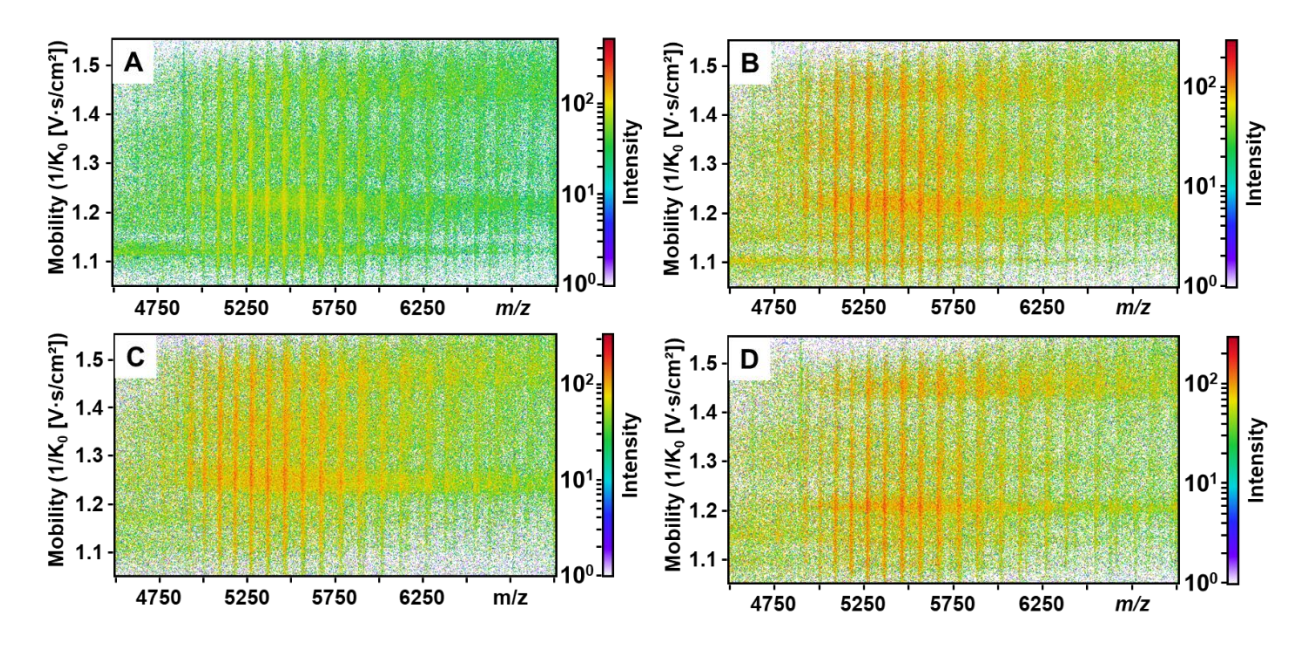


**Figure 3.S7.** TIMS  $\Delta 6$  voltage optimization. Five conditions were screened, 110 V (A), 100 V (B), 90 V (C), and 800 V (D). 100 V provided the most well-defined mobility separation in the low mobility regions (1.1-1.3  $1/K_0$ )

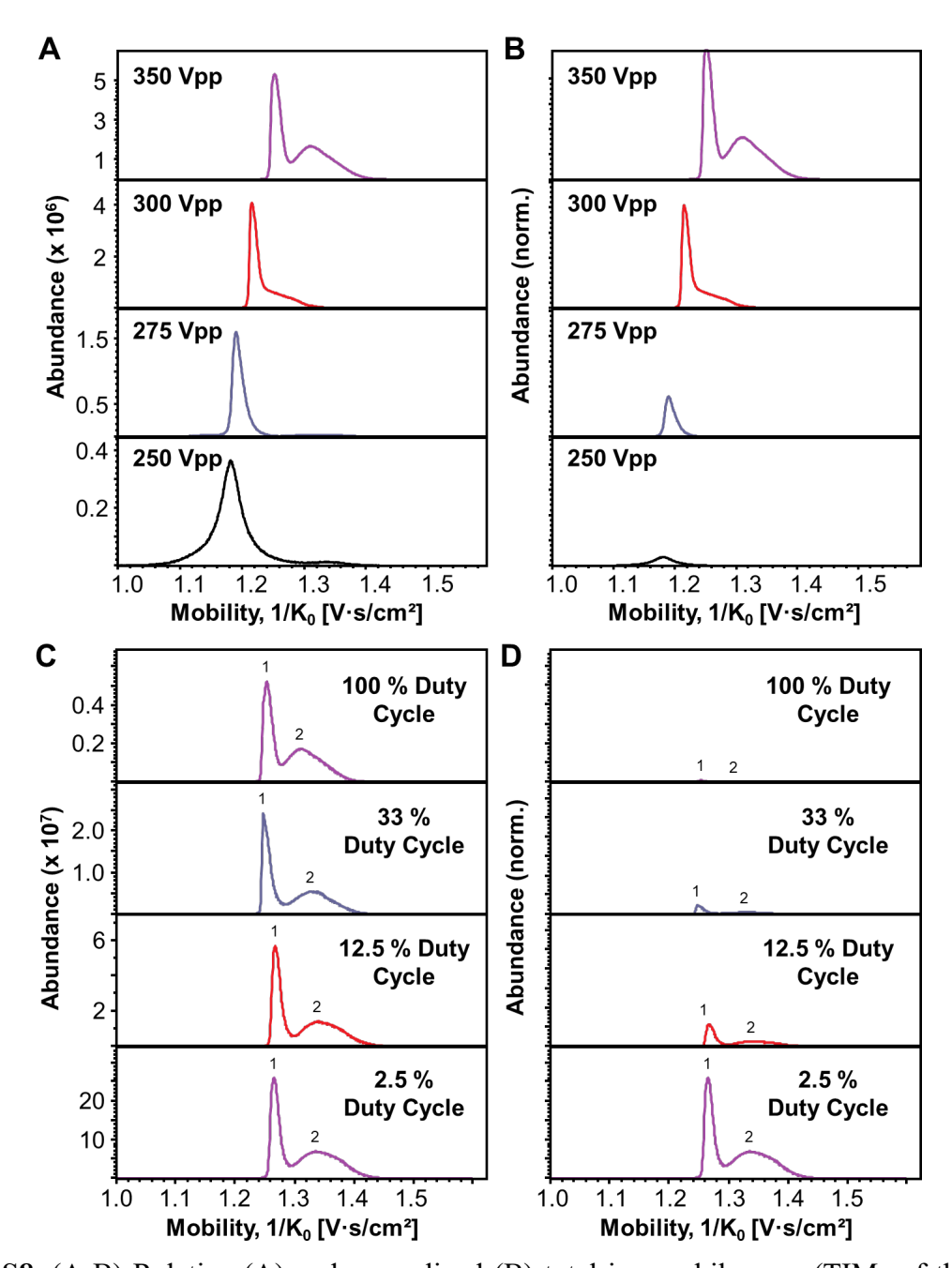


**Figure 3.S8**. (A-B) Relative (A) and normalized (B) total ion mobilogram (TIMs of the native starting AbbVie mAb (z = 29+) as a function of TIMS RF. The native starting mAb was prepared as a 15  $\mu$ M solution in 150 mM ammonium acetate and directly infused into the mass spectrometer. TIMS duty cycle was fixed at 100%. The TIMS RF voltage was varied between 250 Vpp to 350 Vpp (used in this work). (C-D) Relative (C) and normalized (D) TIMs of the native starting monoclonal antibody (mAb, z = 29+) as a function of TIMS duty cycle. The TIMS accumulation time was varied between 400 ms (100%), 133 ms (33%), 50 ms (12.5%), and 10 ms (2.5%) to achieve the various duty cycles shown. The mobility regions observed are annotated as "1" and "2". TIMS RF was fixed at 350 Vpp. The TIMS device was recalibrated following each change in TIMS RF voltage.

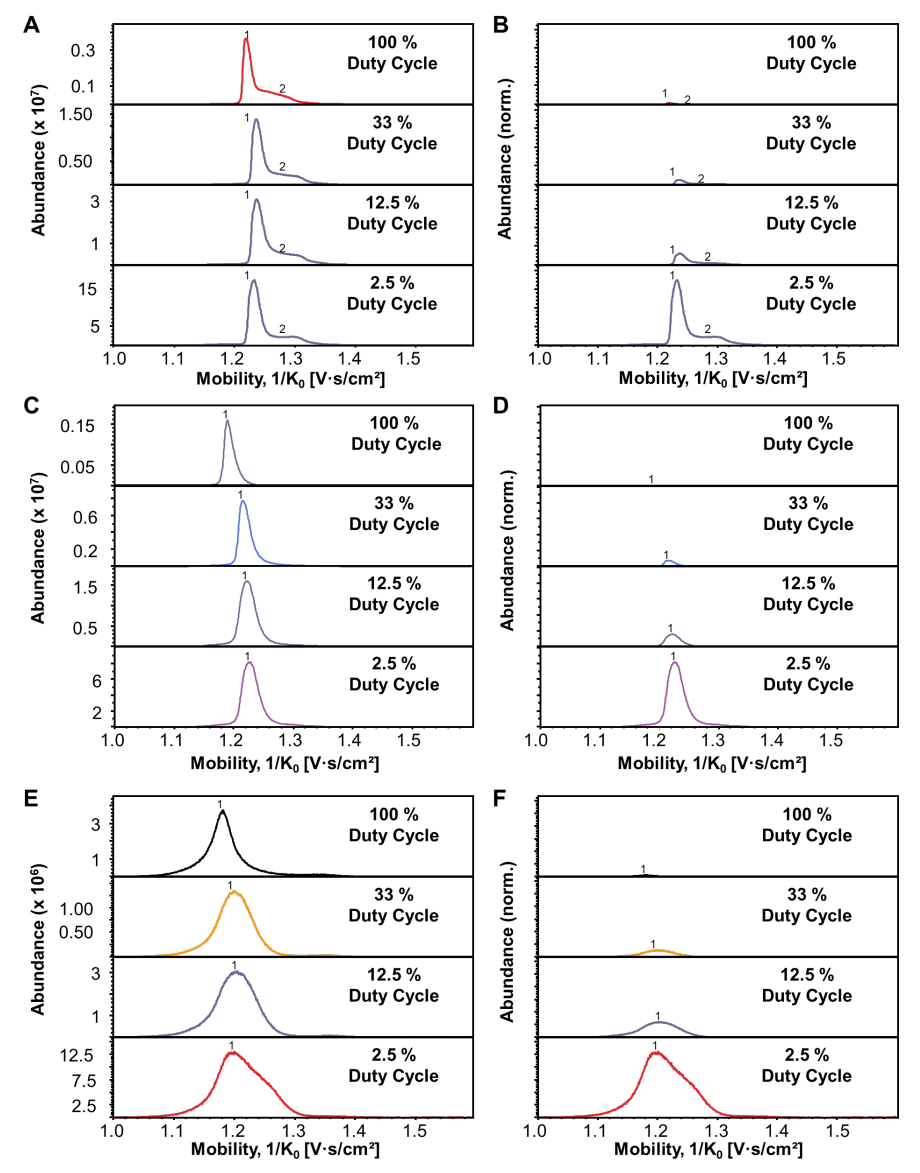


**Figure 3.S9**. (A-B) Relative (A) and normalized (B) TIMs of the native starting mAb (z = 29+) as a function of TIMS duty cycle with TIMS RF fixed at 300 Vpp. The native starting mAb was prepared as a 15 μM solution in 150 mM ammonium acetate and directly infused into the mass spectrometer. The TIMS accumulation time was varied between 400 ms (100%), 133 ms (33%), 50 ms (12.5%), and 10 ms (2.5%) to achieve the various duty cycles shown. The mobility regions observed is annotated as "1" and "2". (C-D) Relative (C) and normalized (D) TIMs of the native starting mAb (z = 29+) as a function of TIMS duty cycle with TIMS RF fixed at 275 Vpp. The TIMS accumulation time was varied between 400 ms (100%), 133 ms (33%), 50 ms (12.5%), and 10 ms (2.5%) to achieve the various duty cycles shown. The mobility region observed is annotated as "1". (E-F) Relative (E) and normalized (F) EIMs of the native starting mAb (z = 29+) as a function of TIMS duty cycle TIMS RF fixed at 250 Vpp. The TIMS accumulation time was varied between 400 ms (100%), 133 ms (33%), 50 ms (12.5%), and 10 ms (2.5%) to achieve the various duty cycles shown. The mobility region observed is annotated as "1". The TIMS device was recalibrated following each change in TIMS duty cycle.

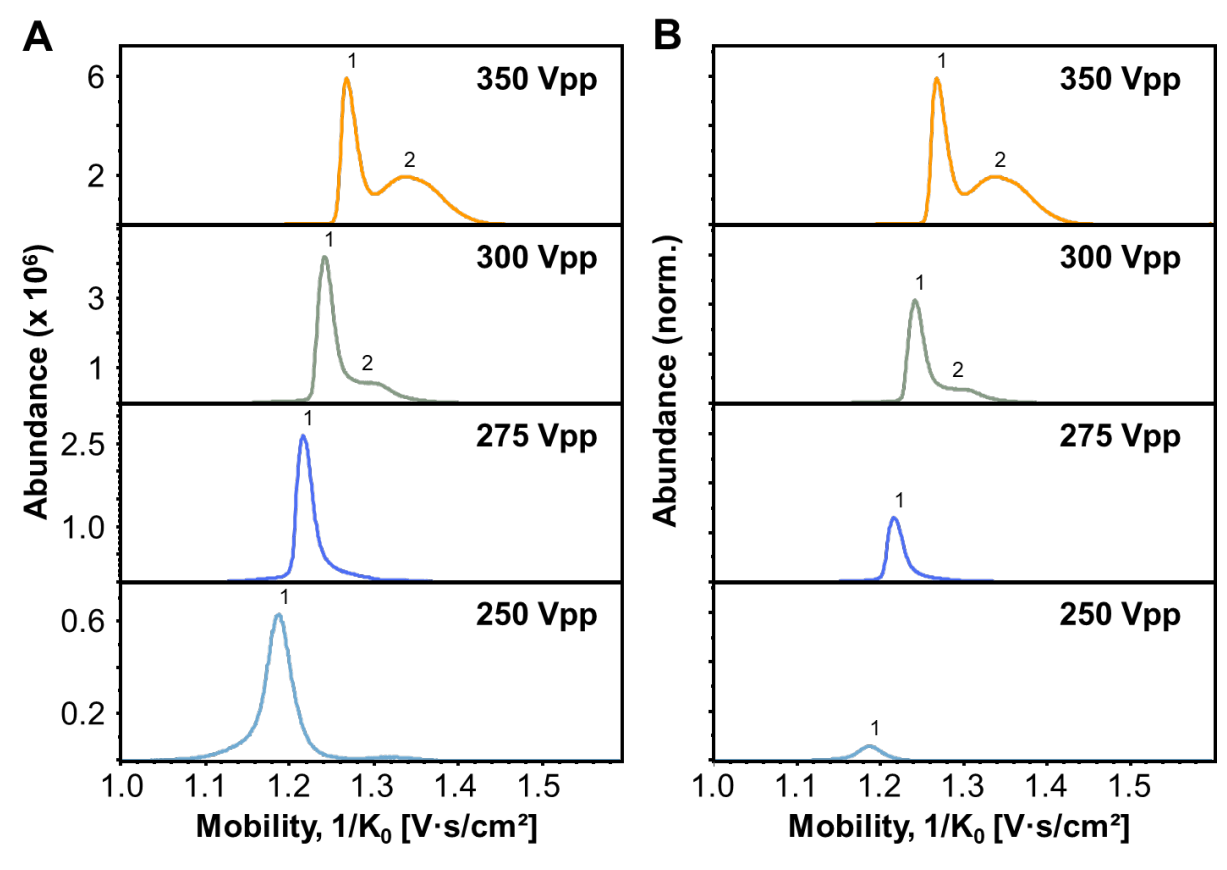


**Figure 3.S10**. (A-B) Relative (A) and normalized (B) TIMs of the NISTmAb (z = 29+) as a function of TIMS RF. The native NISTmAb standard was prepared as a 15  $\mu$ M solution in 150 mM ammonium acetate and directly infused into the mass spectrometer. TIMS duty cycle was fixed at 100%. The mobility regions observed are annotated as "1" and "2". The TIMS RF voltage was varied between 250 Vpp to 350 Vpp (used in this work). The TIMS device was recalibrated following each change in TIMS RF voltage.

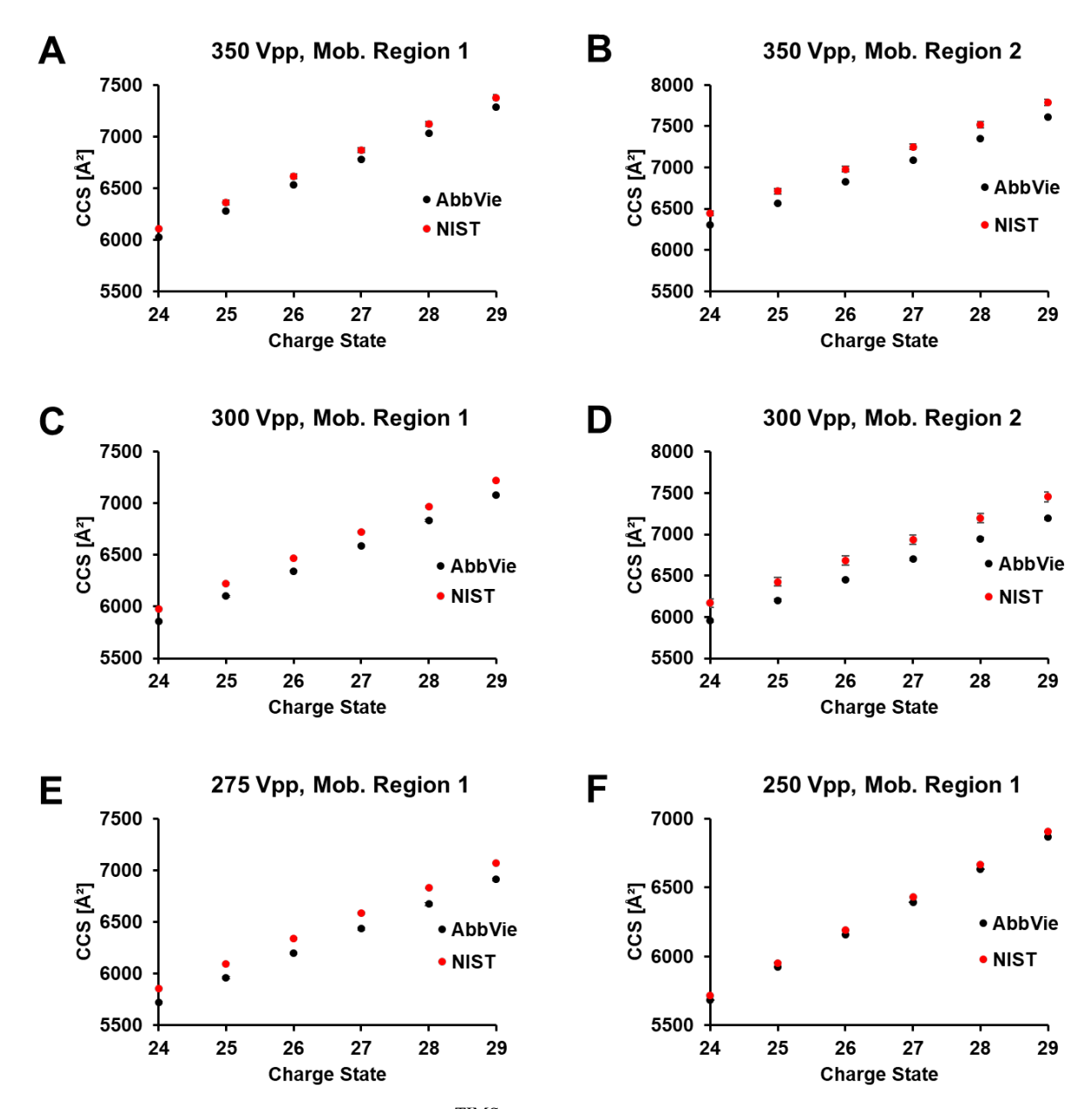


**Figure 3.S11**. (A-F) Plots detailing the  $^{\text{TIMS}}\text{CCS}_{\text{N2}}$  values of the NISTmAb and AbbVie starting mAb at various charge states (z = 24 + to 29 + ) across the various TIMS RF voltages. The native NISTmAb standard and AbbVie starting mAb were prepared as a 15 μM solution in 150 mM ammonium acetate and directly infused into the mass spectrometer. TIMS duty cycle was fixed at 100%. The mobility regions observed are annotated as "1" and "2". The TIMS RF voltage was varied between 250 Vpp to 350 Vpp (used in this work). All  $^{\text{TIMS}}\text{CCS}_{\text{N2}}$  values shown are representative of n = 3 independent samples with errors calculated as the standard deviation. The TIMS device was recalibrated following each change in TIMS RF voltage.

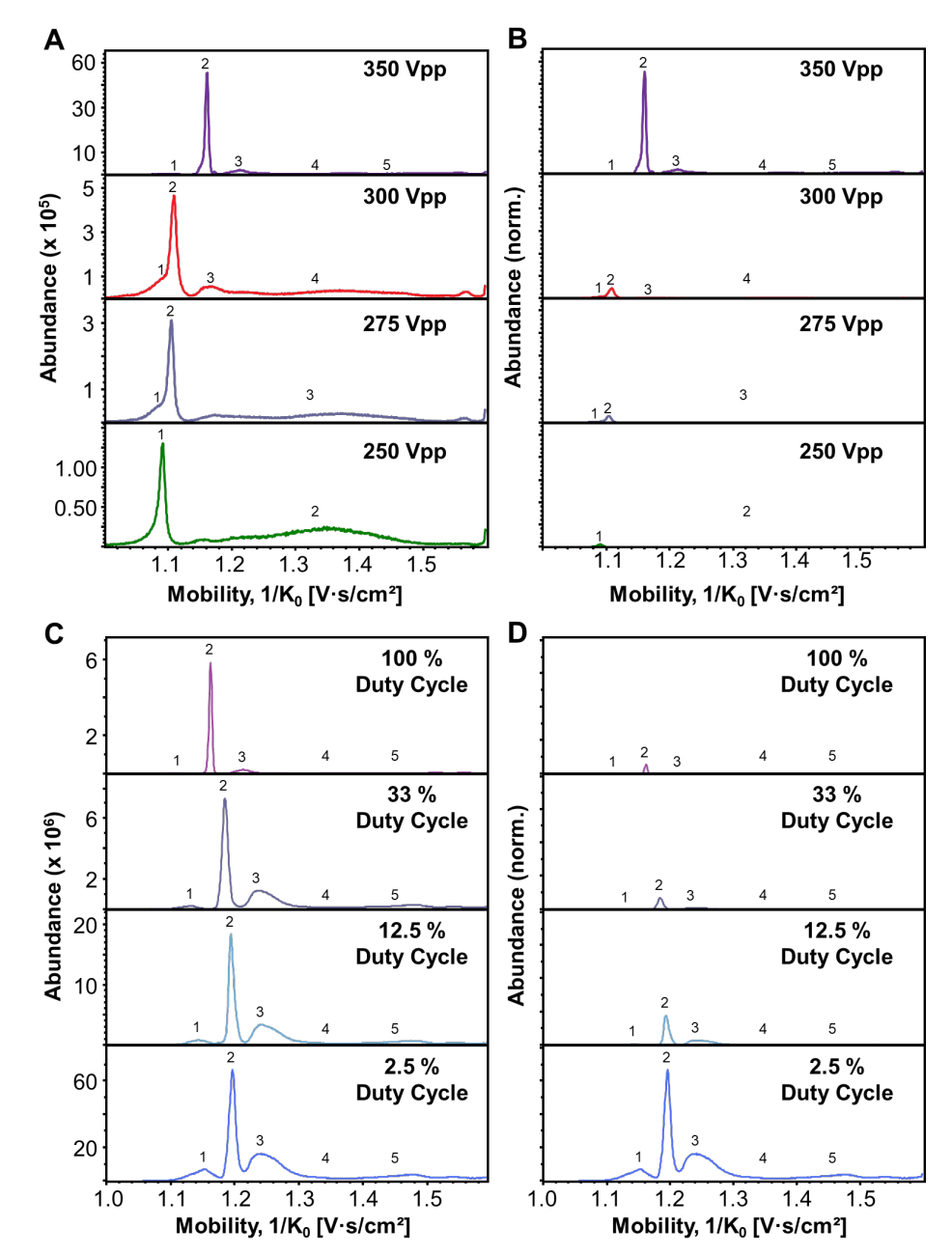


**Figure 3.S12**. (A-B) Relative (A) and normalized (B) TIMs of the ADC (z = 29+) as a function of TIMS RF. The native ADC was prepared as a 15 μM solution in 150 mM ammonium acetate and directly infused into the mass spectrometer. TIMS duty cycle was fixed at 100%. The mobility regions observed are annotated as "1" to "5". The TIMS RF voltage was varied between 250 Vpp to 350 Vpp (used in this work). The TIMS device was recalibrated following each change in TIMS RF voltage. (C-D) Relative (C) and normalized (D) TIMs of the ADC (z = 29+) as a function of TIMS duty cycle. The TIMS accumulation time was varied between 400 ms (100%), 133 ms (33%), 50 ms (12.5%), and 10 ms (2.5%) to achieve the various duty cycles shown. The mobility regions observed are annotated as "1" to "5". TIMS RF was fixed at 350 Vpp. The TIMS device was recalibrated following each change in TIMS duty cycle.

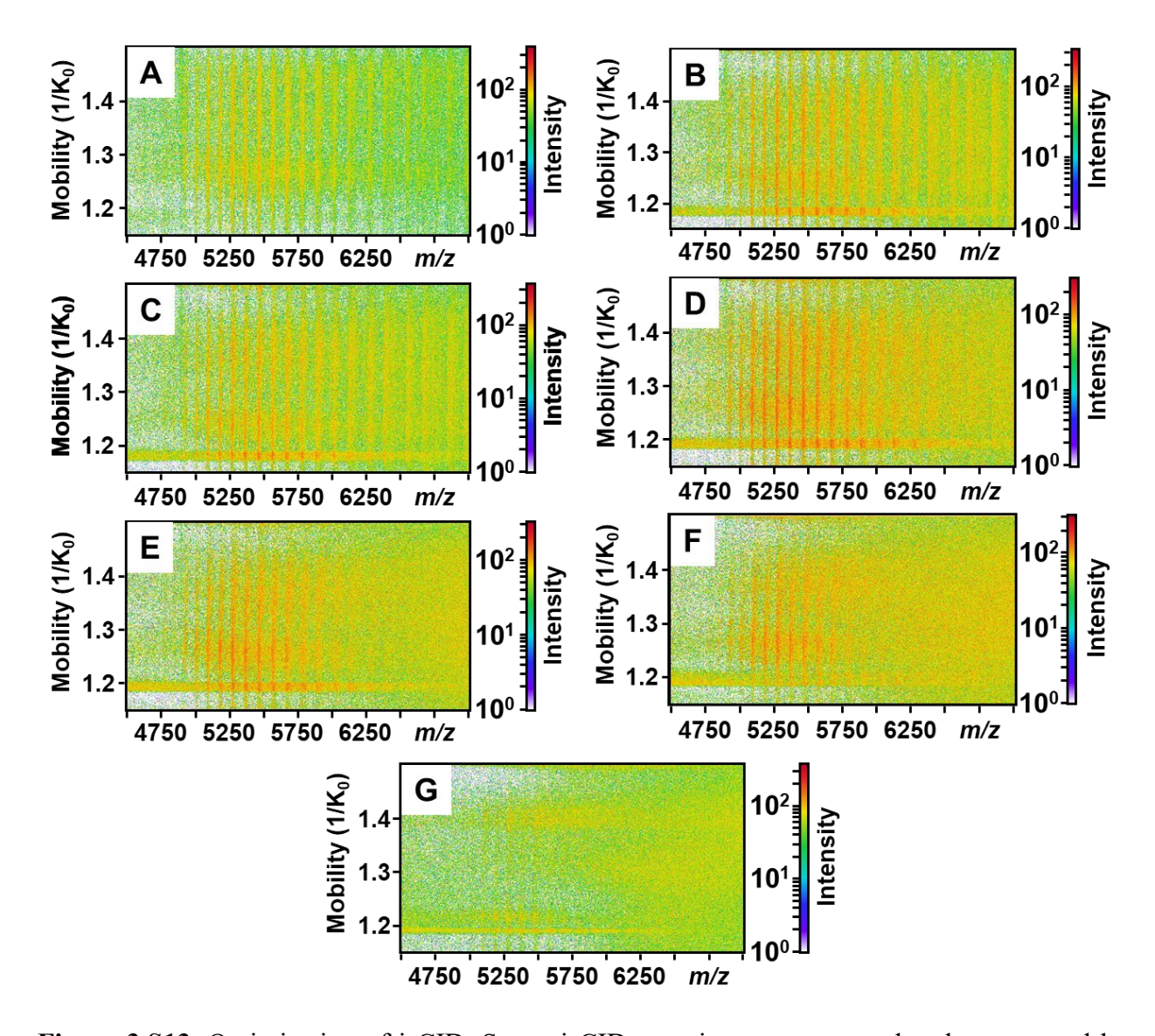


**Figure 3.S13.** Optimization of isCID. Seven isCID energies were screened and represented by mobility heat maps: 180, 160, 140, 120, 100, 80, and 60 eV; shown in A – G respectively.

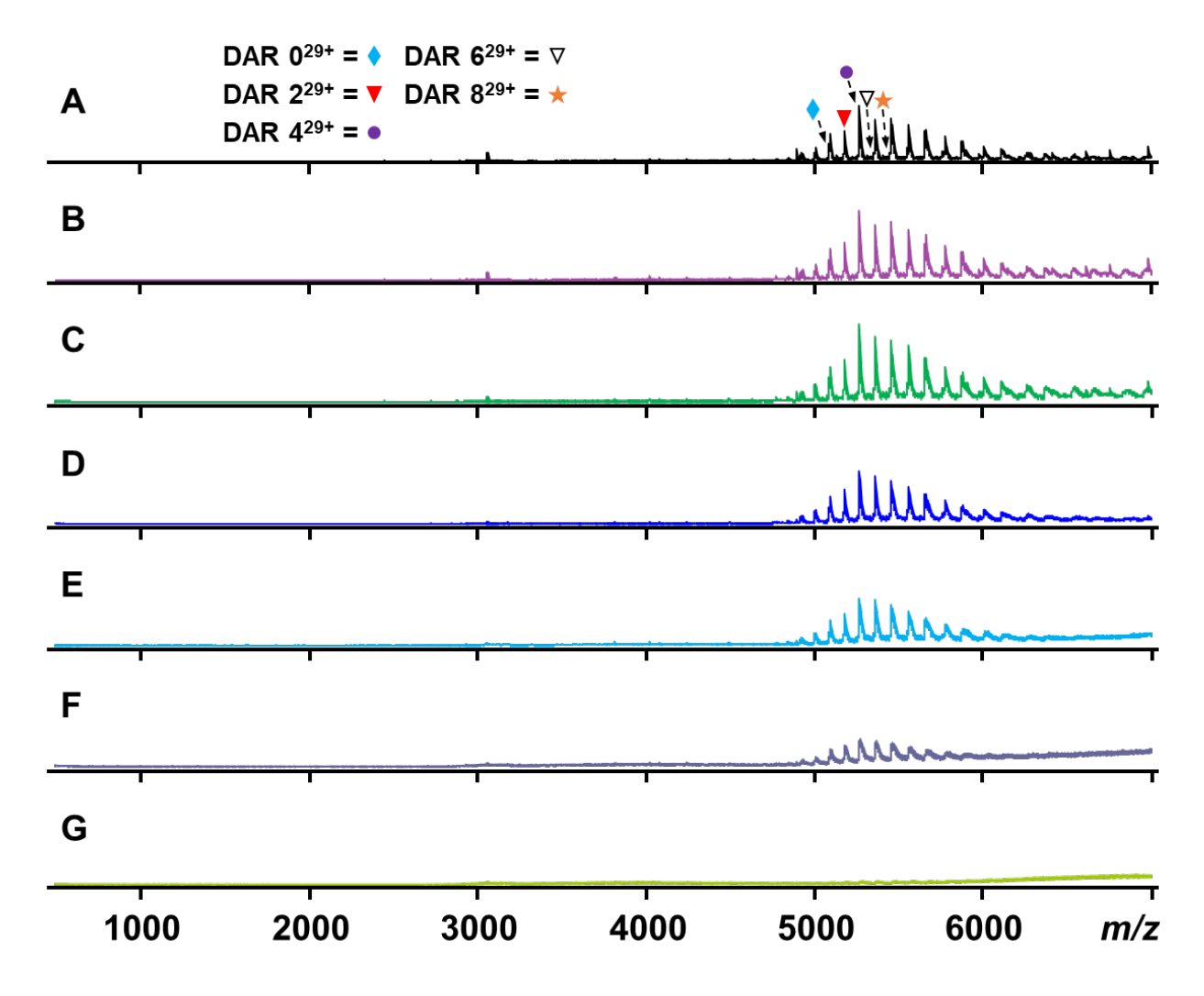


**Figure 3.S14.** Optimization of isCID. Seven isCID energies were screened and represented by MS1 spectra: 180, 160, 140, 120, 100, 80, and 60 eV; shown in A – G respectively.

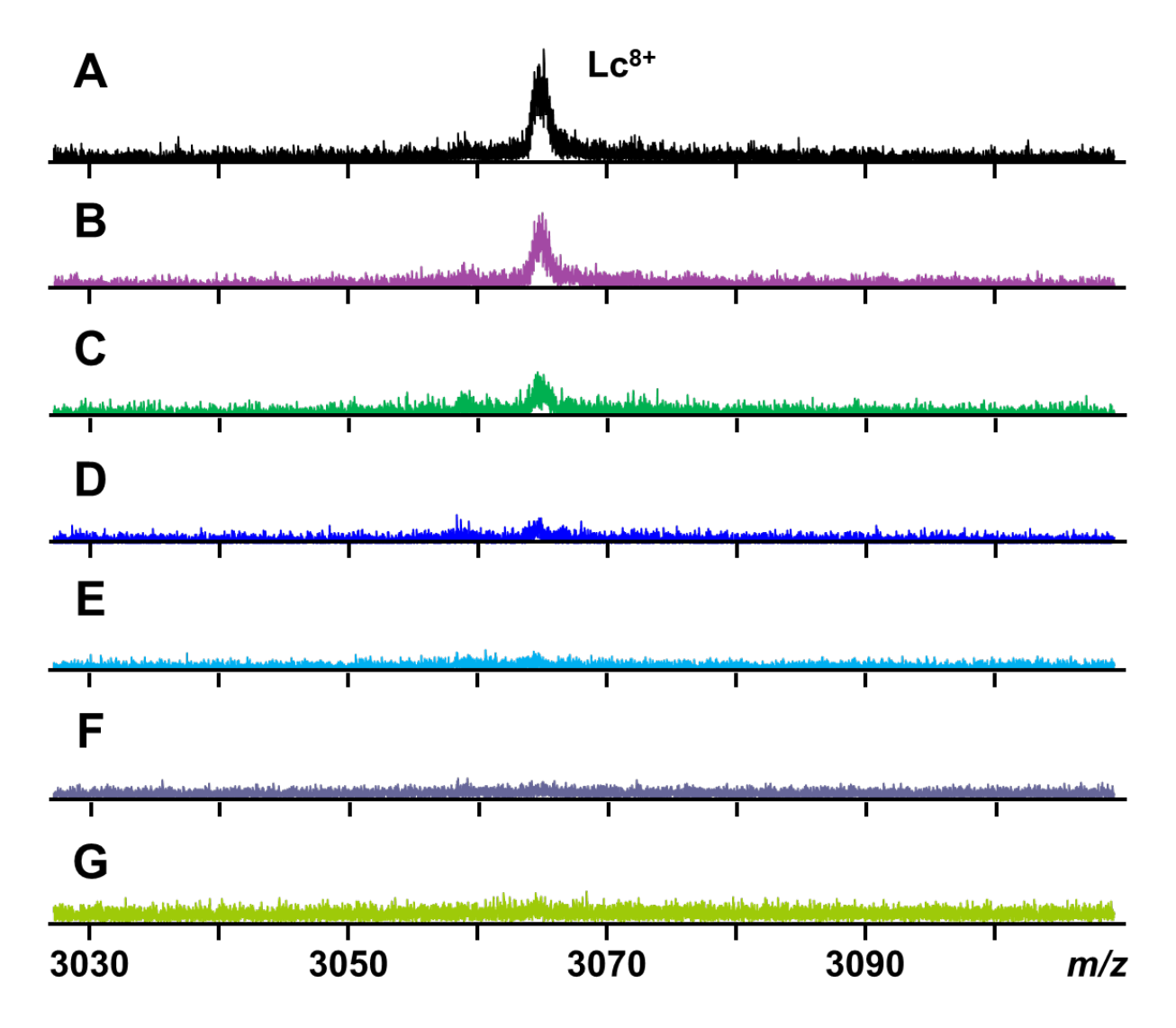


**Figure 3.S15.** Optimization of isCID. Normalized MS1 spectra of dissociated Lc1<sup>8+</sup> subunit at varying isCID energies. Seven isCID energies were screened and represented by MS1 spectra: 180, 160, 140, 120, 100, 80, and 60 eV; shown in A – G respectively.

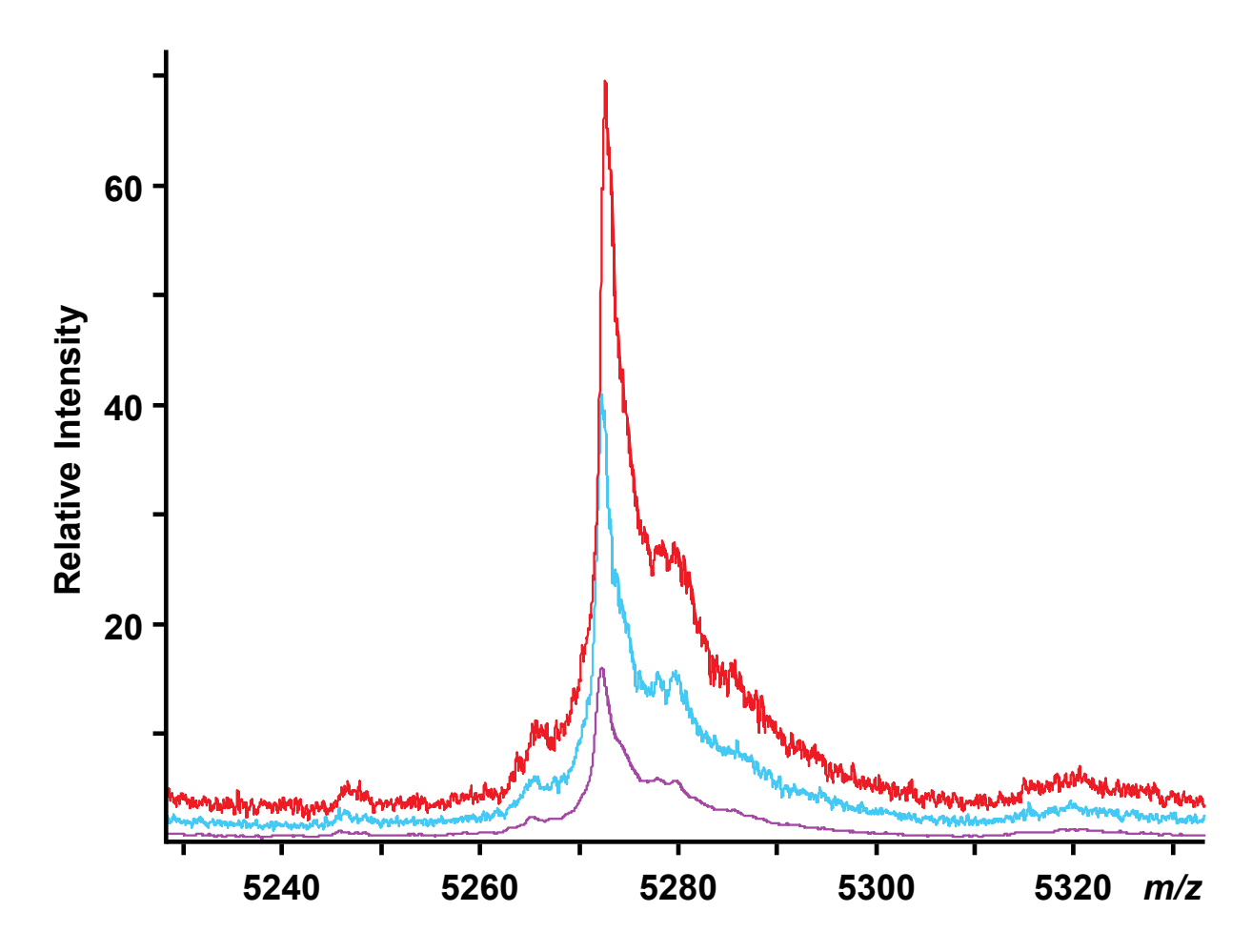


**Figure 3.S16.** Detector TOF voltage optimization. Three conditions were screened, 2204 V (shown in purple), 2304 V (shown in blue), and 2404 V (shown in red). 2404 V provided the highest MS1 response.

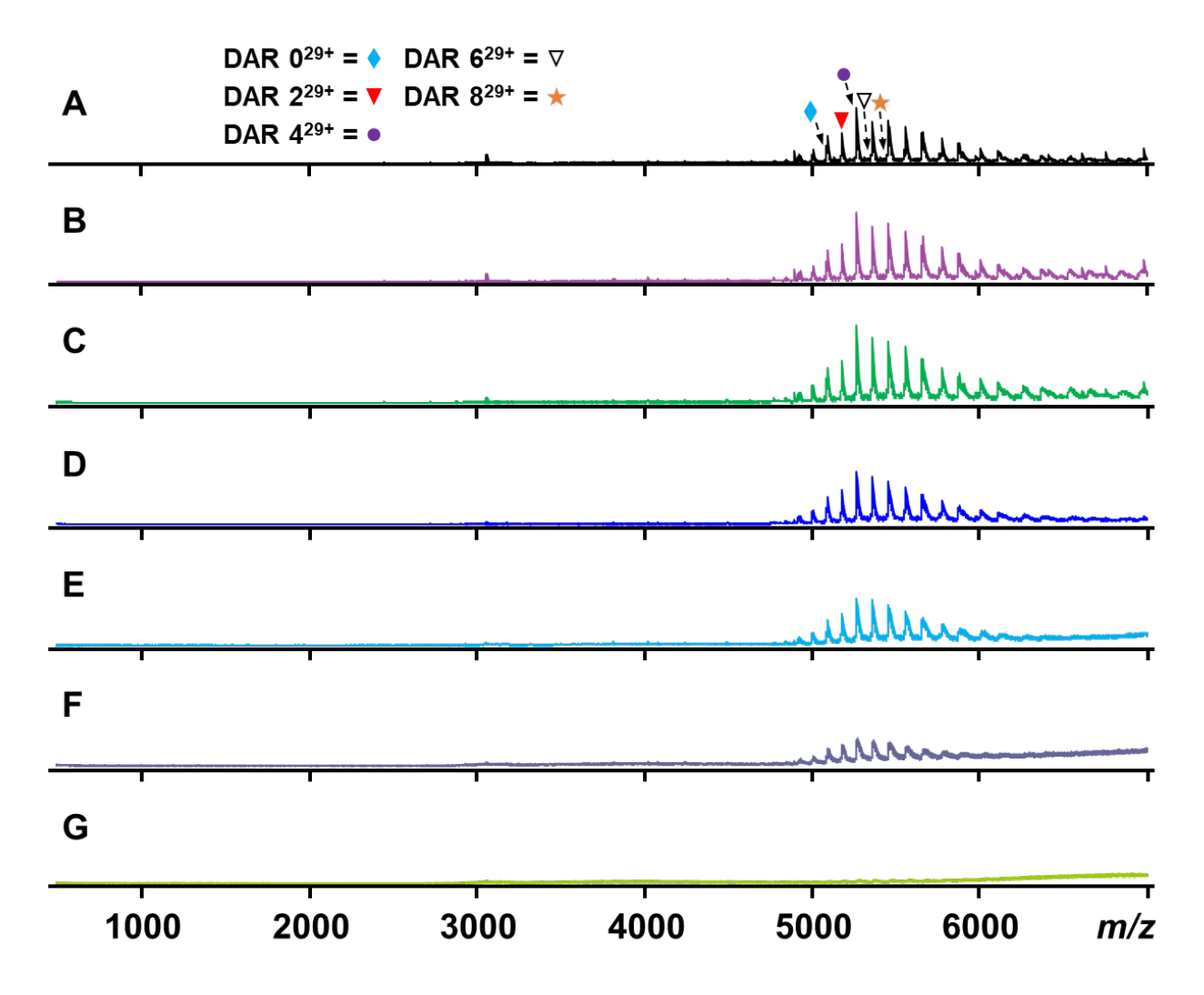


**Figure 3.S17.** TIMS DC gradient voltage optimization. Four conditions were screened, 300 V (A), 250 V (B), 200 V (C), and 150 V (D). Signals normalized to 150 V MS1 spectra, which provided the most intense MS1 response.

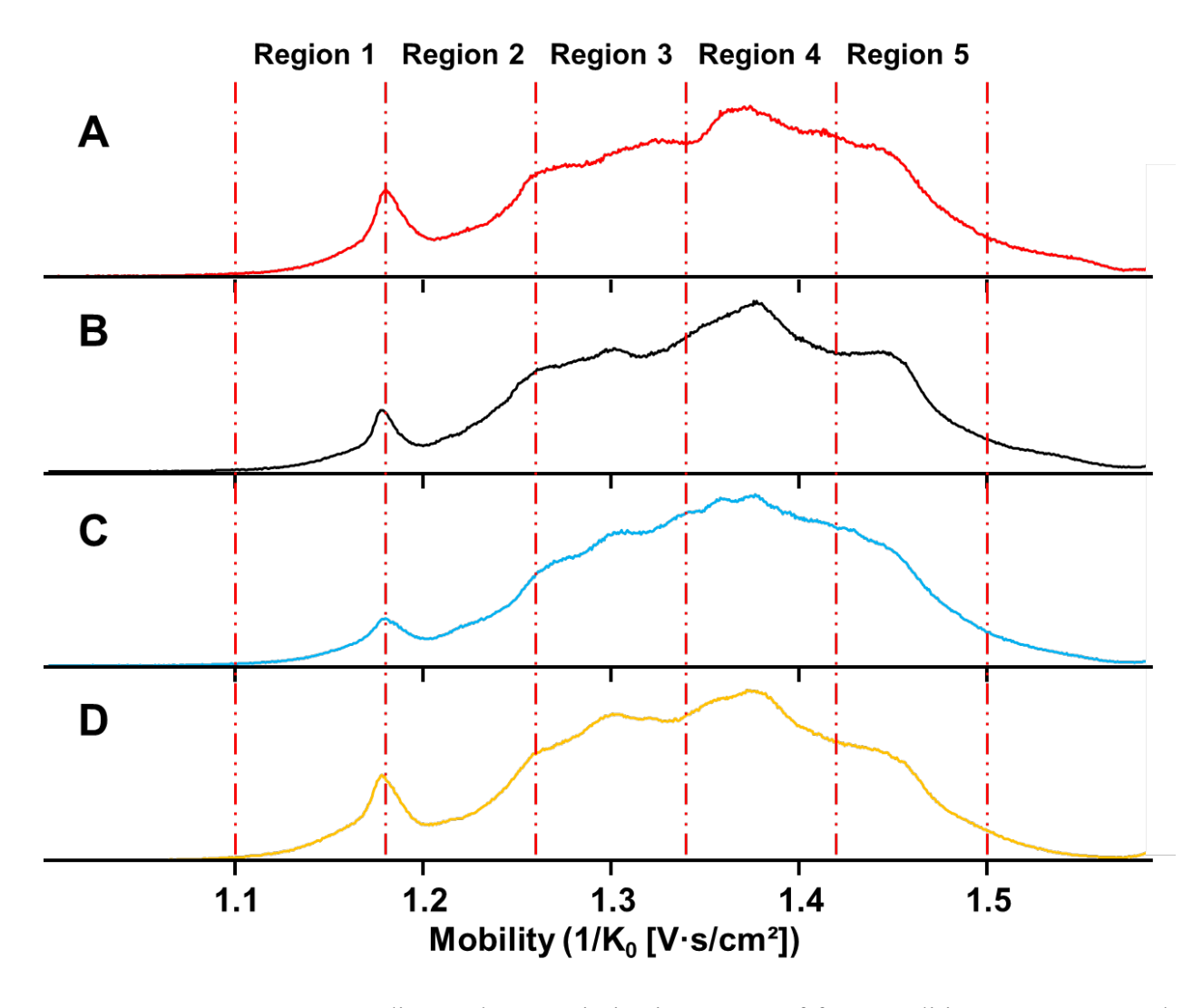


**Figure 3.S18.** TIMS DC gradient voltage optimization. TIMs of four conditions were screened, 300~V~(A), 250~V~(B), 200~V~(C), and 150~V~(D). 200~V~ provided the most well-defined mobility separation.

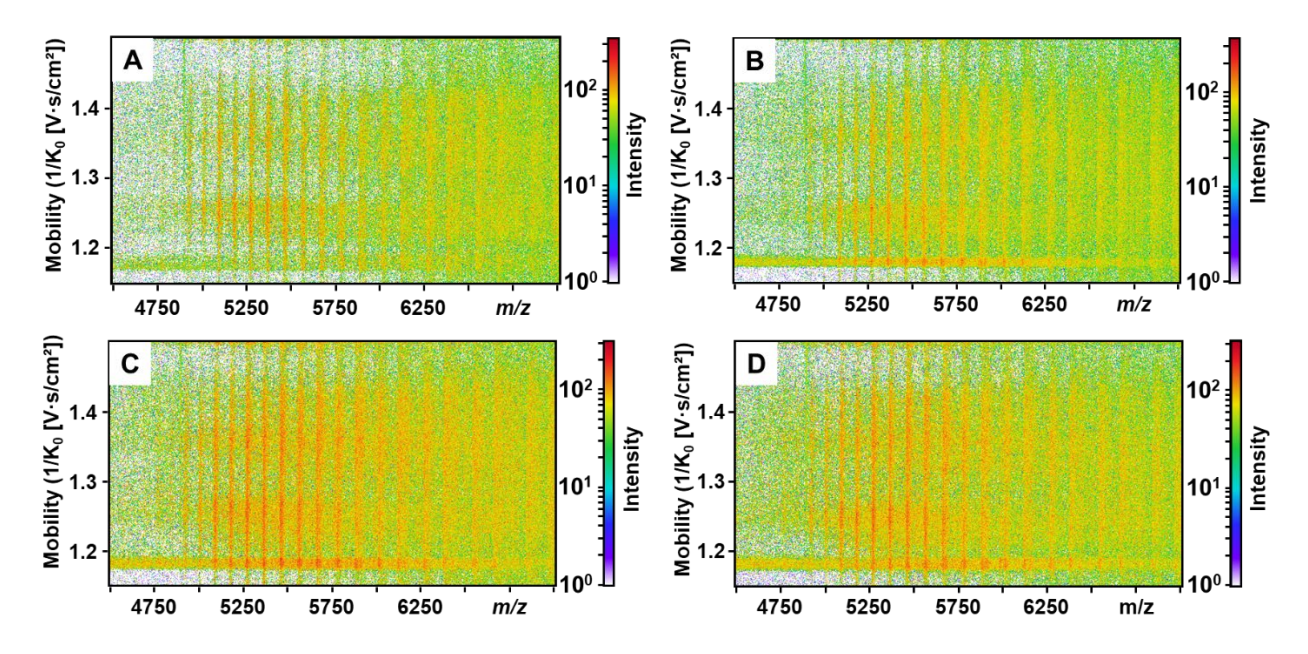


**Figure 3.S19.** TIMS DC gradient voltage optimization. Four conditions were screened, 300 V (A), 250 V (B), 200 V (C), and 150 V (D). 200 V provided the most well-defined mobility separation.

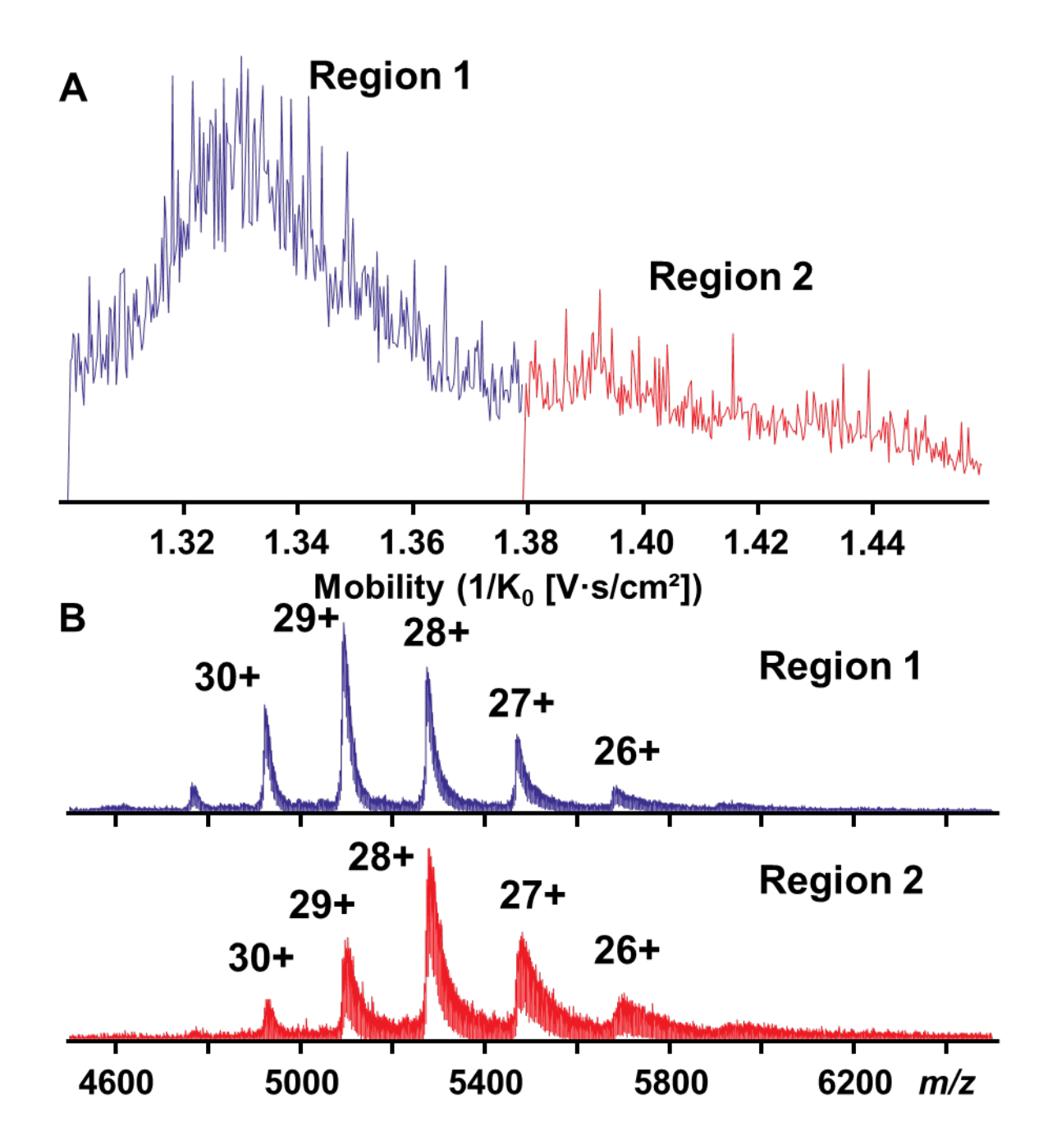


**Figure 3.S20.** Analysis of native starting mAb by direct infusion using the timsTOF Pro. Two distinct mobility regions were observed (A). The presence of two conformers is further supported by a shift in MS1 charge state profiles shown in (B).

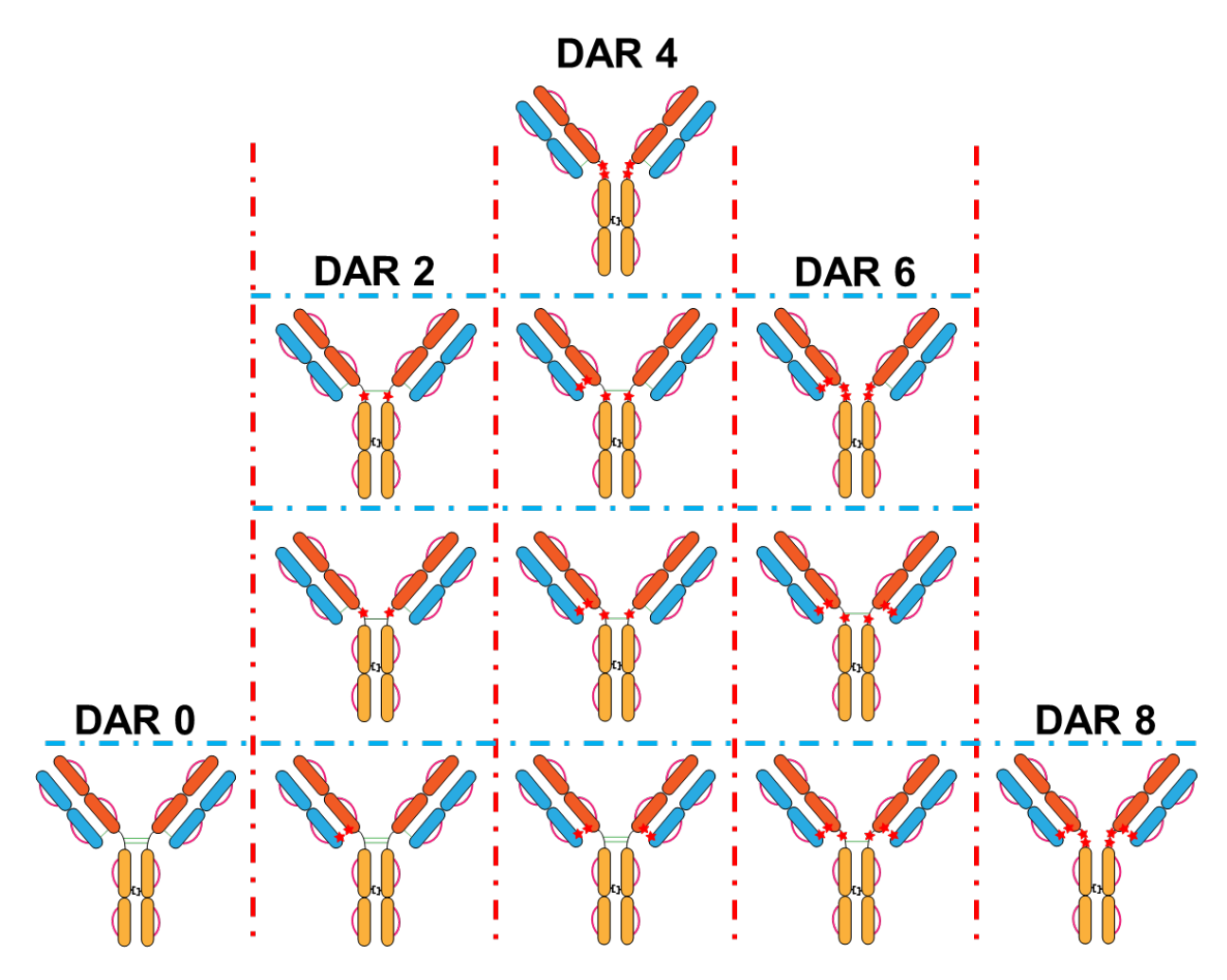


**Figure 3.S21.** Conjugation products of cysteine conjugation for an IgG 1 type antibody. Columns show DAR states, rows show drug conjugation positional isomers.

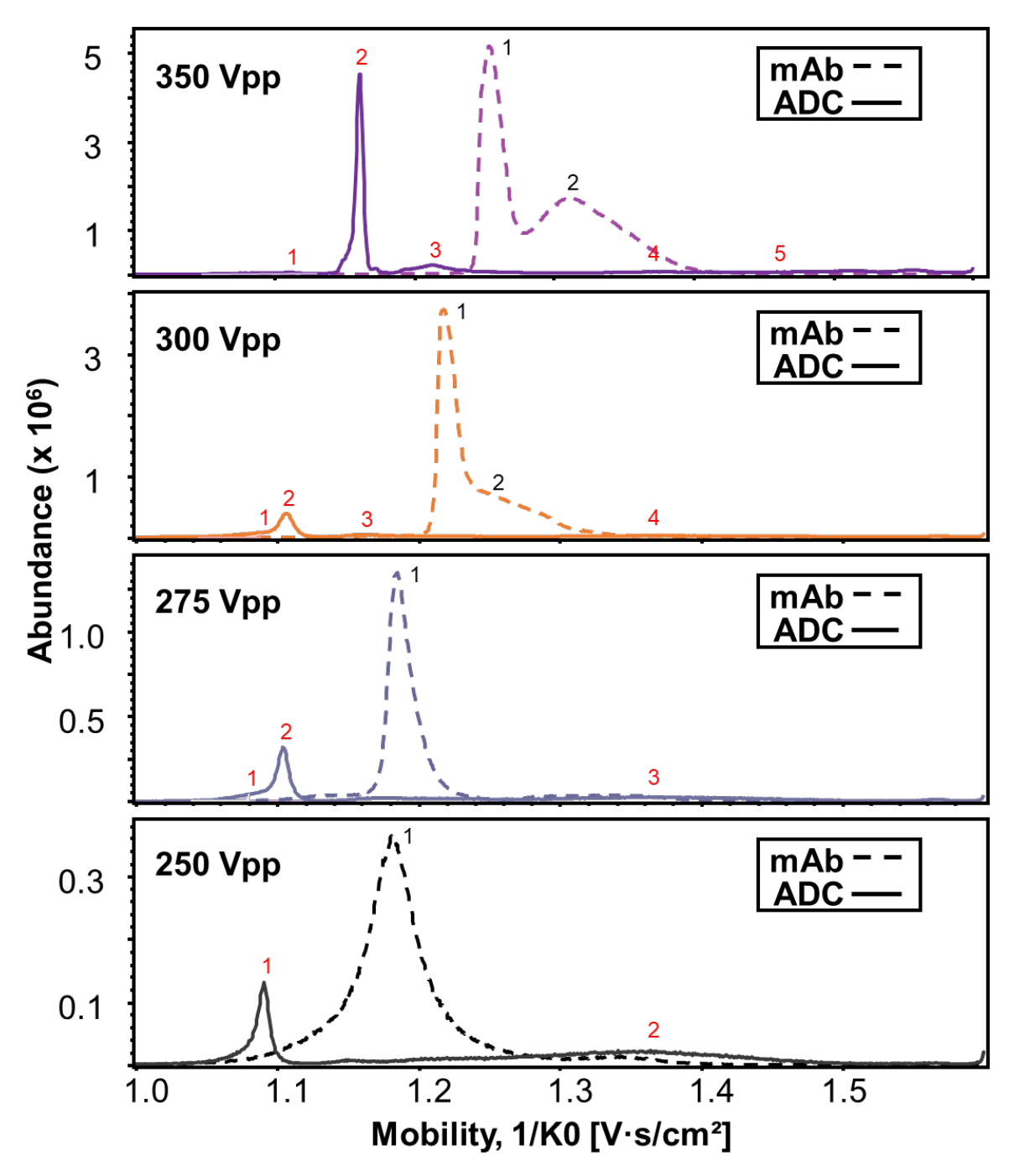


**Figure 3.S22.** Total ion mobilograms (TIMs) of the AbbVie starting mAb and ADC (z = 29+) as a function of TIMS RF. The native starting mAb and native ADC were prepared as a 15  $\mu$ M solution in 150 mM ammonium acetate and directly infused into the mass spectrometer. TIMS duty cycle was fixed at 100%. The mobility regions observed for the mAb are annotated as black "1" and "2", and the mobility regions for the ADC are annotated as red "1" to "5". The ADC shows more compact mobility regions (1-3) compared to the starting mAb (1-2). The TIMS RF voltage was varied between 250 Vpp to 350 Vpp (used in this work). The TIMS device was recalibrated following each change in TIMS RF voltage.

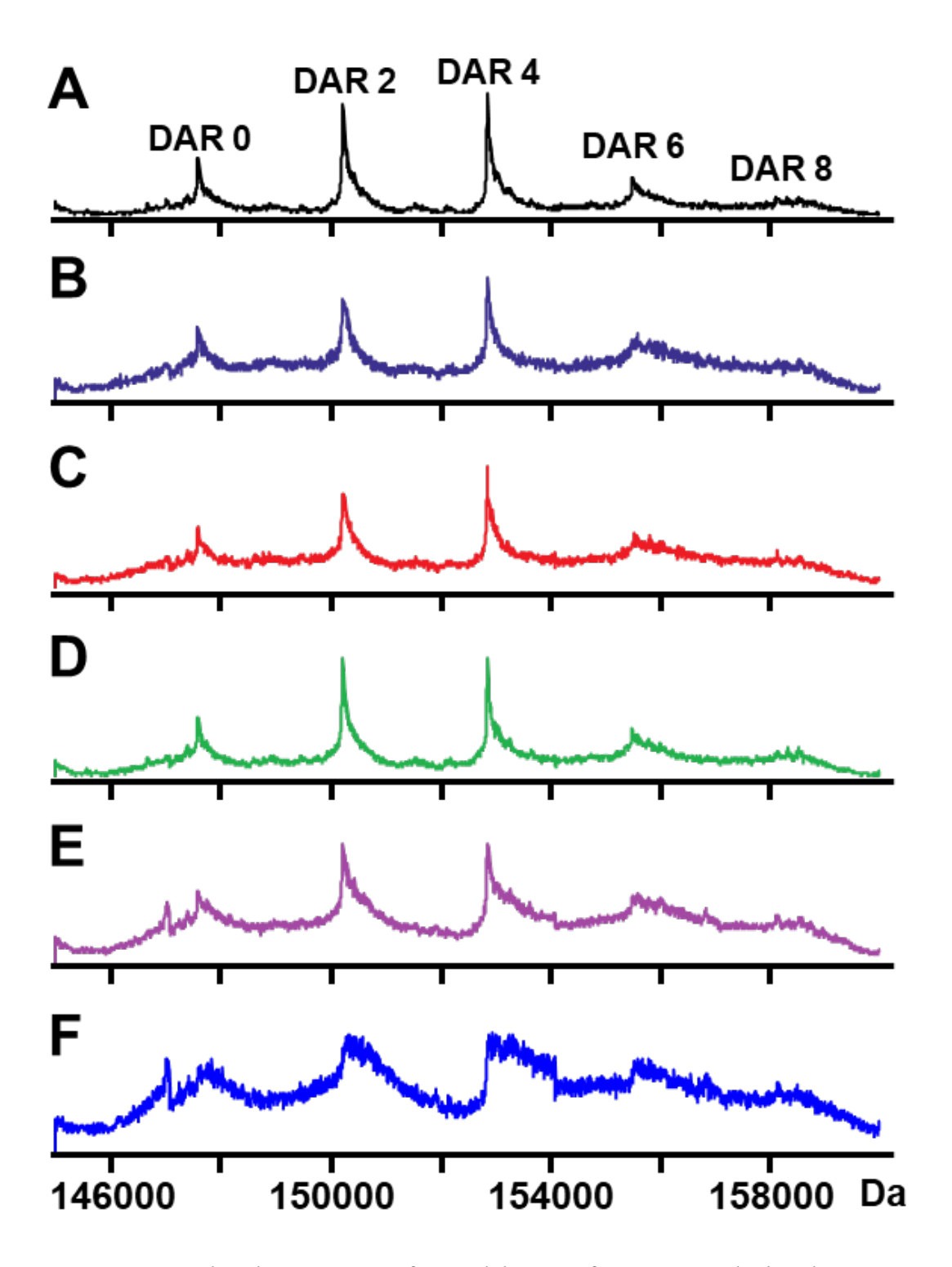


**Figure 3.S23.** Deconvoluted MS1 spectra for model ADC after TIMS analysis. The average MS1 spectra for all mobility regions (A) is listed along with the mobility region-specific deconvoluted MS1 for regions 1 - 5 (B-F respectively).

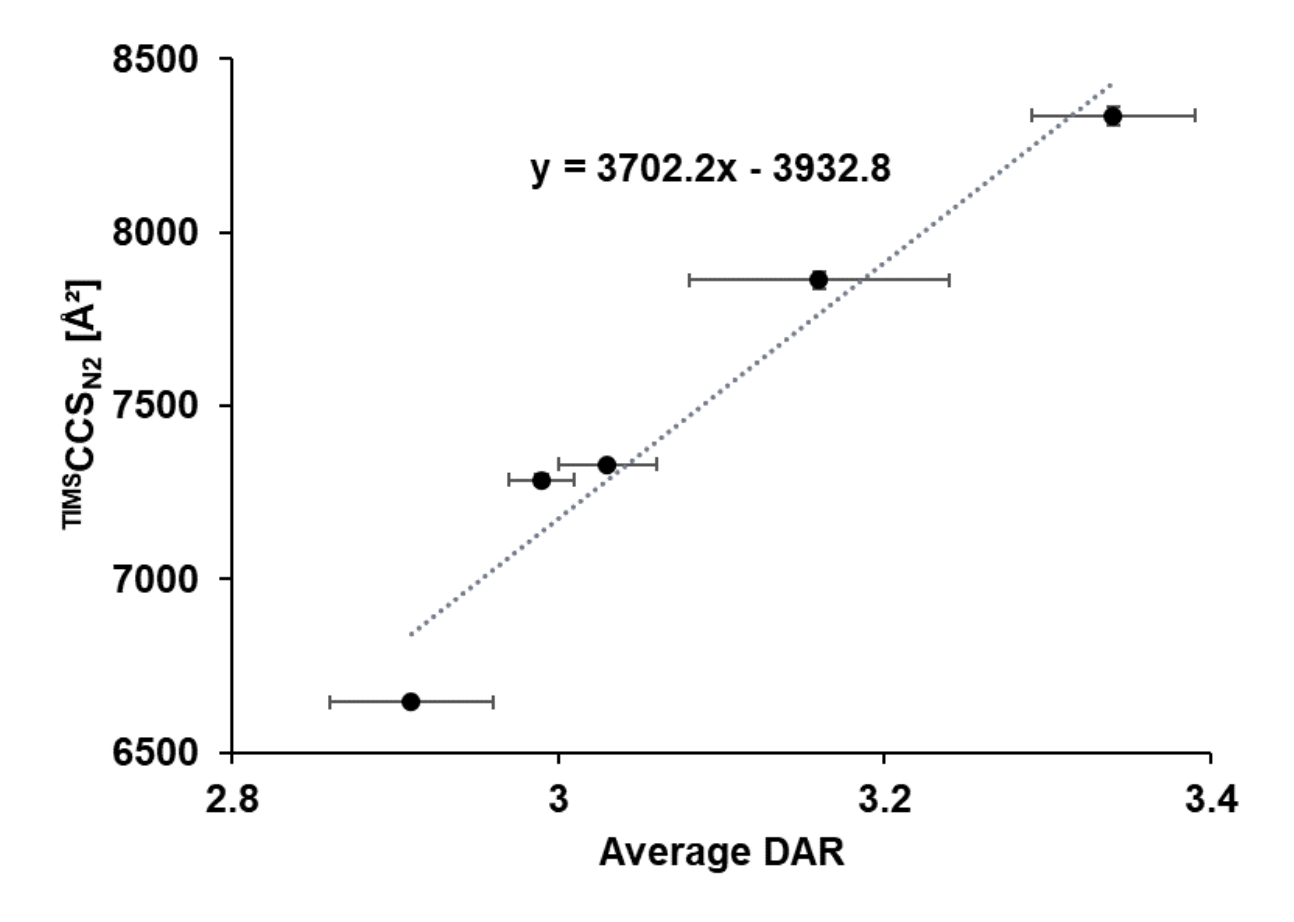


**Figure 3.S24.** Plot of  $^{TIMS}CCS_{N2}$  of the most abundant regional charge state and average DAR for each of the five mobility regions defined after timsTOF Pro analysis of the model ADC using optimal TIMS parameters. Standard deviations of DAR and  $^{TIMS}CCS_{N2}$  are plotted as error bars. Points were fitted to a linear model, yielding a trendline described by the equation y = 3702.2x - 3932.8. The  $R^2$  value was determined to be 0.95.

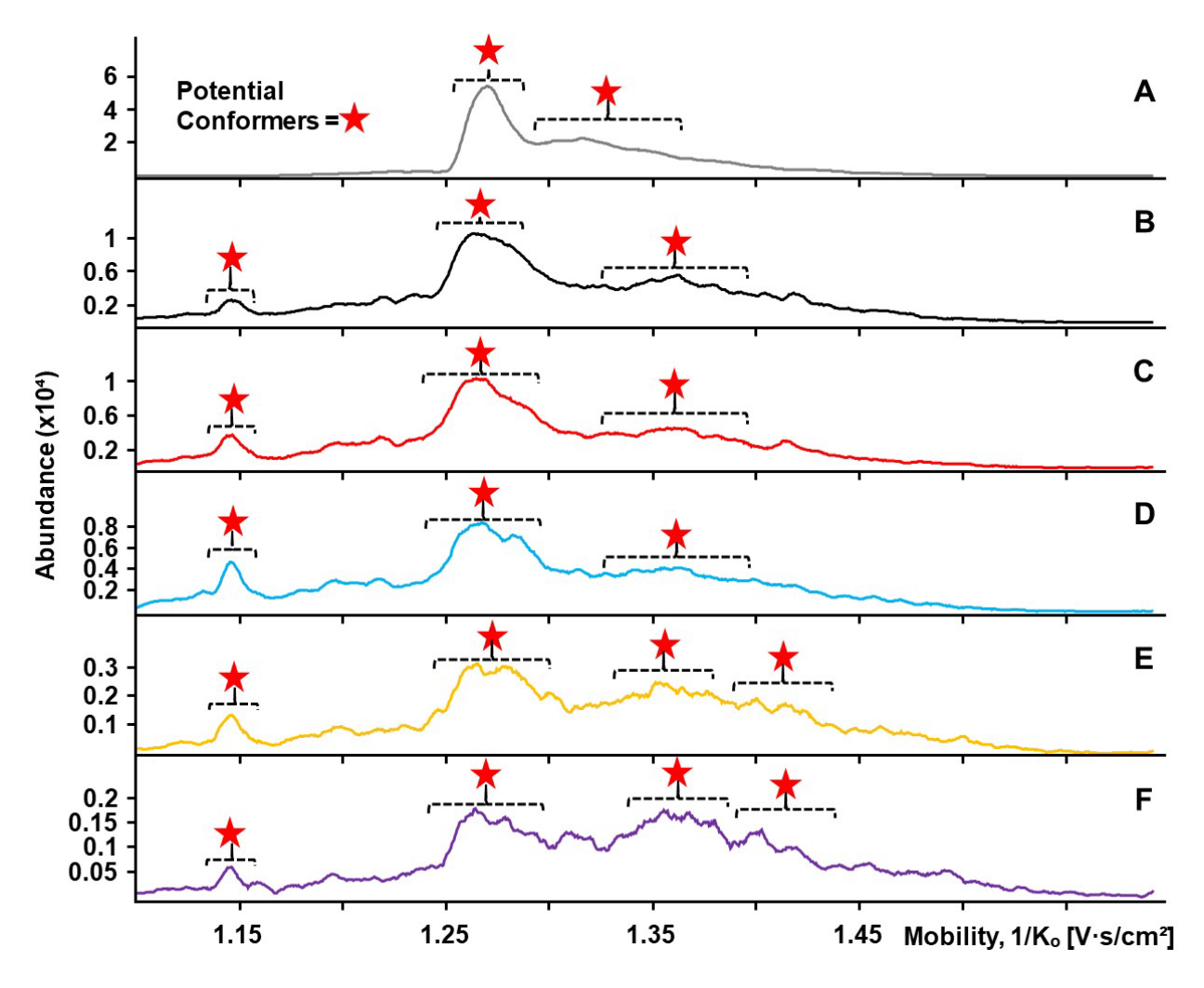


**Figure 3.S25.** Extracted ion mobility spectra (EIMs) of the various DAR values for the model cysteine-linked ADC. EIM distributions for mAb (A), DAR 0 (B), DAR 2 (C), DAR 4 (D), DAR 6 (E), and DAR 8 (F) were generated using charge states z = 29+ to 24+ with a 0.1 m/z window. Potential conformers of individual DAR states noted by a red star.

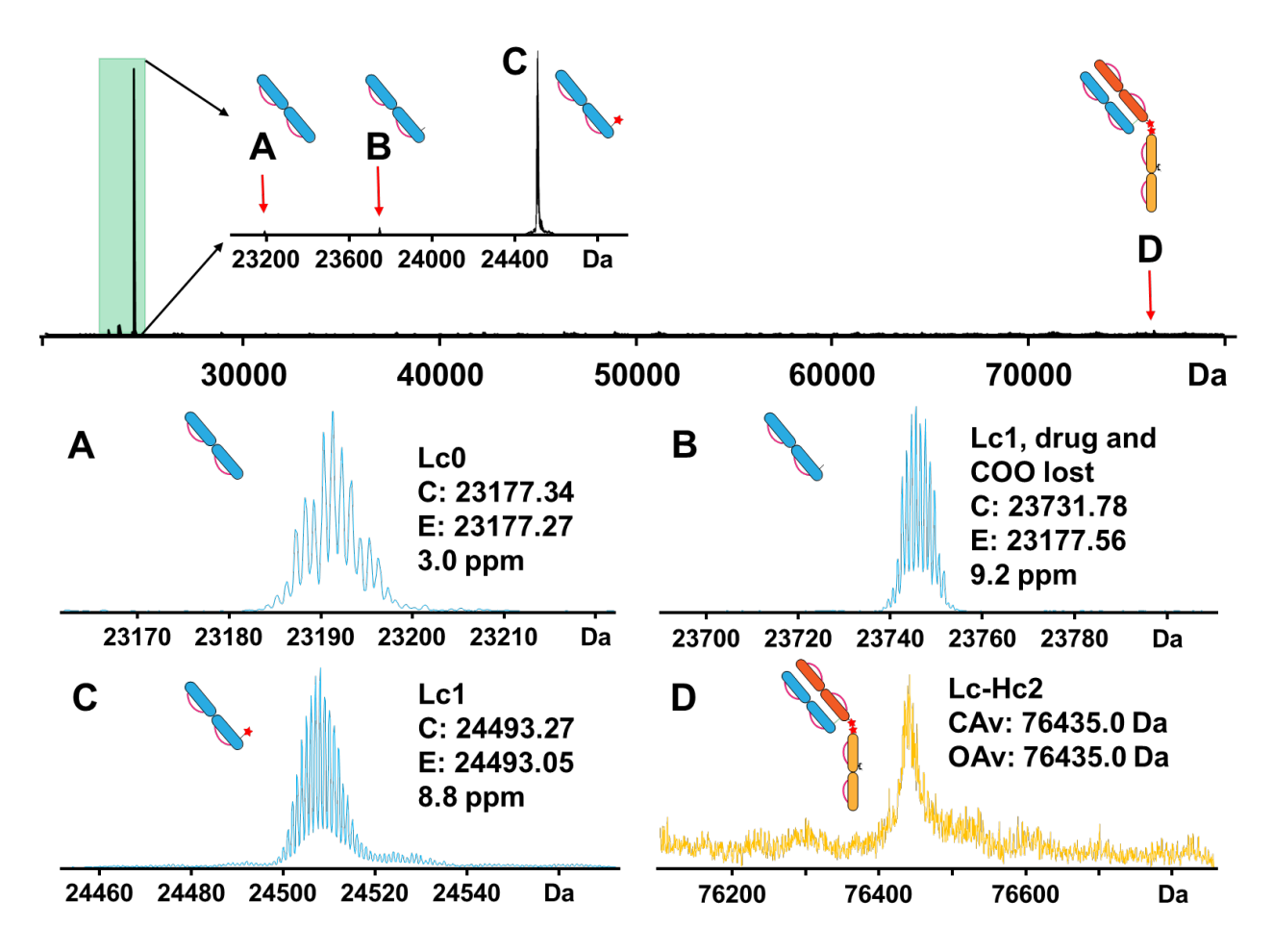


**Figure 3.S26.** Deconvoluted MS1 spectra for observed dissociated subunits, showing the monoisotopic mass for panel A-C and the average mass for panel D. Three Lc species were observed: Lc0 (A), Lc1 with the drug dissociated from the linker and a carboxyl group lost from the linker (B), and Lc1 (C). The Lc-Hc2 subunit, Lc bound to Hc with two drugs attached by an interchain disulfide bond, also detected with the observed average mass matching the calculated average mass (D).

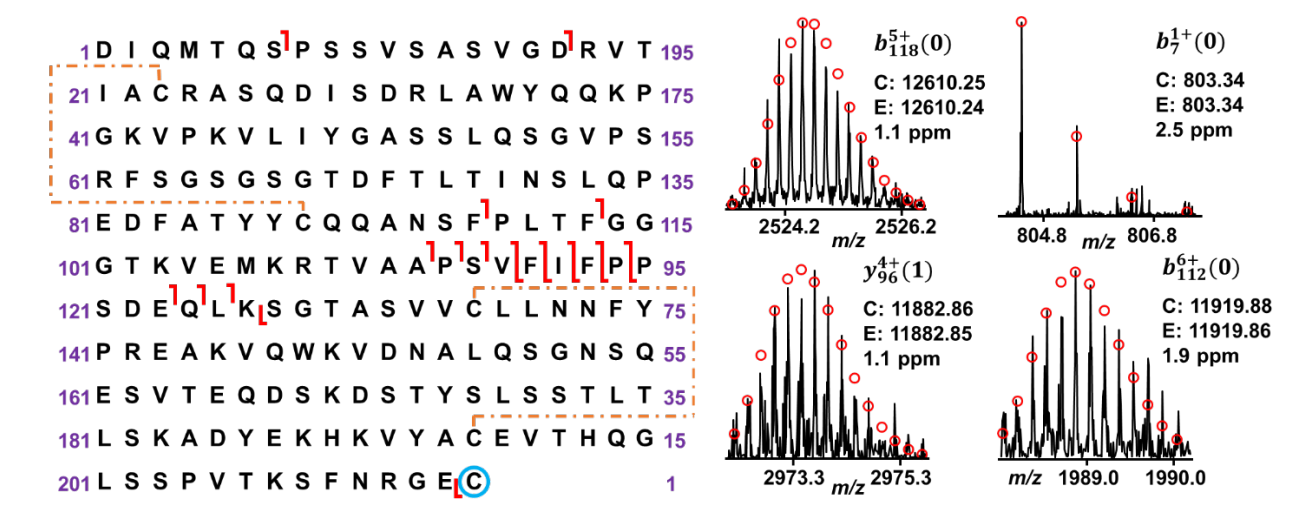


**Figure 3.S27.** Targeted CID of dissociated Lc1 subunit combining three fragmentation energies, 80, 90, and 100 eV with representative ions. Intrachain disulfide bonds are represented with brown dashed lines, drug conjugation site is shown as a blue circle. A total of 17 out of 213 possible bond cleavages were observed, resulting in 8.0 % total residue cleavage.

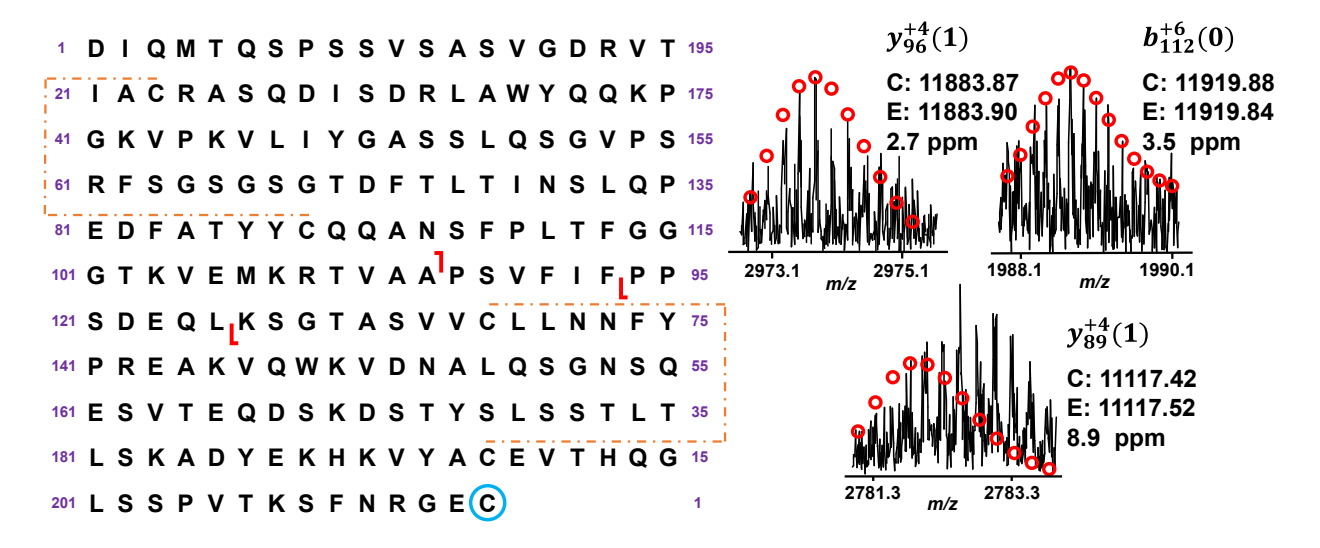


**Figure 3.S28.** Fragmentation of Lc species by bbCID using three CID energies: 80, 90, 100 eV. Intrachain disulfide bonds are represented with brown dashed lines, drug conjugation site is shown as a blue circle. 3 pf 213 possible bond cleavages, or 1.5% of total cleavages. y<sup>96</sup> and y<sup>89</sup> confirmed drug conjugation and location.

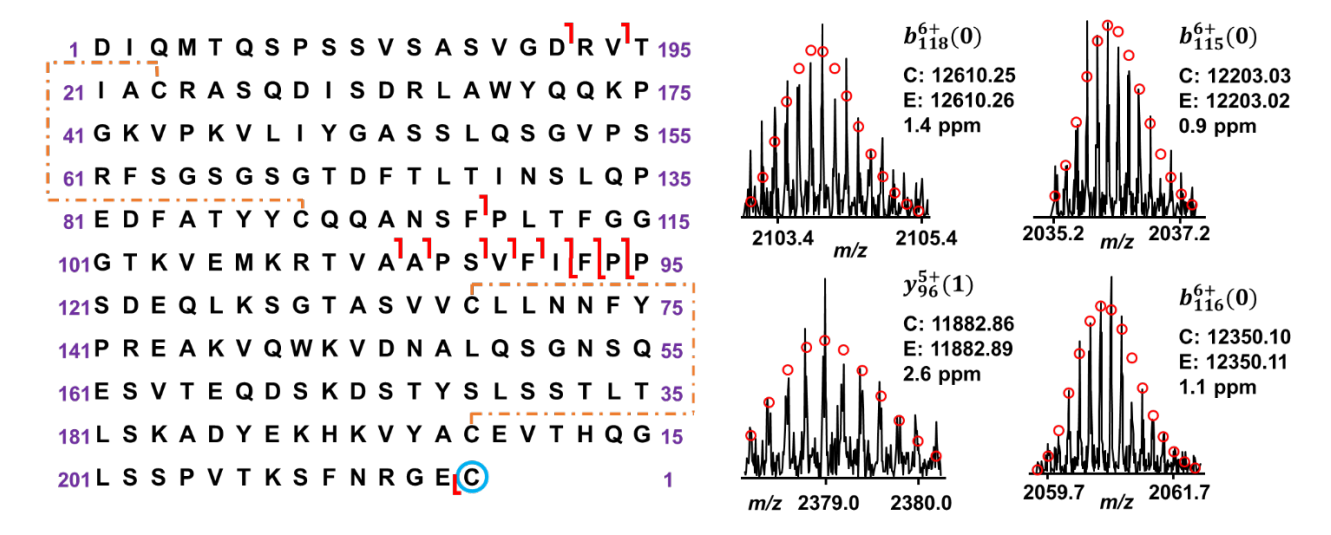
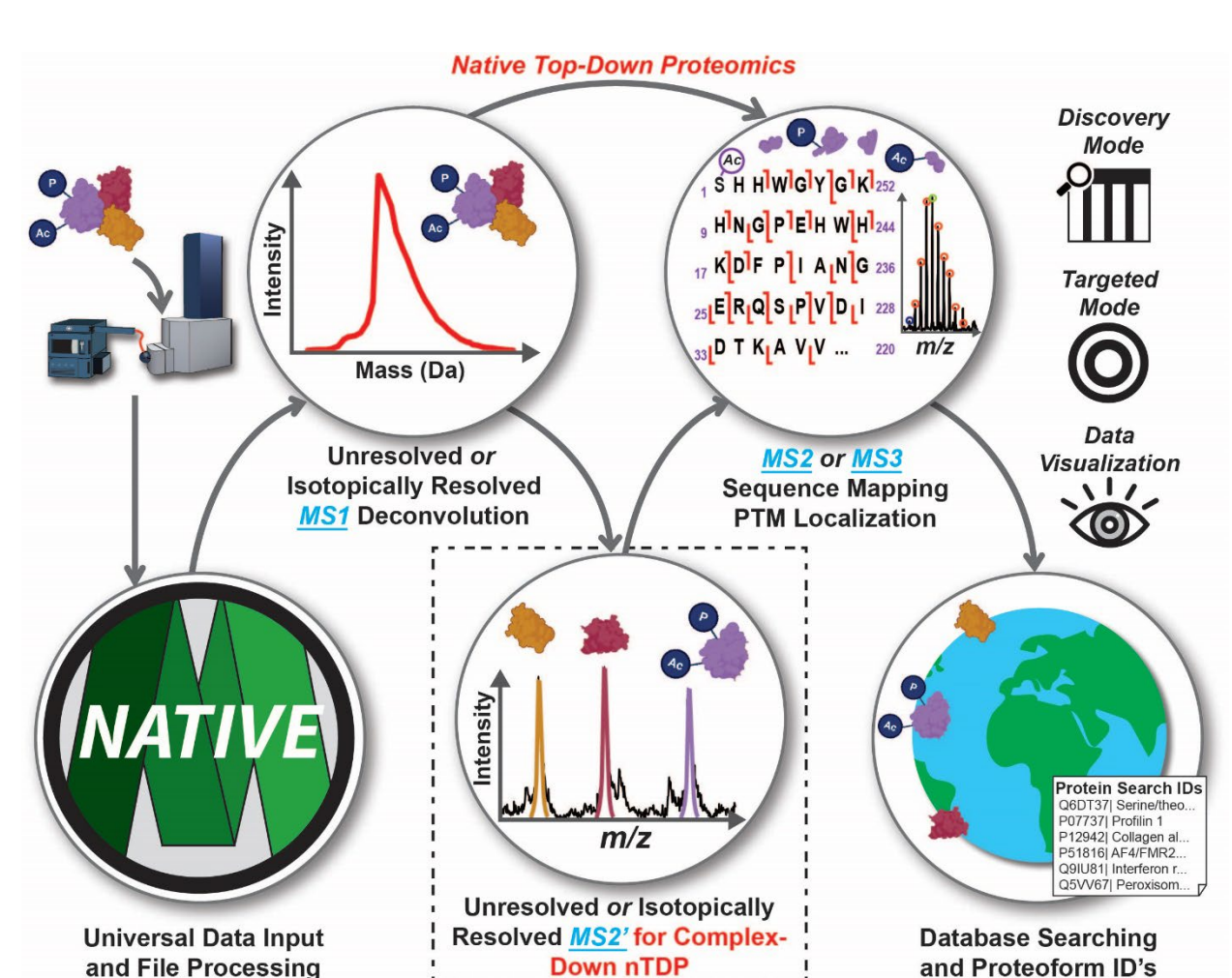


**Figure 3.S29.** Targeted CID from a segmented 90 second fragment of dissociated Lc1 subunit combining three fragmentation energies, 80, 90, and 100 eV with diagnostic ions. Intrachain disulfide bonds are represented with brown dashed lines, drug conjugation site is shown as a blue circle. A total of 13 out of 213 possible bond cleavages were observed, resulting in 6% total residue cleavage. This is comparable to the performance seen in Figure 6, validating the use of segmentation for MS1 and MS2 analyses in a single run.



Chapter 4

MASH Native: A Unified Solution for Native Top-Down Proteomics Data Processing

This chapter has been published and is adapted from:

Larson, E. J.; Pergande, M. R.; Moss, M. E.; Rossler, K. J.; Wenger, R. K.; Krichel, B.; Josyer, H.; Melby, J. A.; Roberts, D. S.; Pike, K.; Shi, Z.; Chan, H.; Knight, B.; Rogers, H. T.; Brown, K. A.; Ong, I. M.; Jeong, K.; Marty, M. T.; McIlwain, S. J.; Ge. Y. MASH Native: a unified solution for native top-down proteomics data processing. *Bioinformatics*. 2023.

### **Abstract**

*Motivation*: Native top-down proteomics (nTDP) integrates native mass spectrometry (nMS) with top-down proteomics (TDP) to provide comprehensive analysis of protein complexes together with proteoform identification and characterization. Despite significant advances in nMS and TDP software developments, a unified and user-friendly software package for analysis of nTDP data remains lacking.

Results: We have developed MASH Native to provide a unified solution for nTDP to process complex datasets with database searching capabilities in a user-friendly interface. MASH Native supports various data formats and incorporates multiple options for deconvolution, database searching, and spectral summing to provide a "one-stop shop" for characterizing both native protein complexes and proteoforms.

Availability and implementation: The MASH Native app, video tutorials, written tutorials and additional documentation are freely available for download at https://labs.wisc.edu/gelab/MASH\_Explorer/MASHSoftware.php. All data files shown in user tutorials are included with the MASH Native software in the download .zip file.

## Introduction

Native mass spectrometry (nMS) analyzes intact proteins and protein complexes under non-denaturing conditions to preserve their tertiary structure and non-covalent interactions in the gas phase, which has emerged as a powerful structural biology tool to define protein structure-function relationships <sup>286–290</sup>. Native top-down proteomics (nTDP) integrates nMS with top-down proteomics (TDP) <sup>29,30,32,291</sup>, which enables structural characterization of protein complexes together with proteoform sequencing to locate non-covalent ligand binding sites, posttranslational modifications (PTMs), and mutations <sup>35,90,290,292</sup>. nTDP first measures intact proteins and protein

complexes under non-denaturing conditions (MS1) then directly fragments proteins and protein complexes in the gas phase (MS2) to obtain primary sequence information from a single dissociation event <sup>35</sup>. Alternatively, nTDP may be implemented in the "complex-down" mode using two separate dissociation events: 1) dissociation of intact protein complexes (MS1) into protein subunits (MS2') by low-energy collision-induced dissociation (CID) or surface induced dissociation (SID), and 2) fragmentation of subunits (MS3) by tandem mass spectrometry techniques such as high-energy CID, electron capture dissociation (ECD), electron transfer dissociation (ETD) or ultraviolet photodissociation (UVPD) to provide primary sequence coverage and localize modifications <sup>34,90,293</sup>.

Currently one of the major challenges in nTDP is the analysis of complex nTDP datasets which include both isotopically resolved and isotopically unresolved MS1 and MS2' spectra as well as the complicated MS2 and MS3 data, and difficulties in database searching. Although multiple software packages have been developed for nMS of known proteins and complexes <sup>171,173,294,295</sup>, the lack of any MS2/MS3 fragmentation assignment and database searching prevent the identification of unknown proteins. Meanwhile, significant efforts have been allocated towards the development of software packages for denatured TDP with capability in analyzing complicated MS2/MS3 datasets with database search algorithms to identify unknown proteins <sup>165,177,179,240,296</sup>, but these denatured TDP software packages lack the capability to analyze the isotopically unresolved MS1/MS2' that are characteristic of nMS data. Hence, there is a critical need for a universal software package to address this major challenge in nTDP that can process MS1, MS2, MS2' and MS3 datasets with database search capabilities.

Herein, we introduce MASH Native (https://labs.wisc.edu/gelab/MASH Explorer/MASHNativeSoftware.php), a unified solution for

nTDP which can process isotopically unresolved MS1 and MS2' data together with isotopically resolved MS1, MS2, and MS3 deconvolution and database searching (Figure 4.1). MASH Native supports various nTDP applications in both targeted mode to characterize known proteins and discovery mode to identify unknown native proteins. It supports various MS file types with different vendor formats and integrates multiple deconvolution/search algorithms into one package. We detail the functions and features of MASH Native and provide examples of processing nTDP data to showcase its capabilities as a "one-stop shop" for nTDP.

#### Results

The MASH Native user interface is a multithreaded Windows desktop application written under a .NET framework environment in Visual Studio using the C# programming language <sup>165</sup>. MASH Native provides universal MS file support through ProteoWizard's file conversion engine, MSConvert <sup>297</sup>, and directly imports both vendor-specific MS file types (Thermo \*.RAW, Bruker \*.d/\*.baf/\*.ascii) and general file formats (\*.mgf, \*.mzML, \*.mzXML). It is recommended that users perform MASH Native data processing on a computer with at least 4 GB of memory ensure optimal function of all included algorithms and workflows, however, some deconvolution algorithms may require additional memory for multi-scan, isotopically resolved deconvolution events. The latest version of MASH Native is freely-available for download on the MASH website (https://labs.wisc.edu/gelab/MASH\_Explorer/MASHNativeSoftware.php) along with licensing information, and written and video user tutorials (also included in the "Supporting Documents for Users" section of the Supplementary Information). All data files used to generate these tutorials are freely available for download on MassIVE as a complete submission (MSV000091693, doi:10.25345/C5NP1WV0N).

MASH Native software can deconvolute both isotopically resolved and isotopically unresolved data at the MS1, MS2, and MS3 level and enables database searching of nTDP results (Figure 4.1, Table 4.S1). It can process nTDP, nMS, and complex-down proteomics data using multiple deconvolution and database search algorithms with flexible data output options (Figure 4.S1). It also maintains the functions and capabilities previously developed for denaturing TDP so users can process both nTDP and TDP in the same software. To address challenges with low signalto-noise (S/N) ratios of intact and fragment mass spectra, MASH Native includes a variety of spectral summing algorithms that may be applied prior to data processing workflows (Figure 4.S2 and 4.S3). To deconvolute isotopically unresolved MS1 spectra, MASH Native includes UniDec <sup>171</sup>, a powerful deconvolution algorithm, to characterize both isotopically unresolved and isotopically resolved nMS data (Figure 4.S4). Isotopically resolved spectral deconvolution can also be performed in MASH Native (Figure 4.S5), including TopFD <sup>179</sup>, MsDeconv <sup>298</sup>, eTHRASH <sup>271</sup>, and pParseTD <sup>299</sup>. Users may also import previously deconvoluted results from external deconvolution algorithms, such as FLASHDeconv <sup>174</sup>, ProMEX <sup>176</sup> or Maximum Entropy <sup>169</sup>. Deconvolution results of separate deconvolution workflows can be combined into a single output table, allowing users to view MS1, MS2, and MS3 results simultaneously and combine multiple deconvolution types to improve protein sequence coverage <sup>170</sup>. Results of deconvolution may be searched against a user-selected \*.FASTA file or user-defined protein sequence with TopPIC <sup>179</sup>, MS-Align+ <sup>178</sup>, or pTop <sup>177</sup> to identify proteoforms in a complex mixture. Search results are reported as both gene-level and proteoform-level identifications. Identified proteoforms are scored and ranked, with scoring techniques varying for each algorithm <sup>177–179,300</sup>.. Search results generated through MASH Native or from additional search tools such as MSPathFinderT <sup>176</sup>, may then be

imported in MASH Native to view identifications, generate fragment ion maps, view fragment ions, and validate for all identified proteins and proteoforms.

To facilitate high-throughput data analysis, user-defined MASH Native processing workflows can be designed, saved, and queued to allow batch processing of data files using two different approaches: Discovery and Targeted Mode. Discovery Mode facilitates identification of unknown proteins though database searching, a critical processing feature absent from current nMS or native top-down software tools. This mode combines MS1 processing with isotopically resolved MS2 or MS3 deconvolution and database searching in a single workflow for nTDP datasets (Figure 4.S6). To demonstrate MASH Native Discovery Mode for data processing, we accessed and reanalyzed data files from a previously published nTDP dataset of endogenous protein complex previously published by Kelleher and co-workers (MassIVE dataset # MSV000080328) <sup>301</sup>. The workflow to identify and characterize subunits of this complex is shown in figure 4.S6A. Deconvolution of both the MS1 and MS2' spectra by UniDec finds the intact complex mass and released subunit masses. Subsequent isotopically resolved MS3 deconvolution by eTHRASH and database searching with TopPIC identified the two subunits and localized modifications sites on each subunit. This underlines that MASH Native is capable of analyzing complex nTDP data in the Discovery Mode. To identify novel complexes using a complex-down approach, users must begin at the MS3 level by database searching. Next, identified subunits are matched to associated MS2' spectra with intact subunit masses to protein complex interactors. Finally, users must match the detected MS1 mass by testing different stoichiometries of each detected subunit to determine complex stoichiometry and composition. Automation of this process will eliminate the need for manual testing of novel complexes in future MASH Native releases.

Targeted Mode allows users to comprehensively analyze native top-down or complexdown data for a known protein/protein complex, confirm results generated in Discovery Mode, or potentially find new possible complex associations with database searching. At the MS1 and MS2' level, MASH Native enables isotopically unresolved and isotopically resolved native deconvolution through UniDec <sup>171</sup>. Deconvolution and searching of MS2 or MS3 data in Targeted Mode may be performed using all high-resolution deconvolution algorithms and database search options (vide supra). We have used MASH Native to process a native top-down MS dataset of the bovine glutamate dehydrogenase (GDH) hexamer previously published by Loo and co-workers 35 to demonstrated the utility of this targeted workflow (Figure 4.S7). MASH Native allowed isotopically unresolved MS1 deconvolution and isotopically resolved MS2 deconvolution along with sequence mapping and data visualization in a single software package (Figure 4.S7). Recently, our group has demonstrated the utility of MASH for targeted analysis in a complexdown workflow for a native cysteine-linked antibody-drug conjugate (ADC) (Figure 2.S8) 143. The presence of intrachain disulfide bonds limits the fragmentation efficiency of the ADC and reduces sequence coverage by terminal fragment assignment. MASH Native incorporates searching and assignment of internal fragment ions, increasing sequence coverage and revealing sequence coverage of regions bounded by disulfide bonds (Figure 4.S9) to provide additional higher-order structural information for proteins and complexes <sup>302,303</sup>.

# Conclusion

MASH Native provides a unified software solution for the analysis of a variety of complex nTDP data for the first time. As a freely available and universal processing tool, MASH Native is a "one-stop shop" for nTDP data processing that can handle a variety of complex nTDP datasets including isotopically unresolved and isotopically MS1, MS2', MS2, and MS3 in both Discovery

and Targeted Modes with database search algorithms as well as data visualization and validation in a user-friendly interface. It can process raw data from various vendor formats and integrates multiple deconvolution/search algorithms into one package. MASH Native has been well-recognized since its release on April 7, 2022 <sup>36</sup>, and downloaded more than 1,400 times by users all around the world (66 % from North America, 22 % from Europe, 7 % from Asia, 4% from Oceania, 0.6% from South America, and 0.4% from Africa) (Figure 4.S10). As the nTDP community gains momentum to grow rapidly, MASH Native will play an increasingly important role to streamline nTDP data processing and accelerate the use of nTDP in structural biology and biomedical applications.

## Acknowledgements

This work was supported by the NIH R01 GM125085. We also thank all the MASH users worldwide for their excellent feedback, which has greatly helped the development of the software. UniDec development and integration was supported by the National Science Foundation (CHE-1845230 to M.T.M.). J.A.M. acknowledges support from the Training Program in Translational Cardiovascular Science, T32 HL007936-20 and T32 HL007936-21, for funding during the duration of this project. D.S.R. acknowledges the support from the American Heart Association Predoctoral Fellowship Grant No. 832615/David S. Roberts/2021. K.A.B. acknowledges the Vascular Surgery Research Training Program Grant T32 HL110853. K.J.R acknowledges the National Science Foundation Graduate Research Fellowship Program under Grant No. DGE-1747503 and the Graduate School and the Office of the Vice Chancellor for Research and Graduate Education at the University of Wisconsin-Madison, funded by Wisconsin Alumni Research Foundation. B.K. was supported by the European Union grant 101068151, Top-AMPK, HORIZON-MSCA-2021-PF-01. I.M.O. acknowledges the Clinical and Translational Science

Award (CTSA) program (ncats.nih.gov/ctsa), through the National Institutes of Health National Center for Advancing Translational Sciences (NCATS), grants UL1TR002373 and KL2TR002374.

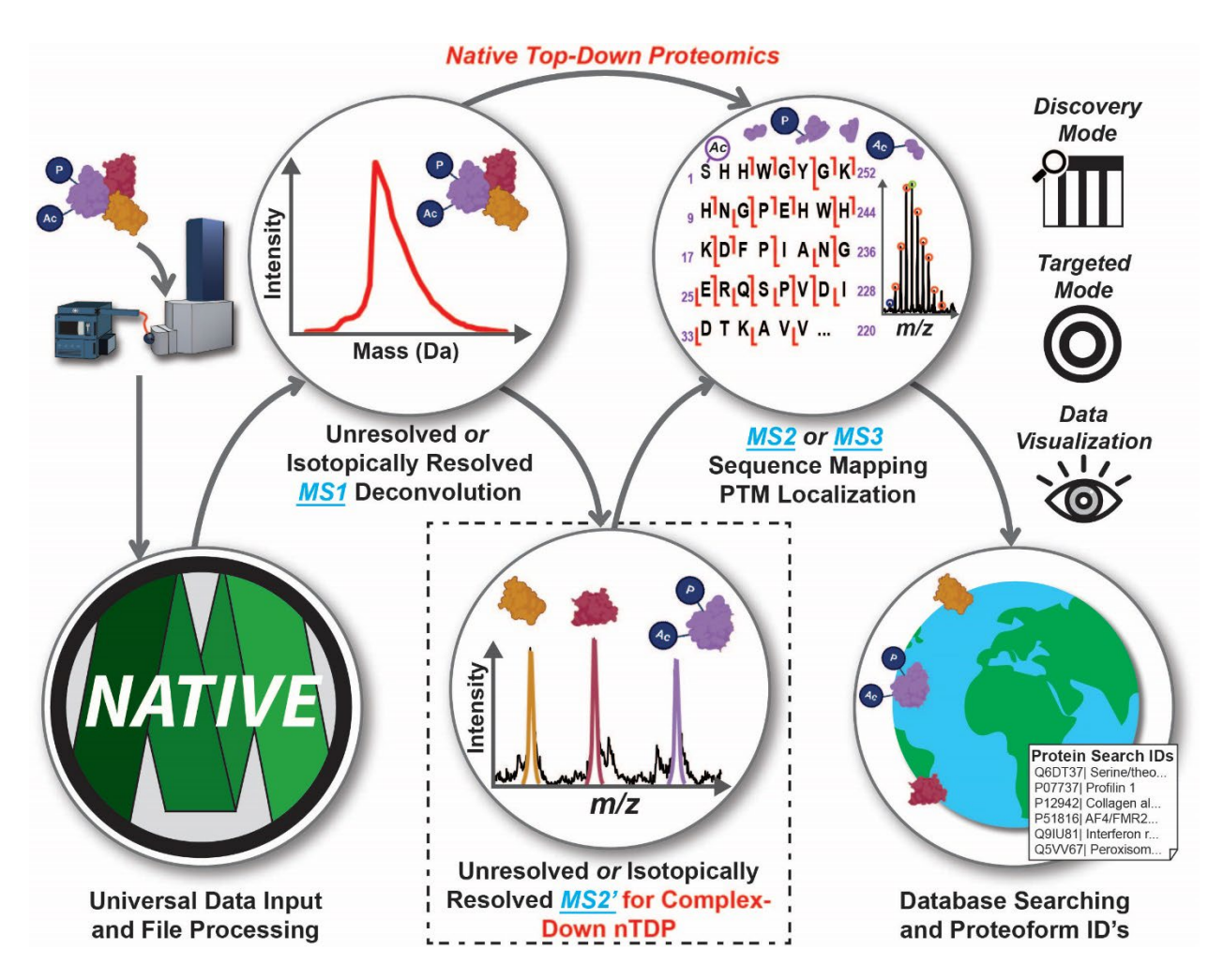


**Figure 4.1.** MASH Native provides a universal and comprehensive data processing software for a variety of nTDP analyses. MASH Native is capable of deconvoluting unresolved protein/protein complex (MS1) and released protein subunits (MS2') spectra, deconvoluting isotopically resolved MS1, MS2', MS2, and MS3 spectra, and performing database searches to identify unknown proteins. MASH Native can process nTDP data in both Discovery Mode and Targeted Mode approaches. It supports various MS file types and integrates multiple deconvolution/search algorithms into one package. MASH Native is a user-friendly software package capable of providing a "one-stop shop" for nTDP data processing.

# **Chapter 4**

# **Supplementary Information for**

# MASH Native: A Unified Solution for Native Top-Down Proteomics Data Processing

Table of Contents	<b>Pages</b>
Table 4.S1 Deconvolution algorithms included in MASH Native and supported function	ıs131
Figure 4.S1 Software GUI of MASH Native	132
Figure 4.S2 Scheme of spectral summing workflow in MASH Native	133
Figure 4.S3 Spectral summing tool panel in MASH Native	134
Figure 4.S4 UniDec deconvolution support in the MASH Native process wizard	135
Figure 4.S5 MASH Native configuration panel	136
Figure 4.S6 Discovery complex-down data processing using MASH Native	137
Figure 4.S7 Targeted native top-down data processing with MASH Native	138
Figure 4.S8 Targeted complex-down data processing using MASH Native	139
Figure 4.S9 Internal fragment matching in MASH Native	140
Figure 4.S10 MASH Native user downloads by geographic region	141
Supporting Documents for Users	142

**Table 4.ST1.** Included deconvolution algorithm compatibility with isotopically unresolved and isotopically resolved data handling for MSn data and database searching in MASH Native.

	MS1 Data	MS2' Data	MS2 Data	MS3 Data	Database Search Compatible
Isotopically Unresolved	UniDec	UniDec	Not Supported	Not Supported	Not Supported
Isotopically Resolved	TopFD, MsDeconv, eTRHASH, pParseTD, UniDec	TopFD, MsDeconv, eTRHASH, pParseTD, UniDec	TopFD, MsDeconv, eTRHASH, pParseTD, UniDec	TopFD, MsDeconv, eTRHASH, pParseTD, UniDec	TopFD, MsDeconv, eTRHASH, pParseTD, UniDec

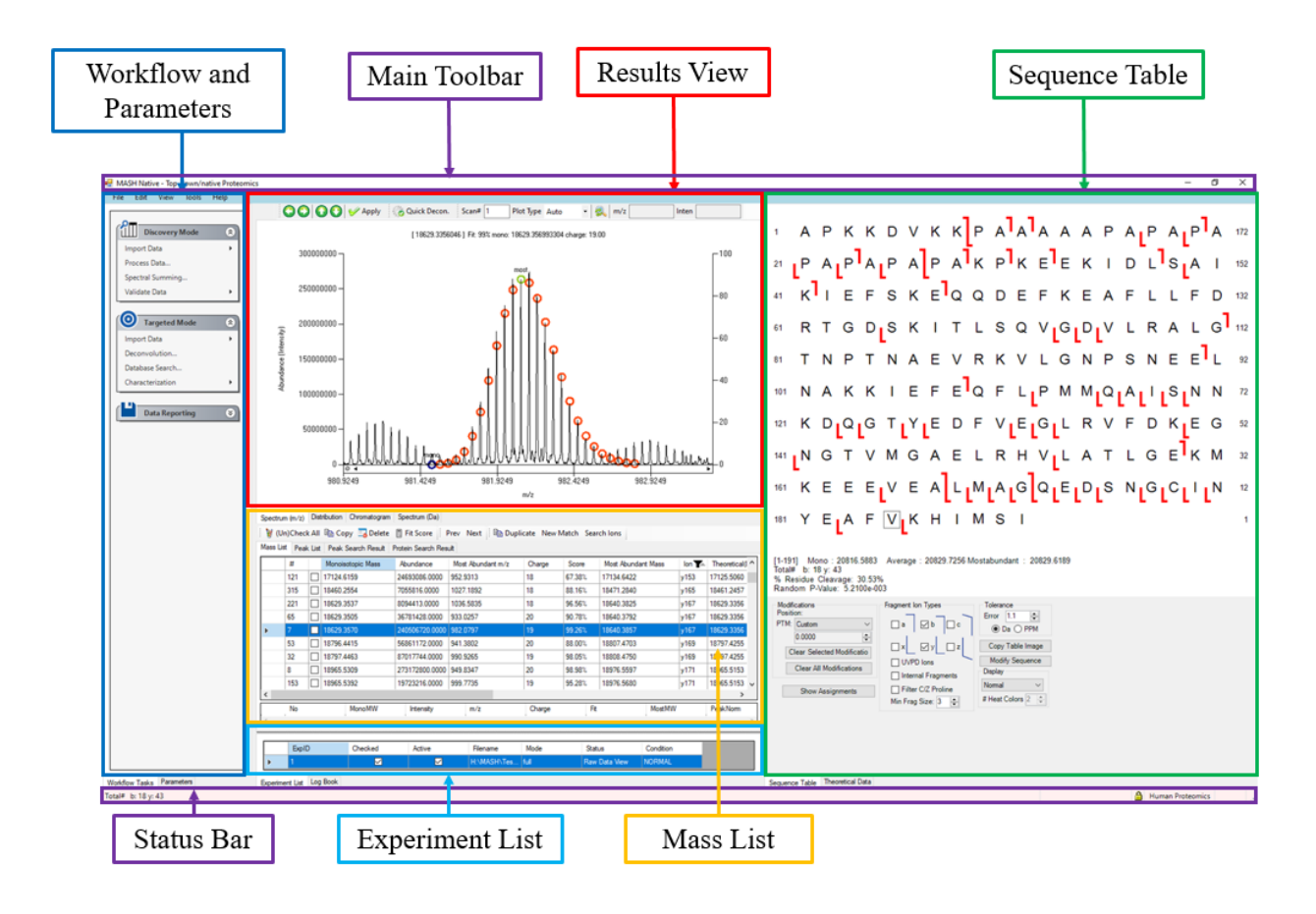
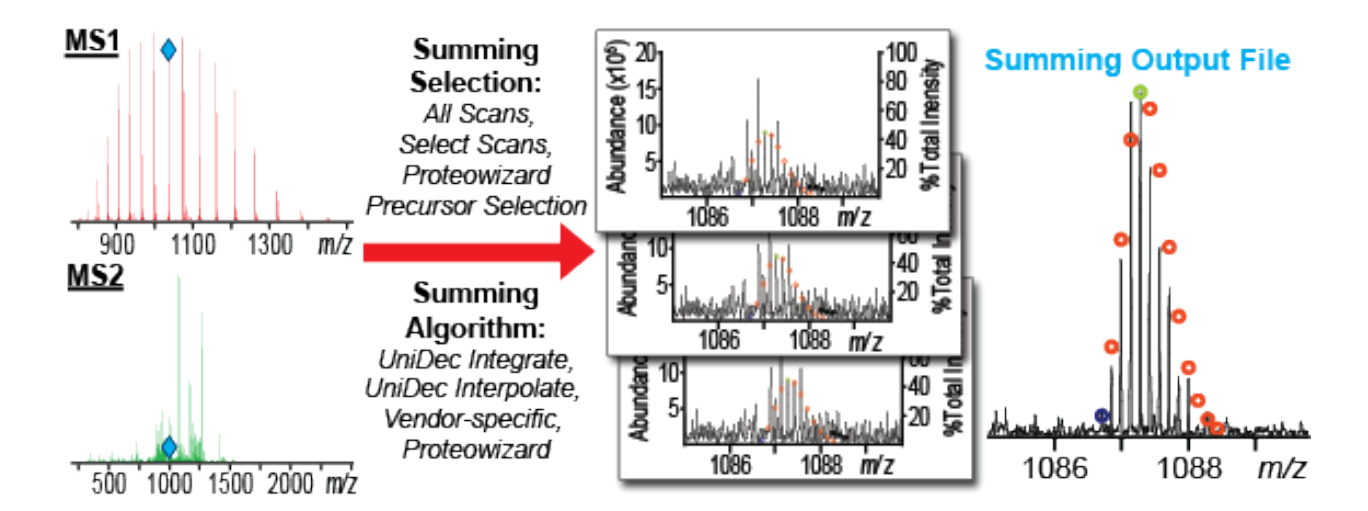
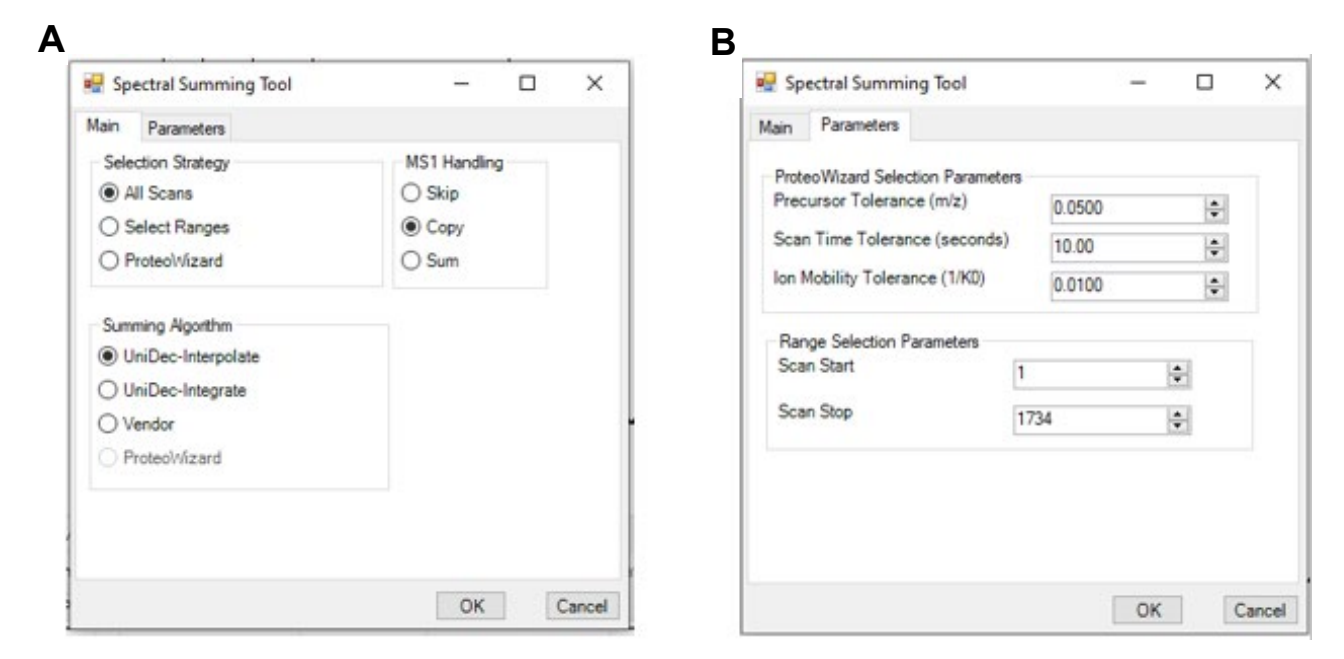


Figure 4.S1. The main interface of MASH Native includes seven main panels. 1) The Workflow and Parameters panel handle all the core data processing. Here, users can find the Discovery Mode, Targeted Mode, and Data Reporting Nodes. 2) The Results View panel provides visualization of MS, MS/MS, LC-MS, and LC-MS/MS data. Users can also review spectral deconvolution results, access the Quick Deconvolution feature, and manually adjust the theoretical ion distribution to the actual experimental spectra. 3) The Mass List panel allows users to select deconvoluted fragment ions for manual processing. 4) The Logbook and Status panels provide updates on the progress of data processing. 5) The Experiment List panel allows users to load multiple experiments into MASH Native and easily navigate between them, allowing for efficient processing. 6) The Sequence Table visualizes the fragment ions that match the identified proteoform sequence. 7) The Main Toolbar is where you can exit or minimize the MASH Native window. All these features are discussed in further detail in the MASH Native Supporting Documents, which are automatically downloaded with the software and are also found in the supporting documents linked below (Supporting Documents 4.1–4.6). Video tutorials for new users to MASH Native are linked in the supporting documents (Supporting Documents 4.7– 4.11).



**Figure 4.S2. Spectral summing workflow in MASH Native.** Users can choose to sum all MS2/MS3 scans, specific scan regions, or use ProteoWizard's precursor detection algorithms to sum all MS2/MS3 scans for a given precursor ion mass. Once selected, scans can be summed for both MS1 and MS2 using UniDec summing (Integrate or Interpolate), vendor-specific summing for Thermo data, or ProteoWizard summing to improve signal-to-noise (S/N) (**Supporting Document 4.5**).



**Figure 4.S3. Spectral Summing Tool in MASH Native.** The spectral summing algorithm allows users to sum scans within their original experiment file. The summing process generates a mzML file which can then be processed by MASH Native, including deconvolution and searching. The summing tool is designed to be flexible by giving users control over the scan selection, the summing algorithm to use, and how to handle MS1 scans in the dataset (A). ProteoWizard selection parameters and scan range selection details can be edited in the "Parameters" tab (B). See the "Best Practices for Spectral Summing" for suggested parameters when performing spectral summing (**Supporting Document 4.5**).

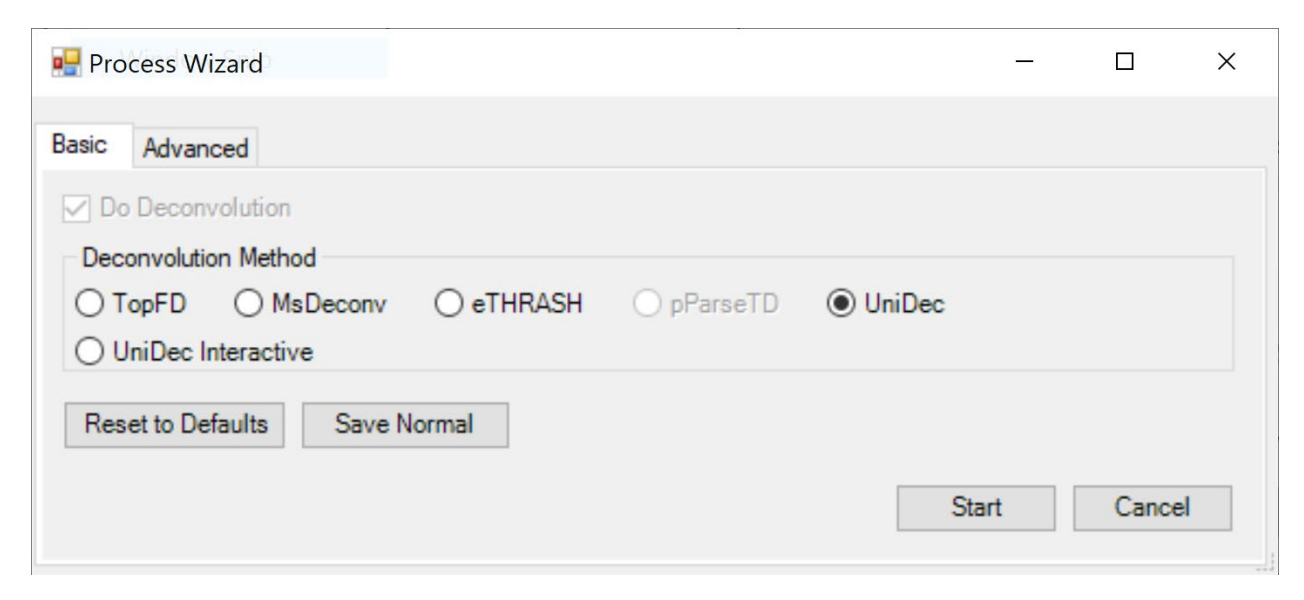


**Figure 4.S4.** UniDec deconvolution support in MASH Native. UniDec deconvolution is a powerful tool to perform charge state deconvolution on both native and denatured protein mass spectra. Correct selection of parameters is critical. The Marty lab has provided a number of different pre-set deconvolution conditions through UniDec which offer parameter suggestions for UniDec for general applications (default), low resolution native MS, high resolution native MS, and isotopically resolved MS (**Supporting Document 4.6**). Additionally, the Marty lab has recently published an excellent book chapter tutorial to guide user selection of UniDec parameters <sup>304</sup>. MASH Native also supports "UniDec Interactive" deconvolution, which allows users to load any MASH-compatible data file in the UniDec GUI, perform all processing through the UniDec GUI, then import deconvolution results back into MASH Native for any additional processing.

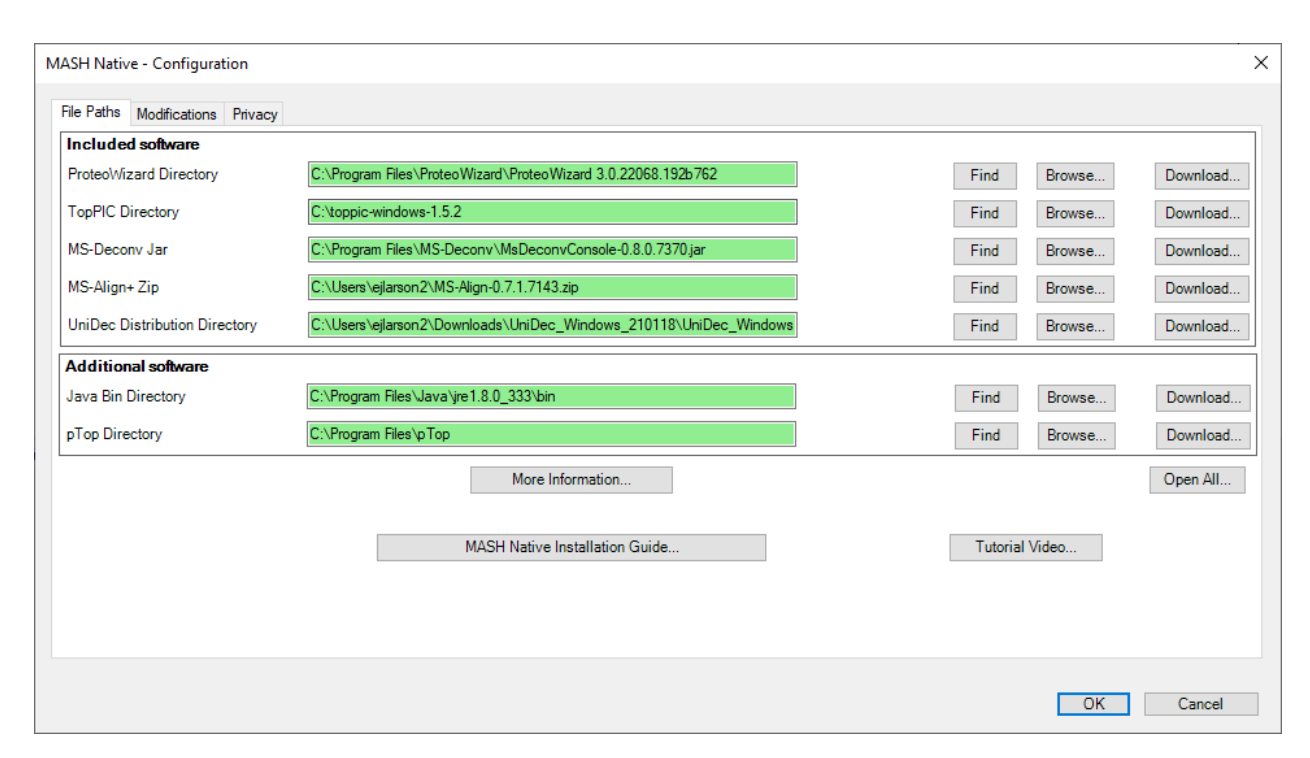


**Figure 4.S5.** Configuration of additional deconvolution and search algorithms in MASH Native. In the MASH Native application, the Configuration tool provides users with an intuitive directory for installation of all associated deconvolution and database search algorithms. In this interface, users can use either the "Find" feature to look for the default directory locations where the software was installed or use "Browse" feature to manually locate the correct directory through a file browser dialog. Clicking the "Download" feature will direct users to the website where the software can be downloaded. Directories found by MASH Native will be displayed in green, while the unidentified directories will be displayed in pink. Software in the "Included software" section is automatically downloaded upon MASH Native installation. "Additional software" is not automatically downloaded but may be installed if users desire (**Supporting Document 4.3—4.4**). Additionally, a link for the MASH Native Installation Manual can also be found at the bottom of the Configuration tool.

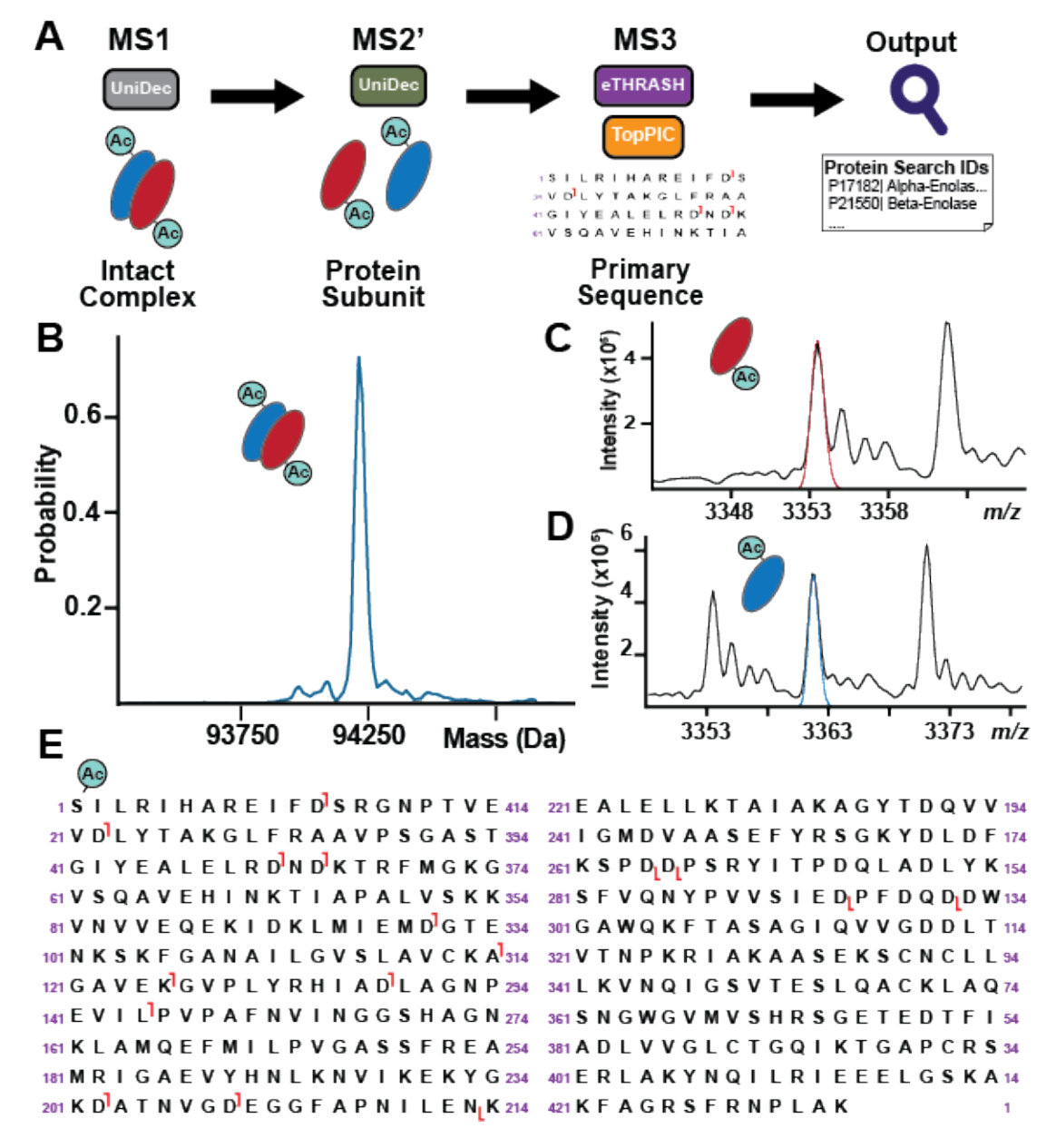


**Figure 4.S6. MASH Native's Discovery Mode workflow.** Workflow for the analysis of complex-down mass spectrometry data (A). The Discovery Mode in MASH Native was used to process complex-down MS analysis of enolase complex from *mus musculus* (MassIVE dataset # MSV000080328)<sup>305</sup>. The Discovery Mode workflow allowed detection of the unresolved intact enolase complex (B), the released α-enolase subunit (C), and β-enolase subunit (D) through low-resolution UniDec deconvolution. High-resolution MS3 processing provided primary sequence coverage for both α-enolase (E) and β-enolase (not shown) and enabled detection and localization of N-terminal acetylation on both subunits. Data can be deconvoluted at the MS1/MS2' level with either low or high-resolution followed by high-resolution MS2/MS3 fragment spectra deconvolution using a suite of algorithms, including MS-Deconv, pParseTD, eTHRASH, and TopFD. Database search by MS-Align+, pTop, and TopPIC provide the first combination of low-resolution native deconvolution and database search in a single software package.

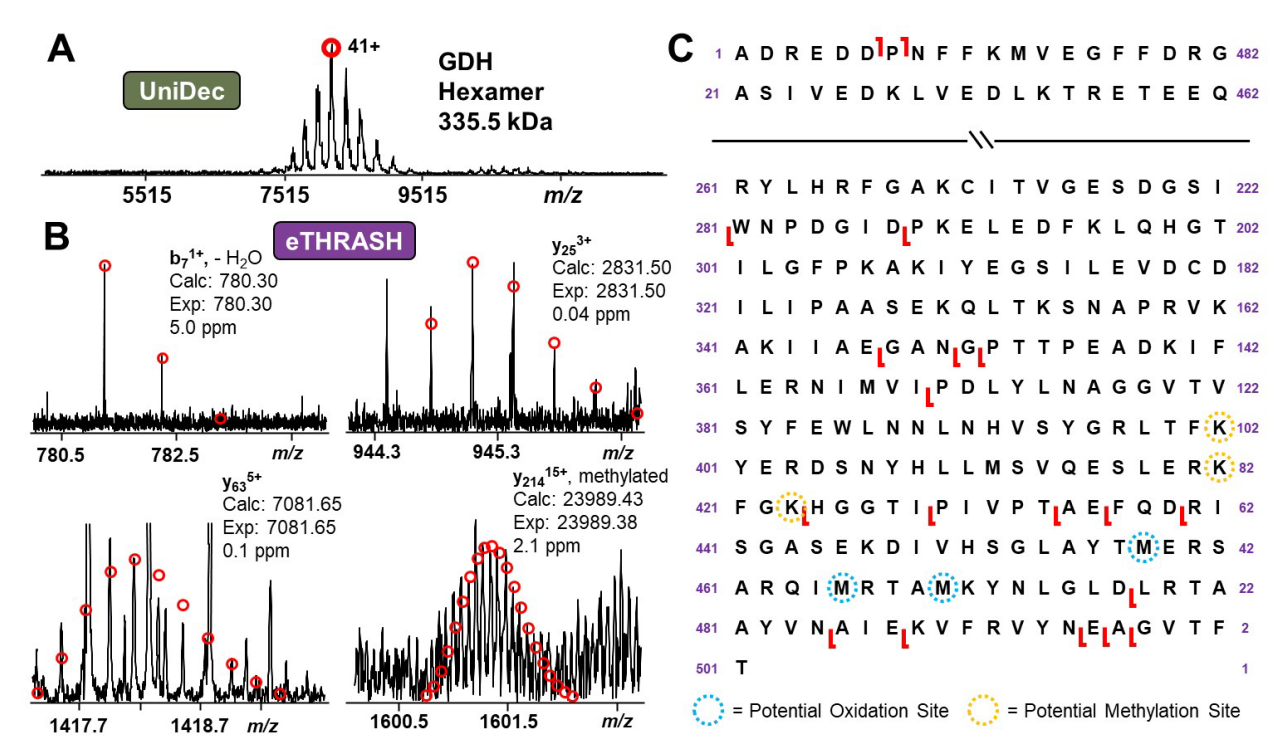


**Figure 4.S7. MASH Native's Targeted Mode workflow**. Native top-down MS analysis of the hexamer of Bovine glutamate dehydrogenase (GDH) <sup>35</sup>. Analysis of the unresolved MS1 spectra of the GDH hexamer was performed using UniDec (A). Representative fragment ions found using eTHRASH deconvolution of MS2 data (B) and sequence coverage map (C). These results confirm the results reported in Li *et al.* and highlight MASH Native's user-friendly and intuitive interface.

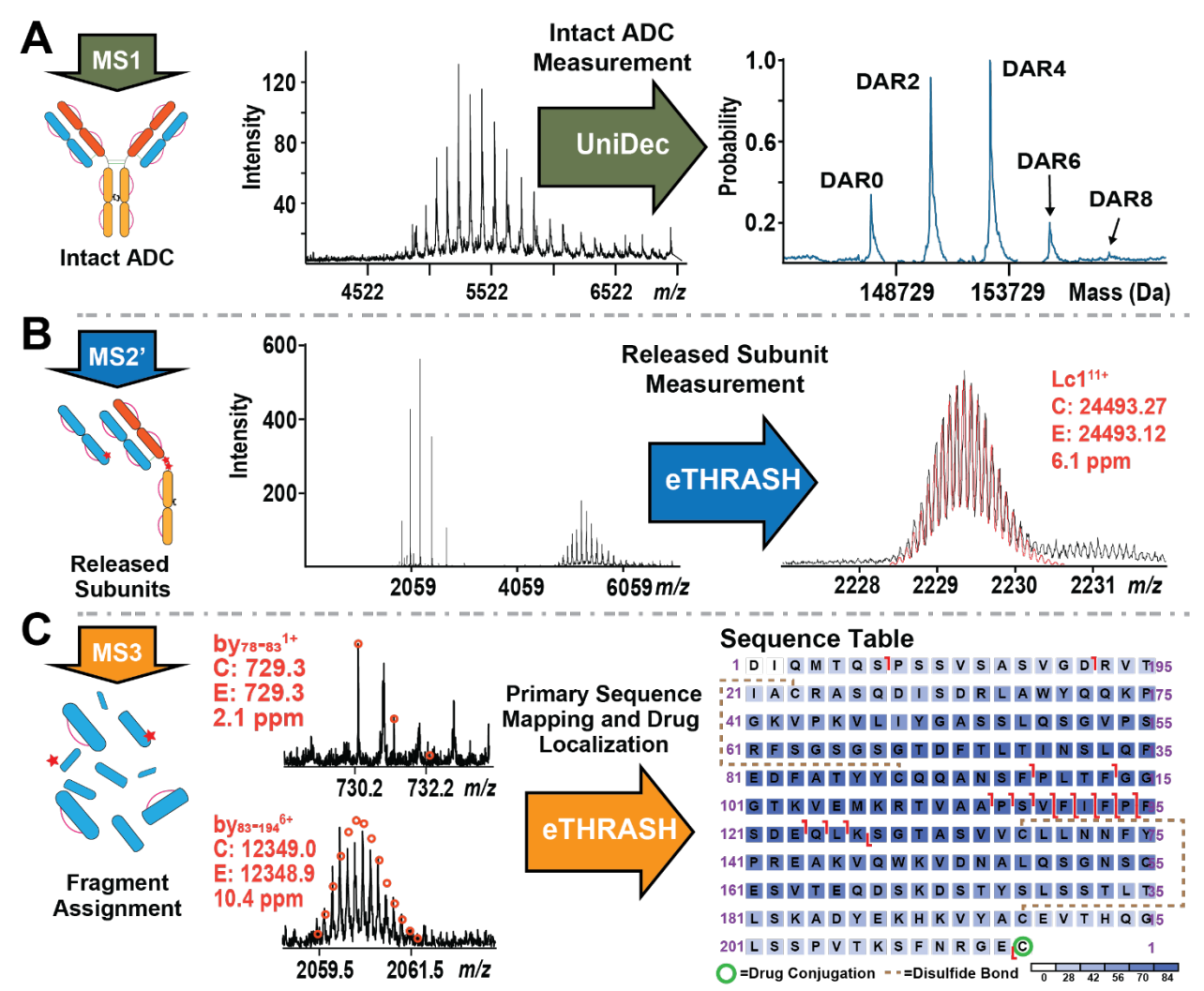


**Figure 4.S8.** Analysis of a native cysteine-linked antibody-drug conjugate. Data processing of an antibody-drug conjugate (ADC) <sup>143</sup>. UniDec processes isotopically unresolved MS1 which provides charge state matching to find individual charge states for specific drug-to antibody ratio (DAR) species and enables viewing of the charge deconvoluted spectra (A). Quantitative output of UniDec even allows calculation of the average DAR value, a critical metric for ADC quality control. High-resolution MS2 deconvolution of collisionally dissociated non-covalently bound species enables high-accuracy subunit mass detection (B). Fragmentation of released subunits, specifically the light chain with one bound drug (Lc1), provides MS3 characterization of the primary sequence through assignment of both terminal and internal fragment ions to confirm the location of intrachain disulfide bonds and the drug binding site (C). Uniquely, internal fragment matches provide sequence coverage in disulfide bound regions, which are not typically accessible to fragmentation by terminal fragment ions.

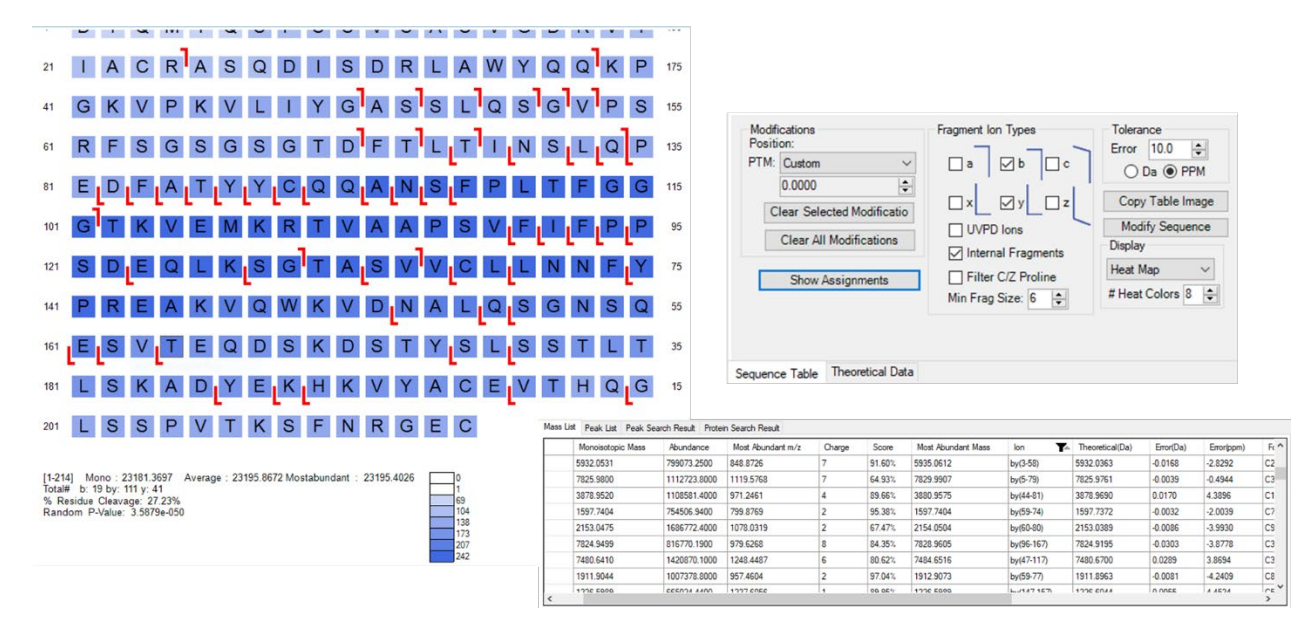


**Figure 4.S9. Internal fragment matching in MASH Native.** In MASH Native's main interface, users can select "Internal Fragments" under the fragment type and then push the "Show Assignments" function under the sequence table window.

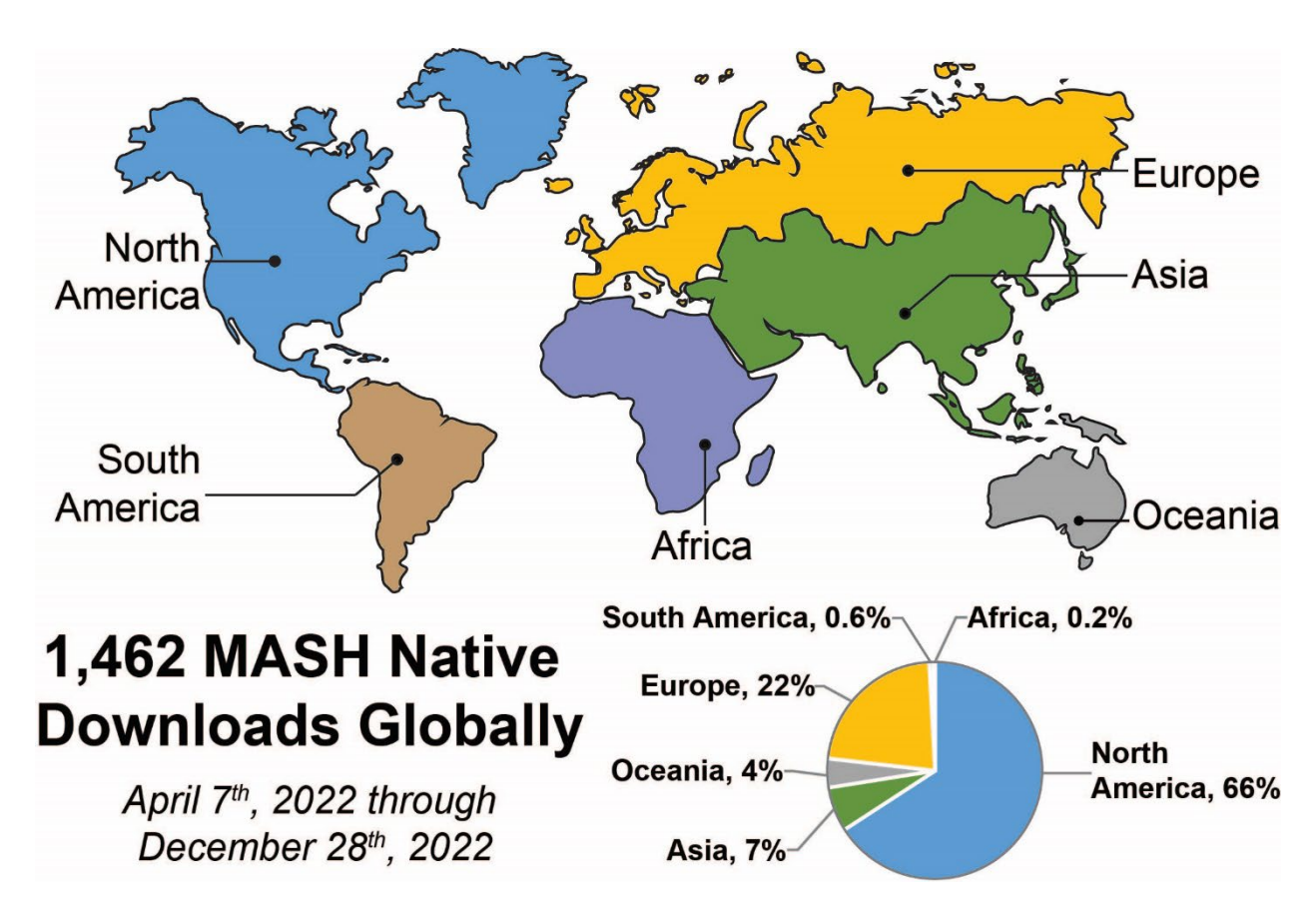


**Figure 4.S10. Global MASH download by geographic region.** MASH Native has been used by many labs globally and is primed to become an integral tool for further developments in native top-down proteomics.

## Supporting Documents for Users

The following MASH Native user documents and video tutorials are provided:

- Supporting document 4.1 MASH Native License Agreement
- Supporting document 4.2 MASH Native user manual
- Supporting document 4.3 MASH Native installation guide
- Supporting document 4.4 MASH Native getting started guide
- Supporting document 4.5 Best practices for spectral summing
- Supporting document 4.6 <u>Best practices for UniDec deconvolution in MASH</u>
   Native
- Supporting document 4.7 <u>Video Tutorial Part 1: Introduction to MASH Native</u>
- Supporting document 4.8 <u>Video Tutorial Part 2: MASH Native configuration</u>
- Supporting document 4.9<u>Video Tutorial Part 3: Using the Discovery Mode</u>
   workflow for identification of an unknown protein
- Supporting document 4.10 <u>Video Tutorial Part 4: Using the Targeted Mode</u> workflow for characterization of a known protein
- Supporting document 4.11 <u>Video Tutorial Part 5: Post-translational modification</u>
   analysis using UniDec in MASH Native

## Chapter 5

Expanding Global Top-Down Proteomics Coverage by Sequential Protein Extraction and Online Two-Dimensional Liquid Chromatography

This chapter is adapted from a manuscript in preparation:

<u>Larson, E. J.</u>; Fischer, M.; Melby, J. A.; Rogers, H. T.; Reasoner, E. A.; Knight, B. A.; Aballo, T. J.; Pergande, M. R.; Krichel, B.; Zhu, Y.; Ge, Y. "Expanding Global Top-Down Proteomics Coverage by Sequential Protein Extraction and Online Two-Dimensional Liquid Chromatography.

#### Abstract

Understanding the expression of proteins in the body is critical to determining their activity. The protein products of a single gene including splicing variants, mutants, and post-translationally modifications, called proteoforms, alter cellular function and can mark the progression or onset of disease. Top-down proteomics has become an indispensable tool to study proteoforms and provides a clear view of the "landscape" of proteoform expression. Despite these benefits, the implementation of top-down proteomics for global discovery workflows is historically difficult due to the range of size, expression, and physicochemical properties present in the intact proteome. These challenges are conventionally addressed using front-end separations in the form of liquid chromatography-mass spectrometry (LC-MS) workflows. While new MS instruments and methods designed to address the needs of top-down workflows have developed rapidly over the past decade, development of front-end LC separations for top-down has lagged behind that of MS. To improve global proteome coverage by top-down proteomics, we have developed an online twodimensional (2D) LC method coupling serial size exclusion (sSEC) and reversed phase LC (RPLC). Combining size-based fractionation via sSEC and the high chromatographic resolving power of RPLC in this 2DLC approach yields a method with four-fold greater peak capacity than traditional one-dimensional RPLC-MS. Here, the developed online 2D sSEC-RPLC-MS method is applied to a three-step sequential extraction, which samples the cytosolic, sarcomeric, and membrane subproteomes of human heart tissue. This approach offers an easy to use, automated approach to expand global proteome coverage by top-down proteomics that is compatible with future disease and large-scale studies by top-down proteomics.

#### Introduction

Proteins drive cellular function, with altered expression and activities leading to dysfunction and disease onset. A robust understanding of protein expression is critical to determining how protein-level changes affect biological function. Currently, bottom-up proteomics, which relies on enzymatic digestion of protein sample followed by mass spectrometry (MS) and tandem MS (MS2) analysis, is the most developed technique to study protein-level expression changes.<sup>29,30</sup> However, bottom-up proteomics faces several critical challenges including possible alterations to post-translational modifications (PTMs), <sup>26</sup> detection bias between modified and unmodified peptides, <sup>27</sup> and peptide to protein inference problems. <sup>28</sup> These challenges hinder analysis of proteoforms, or all protein products of a single gene including splice variants and modified forms, 8 which are known to alter protein function and change during disease onset and progression. Alternatively to bottom-up proteomics, top-down proteomics can provide a "bird's eye view" of proteoform-level changes.<sup>29,30</sup> Top-down proteomics forgoes enzymatic digestion and ionizes intact proteins, identifying and characterizing sequence variants by gas phase dissociation. This approach reduces sample preparation time, preserves endogenous PTMs, and enables easy relative quantitation of proteoform expression changes. 306–308 These benefits have uniquely positioned top-down proteomics as an excellent tool to study proteoform-level changes.<sup>30</sup> However, implementation of global top-down proteomics is challenged by several factors, including the decrease in MS signal-to-noise ratio as protein molecular weight increases,<sup>37</sup> the wide range of protein expression levels in the proteome, 11 and the greater chemical diversity of intact proteins compared to peptides.<sup>144</sup> These challenges may be addressed through use of frontend separations.

To broaden the scope of global top-down proteomic studies, sample complexity must be reduced prior to MS detection. This is most often achieved using a one-dimensional (1D) liquid chromatography (LC) approach, typically by reversed phase LC (RPLC). <sup>29,30</sup> While 1D RPLC-MS can provide high chromatographic resolution by hydrophobicity<sup>309</sup> it fails to address the full range of protein sizes and physiochemical properties. This results in smaller or higher abundance proteins dominating MS spectra and challenging detection of large or low abundance proteins. 30,83 The introduction of serial size exclusion chromatography (sSEC) in 2017 sought to address this challenge, and provided a more effective approach to bin proteins by molecular weight than conventional one-column SEC.83 However, 1D sSEC alone does not address the range of physiochemical properties present in the proteome, and a two-dimensional liquid chromatography (2DLC) approach is needed to recognize the full benefit of this technique for global top-down proteomics. 83,146 Offline 2DLC coupling sSEC and RPLC, 83,146 and high pH RPLC with low pH RPLC<sup>148</sup> have shown improved proteome coverage relative to 1D RPLC-MS top-down, but often requires replicate injection pooling, buffer exchange, and significant hands-on time. Recently, new online 2DLC approaches for intact protein separation have automated dimensional coupling through valve interfaces to facilitate by targeted subproteome sampling 153,156 and whole proteome sampling<sup>154,155</sup>.

Here, for the first time, we report online top-down 2DLC-MS coupling microscale serial size exclusion (sSEC) coupled to RPLC-MS to expand global coverage of the human heart proteome by top-down proteomics. Online 2DLC-MS analysis improves separation power of the method by four-fold relative to conventional 1D RPLC and enables easy automation to eliminate hands-on time required in offline 2D workflows. The developed method was applied to a three-step sequential extraction of human heart tissue that enriched cytosolic proteins, sarcomeric

proteins, and membrane-associated proteins. This enabled more effective whole-proteome sampling and provided deeper proteome coverage by further fractionating the proteome prior to MS analysis. Our developed approach provides a firm foundation for future disease studies and large-scale top-down analyses.

#### Methods

## Reagents and Consumables

The reagents used were purchased from Thermo Fischer Scientific (Waltham, MA, USA). unless otherwise specified. LCMS grade formic acid, hexafluoroisopropanol (HFIP) were purchased from Millipore Sigma (Burlington, MA, USA). Azo surfactant was synthesized in-house following the established protocol. SEC columns were provided by PolyLC Inc. (Columbia, MD, USA) and RPLC materials were purchased from Advanced Material Technologies (Wilmington, DE, USA).

### Protein Standards for 2DLC Method Development

A mixture of eight standard proteins was used for chromatographic method development, chosen to span a range of hydrophobicities (GRAVY = 0 to -0.54 by sequence-based calculation)<sup>311</sup> and molecular weights (10.9 kDa to 606 kDa). An equal mass/unit volume mixture was made in RPLC mobile phase A using aprotinin (Apr) from bovine lung (P00974), lysozyme (Lyo) from chicken egg white (P00698), myoglobin (Myo) from equine heart (P68072), carbonic anhydrase (CA) from bovine erythrocytes (P00921), ovalbumin (Ova) from chicken egg white (P01012), alcohol dehydrogenase (ADH) from brewer's yeast (P00330), serum albumin (BSA) from bovine serum (P02769), and Thyroglobulin (Thy) from bovine thyroid (P01267).

#### Protein Extraction

A three-step sequential extraction procedure was used to extract proteins from 50 mg of human heart tissue. Prior to extraction, the tissue was vortexed in 1 mL of 1x diphosphate buffered saline to deplete serum albumin. For the first extraction step, cytosolic proteins were extracted using HEPES buffer (25 mM 4-(2-hydroxyethyl)-1-piperazineethanesulfonic acid (HEPES), 50 mM sodium fluoride, 0.25 mM sodium orthovanadate, 0.25 mM phenylmethylsulfonyl fluoride, 2.5 mM ethylenediaminetetraacetic acid, 1x HALT Protease and Phosphatase inhibitor at pH 7.4). Second, sarcomeric proteins were extracted using TFA buffer (0.1 % trifluoroacetic acid (TFA) and 1 mM tris(2-carboxyethyl)phosphine at pH 2.2). Finally, membrane and other low solubility proteins were extracted using Azo buffer (0.5 % 4-hexylphenylazosulfonate (Azo), 25 mM ammonium bicarbonate, 1 mM dithiothreitol, 1x HALT protease and phosphatase inhibitor at pH 8.0). For each extraction step, tissue was homogenized in 500 µL of buffer solution using a Pro 200 electronic homogenizer from Pro Scientific. After each extraction, homogenate was centrifuged at 21.1 xg, supernatant was collected, and the tissue pellet was snap frozen in liquid nitrogen to prevent protein degradation or alteration before subsequent extractions.

### LC-MS Conditions

LC-MS analyses were performed using a Waters M-Class nano2DLC system and a Bruker Maxis II quadrupole time-of-flight mass spectrometer. Separation was performed using an online 2D sSEC-RPLC approach with coupling by single heart-cutting using a 6-port 2-position valve. The first dimension (<sup>1</sup>D) sSEC separation was performed using two 2.1 x 200 mm PolyHYDROXYETHYL A columns connected in series with 2 µm particles and pore sizes of 1000 Å and 300 Å, respectively. The <sup>1</sup>D was performed under isocratic conditions with a mobile phase composition of 1% formic acid and 2 % HFIP in water at 29 µL/min flow rate. Interdimensional transfer was performed by single heart-cutting stationary phase-assisted modulation (SPAM)<sup>151</sup> at

ambient temperature using a homepacked 0.5 x 30 mm HALO C4 trap column with 2.7 µm particles and an effective pore size of 1000 Å. Eluent from the <sup>1</sup>D was loaded on to the trap column for one minute for each single heart-cutting 2DLC analysis. To sample the full <sup>1</sup>D elution window, multiple 2DLC runs were performed for a single sample with each analysis sampling a different one-minute section of the <sup>1</sup>D elution window to enable all time points in the <sup>1</sup>D to be analyzed in the second dimension (<sup>2</sup>D). The <sup>2</sup>D separation was performed at 70 °C using a home packed 0.25 x 100 mm HALO C4 with 3.4 µm particles and an effective pore size of 400 Å. The <sup>2</sup>D separation was performed by gradient elution with 0.1 % formic acid in water as mobile phase A and 0.1 % formic acid in acetonitrile as mobile phase B. Gradient conditions used were: 10-10-16-65-100-100-10-10 % B over 0-3-3.1-28-28.1-31-31.1-34 min. The developed sSEC and RPLC conditions were the same for all 1D and 2D analyses. For MS1 analysis, a scan rate of 2 Hz was used with a mass range from 200-3500 m/z, quadrupole low mass cutoff set at 500 m/z, and quadrupole energy of 4 eV used. The ion transfer optics were optimized at a funnel 1 RF of 400 Vpp, Multipole RF of 800 Vpp, and isCID energy of 40 eV. Collision cell energy of 4 eV was selected, with a collision cell RF of 2500 Vpp, a transfer time of 150 μs, and a pre pulse storage time of 25 μs. For MS2 analysis, autoMS/MS was enabled, selecting the four most abundant precursors for fragmentation, with active exclusion of precursors after 4 scans and an exclusion time of 2 minutes selected.

### Data Analysis

To analyze MS1 spectra, Bruker Compass v4.3 was used, performing charge deconvolution by MaxEnt. For proteoforms below 50 kDa, MaxEnt resolving power was set to 80,000, and peak picking was performed by the sophisticated numerical approximation of peaks (SNAP) algorithm to determine the monoisotopic mass and average mass. Proteoforms above 50 kDa used MaxEnt deconvolution with a resolving power of 10,000 followed by peak picking using the SumPeak

algorithm to determine average mass. For MS2 analysis, data files were converted from Bruker \*.baf files to \*.mzML files use ProteoWizard's<sup>312</sup> v3.0.22068 MSConvert GUI with vendor-specific peak picking selected. The converted files were deconvoluted using default parameters in FLASHDeconv<sup>174</sup> from OpenMS v3.0.0, generating TopFD deconvolution outputs. Deconvoluted results were searched using TopPIC v1.6.2<sup>179</sup> with an E-value cutoff of 0.01, a 15 ppm error tolerance, ± 500 Da unexpected single mass shift, and five variable modifications: oxidation, methylation, dimethylation, acetylation, and phosphorylation. TopPIC search outputs were manually validated, and results were visualized using MASH Native v1.1<sup>38</sup>. Network analysis and gene ontology (GO) analysis were performed using STING v11.5<sup>313</sup> and Cytoscape v3.9.0.<sup>314</sup> Identified proteins were clustered in STRING by unsupervised hierarchical clustering using the Markov clustering algorithm with an inflation parameter of 1.1 for stringent cluster identification.

Assessing Chromatographic Performance

The theoretical peak capacity ( $n_c$ ) for RPLC was determined by averaging the calculated  $n_c$  for each protein in the 8-protein standard mixture, first calculating the number of theoretical plates (N)<sup>315</sup>:

Equation 1: 
$$N = 16 \left(\frac{t_r}{t_d}\right)^2$$

Equation 2: RPLC 
$$n_c = 1 + \left(\frac{N^2}{4}\right) * \ln\left(\frac{t_r}{t_d}\right)$$

Where  $t_r$  is the retention time and  $t_d$  is the dwell time of the separation. The theoretical peak capacity for sSEC was calculated using the following equation<sup>316</sup>:

Equation 3: sSEC 
$$n_c = 1 + \frac{\sqrt{\frac{v_p}{v_t} + \frac{L}{h*dp}}}{4R_S}$$

Where  $V_p$  is the volume of the pores,  $V_t$  is volume of a totally permeating peak, L is the column length, h is the experimentally determined plate height,  $d_p$  is the diameter of column particles, and  $R_s$  is resolution of adjacent peaks. The 2D  $n_c$  is reported as both the ideal 2D  $n_c$ , the product of sSEC  $n_c$  and RPLC  $n_c$ , and the Davis  $n_c$ ,  $^{317}$  which is corrected to address under sampling of the  $^1D$  by the  $^2D$  separation:

Equation 4: Davies 2D 
$$n_c = \frac{Optimal 2D n_c}{\sqrt{1+3.35\left(\frac{t_d}{W_{4\sigma}}\right)^2}}$$

Where  $w_{4\sigma}$  is the baseline peak width.

#### **Results and Discussion**

Sequential Protein Extraction and Online 2D sSEC-RPLC-MS to Expand Top-Down Proteomics Global Proteome Coverage

Here, global top-down proteome coverage is expanded using two combined strategies to reduce sample complexity entering the MS: a three-step sequential extraction and online 2D sSEC-RPLC-MS (Figure 5.1). First, sequential extraction reduces sample complexity by splitting the global proteome into three subproteomes which are enriched in the three different extracts (Figure 5.1A). HEPES extracts primarily cytosolic proteins, TFA extracts sarcomeric proteins and other acid-soluble proteins, and the Azo extracts membrane proteins along with other difficult to solubilize proteins. Second, extracts are analyzed individually using online 2D sSEC-RPLC-MS, which separates proteins by both size and hydrophobicity prior to MS analysis (Figure 5.1B). The valve-actuated online coupling approach enables a facile, automated combination of two dimensions of separation to improve chromatographic resolution of intact proteins relative to traditional 1D RPLC analyses. These two combined strategies to reduce sample complexity

facilitated top-down MS analysis of proteins to expand the scope of proteoform families observed (Figure 5.1C).

Development of Online sSEC-RPLC-MS For Top-Down Proteomics

Development of the online sSEC-RPLC-MS method for intact protein separation was first performed using an eight-protein standard mixture, specified in the methods section. First, 1D sSEC-MS conditions were optimized and replicate injections were performed to ensure separation reproducibility (Figure 5.S1). Next, a 1D RPLC-MS method was developed and applied to the standard protein mixture (Figure 5.S2). Coelution of standards occurs in both 1D sSEC and 1D RPLC, with varying degrees of severity. The developed separation techniques were then combined as an online single heart-cutting sSEC-RPLC-MS approach, enabling chromatographic resolution of all protein standards (Figure 5.S3). By sequentially heart-cutting 1-minute windows of <sup>1</sup>D eluent (Figure 5.3A), proteins separated by sSEC were analyzed by RPLC in <sup>2</sup>D. chromatograms (TICs) of <sup>2</sup>D RPLC separations show clear differences in chromatographic profiles that reflect changes in the composition of proteins entering <sup>2</sup>D after <sup>1</sup>D separation (Figure 5.3B-G). This is also highlighted when comparing MS1 spectra from a traditional 1D RPLC approach to those generated by 2D sSEC-RPLC (Figure 5.S4). Notably, the coelution of BSA and Myo, ADH and Ova, and Ova and Thy present in traditional 1D RPLC are resolved when using a 2D sSEC-RPLC approach. Improvements in chromatographic performance in the 2D mode can be quantified by the theoretical peak capacity (n<sub>c</sub>), a measure of the total number of analytes which may be theoretically baseline resolved by the selected separation conditions.<sup>315</sup> While the chosen 1D RPLC method yields  $n_c = 33$ , the 2D sSEC-RPLC approach increases  $n_c$  to 133 (Figure 5.S5). This represents a four-fold improvement in chromatographic performance by online 2D sSEC-RPLC over traditional 1D RPLC approaches for front-end separations in top-down proteomics.

## Online 2D sSEC-RPLC-MS For Human Heart Extract Analysis

The developed 2DLC method was used to analyze each extract from serial extraction separately to improve global top-down proteome coverage for human heart tissue sequential extraction. Once again, 1D RPLC-MS analysis of the TFA extract was compared with the online the 2D sSEC-RPLC method to assess the utility of 2D sSEC-RPLC for complex samples (Figure 2). As anticipated, 1D sSEC fails to chromatographically resolve any proteins (Figure S6) and 1D RPLC-MS also reveals co-elution of proteins (Figure 5.2A). The MS1 spectra averaged from 18 to 19 minutes in 1D RPLC shows co-elution of cardiac α Actin (ACTC1, 41.8 kDa) and cardiac troponin C (TNNC1, 18.4 kDa). Application of 2D sSEC-RPLC chromatographically resolved cardiac α Actin and cardiac troponin C, as well as revealing cardiac β Myosin heavy chain (MYH7, 223.1 kDa) which is not observed in 1D RPLC alone (Figure 5.2B). In addition to benefits at the MS1 level, the online 2D approach also improves the quality of MS2 spectra due to the increased chromatographic resolution of this approach (Figure 5.S7). The use of the 2D approach increases the percent residue cleavage of trimethylated ventricular isoform of cardiac myosin light chain (MLC-V2) by 32 % relative to a 1D RPLC approach by autoMSMS (Figure 5.S7A, C) and boost the percent residue cleavage of the trimethylated and phosphorylated proteoform of MLC-V2 by 28 % (Figure 5.S7B, D). Increased sequence coverage also results in a lower random P-value for each sequence, increasing confidence of identifications made for global discovery top-down workflows.

## Complimentary Proteome Sampling of Sequential Extraction

Compilation of all sequential extracts revealed 116 proteins identified by MS2 analysis with a total of 160 proteoforms detected by top-down proteomic analysis (Figure 3). Generating histograms of identified proteins (Figure 5.3A) and proteoforms (Figure 5.3B) binned by

molecular weight in 10 kDa bins shows the size distribution of identified features. The average molecular weight of MS2 identified proteins was 27.4 kDa, while the average proteoform mass was slightly lower at 24.4 kDa. This is likely caused by the detection of a large number of histone proteoforms with masses between 11 and 15 kDa. It is important to note the disparity between proteoforms detected at the MS2 level and the number of MS1 features observed by MS1 deconvolution and peak picking (Figure 5.S8), particularly for larger proteoforms. While the results of Figure S8 are likely influenced by MS1 deconvolution artifacts<sup>172</sup>, it is clear that the MS2 identified proteins and proteoforms do not reflect the full range of sizes present in the sequential extracts. This challenge has been faced by the field top-down down proteomics unilaterally, with recent longitudinal studies reporting average MS2 identified proteoform masses of 6.2 kDa<sup>318</sup> and 8.1 kDa<sup>319</sup>, despite both studies employing offline size-based fractionation techniques.

Genes encoding MS2 identified proteins were mapped in STRING to visualize interactions among identified proteins (Figure 5.3C). Unsupervised clustering performed under stringent conditions revealed that three distinct clusters were observed, roughly divided by portions of the subproteome that were sampled in each extract: cytosolic/mitochondrial matrix proteins (HEPES), sarcomeric proteins (TFA), and membrane/low-solubility proteins (Azo). Node color coding shows the complimentary nature of the three extracts. Specifically, subunits of the cytochrome c oxidase (COX) protein complex are largely extracted in the Azo extract because many subunits are membrane imbedded.<sup>320</sup> However, peripheral COX subunits COX5B and COX6A2 are only observed in the TFA extract, underscoring the benefit of complimentary extractions method to broaden global proteome analysis. Overall, minimal protein overlap was observed between the HEPES, TFA, and Azo extracts and only 14 % of identified proteins detected in multiple extracts

(Figure 5.3D). It is important to note that Azo alone has been shown to effectively solubilize the whole proteome in a single-step extraction previously.<sup>321,322</sup> However, by reducing sample complexity prior to 2DLC-MS analysis and enriching three distinct subproteomes, higher relative loading masses of each extracted proteoform are achieved, leading to greater potential for detection of a given proteoform than what is possible by a one-step extraction.

Subcellular gene ontology analysis was performed on proteins identified in each extract separately to assess the contribution of each extract to proteome sampling (Figure 5.4). For GO terms which appeared in multiple extracts, the terms with the ten highest -log<sub>10</sub> FDR values were plotted (Figure 5.4A). While several GO subcellular localizations terms including "sarcomere", "cytosol", and "cytochrome complex" appear to be best accessed through one of the three extracts, other terms initially appear to be caused by overlap of protein identifications between extracts and display similar -log<sub>10</sub> FDR values. Despite these shared GO terms, the majority of protein IDs for a given GO term are unique to a single extract (Figure 5.89), and comparison of protein encoding genes identified in one extract for a given GO term most often compliment genes in other extracts of the same term (Table 5.S1). Examining subcellular GO terms that are unique to a single extract further supports the complimentary nature of this method (Figure 5.4B), showing that each extract provides a unique view of the proteome for global top-down analysis.

Accessing Subproteome Sections by Global Top-Down Proteomics

Integration of data from all extracts can provide a more holistic view of the proteome by assessing the subproteomes of specific organelle within the broader context of the global proteome. The mitochondrial subproteome is of considerable interest due to its role in cellular metabolism<sup>323</sup> and the interplay between the mitochondria and other subproteomes such as the actin cytoskeleton<sup>324</sup> and nucleosome<sup>325,326</sup>. Compiling the results of a three-step extraction analyzed by

online top-down 2D sSEC-RPLC-MS revealed 37 unique proteins detected from mitochondria (Figure 5.5). Cellular component GO analysis showed effective sampling of mitochondrial envelope proteins (Figure 5.5A), mitochondrial matrix proteins (Figure 5.5B), and mitochondrial membrane proteins (Figure 5.5C). The power of top-down proteomics allows detection of multiple proteoforms based on MS1 mass shift (Figure 5.5A-C), confirming results and localizing modifications at the MS2 level (Figure 5.5D-F). This enabled detection and localization of mitochondrial cytochrome c oxidase subunit 8A (COX8A) methylation for the first time, and sitespecific localization to C47 (or C22 after mitochondrial transit peptide removal), part of the membrane embedded region of COX8A.<sup>320</sup> For mitochondrial matrix proteins 2,4-dienoyl-CoA reductase (DECR1) and malate dehydrogenase (MDH2), possible succinvlation is observed at the MS1 level (Figure 5.5B), but cannot be confirmed by MS2 analysis (Figure 5.5E, 5.S10). Topdown analysis of the mitochondrial membrane proteins cytochrome c oxidase subunit 6A2 (COX6A2) revealed two possible oxidation events (Figure 5.5C) and localized oxidation between L53 and N87 (Figure 5.5F), a part of the mitochondrial intermembrane region (H50 to P97). This subunit has been shown to be a critical regulator of oxidative stress<sup>327,328</sup> and deficiency can even lead to cardiac remodeling.<sup>329</sup>

Shifting the focus to another critical subproteome, the nucleosome, began to reveal the complex combinatorial modifications of histones (Figure 5.6). The nucleosome is extracted only in the Azo extract, but the is well represented in this dataset (Figure 5.6A). Example top-down analyses of three histones proteoform families demonstrate the challenges associated with these proteins in a non-targeted top-down proteomics analysis (Figure 5.6B-D). The protein distribution of H2B1C overlaps with H2B1N in the mass spectral domain, and multiple possible sites for modifications in close proximity hinder site-specific localization (Figure 5.6B). Despite these

challenges, a previously unreported methylation in the N-terminal region was detected and localized to the region between K5 and K20. While H2AC2 appeared to show a lower number of potential proteoforms, combinatorial modifications and limited fragmentation still challenged localization of a detected phosphorylation even beyond two previously reported sites (Figure 5.6C). Similar to the other two examples, histone H4 MS1 spectra revealed a number of unidentified peaks (Figure 5.6D). While some putative identifications of complex histone proteoforms are possible in this discovery-based approach, using a discovery approach to identify possible targets for further top-down analysis can provide the greatest potential to localize and further characterize these modifications.

### **Conclusions**

Here, we have broadened global coverage of the proteome by top-down proteomics through a combined three-step extraction and online top-down 2D sSEC-RPLC-MS. The developed approach enables future top-down proteomics disease studies, and the automated online 2D approach is compatible with large-scale analyses. When combined with online 2D sSEC-RPLC-MS, the three-step sequential extraction enabled sampling of multiple subproteomes, offering great potential to assess the interplay in proteoform changes between various cellular components. While global top-down is still challenged by the detection and fragmentation of large proteoforms, this approach provides a firm foundation for improved front-end separations as MS capabilities continue to increase.

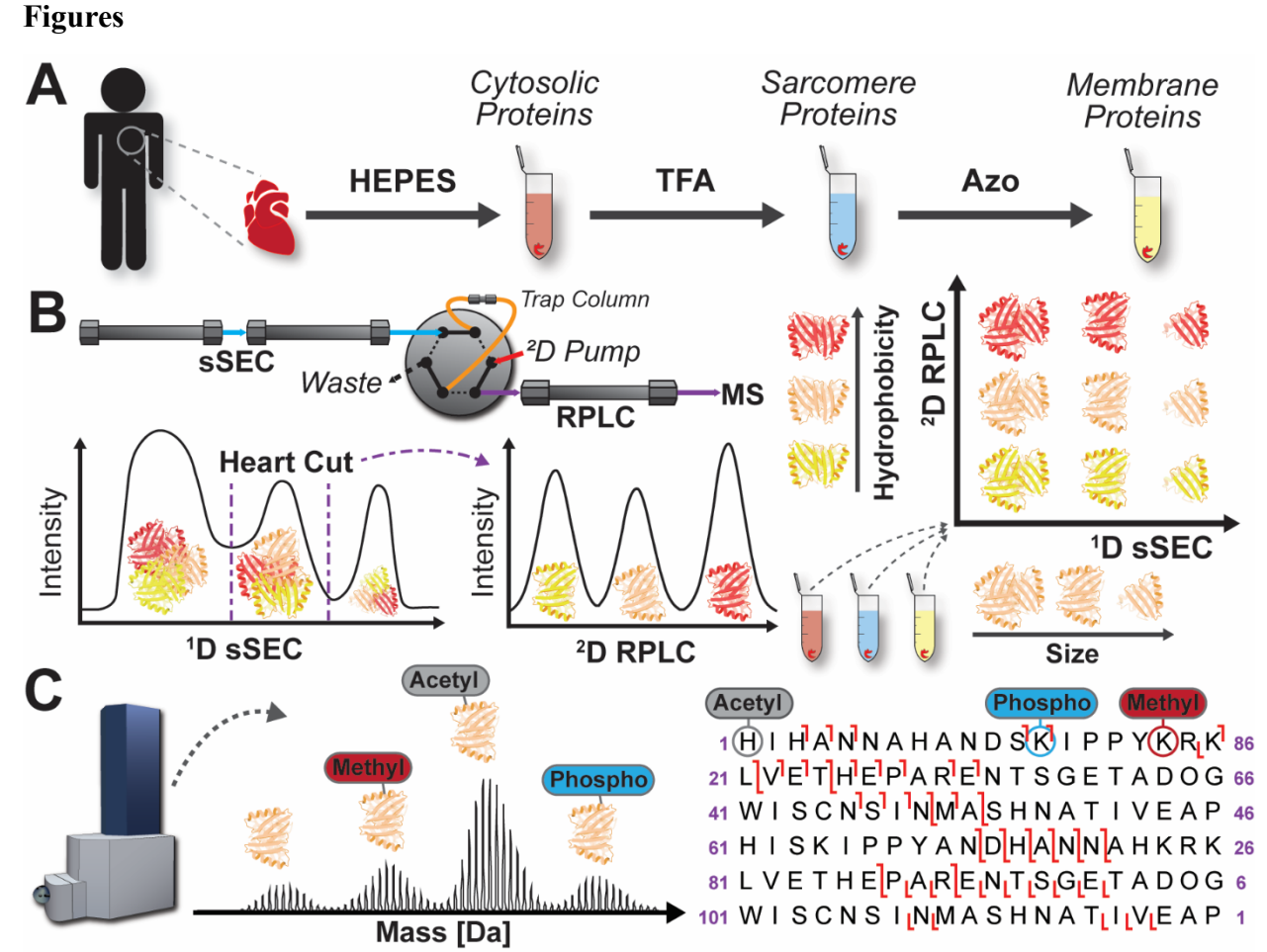


**Figure 5.1.** Expansion of global top-down proteomics coverage through a combined sequential extraction approach and online 2D sSEC-RPLC-MS. A three-step sequential extraction allowed cytosolic, sarcomeric, and membrane proteins to be enriched in three separate sample fractions to reduce sample complexity (A). Online 2D sSEC-RPLC-MS separated proteins by size then hydrophobicity to further reduce sample complexity and facilitate detection of low-abundance proteins and large proteins by improved chromatographic performance relative to 1DLC (B). Online top-down analysis enabled detection of proteins and proteoforms and provided a "bird'seye-view" of the proteoform landscape (C).

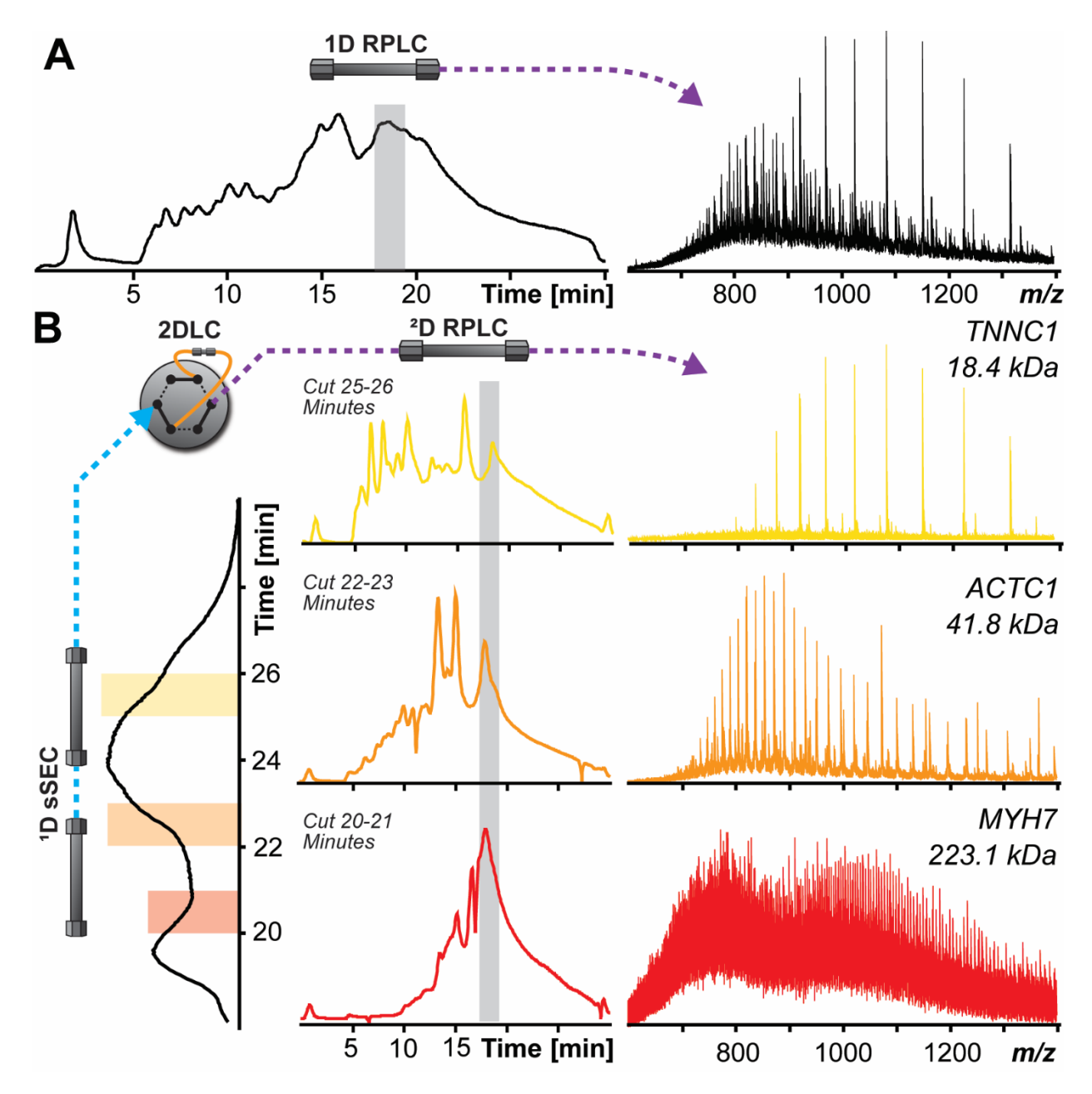


**Figure 5.2.** Benefits of an online 2DLC approach coupling sSEC and RPLC. For a traditional 1D RPLC-MS analysis of the TFA extract, only the small, abundance MLC-V2 is observed at a retention time of 18 to 19 minutes (A). The use of online 2D sSEC-RPLC reveals that within the 18 to 19 minute RPLC retention window two larger proteins also coelute, but are separable in the sSEC dimension of separation (B).

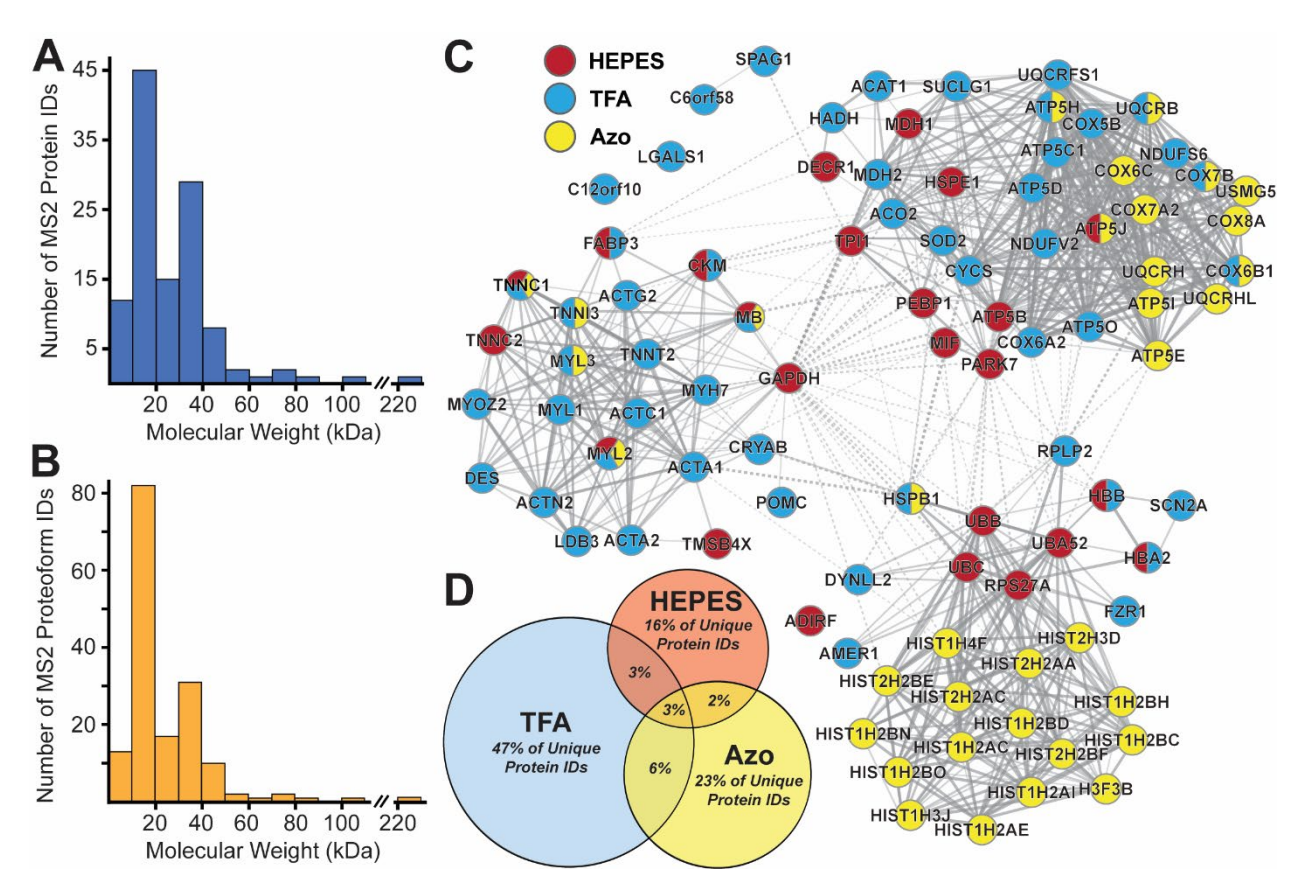


**Figure 5.3.** Detected proteins across all portions of the three-step sequential extraction. (A) when compared to the number of MS2 IDs binned by molecular weight (B). A string network of genes encoding the MS2 identified proteins shows the complimentary nature of sequential extraction (C). Each extract represents a unique portion of the proteome with minimal overlap of IDs (D).

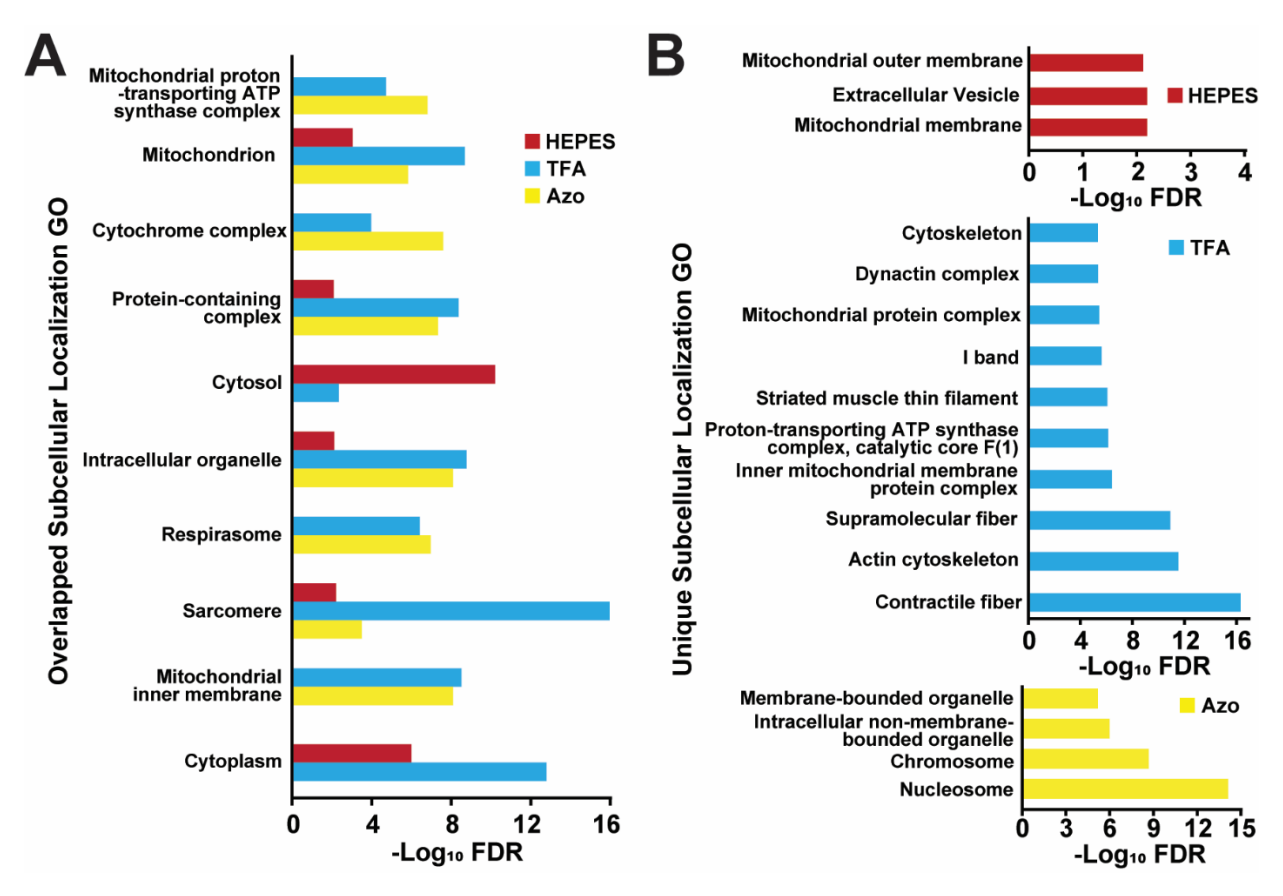


**Figure 5.4.** Comparison of subcellular localization GO terms observed in each extract. For GO terms observed in multiple extract fractions, the ten terms with the highest -Log<sub>10</sub> FDR values (when averaged for all extracts in which the term was detected) are reported (A). These results show that while specific subcellular localizations can be sampled by multiple extracts, specific extracts sample distinct subcellular regions more effectively than others. Analysis of subcellular localization GO terms observed in only one extract further underscores the complementary nature of each extract to access unique portions of the proteome (B).

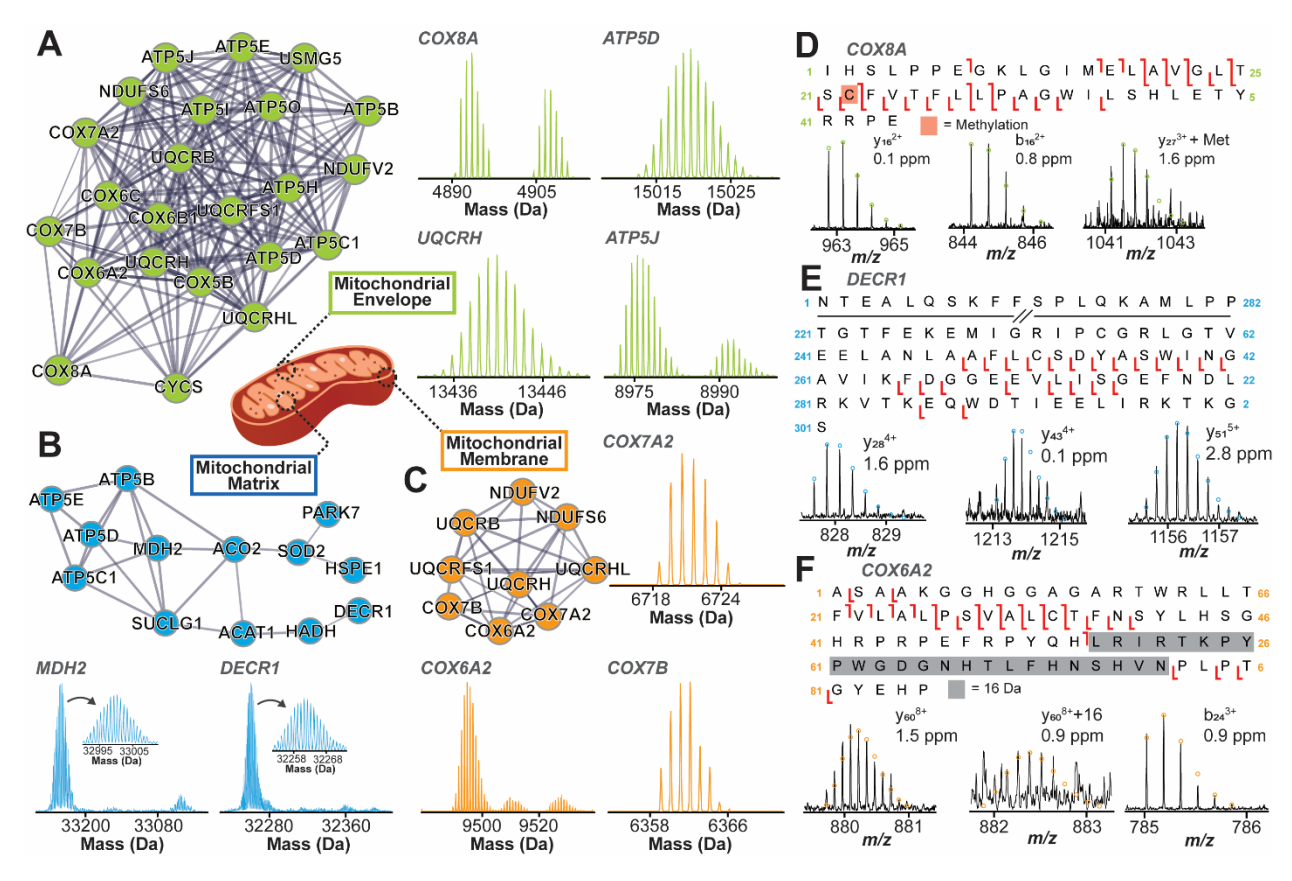


**Figure 5.5.** Mitochondrial protein IDs mapped by cellular component GO analysis. Detection of mitochondrial envelope proteins (A), mitochondrial matrix proteins (B), and mitochondrial membrane proteins (C) are enabled by the sequential extraction, which solubilizes proteins with a broader range of physiological properties than traditional single extraction approaches. Online 2DLC also facilitates detection of low abundance modifications and novel modifications (D-F) when combined with top-down proteomics.

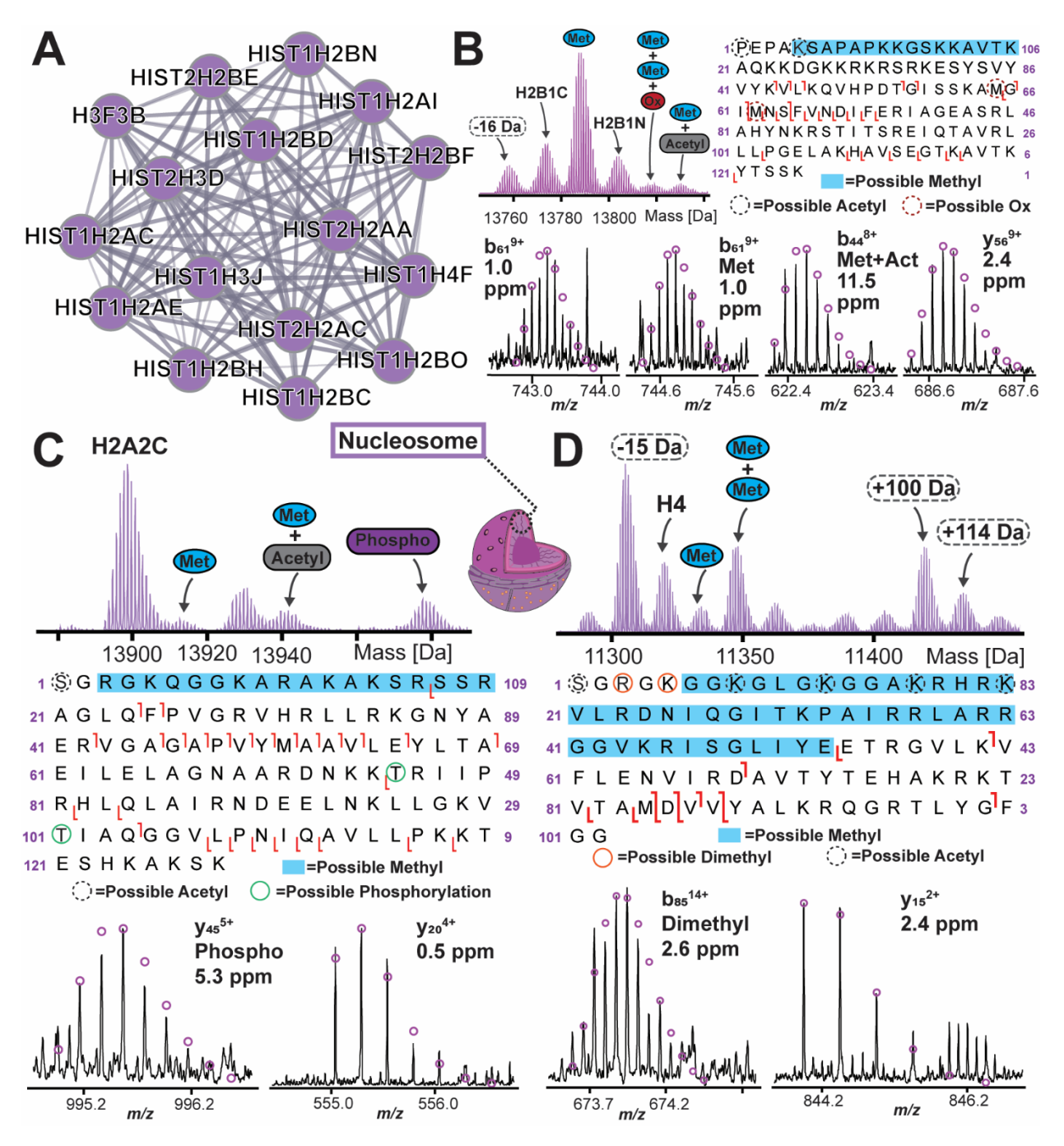


**Figure 5.6.** Map of detected nucleosome components by cellular component GO (A). The developed method enabled detection of previously unreported methylation to the N terminal region of H2B1C (B), localized phosphorylation on H2A2C to confirm previously detected results (C) and provides a critical bird's-eye-view of histone H4 and the complexity of associated proteoforms (D).

# **Supplementary Information for**

# **Chapter 5**

# Expanding Global Top-Down Proteomics Coverage by Sequential Protein Extraction and Online Two-Dimensional Liquid Chromatography

<u>Table of Contents</u> <u>Pages</u>
Figure 5.S1 Triplicate top-down 1D SEC-MS analysis of 8-protein standard mixture165
Figure 5.S2 Triplicate top-down 1D RPLC-MS analysis of 8-protein standard mixture166
Figure 5.S3 Online top-down 2D sSEC-RPLC-MS analysis of 8-protein standard mixture167
Figure 5.S4 MS1 spectra of 8-protein standard mixture generated by 1D RPLC-MS and online 2D sSEC-RPLC-MS
Figure 5.S5 Comparison of theoretical peak capacities from 1D RPLC-MS and online 2D sSEC-RPLC-MS
Figure 5.S6 Top-down 1D sSEC-MS analysis of TFA extract from human heart tissue170
Figure 5.S7 Comparison of CID fragmentation performance between 1D-RPLC-MS and 2D sSEC-RPLC-MS analysis of MLC-V2
Figure 5.S8 Histogram of all MS1 features observed in at least one extraction step binned by molecular weight
Figure 5.S9 Overlap of subcellular GO term proteins identified between extracts
Figure 5.S10 Fragmentation of MDH2 by CID using online top-down 2D sSEC-RPLC-MS174
Table 5.ST1 Subcellular GO terms observed across extracts with gene counts and -log <sub>10</sub> FDR175

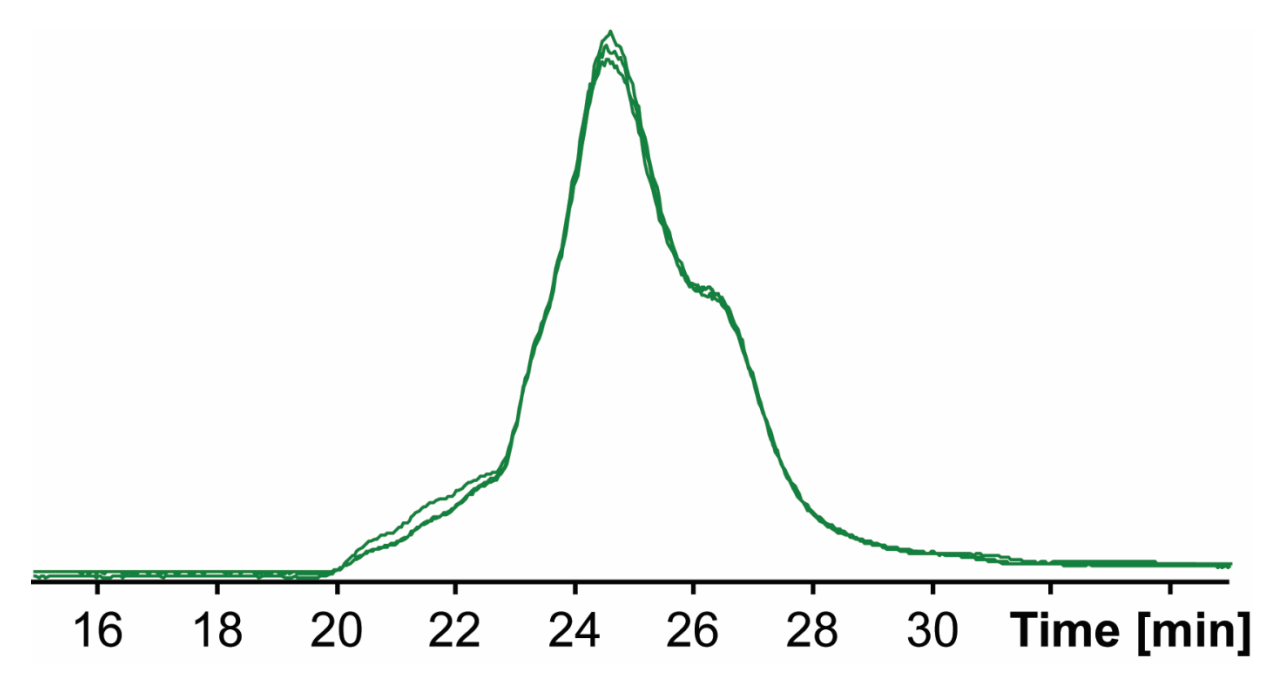


**Figure 5.S1.** 1D sSEC-MS analysis of eight protein standard mixture with equal mass loading of Apr, Lys, Myo, CA, Ova, ADH, BSA, and Thy. Overlay of three total ion chromatograms (TICs) of injection replicates shows excellent reproducibility.

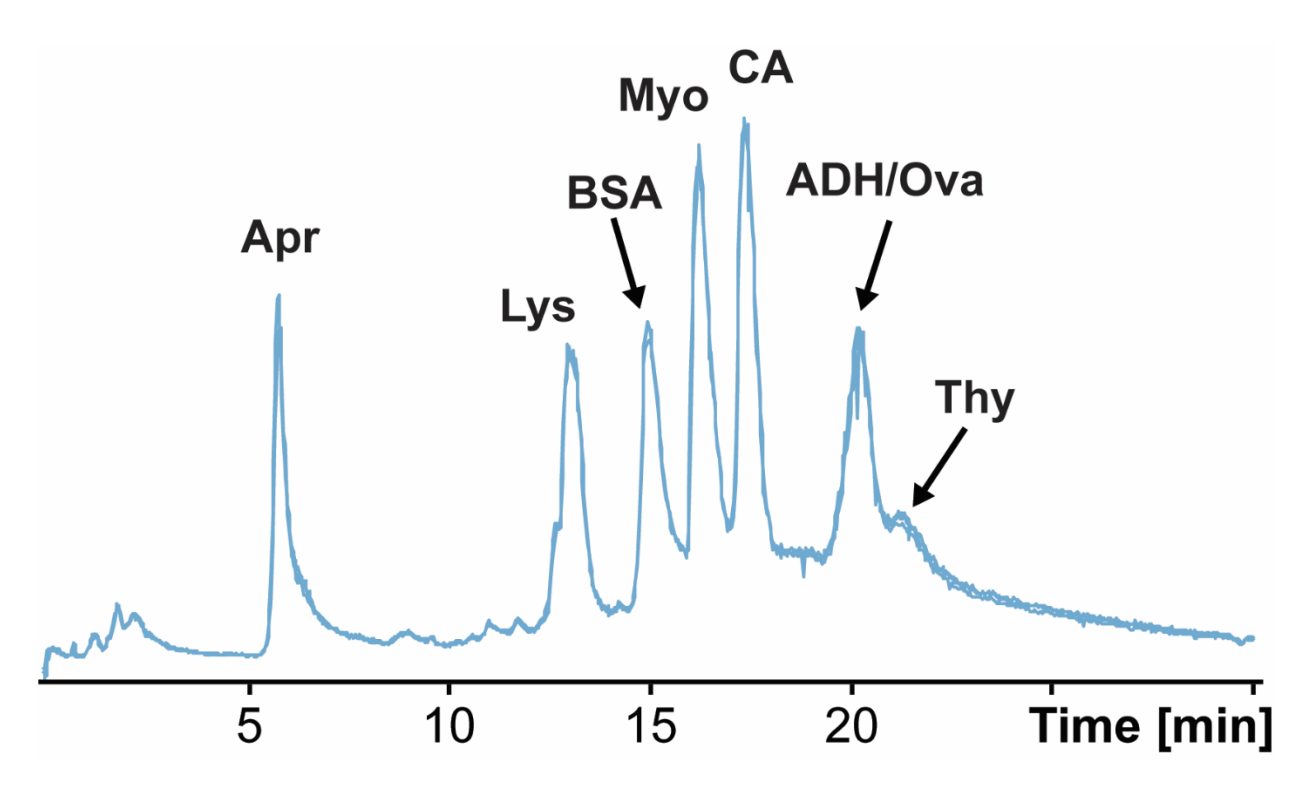


**Figure 5.S2.**1D RPLC-MS analysis of eight protein standard mixture with equal mass loading of Apr, Lys, Myo, CA, Ova, ADH, BSA, and Thy. Overlay of three TICs of injection replicates shows excellent reproducibility.

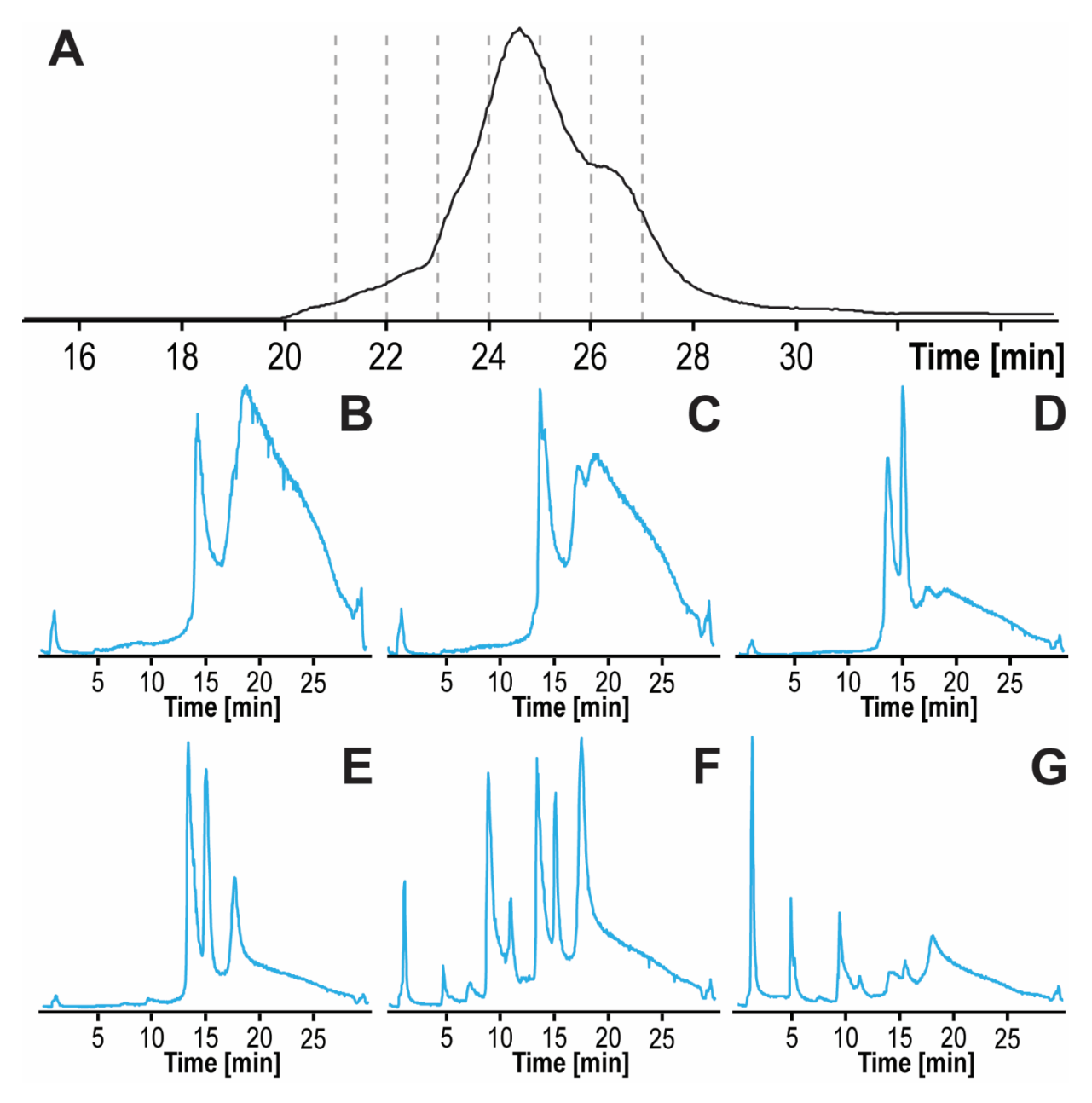


**Figure 5.S3.** Online 2D sSEC-RPLC-MS analysis of eight protein standard mixture with equal mass loading of Apr, Lys, Myo, CA, Ova, ADH, BSA, and Thy. The first dimension (<sup>1</sup>D) sSEC elution window, shown by the TIC (A) is sampled in one-minute windows for second dimension (<sup>2</sup>D) RPLC analysis. TICs of <sup>2</sup>D RPLC analysis show changes in the chromatographic profile moving from early cuts to later cuts. Cuts from 21-22 minutes (B), 22-23 minutes (C), 23-24 minutes (D), 24-25 minutes (E), 25-26 minutes (F), and 26-27 minutes (G) of sSEC elution time are shown.

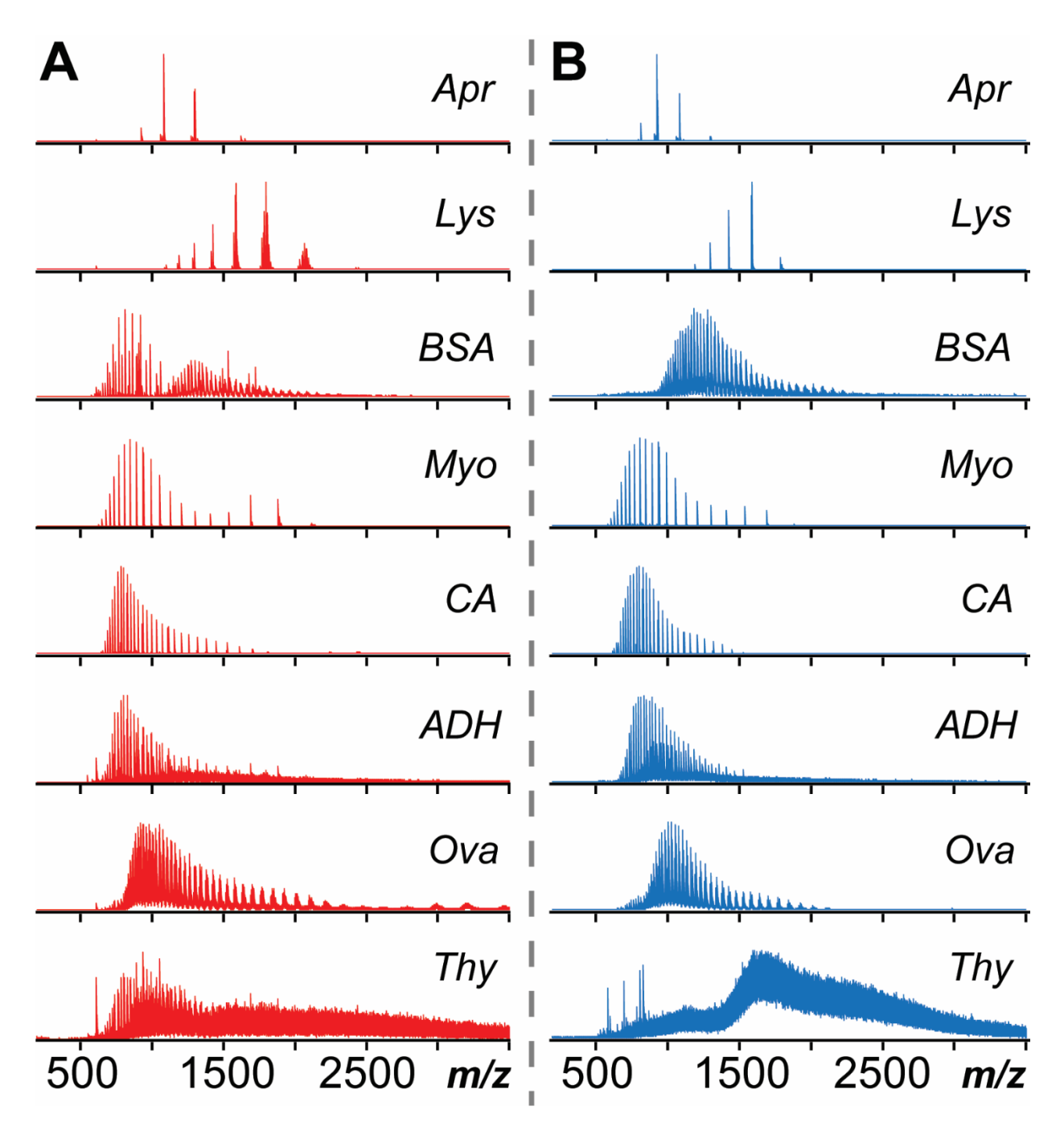


**Figure 5.S4.** MS1 spectra of the eight protein standard mixture generated by 1D RPLC-MS (A) and 2D sSEC-RPLC-MS (B). The 2D method eliminates coelution of standards, facilitating better MS1 detection.

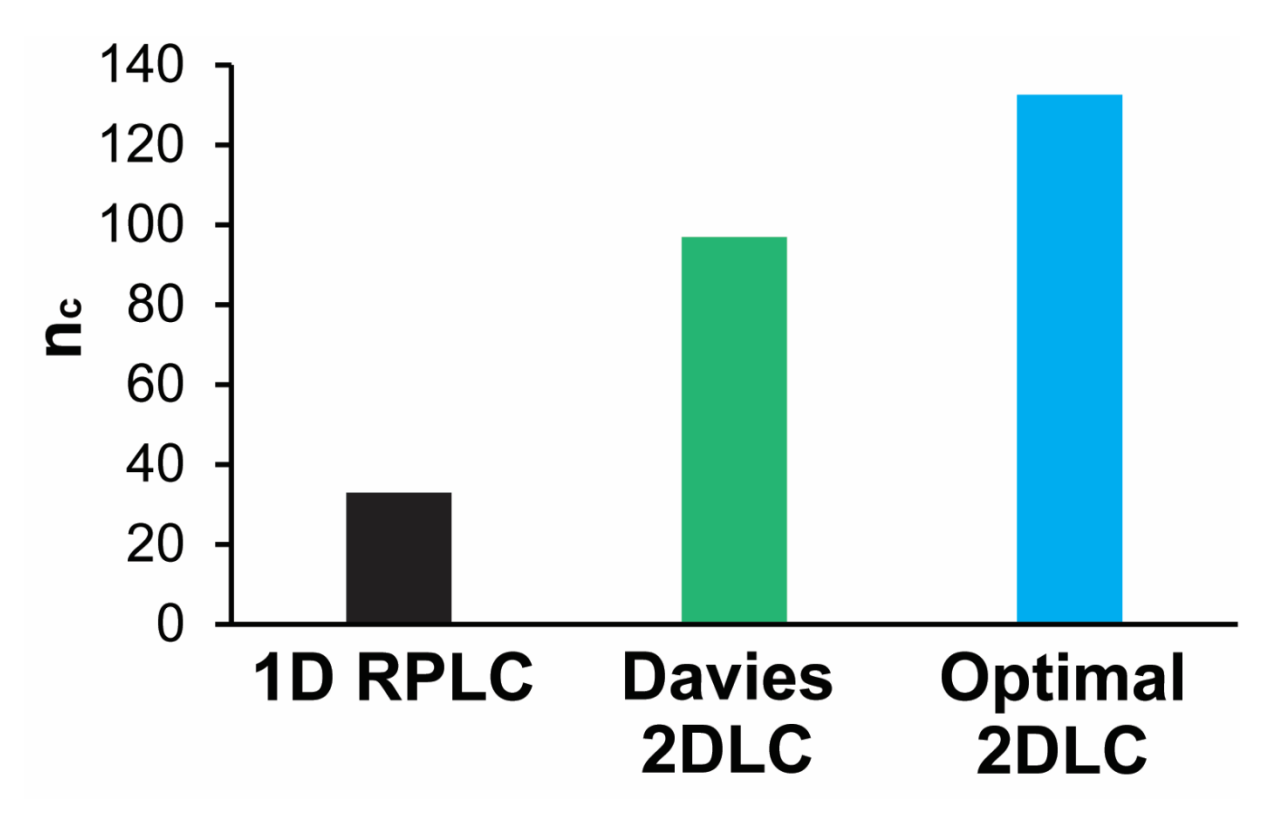


**Figure 5.S5.** Comparison of theoretical peak capacity ( $n_c$ ) observed for 1D and 2DLC methods, with both the suboptimal (Davies) and optimal 2D  $n_c$  reported. Even under suboptimal conditions, the  $n_c$  for 2DLC increases relative to 1DLC by ~300%. Optimal 2DLC conditions represent a four-fold increase in separation performance over a traditional 1D RPLC approach.

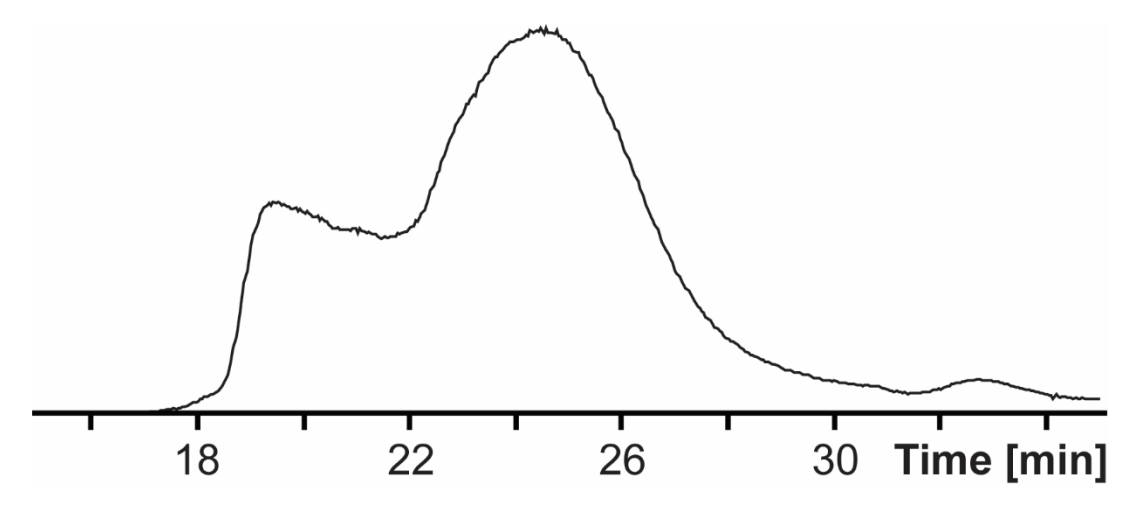


**Figure 5.S6.** 1D sSEC-MS analysis of TFA extract from human heart tissue. sSEC can separate proteins by size, but no proteins are chromatographically resolved by sSEC alone.

#### 1D RPLC-MS2

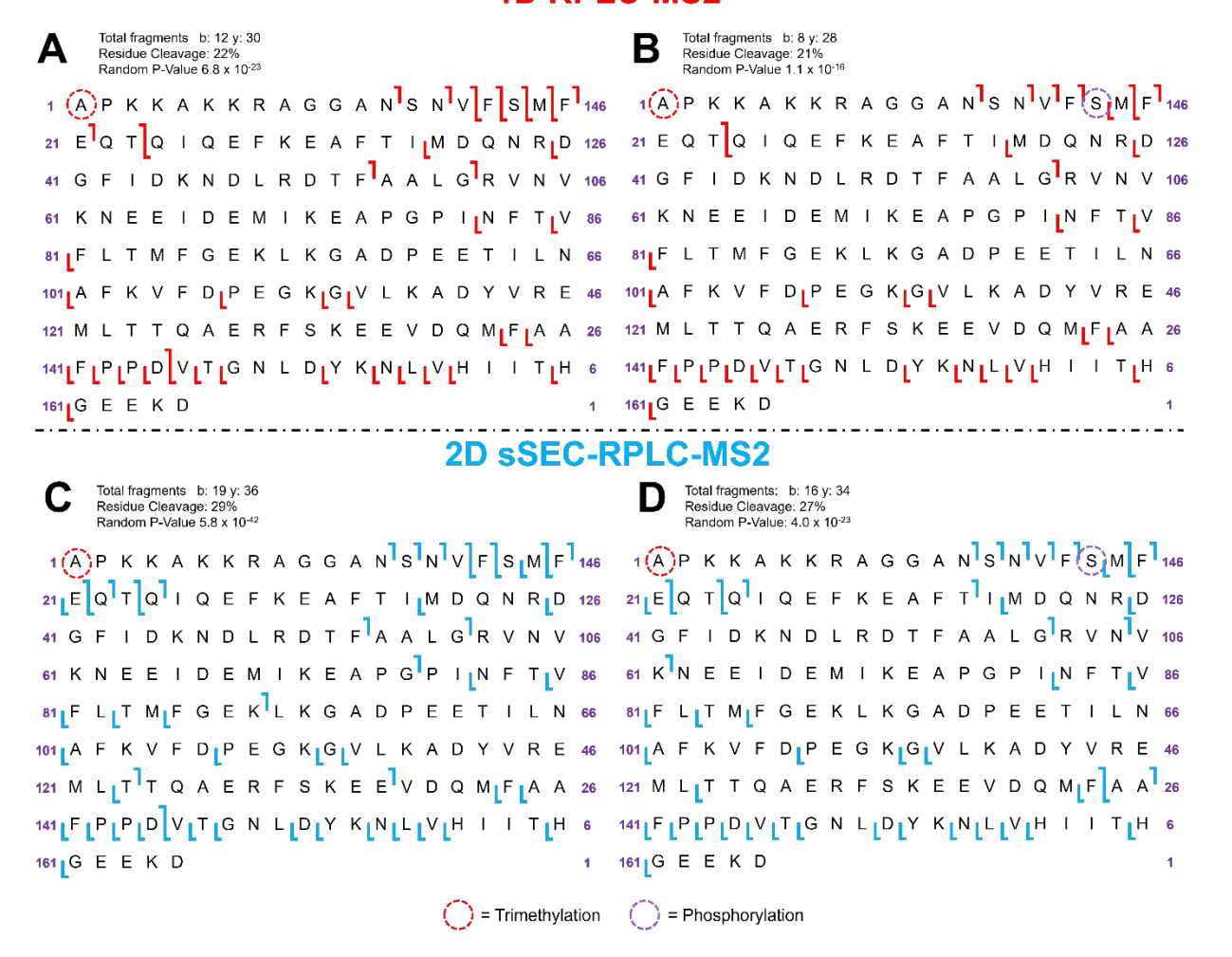


**Figure 5.S7.** Fragmentation of myosin light chain ventricular isoform 2 (MLC-V2) by autoMSMS with online 1D RPLC-MS2 separation (A, B) and online 2D sSEC-RPLC-MS2 (C, D). The most abundant proteoform (N-terminal methionine excision followed by alanine acetylation) (A, C) shows greater sequence coverage than the phosphorylated proteoform (B, D). The 2D approach removes co-eluting features, increasing sequence coverage by 32% relative to 1D sequence coverage for the unphosphorylated proteoform and 28% relative to the phosphorylated proteoform.

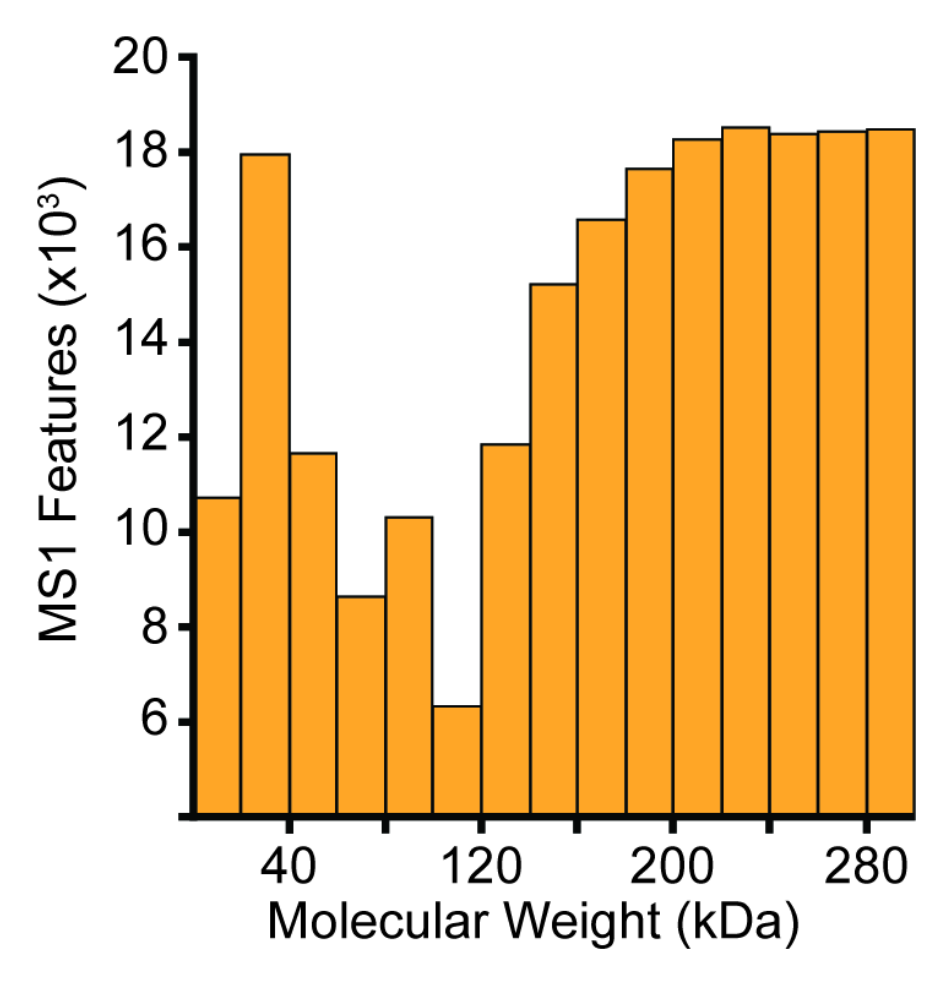


**Figure 5.S8.** Histogram of all MS1 features from 2,000 to 300,000 kDa detected by MaxEnt deconvolution. Peaks below 50 kDa were deconvoluted at 80,000 resolving power and peak picked by SNAP. Peaks above 50 kDa were deconvoluted at 10,000 resolving power and peak picked by SumPeak. The number of observed MS1 features shows the large number of features that are not selected for MS2 analysis or are not adequately fragmented. Additionally, these results underscore the challenges associated with deconvolution artifacts that are present in MS1 level features as size increases.

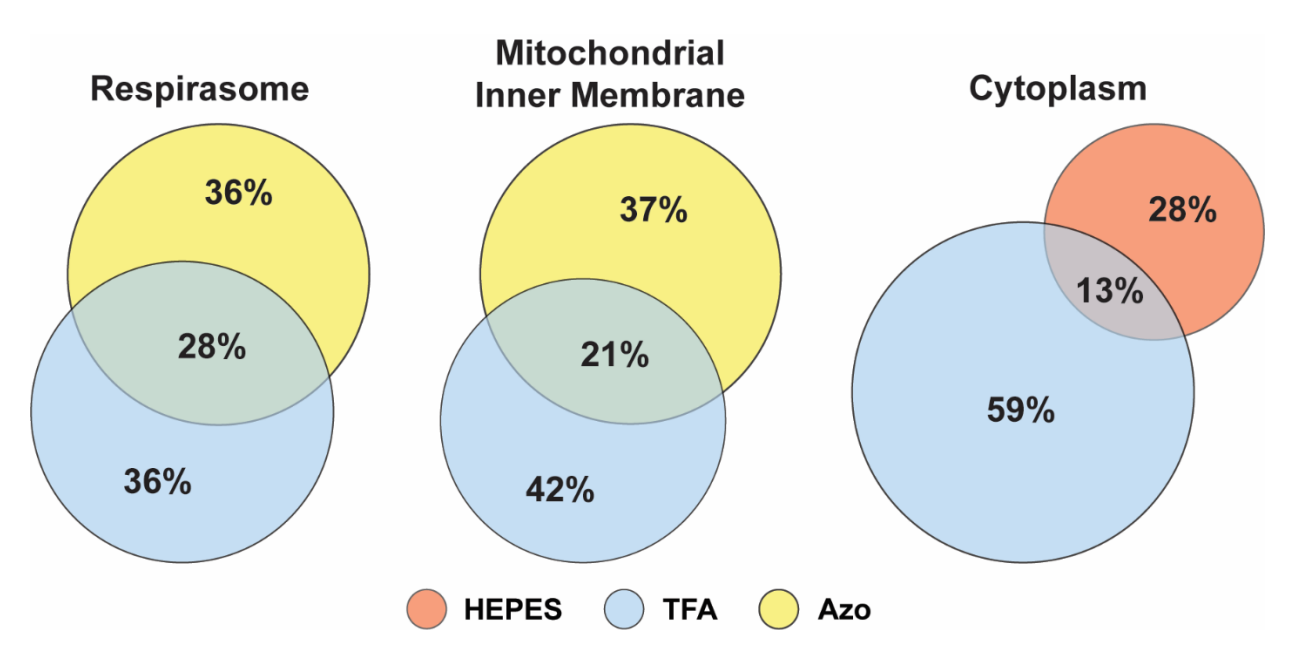


**Figure 5.S9.** Overlap of proteins identified for select subcellular localization gene ontology (GO) terms between extracts. Despite similar -log<sub>10</sub> FDR values generated in by GO analysis of individual extracts, each extract offers orthogonal sampling of the proteome.

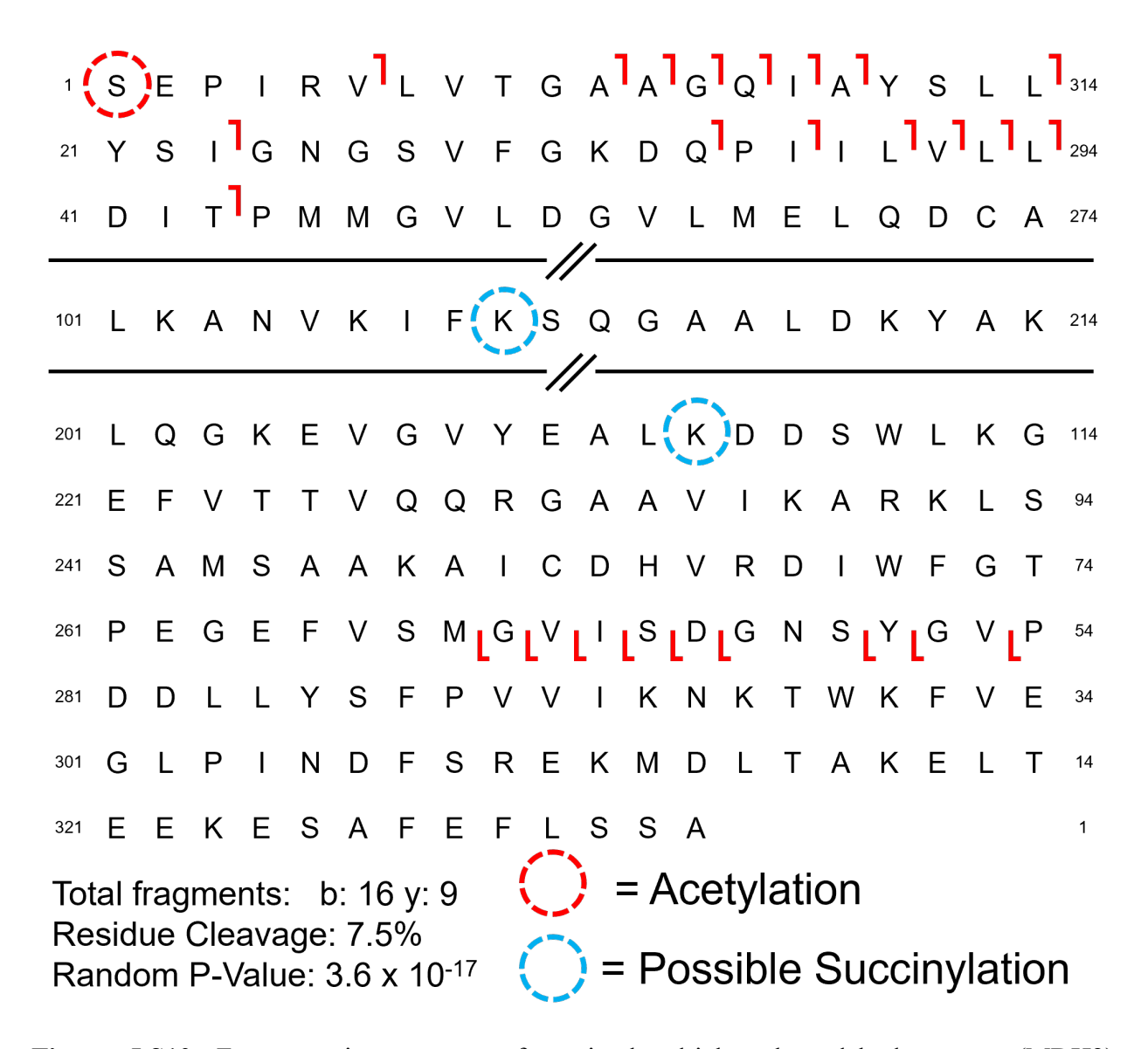


**Figure 5.S10.** Fragmentation coverage for mitochondrial malate dehydrogenase (MDH2). Identification of N-terminal methionine excision and acetylation was possible, and succinylation was not detected at two known sites near the N and C termini, indicating that possible succinylation events could occur in the core of the protein.

**Table 5.ST1.** Subcellular gene ontology terms observed in each extract, with gene counts,  $-log_{10}$  FDR and gene names specified.

Subcellular GO Term	Extract	Observed Gene Count	Background Gene Count	-log <sub>10</sub> FDR	Genes
Cellular anatomical entity	HEPES	27	13853	2.1	MIF,DECR1,CKM, MYL2,GAPDH,TPI1, TNNC1,HSPE1,HBA2, PEBP1,ATP5B, C12orf10,RPS27A, UBB,HBB,ADIRF, TNNC2,FABP3,SCN2A, TMSB4X,SPAG1,MB, UBA52,ATP5J,PARK7, MDH1,UBC
	TFA	48	13853	5.3	ATP5D,LGALS1,ACO2, CKM,MYL2,TNNC1, TNNT2,ATP5E,COX6B1, HSPB1,HBA2,COX5B, ACAT1,C12orf10,NDUFS6, ATP5O,ACTC1,UQCRFS1, MYOZ2,MYL1,CYCS, MDH2,NDUFV2,C6orf58, AMER1,HBB,TNNI3, MYH7,ATP5C1,ACTA1, FABP3,DES,SCN2A, SUCLG1,FZR1,MYL3, MB,POMC,ACTG2, LDB3,ACTA2,COX7B, UQCRB,CRYAB,ACTN2, SOD2,HADH,DYNLL2
Creatine kinase complex	HEPES	2	7	2.1	CKM,MB
	TFA	2	7	2.1	CKM,MB
Cytochrome complex	TFA	4	31	4.0	COX6B1,UQCRFS1, COX7B,UQCRB
	Azo	6	31	7.6	COX6B1,COX6A2,UQCRH, COX8A,COX7B,UQCRB
Cytoplasm	HEPES	26	7871	6.0	MIF,DECR1,CKM, MYL2,GAPDH,TPI1, TNNC1,HSPE1,HBA2, PEBP1,ATP5B,C12orf10, RPS27A,UBB,HBB, ADIRF,TNNC2,FABP3, TMSB4X,SPAG1,MB, UBA52,ATP5J,PARK7, MDH1,UBC
	TFA	46	7871	12.8	ATP5D,LGALS1,ACO2, CKM,MYL2,TNNC1,

	1			T	
					TNNT2,ATP5E,COX6B1,
					HSPB1,HBA2,COX5B,
					ACAT1,C12orf10,NDUFS6,
					ATP5O,ACTC1,UQCRFS1,
					MYOZ2,MYL1,CYCS,
					MDH2,NDUFV2,AMER1,
					HBB,TNNI3,MYH7,
					ATP5C1,ACTA1,FABP3,
					DES,SUCLG1,FZR1,
					MYL3,MB,POMC,
					ACTG2,LDB3,ACTA2,
					COX7B,UQCRB,CRYAB,
					ACTN2,SOD2,HADH,
					DYNLL2
Cytosol	HEPES	22	2919	10.2	MIF,CKM,MYL2,
					GAPDH,TPI1,
					TNNC1,HSPE1,HBA2,
					PEBP1,RPS27A,UBB,
					HBB,ADIRF,TNNC2,
					FABP3,TMSB4X,SPAG1,
					MB,UBA52,PARK7,
					MDH1,UBC
	TFA	18	2919	2.3	CKM,MYL2,TNNC1,
					TNNT2,HSPB1,HBA2,
					ACTC1,MYL1,CYCS,
					HBB,ACTA1,FABP3,
					MYL3,MB,ACTG2,
					ACTA2,ACTN2,DYNLL2
Extracellular	TFA	11	985	3.0	HSPB1,HBA2,ACTC1,
space					C6orf58,HBB,ACTA1,
					MB,POMC,ACTG2,
					ACTA2,SOD2
Hemoglobin	HEPES	3	22	2.6	HBA2,HBB,MB
complex					
	TFA	3	22	2.9	HBA2,HBB,MB
Intracellular	HEPES	23	9242	2.1	MIF,DECR1,CKM,
organelle					MYL2,GAPDH,TPI1,
					TNNC1,HSPE1,HBA2,
					ATP5B,C12orf10,
					RPS27A,UBB,HBB,
					ADIRF,TNNC2,TMSB4X,
					MB,UBA52,ATP5J,PARK7,
					MDH1,UBC
	TFA	45	9242	8.8	ATP5D,LGALS1,ACO2,
					CKM,MYL2,TNNC1,
					TNNT2,ATP5E,COX6B1,
					HSPB1,HBA2,COX5B,
					ACAT1,C12orf10,
					NDUFS6,ATP5O,ACTC1,
					UQCRFS1,MYOZ2,MYL1,

	T			1	CVCC MDII2 NDI IEV2
					CYCS,MDH2,NDUFV2, AMER1,HBB,TNNI3,
					MYH7,ATP5C1,ACTA1,
					DES,SUCLG1,FZR1,MYL3,
					MB,POMC,ACTG2,LDB3,
					ACTA2,COX7B,UQCRB,
					CRYAB,ACTN2,SOD2,
					HADH,DYNLL2
	Azo	37	9242	8.1	MYL2,TNNC1,ATP5E,
					HIST1H4F,COX6B1,
					H3F3B,C12orf10,COX6A2,
					HIST1H2BD,ATP5H,
					HIST1H2AE,ATP5I,
					UQCRH,COX8A,
					HIST1H2BC,RPLP2,
					HIST2H2AC,HIST2H3D,
					TNNI3,HIST1H2AI,
					HIST1H3J,HIST2H2BE,
					HIST2H2AA,USMG5,
					COX7A2,HIST1H2AC,
					MYL3,MB,ATP5J,
					COX7B,COX6C,UQCRB,
					CRYAB,HIST2H2BF,
					HIST1H2BO,HIST1H2BH,
					HIST1H2BN
Membrane	TFA	12	1321	2.5	ATP5D,ATP5E,COX6B1,
protein complex					NDUFS6,ATP5O,UQCRFS1,
					CYCS,NDUFV2,ATP5C1,
					SCN2A,COX7B,UQCRB
	Azo	11	1321	2.7	ATP5E,COX6B1,COX6A2,
	1120		1321	2.,	ATP5H,ATP5I,UQCRH,
					COX8A,USMG5,ATP5J,
					COX7B,UQCRB
Mitochondrial	TFA	12	314	8.5	ATP5D,ATP5E,COX6B1,
inner membrane	1111	12		0.5	COX5B,NDUFS6,ATP5O,
miner inclinoranc					UQCRFS1,CYCS,NDUFV2,
					ATP5C1,COX7B,UQCRB
	Azo	11	314	8.1	ATP5E,COX6B1,ATP5H,
	AZU	11	317	0.1	ATP5I,UQCRH,COX8A,
					USMG5,ATP5J,COX7B,
					COX6C,UQCRB
Mitochondrial	TFA	4	20	4.7	ATP5D,ATP5E,ATP5O,
proton-	IFA	<b>+</b>	20	4./	ATP5D,ATP5E,ATP5O,
-					AIPSCI
transporting					
ATP synthase					
complex		5	20	6.7	ATDSE ATDSU ATDS
	Azo	5	20	6.7	ATP5E,ATP5H,ATP5I,
			1110	2.6	USMG5,ATP5J
Mitochondrion	HEPES	10	1149	3.0	DECR1,HSPE1,ATP5B,
Î.	1	1	I	ĺ	C12orf10,RPS27A,UBB,

					UBA52,ATP5J,PARK7,UBC
	TFA	19	1149	8.6	ATP5D,ACO2,ATP5E,
					COX6B1,COX5B,ACAT1,
					C12orf10,NDUFS6,ATP5O,
					UQCRFS1,CYCS,MDH2,
					NDUFV2,ATP5C1,SUCLG1,
					COX7B,UQCRB,SOD2,
					HADH
	Azo	14	1149	5.8	ATP5E,COX6B1,C12orf10,
					COX6A2,ATP5H,ATP5I,
					UQCRH,COX8A,USMG5,
					COX7A2,ATP5J,COX7B,
					COX6C,UQCRB
Organelle	HEPES	24	9848	2.2	MIF,DECR1,CKM,
					MYL2,GAPDH,TPI1,
					TNNC1,HSPE1,HBA2,
					ATP5B,C12orf10,RPS27A,
					UBB,HBB,ADIRF,
					TNNC2,FABP3,TMSB4X,
					MB,UBA52,ATP5J,
					PARK7,MDH1,UBC
	TFA	46	9848	8.8	ATP5D,LGALS1,ACO2,
					CKM,MYL2,TNNC1,
					TNNT2,ATP5E,COX6B1,
					HSPB1,HBA2,COX5B,
					ACAT1,C12orf10,NDUFS6,
					ATP5O,ACTC1,UQCRFS1,
					MYOZ2,MYL1,CYCS,
					MDH2,NDUFV2,AMER1,
					HBB,TNNI3,MYH7,
					ATP5C1,ACTA1,FABP3,
					DES,SUCLG1,FZR1,
					MYL3,MB,POMC,
					ACTG2,LDB3,ACTA2,
					COX7B,UOCRB,CRYAB,
					ACTN2,SOD2,HADH,
					DYNLL2
Organelle	HEPES	7	788	2.1	GAPDH,ATP5B,RPS27A,
envelope		'			UBB,UBA52,ATP5J,UBC
F -	TFA	13	788	5.4	ATP5D,ATP5E,COX6B1,
					COX5B,NDUFS6,ATP5O,
					UQCRFS1,CYCS,NDUFV2,
					ATP5C1,FZR1,COX7B,
					UQCRB
Protein-	HEPES	17	5142	2.1	DECR1,CKM,MYL2,
containing	22				GAPDH,TPI1,TNNC1,
complex					HSPE1,HBA2,ATP5B,
<u>r</u>					RPS27A,HBB,TNNC2,
					SCN2A,MB,UBA52,
					ATP5J,UBC
		i			1111 33,000

	TFA	35	5142	8.4	ATP5D,LGALS1,CKM,
	1171	33	3172	0.4	MYL2,TNNC1,TNNT2,
					ATP5E,COX6B1,HSPB1,
					HBA2,NDUFS6,ATP5O,
					, , , , , , , , , , , , , , , , , , , ,
					ACTC1,UQCRFS1,MYL1,
					CYCS,NDUFV2,HBB,
					TNNI3,MYH7,ATP5C1,
					ACTA1,DES,SCN2A,
					SUCLG1,MYL3,MB,
					ACTG2,LDB3,ACTA2,
					COX7B,UQCRB,CRYAB,
					SOD2,DYNLL2
	Azo	29	5142	7.3	MYL2,TNNC1,ATP5E,
					HIST1H4F,COX6B1,H3F3B,
					COX6A2,ATP5H,ATP5I,
					UQCRH,COX8A,HIST1H2B,
					RPLP2,HIST2H2AC,
					HIST2H3D,TNNI3,
					HIST1H3J,HIST2H2BE,
					HIST2H2AA,USMG5,
					MYL3,MB,ATP5J,
					COX7B,UQCRB,CRYAB,
					HIST1H2BO,HIST1H2BH,
ъ :	TEE A	7	0.0		HIST1H2BN
Respirasome	TFA	7	88	6.4	COX6B1,NDUFS6,
					UQCRFS1,CYCS,NDUFV2,
					COX7B,UQCRB
	Azo			6.9	COX6B1,COX6A2,UQCRH,
					COX8A,COX7A2,COX7B,
		7	88		UQCRB
Respiratory	TFA	6	78	5.4	COX6B1,NDUFS6,UQCRFS,
chain complex					NDUFV2,COX7B,UQCRB
	Azo	6	78	5.8	
Respiratory	TFA	3	18	3.0	COX6B1,UQCRFS1,COX7B
chain complex					
IV					
	Azo	4	18	5.1	COX6B1,COX6A2,COX8A,
					COX7B
Sarcomere	HEPES	4	120	2.2	MYL2,TNNC1,TNNC2,MB
	TFA	14	120	16.0	MYL2,TNNC1,TNNT2,
					ACTC1,MYOZ2,MYL1,
					TNNI3,MYH7,ACTA1,
					DES,MYL3,MB,LDB3,
					ACTN2
	Azo	5	120	3.5	MYL2,TNNC1,TNNI3,
					MYL3,MB
Troponin	HEPES	3	13	3.0	TNNC1,TNNC2,MB
complex			-		,,
•	TFA	4	13	5.3	TNNC1,TNNT2,TNNI3,MB
	Azo	3	13	3.6	TNNC1,TNNI3,MB
	AZO	3	13	3.0	ININCI, ININIO, IVIB

		1.5	1255		LOW A TRANSMITTED
Actin	TFA	15	355		MYL2,TNNC1,TNNT2,
cytoskeleton					ACTC1,MYL1,TNNI3,
					MYH7,ACTA1,MYL3,
					MB,ACTG2,LDB3,
					ACTA2,ACTN2,DYNLL2
Actin filament	TFA	4	63	1.2	ACTC1,ACTA1,LDB3,
					ACTN2
Blood	TFA	5	116	1.4	HBA2,ACTC1,HBB,
microparticle					ACTA1,ACTG2
Cardiac	TFA	4	5	1.2	MYL2,TNNT2,TNNI3,DES
myofibril					, , , -,
Cardiac	TFA	3	7	2.5	TNNC1,TNNT2,TNNI3
Troponin	1171		,	2.3	
complex					
Contractile	TFA	15	145	2.2	MYL2,TNNC1,TNNT2,
fiber	IIA	13	143	2.2	ACTC1,MYOZ2,MYL1,
11001					TNNI3,MYH7,ACTA1,
					DES,MYL3,MB,LDB3,
C + 1 1 +	TEL A	1.7	1526	1.6	ACTA2,ACTN2
Cytoskeleton	TFA	17	1526	1.6	MYL2,TNNC1,TNNT2,
					HSPB1,ACTC1,MYL1,
					TNNI3,MYH7,ACTA1,
					DES,MYL3,MB,
					ACTG2,LDB3,ACTA2,
					ACTN2,DYNLL2
Dynactin	TFA	4	12	0.7	ACTC1,ACTA1,
complex					ACTG2,ACTA2
I band	TFA	6	68	2.1	ACTC1,MYOZ2,DES,
					MYL3,LDB3,ACTN2
Inner	TFA	8	143	1.6	ATP5D,ATP5E,NDUFS6,
mitochondrial					ATP5O,UQCRFS1,NDUFV2,
membrane					ATP5C1,UQCRB
protein complex					
Intracellular	TFA	19	3196	1.4	MYL2,TNNC1,TNNT2,
non-membrane-	1171		3170	1	HSPB1,HBA2,ACTC1,
bounded					MYOZ2,MYL1,TNNI3,
organelle					MYH7,ACTA1,DES,MYL3,
organiciic					MB,ACTG2,LDB3,
					, , , , , , , , , , , , , , , , , , , ,
Minnetol	TEA		1.42	0.4	ACTC1 ACTC1 ACTC2
Microtubule	TFA	5	142	0.4	ACTC1,ACTA1,ACTG2,
associated					ACTA2,DYNLL2
complex	mp.		2.60		1 TD 1 CO2 : TD 1
Mitochondrial	TFA	9	369	1	ATP5D,ACO2,ATP5E,
matrix					ACAT1,MDH2,ATP5C1,
					SUCLG1,SOD2,HADH
Mitochondrial	TFA	9	291	1.1	ATP5D,ATP5E,NDUFS6,
protein complex					ATP5O,UQCRFS1,CYCS,
					NDUFV2,ATP5C1,UQCRB
Mitochondrial	TFA	3	4	2.5	ATP5D,ATP5E,ATP5C1
proton-					·
					•

	ı				
transporting					
ATP synthase					
complex,					
catalytic sector					
F(1)					
Mitochondrial	TFA	4	71	1.4	NDUFS6,UQCRFS1,
respirasome					NDUFV2,UQCRB
Muscle myosin	TFA	3	15	1.9	MYL1,MYH7,MYL3
complex					
Myosin	TFA	5	65	1.5	MYL2,MYL1,MYH7,
complex					MYL3,DYNLL2
Oxidoreductase	TFA	5	182	1.1	NDUFS6,UQCRFS1,
complex				1	NDUFV2,UQCRB,SOD2
Proton-	TFA	4	6	2.4	ATP5D,ATP5E,ATP5O,
transporting	1171	•		2. 1	ATP5C1
ATP synthase					7111301
complex,					
catalytic core					
F(1)					
Striated muscle	TFA	5	24	1.9	TNNC1,TNNT2,TNNI3,
thin filament	IIIA	3	24	1.9	ACTA1,MB
Supramolecular	TFA	16	490	1.1	MYL2,TNNC1,TNNT2,
fiber	IFA	10	490	1.1	ACTC1,MYOZ2,MYL1,
Hoer					
					TNNI3,MYH7,ACTA1,
					DES,MYL3,MB,
					ACTG2,LDB3,ACTA2,
7.1	TDTD 4	4	60	1.4	ACTN2
Z disc	TFA	4	60	1.4	MYOZ2,DES,LDB3,ACTN2
Extracellular	HEPES	6	444	2.2	MIF,GAPDH,HSPE1,
vesicle					HBA2,HBB,MB,PARK7
Mitochondrial	HEPES	4	145	2.1	RPS27A,UBB,
outer membrane					UBA52,UBC
Mitochondrial	HEPES	6	461	2.2	ATP5B,RPS27A,
membrane					UBB,UBA52,
					ATP5J,UBC
Chromosome	Azo	16	894	8.7	HIST1H4F,H3F3B,
					HIST1H2BD,HIST1H2AE,
					HIST1H2BC,HIST2H2AC,
					HIST2H3D,HIST1H2AI,
					HIST1H3J,HIST2H2BE,
					HIST2H2AA,HIST1H2AC,
					HIST2H2BF,HIST1H2BO,
					HIST1H2BH,HIST1H2BN
Cardiac	Azo	2	7	2.1	TNNC1,TNNI3
Troponin		_	,		
complex					
Cardiac	Azo	2	5	2.3	MYL2,TNNI3
myofibril	1120			2.5	111112,111113
шуошош	l	1	1		

M 1		122	0.605	5.2	ATDEE HIGHTINE
Membrane-	Azo	33	8685	5.2	ATP5E,HIST1H4F,
bounded					COX6B1,H3F3B,C12orf10,
organelle					COX6A2,HIST1H2BD,
					ATP5H,HIST1H2AE,
					ATP5I,UQCRH,COX8A,
					HIST1H2BC,RPLP2,
					HIST2H2AC,HIST2H3D,
					HIST1H2AI,HIST1H3J,
					HIST2H2BE,HIST2H2AA,
					USMG5,COX7A2,
					HIST1H2AC,MB,ATP5J,
					COX7B,COX6C,UQCRB,
					CRYAB,HIST2H2BF,
					HIST1H2BO,HIST1H2BH,
					HIST1H2BN
Intracellular	Azo	22	3196	6.0	MYL2,TNNC1,HIST1H4F,
non-membrane-					H3F3B,HIST1H2BD,
bounded					HIST1H2AE,HIST1H2BC,
organelle					RPLP2,HIST2H2AC,
					HIST2H3D,TNNI3,
					HIST1H2AI,HIST1H3J,
					HIST2H2BE,HIST2H2AA,
					HIST1H2AC,MYL3,MB,
					HIST2H2BF,HIST1H2BO,
					HIST1H2BH,HIST1H2BN
Nucleosome	Azo	11	70	14.1	HIST1H4F,H3F3B,
					HIST1H2BC,HIST2H2AC,
					HIST2H3D,HIST1H3J,
					HIST2H2BE,HIST2H2AA,
					HIST1H2BO,HIST1H2BH,
					HIST1H2BN
	1	1	l .	1	1110 1 11111111

# Chapter 6 Conclusions and Future Perspectives

Top-down proteomics is a rapidly growing area of MS-based proteomics, but the full potential of the field has not yet been realized and we must work to match the capabilities of frontend separation and data processing solutions with the performance of new MS instruments. In this dissertation, I have developed new targeted separations for top-down proteomic analysis of mAbs and ADCs, provided a new online 2D sSEC-RPLC-MS method for global top-down proteomics, and reported a new software solution for native top-down proteomics data processing.

In chapters 2 and 3, I detailed the use of top-down proteomics to study mAbs and ADCs, a rapidly growing class of biotherapeutics which require a more global view of quality attributes than peptide mapping assays can provide. In chapter 2, I detailed the coupling of RPLC online with FTICR-MS/MS2 to provide high resolution accurate mass information on the LC timescale. This approach was used to characterize a partially and fully reduced cysteine-linked antibody drug conjugate. The partial reduction approach enabled accurate calculation of average DAR and isotopically resolved all Lc (~25 kDa) and Hc (~50 kDa) subunits on the LC timescale, even baseline resolving the low abundance, 54.5 kDa Hc3 subunit in just four MS scans. The full reduction approach enabled sequence analysis by LC-MS2, verifying the site of drug binding on the Lc1 subunits, the site of glycan binding on the Hc subunit, and localizing Hc drug binding between C204 and C233. This approach enabled greater sequence coverage than previous enzymebased middle-down workflows<sup>237</sup> and maintained the global detail which is lost in peptide mapping assays.<sup>228</sup> In chapter 3, the same ADC and its parent mAb were analyzed under native conditions by TIMS-MS. The use of TIMS in place of a liquid phase separation not only increases the speed and throughput of analysis but improves signal to noise by 60 % relative to direct infusion alone and allows changes in CCS of the mAb and ADC to be monitored. Combining the TIMS with a segmented MS approach allows collection of TIMS, MS1, MS2', and MS3 data in only 3 minutes

of instrument acquisition time. The MS1 information allowed determination of the intact mass for all DAR species, and calculation of average DAR. The MS2' revealed the release of several non-covalently associated subunits, including Lc1, Lc-Hc2, and Lc0 which is a product of odd-numbered drug loading. The MS3 analysis confirmed the location of intrachain disulfide bonds and drug binding on the Lc1 subunit. The two methods reported in chapters 2 and 3 are very useful for mAb and ADC characterization, however, further hybrid separation approaches to characterize these complex molecules will be needed as our understanding of their molecular function and inherent complexity changes over time. I have developed one such workflow coupling native microchip CE separation for mAb and ADC charge variant analysis online with TIMS-MS. These unpublished results enable detection of modification-induced changes in gas phase conformation of the mAb and ADC, offering new insight into the formation of mAb and ADC aggregates <sup>330,331</sup> as well as identifying possible sources of instability.

In chapter 4, I reported the development of a new software designed to address the challenges associated with native top-down proteomics, MASH Native. MASH Native is designed as a universal software, supporting flexible data analysis and reporting workflows. Critically, MASH can deconvolute non-isotopically resolved data, a common feature of native MS spectra. Complex-down workflows are supported in MASH, with MS1, MS2, and MS3 data processing in a single software window. Uniquely, MASH is currently the only top-down software capable of deconvoluting non-isotopically resolved MS1 spectra and performing database searches, positioning MASH Native as a foundational tool for discovery mode native top-down proteomics. Additional characterization options such as internal fragment assignment, and multiple spectral summing, deconvolution, and database searching algorithms have enabled far

greater flexibility than previous versions of MASH, while maintaining the architecture to allow denatured top-down proteomics data processing and providing excellent data visualization tools.

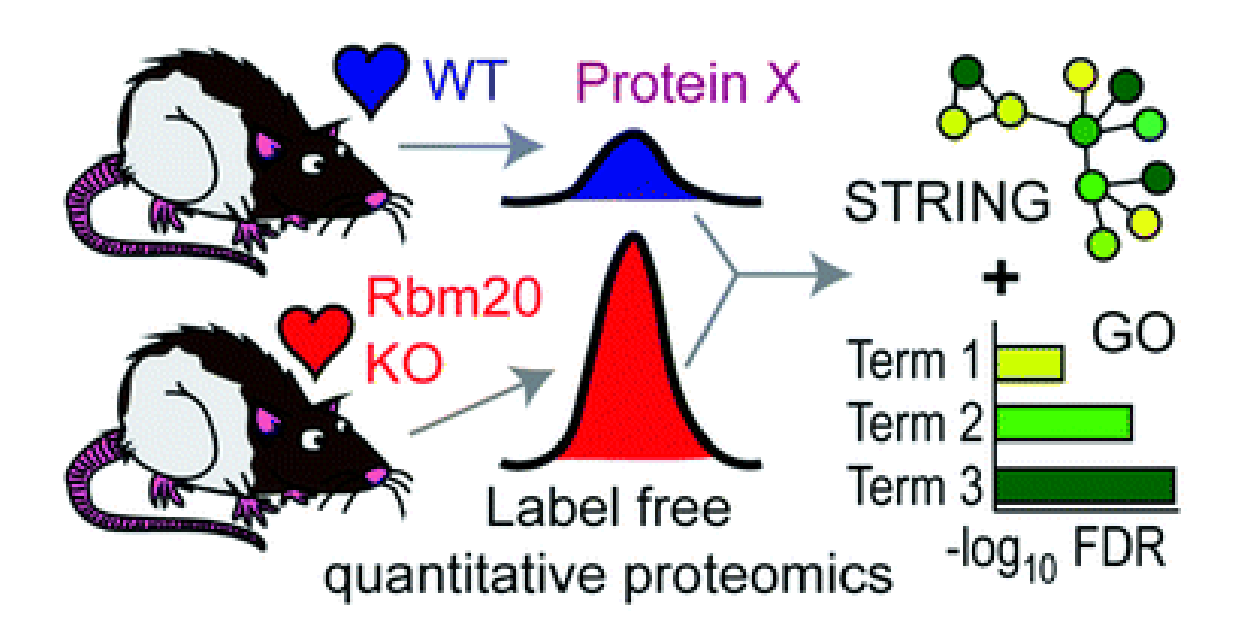
In chapter 5, I detailed the development of online top-down sSEC-RPLC-MS and its application to a three-step sequential extract of human heart tissue. The developed 2DLC approach provides a method of separation which is far better suited to the complexity of the intact proteome than the traditionally used 1D RPLC-MS approach, with a four-fold increase in theoretical peak capacity possible using the developed 2D approach. The approach also benefits from ease of use enabled by automation. While previous offline 2DLC approaches require sample pooling, and/or sample pre-treatment prior to LC-MS injection, the online 2D method eliminates the need for both steps and significantly reduces human labor time. 145 Application of this method to a three-step cytosolic, sarcomeric, and membrane protein extraction found complimentary sampling of the proteome to enable a more complete picture of the proteome than would be achieved by a single extraction step alone. This approach was performed in discovery mode, allowing the identification, and site-specific localization of novel modifications and proteoforms. The developed online 2D method has great potential to improve the depth of proteome coverage achieved by global topdown proteomics and is highly compatible with both disease studies and large-scale top-down proteomics studies.

In Appendix I, I have reported the bottom-up proteomic analysis of control and Rbm20 KO rat heart tissue. This study is the first global proteomic analysis of Rbm20 KO, a mutation known to lead to the onset of dilated cardiomyopathy. By sacrificing rats at three weeks of age, confounding effects from Rbm20-regulated titin isoform switching were avoided, allowing the detection of altered expression for a number of mitochondrial metabolic enzymes. Intriguingly, alterations to Msrb2, a known actor in mitophagy, indicates clearance of dysfunctional

mitochondria from the cell. While this approach was unable to monitor proteoform expression changes, it did allow identification of protein targets for follow-up analysis by top-down proteomics.

In summary, as the use and acceptance of top-down proteomics continues to expand, new tools for separation will be critical to achieve the full potential of the field. I anticipate that over the next five years, demand for new native top-down proteomic solutions will rapidly grow. Techniques such as hybrid LC-IMS-MS, native 2DLC-MS, or possibly 3DLC-MS will become critical tools to better explore the vast landscape of the native top-down proteome. Similarly, new automated data processing and data acquisition algorithms could lower the barrier of entry to the field of top-down proteomics, broadening acceptance from the wider scientific community. Finally, hybrid MS instrumentation with new IMS cell designs and configurations, <sup>137</sup> expanded fragmentation abilities, <sup>332</sup> and even multiple mass analyzers <sup>333</sup> are poised to push the field to new realms discovery in years to come.

Appendix I Rbm20 ablation is associated with changes in the expression of titin-interacting and metabolic proteins



This chapter has been published and is adapted from:

Larson, E. J.; Gregorich, Z. R.; Zhang, Y..; Li, B. H.; Aballo, T. J.; Melby, J. A.; Ge, Y.; Guo, W. Rbm20 ablation is associated with changes in the expression of titin-interacting and metabolic proteins. *Molecular Omics.* 2022.

### Abstract

Dilated cardiomyopathy (DCM) is a major risk factor for developing heart failure and is often associated with an increased risk for life-threatening arrhythmia. Although numerous causal genes for DCM have been identified, RNA binding motif protein 20 (Rbm20) remains one of the few splicing factors that, when mutated or genetically ablated, leads to the development of DCM. In this study we sought to identify changes in the cardiac proteome in Rbm20 knockout (KO) rat hearts using global quantitative proteomics to gain insight into the molecular mechanisms precipitating the development of DCM in these rats. Our analysis identified changes in titin-interacting proteins involved in mechanical stretch-based signaling, as well as mitochondrial enzymes, which suggests that activation of pathological hypertrophy and altered mitochondrial metabolism and/or dysfunction, among other changes, contribute to the development of DCM in Rbm20 KO rats. Collectively, our findings provide the first report on changes in the cardiac proteome associated with genetic ablation of Rbm20.

# Introduction

Dilated cardiomyopathy (DCM) is a non-ischemic heart muscle disease characterized by left or biventricular dilation and impaired systolic function in the absence of abnormal loading conditions or coronary artery disease.<sup>334</sup> DCM is estimated to affect approximately 1 in 250 individuals in the general population and remains a significant cause of worldwide morbidity and mortality despite advances in the management of heart failure in patients with DCM.<sup>335</sup> While mutations in the TTN gene, which encodes the giant sarcomeric protein titin, are the most common cause of DCM, and account for approximately 20–25% of cases,<sup>336</sup> the genetics of DCM are complex with mutations in over 60 genes having been linked to this disease.<sup>337</sup> Among the myriad DCM-linked genes that have been identified, RNA binding motif protein 20 (Rbm20) is unique as

it is one of only a handful of splicing factors that, when mutated or genetically ablated in humans and animal models, leads to the development of DCM.  $^{338-340}$  Mutations in RBM20 are estimated to account for  $\sim 3\%$  of familial cases of DCM.  $^{341,342}$ 

Rbm20 is a trans-acting splicing factor that is highly expressed in skeletal and cardiac muscle.<sup>343</sup> To date, Rbm20 has been shown to regulate the alternative splicing of more than 30 genes, the most well-studied of which is TTN.<sup>343</sup> Loss-of-function studies in Rbm20 knockout (KO) rats and mice demonstrated that Rbm20 not only modulates myocardial stiffness by regulating titin isoform expression, but also affects cardiomyocyte contractility via the splicing regulation of genes involved in Ca2+-handling, such as Ryr2 and Camk2d.<sup>344,345</sup> Indeed, the DCM-like phenotype that develops in Rbm20 KO rats and mice is thought to result primarily from (1) reduced diastolic stiffness due to the expression of more compliant titin isoforms and (2) impaired contractility secondary to alternative splicing of Ca2+-handling genes.<sup>343–346</sup> Yet, the possibility that additional factors contribute to the development of DCM in Rbm20 KO animals cannot be ruled out.

In an effort to identify additional networks of dysregulated genes in Rbm20 KO rats that could contribute to the development of DCM, we previously employed global transcriptome profiling.<sup>344</sup> This approach enabled the identification of changes in the expression of approximately 400 genes, including titin-interacting and Ca2+-handling genes, in the KO rat ventricular myocardium throughout post-natal development;<sup>344</sup> however, given the notoriously poor correlation between transcript and protein levels,<sup>347–349</sup> examination of gene expression at the protein level to identify genes with altered expression in Rbm20 KO animals is warranted. Thus, in this study, we employed global quantitative mass spectrometry (MS)-based proteomics to profile

changes in the cardiac proteome in Rbm20 KO rats and gain insight into alterations precipitating Rbm20 deficiency-associated DCM at the protein level.

# Materials and methods

# Chemicals and reagents

All reagents were purchased from Millipore Sigma unless otherwise noted. HPLC grade water, formic acid, and acetonitrile were purchased from Fisher Scientific (Fair Lawn, NJ, USA).

4-Hexylphenylazosulfonate (Azo) was synthesized in-house as previously described. 310,350

# Animals and tissue collection

Male and female wild type (WT) and Rbm20 homozygous knockout (KO) rats (Rattus norvegics) were used in this study. Rbm20 KO rats have been described previously. All rats were crosses of Sprague-Dawley (SD) Brown Norway (BN) (all strains were originally obtained from Harlan Sprague Dawley, Indianapolis, IN, USA). Rats with mixed genetic background were backcrossed three generations with pure SD strain resulting in rats that have a genetic background that is approximately 96% SD and 4% BN. Animals were maintained on a standard rat chow diet. All procedures involving animals were carried out following the recommendations in the Guide for the Care and Use of Laboratory Animals published by the National Institutes of Health and were approved by the Institutional Animal Care and Use Committee of the University of Wisconsin–Madison. WT and KO rats (n = 8 each) were sacrificed at three weeks-of-age, hearts were excised, snap frozen in liquid nitrogen, and stored at -80 °C for later use.

#### Protein extraction

Proteins were extracted from approximately 120 mg of ventricular tissue using the procedure developed by Aballo et al.<sup>322</sup> to fit the scale used by Jin et al.<sup>86</sup> Briefly, tissue was washed twice in 2 mL of Mg2+/Ca2+-free DPBS containing 1 HALT protease and phosphatase inhibitor cocktail (Thermo Fisher Scientific, Waltham, MA, USA). After washing, tissues were homogenized in 1.5 mL of lysis buffer (25 mM ammonium bicarbonate, 10 mM L-methionine, 1 mM dithiothreitol (DTT), and 1 HALT protease and phosphatase inhibitor cocktail) using a Pro 200 electronic homogenizer from Pro Scientific Inc. (Oxford, CT, USA). After initial homogenization, 1.5 mL of Azo19 extraction buffer (0.2% (w/v) Azo, 25 mM ammonium bicarbonate, 10 mM L-methionine, 1 mM DTT, and 1 HALT protease inhibitor cocktail) was added and samples were homogenized a second time. Homogenates were centrifuged at 21 100 g for 30 min (4 °C) and the supernatants were recovered. The recovered protein extracts were analyzed by SDS-PAGE to assess the reproducibility of protein extraction, digested for liquid chromatography (LC)-tandem MS (MS/MS), and used for Western blot analysis.

# Protein digestion and LC- MS/MS analysis

The concentration of protein extracts was determined using the Bradford protein assay and 100 mg of total protein from each sample was digested using the 1-hour digestion procedure employed by Aballo et al.<sup>322</sup> Resulting peptides were desalted using Pierce C18 Tips from Thermo Fisher (Waltham, MA, USA) following the manufacturer's instructions. Samples were evaporated to dryness under vacuum then reconstituted in mobile phase A (0.2% formic acid in water). The concentration of samples was determined using a NanoDrop Onec Microvolume UV-Vis Spectrophotometer from Thermo Fisher Scientific and all samples were adjusted to a final volume of 0.2 mg mL1 with mobile phase A. Peptides were separated by reverse phase LC (RPLC) using a Bruker nanoElute with an IonOpticks Aurora CSI C18 column, injecting 1 mL and using a 90

minute stepped gradient of 5–5–65–95–100–5–5% mobile phase B (0.2% formic acid in acetonitrile) over 0–5–65–95–105–106–120 minutes at 55 °C. Detection of separated peptides was performed though online coupling with a Bruker timsTOF Pro using datadependent analysis to select the top-10 precursor intensities and fragment by parallel accumulation serial fragmentation (PASEF).<sup>19</sup>

# Western Blot

Azo-containing protein extracts were mixed with 4 Laemmli buffer, boiled at 98 °C for 3 min, and resolved by SDS-PAGE on homemade 10% polyacrylamide gels. Proteins were transferred to Immun-Blot PVDF Membranes for Protein Blotting (0.2 mm pore size, Bio-Rad, cat# 1620177) at 300 mA for 90 min in a cold room (4 °C). To block, membranes were incubated in TBST with 5% (w/v) nonfat dry milk for 1 h at room temperature, followed by incubation in primary antibody solution containing 5% (w/v) nonfat dry milk and diluted Msrb2 (1:500, Proteintech, cat# 17629-1-AP) or Gapdh (1:1000, Cell Signaling Technology, cat# 2118) primary antibodies in TBST overnight at 4 °C. The membranes were removed from primary antibody solution and washed 5x 5 min with TBST followed by incubation in TBST with 3% (w/v) nonfat dry milk and diluted HRP-conjugated secondary antibody (1:3000, Promega, cat# W4018) for 1 h at room temperature. Subsequently, membranes were washed 5x 5 min with TBST, overlayed with SuperSignal West Pico PLUS Chemiluminescent Substrate (Thermo Fisher Scientific, cat# 34577), and imaged using a ChemiDoc Imaging System (Bio-Rad). Band densities were quantified using ImageJ.<sup>352</sup> Msrb2 band densities were first normalized to Gapdh and then to a replicate WT sample loaded on each gel yielding relative Msrb2 intensities normalized to Gapdh. The significance of the difference between group means was determined using a two-tailed Student's t-test.

# Data analysis

Data analysis was performed using MaxQuant (v1.6.5.0) to search all reviewed canonical and isoform data for Rattus norvegicus in Uniprot (downloaded January 12, 2021) and quantify protein expression by label-free quantitation (LFQ). MaxQuant results were processed using both LFQ analyst<sup>353</sup> and Perseus (v1.6.14.0).<sup>354</sup> To allow for statistical analysis of the data, data imputation was carried out in Perseus (for Perseus-type imputation, missing values are replaced by random numbers drawn from a normal distribution with a width of 0.3 and down shift of 1.8).<sup>354</sup> Significance testing in Perseus was performed using a two-tailed Student's t-test with P-value truncation and threshold P-value of 0.05. Protein network analysis of differentially expressed proteins was performed using STRING 11.0<sup>355</sup> and Cytoscape 3.8.2.<sup>314</sup> Gene ontology (GO) analysis was performed in STRING, using the 22,763 distinct protein encoding genes in the Rattus norvegicus database as the enrichment background.

# Results and discussion

# Rbm20 KO rats

To identify changes in the rat cardiac proteome associated with Rbm20 KO, we carried out proteomic analysis of hearts from 3 week-old Rbm20 KO rats. The Rbm20 KO rat strain contains a spontaneous deletion of ~95 kb on the long arm of chromosome 1 that removes all exons following exon 1 of the Rbm20 gene.<sup>343</sup> Consequently, these rats do not express Rbm20 at either the transcript or protein levels.<sup>343</sup> Our previous analysis of cardiac function in these rats revealed that they develop DCM with chamber dilation and cardiac dysfunction by 6 months-of-age.<sup>356</sup> However, rats up to 3 months-of-age lack any apparent phenotype with cardiac structure and function being similar to that in age-matched WT rats despite decreased myocardial stiffness resulting from titin isoform switching.<sup>356</sup> To identify changes in the cardiac proteome associated with Rbm20 ablation, we chose to study rats at 3 weeks-of-age (21 days) as interrogation of the

cardiac proteome at this timepoint would be expected to provide insights into proteome changes associated with Rbm20 loss while avoiding confounding changes associated with DCM itself.

Reproducibility of protein extraction and LC-MS/MS analysis

To assess changes in the cardiac proteome associated with Rbm20 deficiency, proteins were extracted from the myocardium of 3 week-old WT and KO rats (n = 8 each) using a one-step protein extraction procedure with the photocleavable MS-compatible surfactant Azo (Fig. AI.1A).<sup>322</sup> Analysis of protein extracts by SDS-PAGE with Coomassie blue staining confirmed highly reproducible protein extraction from both WT and KO rat myocardium across biological replicates (Fig. AI.1B).

Consistent with the reproducibility of protein extraction, LCMS analysis of protein extracts yielded total ion chromatograms that were consistent across WT and KO biological replicates (Fig. AI.S1). Moreover, log<sub>2</sub> transformed peptide intensities were in accordance across biological replicates as indicated by average Pearson correlation coefficients of 0.98 and 0.97 for all WT and KO biological replicates, respectively (Fig. AI.1C). To determine whether the protein intensity profiles were similar across WT and KO biological replicates, individual log<sub>2</sub> transformed peptide LFQ intensities were binned and plotted in histograms. As shown in Fig. S2 and S3, protein intensity profiles were in good agreement across WT and KO biological replicates, respectively. Collectively, these results demonstrate the high reproducibility of protein extraction and LC-MS analysis.

Identification of proteins in myocardial extracts prepared from WT and KO rats

A total of 2425 and 2379 proteins were identified by LC-MS/MS in all WT and KO biological replicates, respectively (Tables AI.S1 and AI.S2). It should be noted that these numbers

are lower than the number of identifications previously obtained from human myocardial protein extracts (approximately 4000 protein identifications) using the same method. This difference can be explained by the fact that the rat database lacks the completeness of the human database, with only one fifth the number of human entries. Comparison of the protein identifications between WT and KO rat samples yielded a list of 2287 proteins that could be reproducibly quantified across all 16 samples, with an additional 138 and 91 unique proteins that could only be quantified in WT and KO ventricular myocardium, respectively (Fig. AI.2A). To assess patterns among WT and KO biological replicates principal component analysis (PCA) was performed. As expected, PCA showed that biological replicates were generally clustered into two groups, one containing the biological replicates from WT and the other KO biological replicates (Fig. AI.2B)—a result that highlights the difference between the WT and KO cardiac proteomes.

Differentially expressed proteins (DEPs) in RBM20 KO rat myocardium contribute to pathological cardiac remodeling

Quantitative global proteomic analysis enabled the identification of 103 proteins that are differentially expressed in KO versus WT rat myocardium (Fig. AI.3). Of the 103 DEPs, 48 and 55 were up- and down-regulated, respectively, in KO relative to WT. Differences in the expression levels of the nine proteins with the highest log<sub>10</sub> P-values are shown in boxplots to visualize the spread in protein LFQ values for individual biological replicates (Fig. AI.S4). Not surprisingly, one of the proteins with the greatest change in expression was Rbm20 (Fig. AI.3 and Fig. AI.S4), which was not detected in any of the KO rat samples consistent with the complete loss of Rbm20 transcript and protein expression in this rat model.<sup>343</sup> Note that the values for Rbm20 shown in Fig. AI.S4 for the KO rat samples are the result of data imputation to replace the missing values and allow for statistical analysis in the Perseus software platform (see Methods). As expected,

comparison of the list of DEPs to previously identified differentially expressed genes revealed several discrepancies between the proteomics and transcriptomics data at 20 days post-birth, although several changes were consistent, such as upregulation of proenkephalin-A (Penk) (Table AI.S3). Additionally, to identify common processes and functions, as well as interactions, among the DEPs, the gene ontology (GO) and STRING databases were searched using the list of DEPs (Fig. AI.4, AI.5 and Fig. AI.S5).

Notably, quantitative proteomics analysis identified changes in the expression of several titin-interacting proteins in KO rat myocardium. We have previously shown that four and a half LIM domains 1 (Fhl1) and ankyrin repeat domain 1 (Ankrd1, also known as cardiac ankyrin repeat protein or Carp) are upregulated at the transcript level in KO rat myocardium.<sup>344</sup> Upregulated expression of Fhl1 in the Rbm20 KO rat ventricle has also been confirmed at the protein level previously using Western blot. 344 Herein, quantitative proteomic analysis allowed us to confirm the upregulation of Ankrd1 at the protein level at 21 days after birth even though protein transcript expression was not changed until 49 days post-birth for Ankrd1 (Table AI.S3),<sup>344</sup> and also identify a decrease in the expression of four and a half LIM domains 2 (Fhl2) (Fig. AI.3). Ankrd1 has been shown to bind to the N2A region of titin, 357 and is a functionally pleiotropic protein that plays roles in transcriptional regulation, sarcomere assembly, and mechano-transduction in the heart.<sup>358</sup> Importantly, Ankrd1 is upregulated in response to hypertrophic stimuli and in human heart failure; <sup>359,360</sup> and plays a direct role in hypertrophic gene expression via modulation of Erk/Gata4 phosphorylation.<sup>361</sup> Fhl1 has previously been shown to exist as part of a biomechanical stretch sensor complex that is localized to the titin N2B spring element and, similar to Ankrd1, has been shown to be important for the development of stress-induced pathological cardiac hypertrophy.<sup>362</sup> STRING network analysis showed an interaction between Ankrd1 and Fhl2 (Fig. AI.5), and indeed

there is evidence in the literature supporting a direct interaction between Ankrd1 and Fhl2.<sup>363</sup> However, in contrast to Ankrd1, previous studies have demonstrated that Fhl2 negatively regulates cardiac hypertrophy.<sup>364</sup> Specifically, prior studies have shown that Fhl2 prevents activation of the hypertrophic transcription factor NFAT through interactions with activated calcineurin—the phosphatase responsible for dephosphorylating and, thus, activating NFAT.<sup>364</sup> Collectively, these changes suggest that alterations in the expression of titin-interacting proteins involved in mechanical stretch-based signaling and hypertrophic gene program induction in Rbm20 KO rats may contribute to the development of pathological cardiac remodeling in KO animals.

Pathological phenotype in RBM20 KO rats is associated with altered mitochondrial metabolism and/or dysfunction

GO analysis revealed that many of the DEPs are involved in metabolism, including organic substance metabolism, cellular metabolism, and metabolic processes (Fig. AI.4). In agreement with this, the most highly downregulated protein in the KO rat myocardium was 3-hydroxy-3-methylglutaryl-CoA synthase 2 (Hmgcs2), a key mitochondrial enzyme that catalyzes the rate-limiting step in ketogenesis. Motably, we previously found that Hmgcs2 is downregulated at the transcript level for at least 20 days following birth in Rbm20 KO rat myocardium, although expression was not significantly different between WT and KO at 49 days post-birth (Table AI.S4). In addition, the expression of several other proteins with the GO designation "mitochondrion" (GO: 0005739), including enoyl-CoA hydratase 1 (Ech1), pyruvate dehydrogenase kinase 4 (Pdk4), and aldehyde dehydrogenase 1 family member B1 (Aldh1b1), was downregulated in KO rat myocardium (Fig. AI.3). Our previous analysis uncovered several other differentially expressed genes at the transcript level, including Ccnb1, Dguok, and Trub1, all of which were upregulated 20 days after birth (Table AI.S4). The content of the protein in the KO rat myocardium (Fig. AI.3).

In addition to these changes, the mitochondrial chaperone TNF receptor associated protein 1 (Trap1), a member of the HSP90 protein family, was also significantly upregulated in KO versus WT rat myocardium (Fig. AI.3). A prior study has shown that Trap1 expression protects against myocardial ischemia/reperfusion injury by limiting mitochondrial dysfunction.<sup>366</sup> Moreover, the protein with the greatest increase in expression in the KO rat myocardium was mitochondrial methionine-R-sulfoxide reductase B2 (Msrb2) (Fig. AI.3A), which has previously been implicated in mitophagy,<sup>367</sup> a cellular process that removes damaged or unneeded mitochondria.<sup>368</sup> Increased expression of Msrb2 in the Rbm20 KO rat myocardium was confirmed by Western blot (Fig. AI.3B and C). Our group and others have previously shown that the intracellular Ca2+ concentration is increased during diastole in cardiomyocytes from Rbm20 KO rats and mice relative to that in cells from WT rats and mice. 344,345 Given the exquisite sensitivity of mitochondria to intracellular Ca2+ concentrations, <sup>369</sup> it is tempting to speculate that increased Msrb2 may reflect an upregulation of mitophagy to remove damaged/dysfunctional mitochondria and limit cardiomyocyte cell death resulting from mitochondrial Ca2+ overload in Rbm20 KO rats. Nevertheless, it is worth noting that not all identified mitochondrial proteins were downregulated in the hearts of Rbm20 KO rats. Thus, whether the observed changes are reflective of mitochondrial removal or broad rewiring of mitochondrial metabolism will require further investigation. Nevertheless, taken together these findings implicate altered cellular metabolism in the development of DCM secondary to Rbm20 loss.

#### Conclusion

In summary, herein we employed global quantitative MS-based proteomics to identify changes in the cardiac proteome in Rbm20 KO rats and gain insight into alterations potentially involved in the development of DCM resulting from Rbm20 ablation. Our proteomics analysis

uncovered changes in the expression of several known titin-interacting proteins congruent with the induction of pathological cardiac hypertrophy. In addition, we found that the expression of a number of metabolic enzymes localizing to the mitochondria was decreased concomitant with the upregulation of the mitochondrial chaperone Trap1 in Rbm20 KO rat myocardium. These changes are consistent with the idea that Rbm20 ablation is associated with altered mitochondrial metabolism and dysfunction, which may contribute to the development of DCM. Moreover, the upregulation of Msrb2—a protein previously implicated in mitophagy—in the myocardium of Rbm20 KO rats is consistent with this notion and may be an adaptive change to clear dysfunctional mitochondria from cardiomyocytes. It should be noted that, although studying changes in the cardiac proteome of Rbm20 KO rats at 3 weeks-of-age avoids confounding changes associated with DCM, myocardial stiffness is altered in these mice due to titin isoform switching and could contribute to the detected changes in protein expression. Moreover, as Rbm20 is a splicing factor, changes in the splicing of Rbm20 target transcripts likely play an important role in DCM development in Rbm20 KO rats, however, changes in splice isoform expression are difficult to quantify using peptide-based proteomics approaches such as that employed in this study as peptide recovery is limited and recovered peptides often map to multiple protein isoforms (the so called "protein inference problem"<sup>28</sup>). Nevertheless, these findings provide the first report on changes in the cardiac proteome associated with loss of Rbm20 and highlight several changes in the cardiac proteome of Rbm20 KO rats that may contribute to the development of DCM independent of alterations in splicing.

### **Figures**

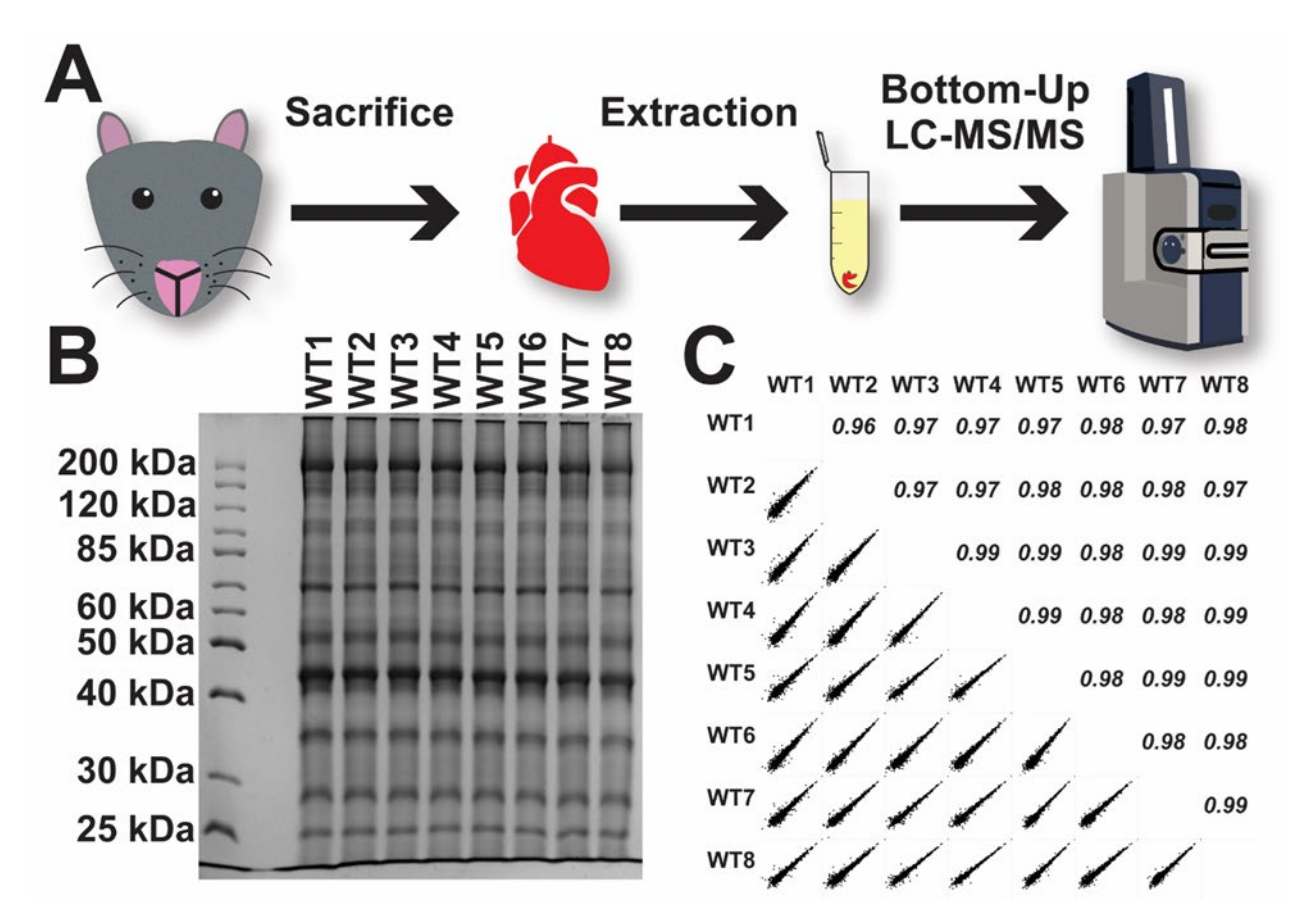


**Figure AI.1.** Schematic of protein extraction workflow and LC-MS/MS analysis (A). Using a one-step Azo-enabled extraction, ventricular tissue from WT and RBM20 KO rats (n = 8 each) was analyzed. SDS-PAGE confirmed reproducibility of extraction performance (B, WT biological replicates shown). Pearson correlation analysis was performed among biological replicates, showing an average r value of 0.98 for the WT samples (C).

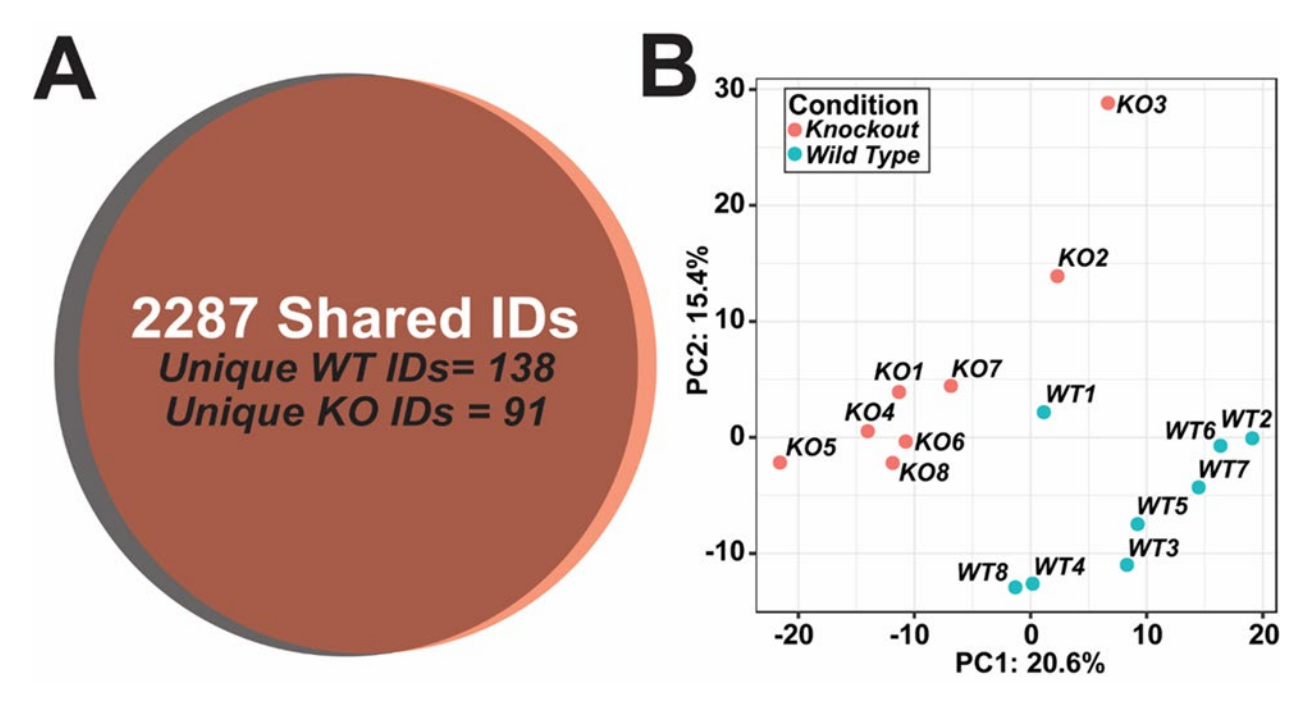


**Figure AI.2.** Bottom-up LC-MS/MS analysis with the timsTOF Pro identified 2,287 proteins common to all WT and KO samples, with 138 additional proteins unique to the eight WT animals and 91 proteins unique to the eight RBM20 KO animals (A). Principal component analysis was performed for all WT and RBM20 KO biological replicates (B).

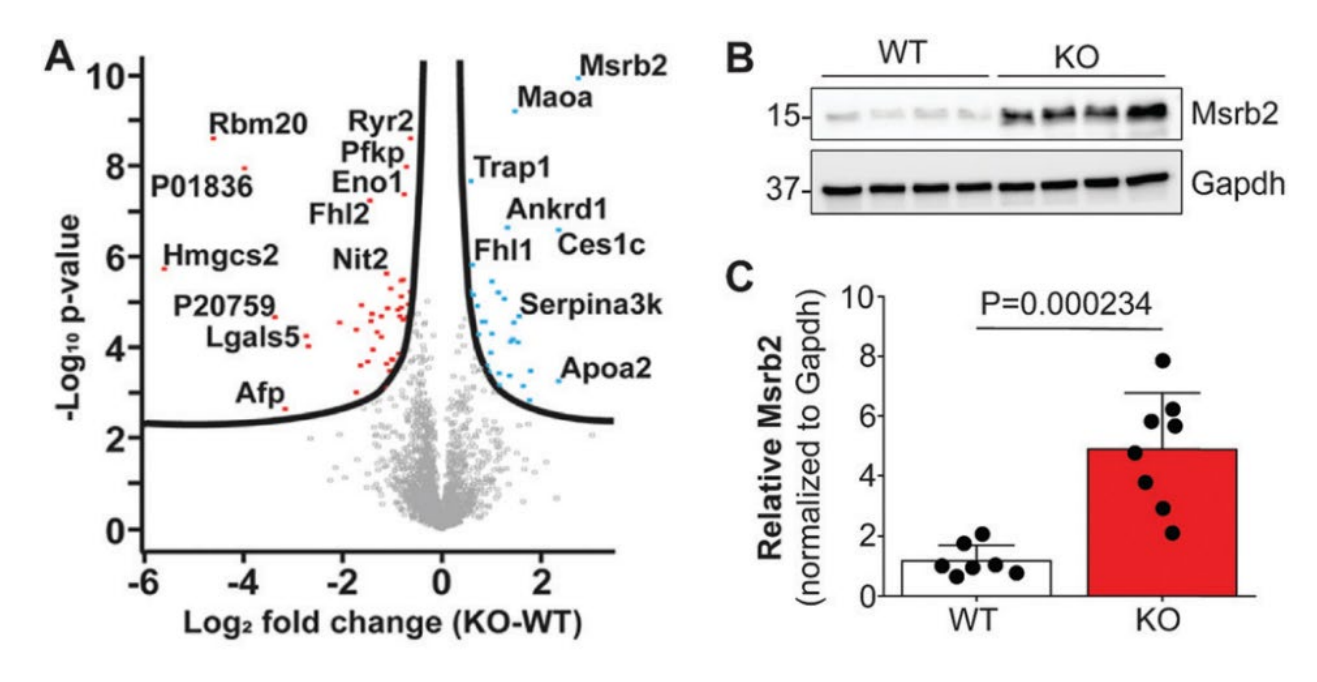


**Figure AI.3.** Volcano plot showing the 103 proteins that are differentially expressed in Rbm20 KO versus WT rat myocardium (A). Western blot analysis of Msrb2 expression in Rbm20 WT (n = 7) and KO (n = 8) rat myocardium. B. Representative Western blot showing Msrb2 expression in Rbm20 WT and KO rat ventricular myocardium. Gapdh served as a loading control. C. Quantification of Msrb2 expression. Bar graphs indicate mean ± SD. The significance of the difference between group means was determined using a two-tailed Student's t-test.

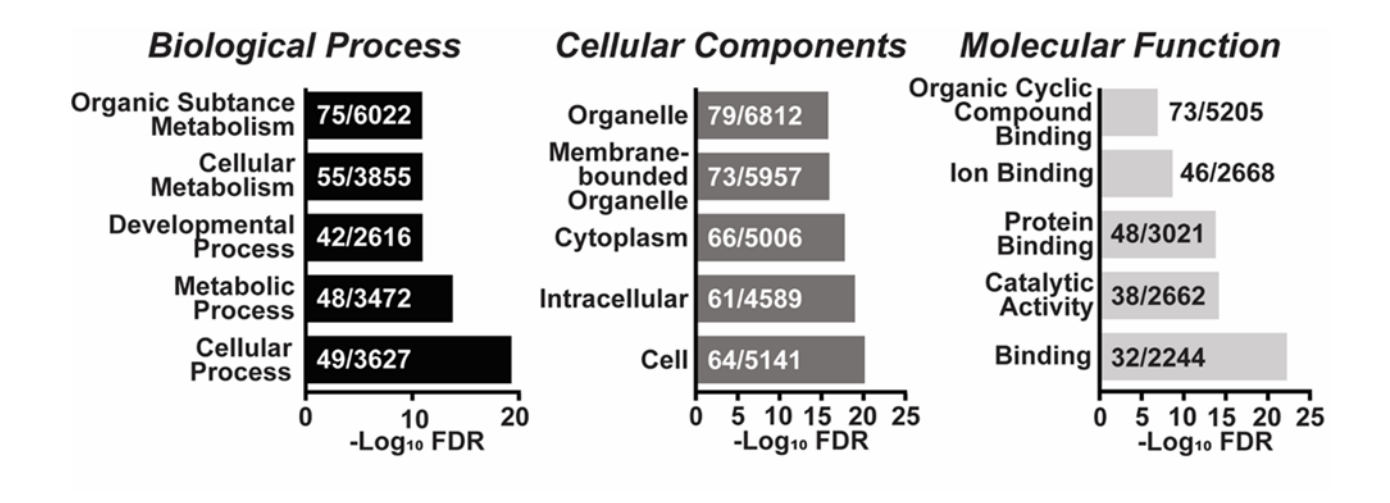


**Figure AI.4.** GO analysis using String for the top-5 terms is plotted against of the –Log<sub>10</sub> FDR, with the number of genes identified/number of background genes overlaid on bar chart bars.

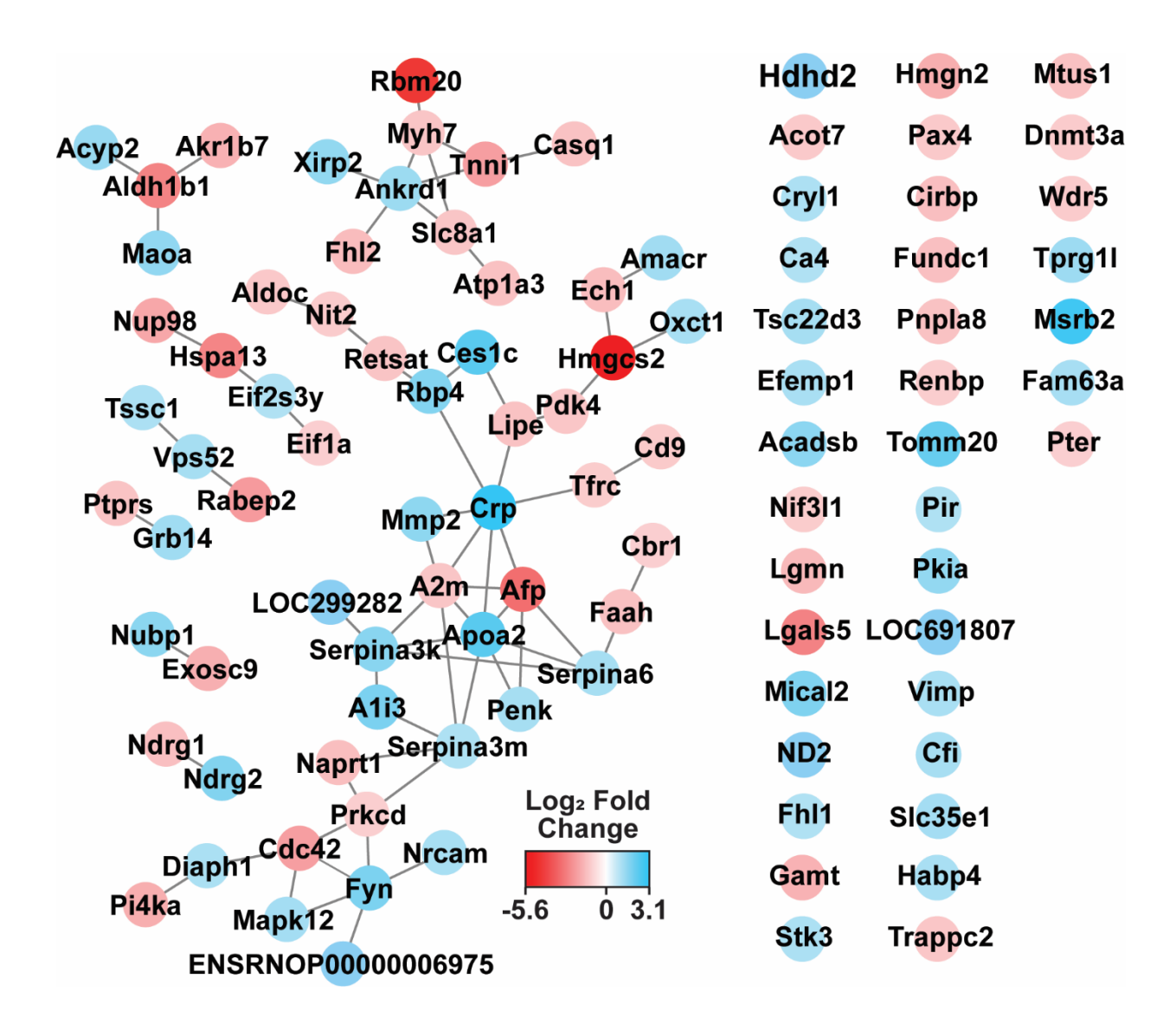


**Figure AI.5.** String also enabled the generated of an interaction map for known proteins, with nodes colored by Log2 fold change in expression. A total of 62 proteins had known interactors within the 99 differentially expressed proteins, while 37 had no known interactors.

# Appendix I

## **Supporting Information**

# Rbm20 ablation is associated with changes in the expression of titin-interacting and metabolic proteins

<u>Contents</u>	<u>Page</u>
Table AI.ST1 Protein IDs by biological replicate for WT rats	207
Table AI.ST2 Protein IDs by biological replicate for Rbm20 KO rats	207
Figure AI.S1 Overlay of RPLC-MS TICs for WT and Rbm20 KO biological replicates	208
Figure AI.S2 Histograms of protein IDs binned by LFQ intensity for WT biolographicates	-
Figure AI.S3 Histograms of protein IDs binned by LFQ intensity for Rbm20 KO biolo replicates	_
Figure AI.S4 Boxplot of WT and Rbm20 KO expression changes for differentially expreproteins with nine highest -log <sub>10</sub> P values	

**Table AI.ST1**. Number of protein groups identified across eight biological replicates of WT rat hearts. A total of 2425 protein group identifications were shared across all eight biological replicates.

Replicate	Protein Groups
WT 1	2644
WT 2	2654
WT 3	2672
WT 4	2645
WT 5	2685
WT 6	2627
WT 7	2670
WT 8	2635
Total Shared	2425

**Table AI.ST2.** Number of protein groups identified across eight biological replicates of RBM20 KO rat hearts. A total of 2379 protein group identifications were shared across all eight biological replicates.

Replicate	Protein Groups
KO 1	2583
KO 2	2647
KO 3	2588
KO 4	2633
KO 5	2655
KO 6	2656
KO 7	2657
KO 8	2619
Total Shared	2379

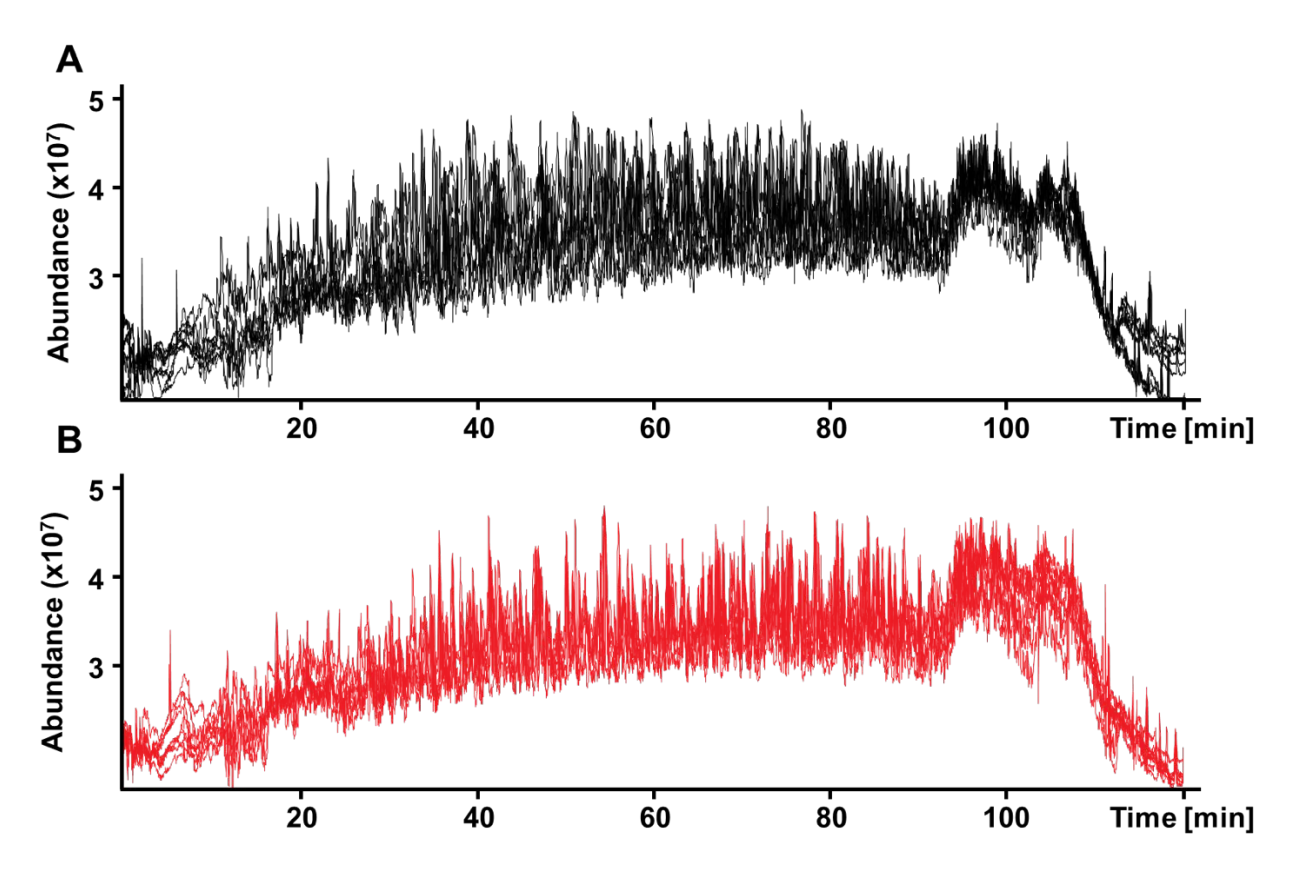


**Figure AI.S1.** Overlay of total ion chromatograms from eight WT (A) and eight RBM20 KO (B) biological replicates. Excellent reproducibility between biological replicates was observed.

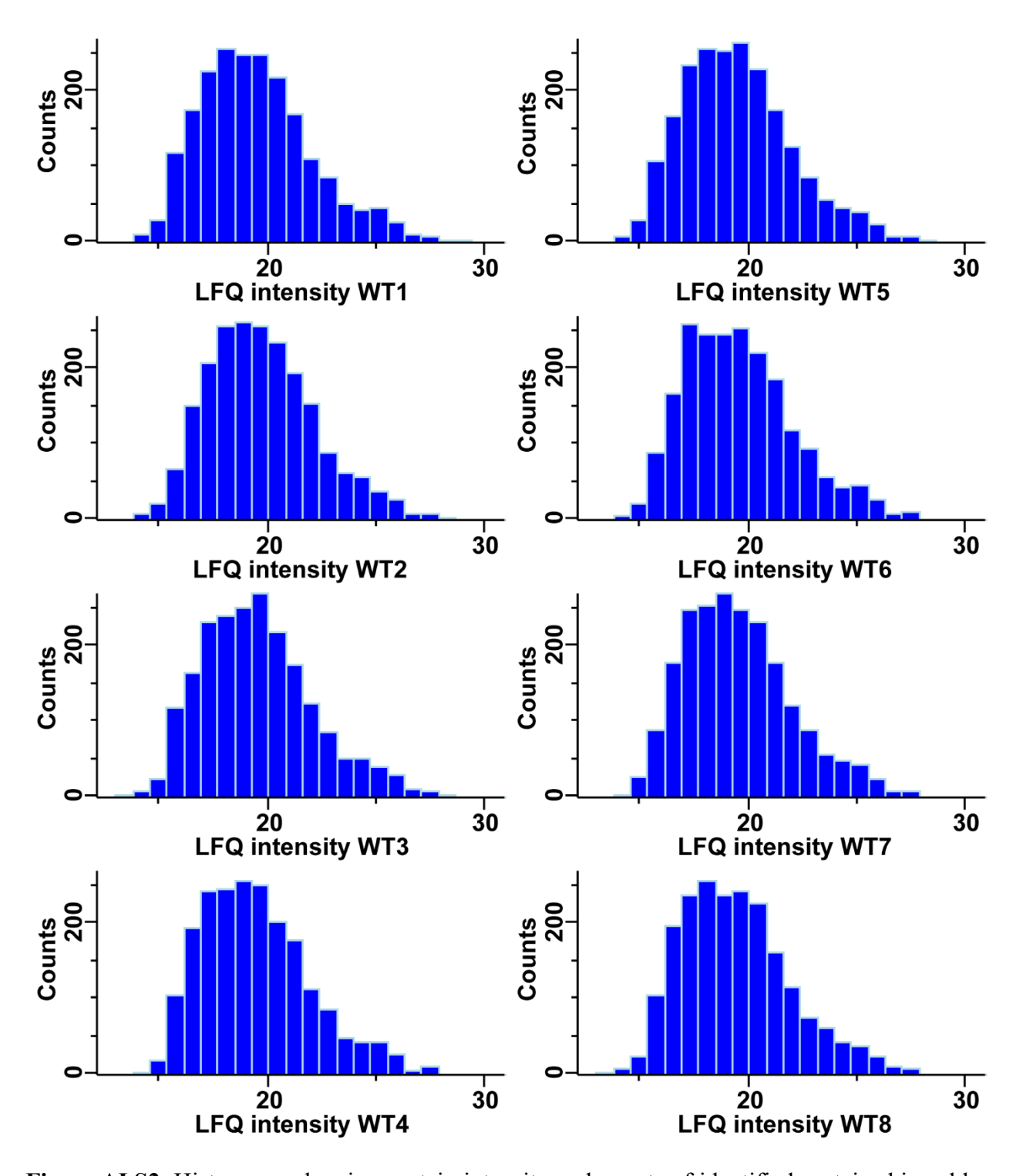


**Figure AI.S2**. Histograms showing protein intensity and counts of identified proteins binned by intensity range for the eight WT rat heart biological replicates.

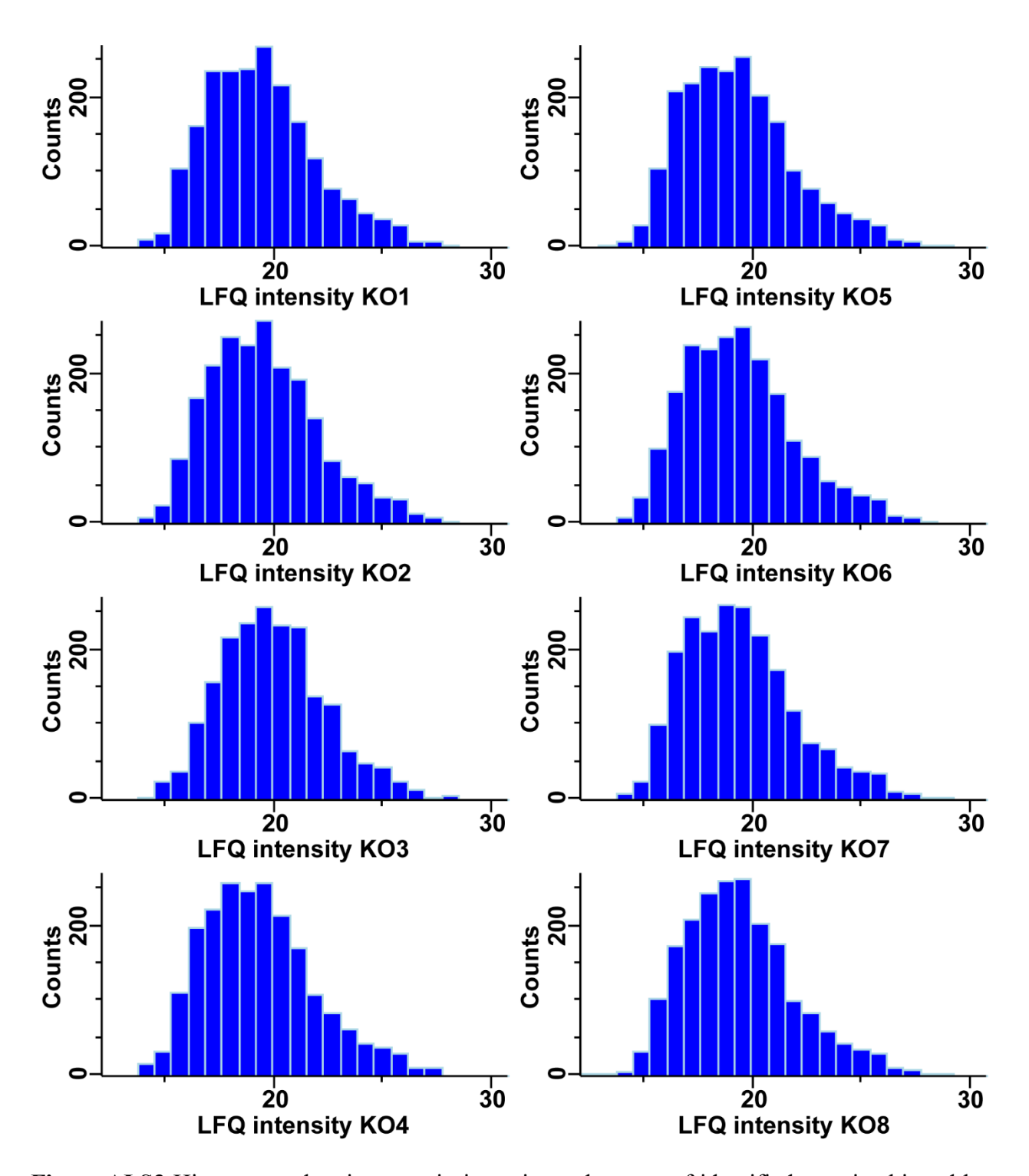


**Figure AI.S3** Histograms showing protein intensity and counts of identified proteins binned by intensity range for the eight RBM20 KO rat heart biological replicates.

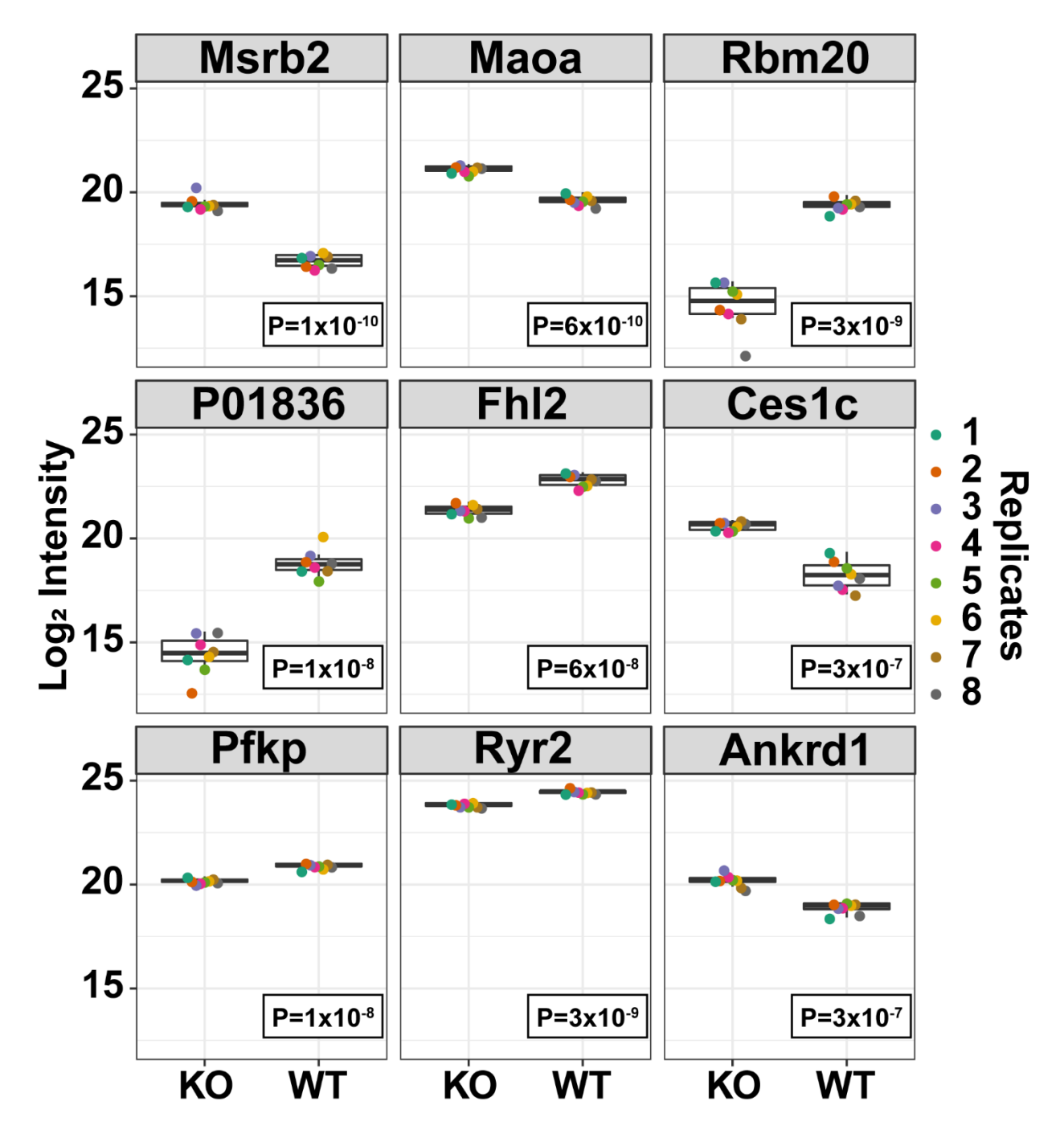


**Figure AI.S4.** Boxplots of the WT and KO expression levels, shown as LFQ intensities, of differentially expressed proteins with the nine highest  $-\log_{10} P$  values. Expression of proteins not detected in a given sample group, such as RBM20 which was not detected in any KO samples, were generated by imputation using Perseus.

#### References

- (1) Peng, Y.; Gregorich, Z. R.; Valeja, S. G.; Zhang, H.; Cai, W.; Chen, Y.-C.; Guner, H.; Chen, A. J.; Schwahn, D. J.; Hacker, T. A.; et al. Top-down Proteomics Reveals Concerted Reductions in Myofilament and Z-Disc Protein Phosphorylation after Acute Myocardial Infarction\* □ S. *Mol. Cell. Proteomics* **2014**, *13*, 2752–2764. https://doi.org/10.1074/mcp.M114.040675.
- (2) Shi, T.; Niepel, M.; McDermott, J. E.; Gao, Y.; Nicora, C. D.; Chrisler, W. B.; Markillie, L. M.; Petyuk, V. A.; Smith, R. D.; Rodland, K. D.; et al. Conservation of Protein Abundance Patterns Reveals the Regulatory Architecture of the EGFR-MAPK Pathway. *Sci. Signal.* **2016**, *9* (436), rs6. https://doi.org/10.1126/scisignal.aaf0891.
- (3) Korzeniecki, C.; Priefer, R. Targeting KRAS Mutant Cancers by Preventing Signaling Transduction in the MAPK Pathway. *European Journal of Medicinal Chemistry*. Elsevier Masson s.r.l. February 5, 2021, p 113006. https://doi.org/10.1016/j.ejmech.2020.113006.
- (4) Knowles, J. R. Enzyme Catalysis: Not Different, Just Better. *Nature* **1991**, *350* (6314), 121–124. https://doi.org/10.1038/350121a0.
- (5) Benkovic, S. J.; Hammes-Schiffer, S. A Perspective on Enzyme Catalysis. *Science*. American Association for the Advancement of Science August 29, 2003, pp 1196–1202. https://doi.org/10.1126/science.1085515.
- (6) Van Der Meide, P. H.; Schellekens, H. Cytokines and the Immune Response. *Biotherapy* **1996**, *8* (3–4), 243–249. https://doi.org/10.1007/BF01877210.
- (7) Panda, S.; Ding, J. L. Natural Antibodies Bridge Innate and Adaptive Immunity. *J. Immunol.* **2015**, *194* (1), 13–20. https://doi.org/10.4049/jimmunol.1400844.
- (8) Smith, L. M.; Kelleher, N. L. Proteoform: A Single Term Describing Protein Complexity. *Nat. Methods* **2013**, *10* (3), 186–187. https://doi.org/10.1038/NMETH.2369.
- (9) Cai, W.; Tucholski, T. M.; Gregorich, Z. R.; Ge, Y. Top-down Proteomics: Technology Advancements and Applications to Heart Diseases. *Expert Rev. Proteomics* **2016**, *13* (8), 717–730. https://doi.org/10.1080/14789450.2016.1209414.
- (10) Aebersold, R. How Many Human Proteoforms Are There? *Nat. Chem. Biol.* **2018**, *14*, 206–214.
- (11) Picotti, P.; Bodenmiller, B.; Mueller, L. N.; Domon, B.; Aebersold, R. Full Dynamic Range Proteome Analysis of S. Cerevisiae by Targeted Proteomics. *Cell* **2009**, *138* (4), 795–806. https://doi.org/10.1016/j.cell.2009.05.051.
- (12) Hortin, G. L.; Sviridov, D. The Dynamic Range Problem in the Analysis of the Plasma Proteome. *J. Proteomics* **2010**, *73* (3), 629–636. https://doi.org/10.1016/j.jprot.2009.07.001.
- (13) Wei, L.; Gregorich, Z. R.; Lin, Z.; Cai, W.; Jin, Y.; McKiernan, S. H.; McIlwain, S.; Aiken, J. M.; Moss, R. L.; Diffee, G. M.; et al. Novel Sarcopenia-Related Alterations in Sarcomeric Protein Post-Translational Modifications (PTMs) in Skeletal Muscles Identified by Top-down Proteomics. *Mol. Cell. Proteomics* **2018**, *17* (1), 134–145.

- https://doi.org/10.1074/mcp.RA117.000124.
- (14) Anbalagan, M.; Huderson, B.; Murphy, L.; Rowan, B. G. Post-Translational Modifications of Nuclear Receptors and Human Disease. *Nucl. Recept. Signal.* **2012**, *10* (Figure 1). https://doi.org/10.1621/nrs.10001.
- (15) Zhang, J.; Guy, M. J.; Norman, H. S.; Chen, Y. C.; Xu, Q.; Dong, X.; Guner, H.; Wang, S.; Kohmoto, T.; Young, K. H.; et al. Top-down Quantitative Proteomics Identified Phosphorylation of Cardiac Troponin i as a Candidate Biomarker for Chronic Heart Failure. *J. Proteome Res.* **2011**, *10* (9), 4054–4065. https://doi.org/10.1021/pr200258m.
- (16) Aebersold, R.; Mann, M. Mass Spectrometry-Based Proteomics. *Nature*. March 13, 2003, pp 198–207. https://doi.org/10.1038/nature01511.
- (17) Yates, J. R.; Ruse, C. I.; Nakorchevsky, A. Proteomics by Mass Spectrometry: Approaches, Advances, and Applications. *Annu. Rev. Biomed. Eng.* **2009**, *11*, 49–79. https://doi.org/10.1146/annurev-bioeng-061008-124934.
- (18) Sinitcyn, P.; Richards, A. L.; Weatheritt, R. J.; Brademan, D. R.; Marx, H.; Shishkova, E.; Meyer, J. G.; Hebert, A. S.; Westphall, M. S.; Blencowe, B. J.; et al. Global Detection of Human Variants and Isoforms by Deep Proteome Sequencing. *Nat. Biotechnol.* **2023**. https://doi.org/10.1038/s41587-023-01714-x.
- (19) Meier, F.; Brunner, A. D.; Koch, S.; Koch, H.; Lubeck, M.; Krause, M.; Goedecke, N.; Decker, J.; Kosinski, T.; Park, M. A.; et al. Online Parallel Accumulation—Serial Fragmentation (PASEF) with a Novel Trapped Ion Mobility Mass Spectrometer. *Mol. Cell. Proteomics* **2018**, *17* (12), 2534–2545. https://doi.org/10.1074/mcp.TIR118.000900.
- (20) Stejskal, K.; De Beeck, J. O.; Durnberger, G.; Jacobs, P.; Mechtler, K. Ultrasensitive NanoLC-MS of Subnanogram Protein Samples Using Second Generation Micropillar Array LC Technology with Orbitrap Exploris 480 and FAIMS PRO. *Anal. Chem.* **2021**. https://doi.org/10.1021/acs.analchem.1c00990.
- (21) Cox, J.; Mann, M. MaxQuant Enables High Peptide Identification Rates, Individualized p.p.b.-Range Mass Accuracies and Proteome-Wide Protein Quantification. *Nat. Biotechnol.* 2008 2612 2008, 26 (12), 1367–1372. https://doi.org/10.1038/nbt.1511.
- (22) Zhong, X.; Frost, D. C.; Yu, Q.; Li, M.; Gu, T. J.; Li, L. Mass Defect-Based DiLeu Tagging for Multiplexed Data-Independent Acquisition. *Anal. Chem.* 2020, 92 (16), 11119–11126. https://doi.org/10.1021/acs.analchem.0c01136.
- (23) Sivanich, M. K.; Gu, T. J.; Tabang, D. N.; Li, L. Recent Advances in Isobaric Labeling and Applications in Quantitative Proteomics. *Proteomics* **2022**, *22* (19–20), 1–17. https://doi.org/10.1002/pmic.202100256.
- (24) Meyer, J. G.; Niemi, N. M.; Pagliarini, D. J.; Coon, J. J. Quantitative Shotgun Proteome Analysis by Direct Infusion. *Nat. Methods* **2020**, *17* (12), 1222–1228. https://doi.org/10.1038/s41592-020-00999-z.
- (25) Messner, C. B.; Demichev, V.; Bloomfield, N.; Yu, J. S. L.; White, M.; Kreidl, M.; Egger, A. S.; Freiwald, A.; Ivosev, G.; Wasim, F.; et al. Ultra-Fast Proteomics with Scanning SWATH. *Nat. Biotechnol.* **2021**, *39* (7), 846–854. https://doi.org/10.1038/s41587-021-

- 00860-4.
- (26) Krokhin, O. V.; Antonovici, M.; Ens, W.; Wilkins, J. A.; Standing, K. G. Deamidation of Asn-Gly- Sequences during Sample Preparation for Proteomics: Consequences for MALDI and HPLC-MALDI Analysis. *Anal. Chem.* **2006**, *78* (18), 6645–6650. https://doi.org/10.1021/ac061017o.
- (27) Steen, H.; Jebanathirajah, J. A.; Rush, J.; Morrice, N.; Kirschner, M. W. Phosphorylation Analysis by Mass Spectrometry: Myths, Facts, and the Consequences for Qualitative and Quantitative Measurements. *Mol. Cell. Proteomics* **2006**, *5* (1), 172–181. https://doi.org/10.1074/mcp.M500135-MCP200.
- (28) Nesvizhskii, A. I.; Aebersold, R. Interpretation of Shotgun Proteomic Data: The Protein Inference Problem. *Mol. Cell. Proteomics* **2005**, *4* (10), 1419–1440. https://doi.org/10.1074/mcp.R500012-MCP200.
- (29) Chen, B.; Brown, K. A.; Lin, Z.; Ge, Y. Top-Down Proteomics: Ready for Prime Time? *Anal. Chem.* **2018**, *90* (1), 110–127. https://doi.org/10.1021/acs.analchem.7b04747.
- (30) Melby, J. A.; Roberts, D. S.; Larson, E. J.; Brown, K. A.; Bayne, E. F.; Jin, S.; Ge, Y. Novel Strategies to Address the Challenges in Top-Down Proteomics. *J. Am. Soc. Mass Spectrom.* **2021**, *32* (6), 1278–1294. https://doi.org/10.1021/JASMS.1C00099.
- (31) Kelleher, N. L. Top-Down Proteomics. *Anal. Chem.* **2004**, *76* (11), 197–203. https://doi.org/10.1016/B978-0-444-63688-1.00010-0.
- (32) Catherman, A. D.; Skinner, O. S.; Kelleher, N. L. Top Down Proteomics: Facts and Perspectives. *Biochem. Biophys. Res. Commun.* **2014**, *445* (4), 683–693. https://doi.org/10.1016/j.bbrc.2014.02.041.
- (33) Chapman, E. A.; Aballo, T. J.; Melby, J. A.; Zhou, T.; Price, S. J.; Rossler, K. J.; Lei, I.; Tang, P. C.; Ge, Y. Defining the Sarcomeric Proteoform Landscape in Ischemic Cardiomyopathy by Top-Down Proteomics. *J. Proteome Res.* **2023**, *22* (3), 931–941. https://doi.org/10.1021/acs.jproteome.2c00729.
- (34) Skinner, O. S.; Haverland, N. A.; Fornelli, L.; Melani, R. D.; Do Vale, L. H. F.; Seckler, H. S.; Doubleday, P. F.; Schachner, L. F.; Srzentić, K.; Kelleher, N. L.; et al. Top-down Characterization of Endogenous Protein Complexes with Native Proteomics. *Nat. Chem. Biol.* **2018**, *14* (1), 36–41. https://doi.org/10.1038/nchembio.2515.
- (35) Li, H.; Nguyen, H. H.; Loo, R. R. O.; Campuzano, I. D. G.; Loo, J. A. An Integrated Native Mass Spectrometry and Topdown Proteomics Method That Connects Sequence to Structure and Function of Macromolecular complexes. *Nat. Chem.* **2018**, *10* (2), 139–148. https://doi.org/10.1038/NCHEM.2908.
- (36) Liu, R.; Xia, S.; Li, H. Native Top-down Mass Spectrometry for Higher-Order Structural Characterization of Proteins and Complexes. *Mass Spectrometry Reviews*. 2022, pp 1–51. https://doi.org/10.1002/mas.21793.
- (37) Compton, P. D.; Zamdborg, L.; Thomas, P. M.; Kelleher, N. L. On the Scalability and Requirements of Whole Protein Mass Spectrometry. *Anal. Chem.* **2011**, *83* (17), 6868–6874. https://doi.org/10.1021/ac2010795.

- (38) Larson, E. J.; Pergande, M. R.; Moss, M. E.; Rossler, K. J.; Wenger, R. K.; Krichel, B.; Josyer, H.; Melby, J. A.; Roberts, D. S.; Pike, K.; et al. MASH Native: A Unified Solution for Native Top-Down Proteomics Data Processing. *Bioinformatics* **2023**, *39* (6), btad359.
- (39) Tran, J. C.; Zamdborg, L.; Ahlf, D. R.; Lee, J. E.; Catherman, A. D.; Durbin, K. R.; Tipton, J. D.; Vellaichamy, A.; Kellie, J. F.; Li, M.; et al. Mapping Intact Protein Isoforms in Discovery Mode Using Top-down Proteomics. *Nat. 2011 4807376* **2011**, *480* (7376), 254–258. https://doi.org/10.1038/nature10575.
- (40) Gregorich, Z. R.; Ge, Y. Top-down Proteomics in Health and Disease Challenges and Opportunities. *Proteomics* **2014**, *14*, 1195–1210.
- (41) Doucette, A. A.; Tran, J. C.; Wall, M. J.; Fitzsimmons, S. Intact Proteome Fractionation Strategies Compatible with Mass Spectrometry. http://dx.doi.org/10.1586/epr.11.67 2014, 8 (6), 787–800. https://doi.org/10.1586/EPR.11.67.
- (42) Zhang, Z.; Wu, S.; Stenoien, D. L.; Paša-Tolić, L. High-Throughput Proteomics. *Annu. Rev. Anal. Chem.* **2014**, *7*, 427–454. https://doi.org/10.1146/annurev-anchem-071213-020216.
- (43) Washburn, M. P.; Wolters, D.; Yates, J. R. Large-Scale Analysis of the Yeast Proteome by Multidimensional Protein Identification Technology. *Nat. Biotechnol.* **2001**, *19* (3), 242–247. https://doi.org/10.1038/85686.
- (44) Wang, Y.; Olesik, S. V. Enhanced-Fluidity Liquid Chromatography-Mass Spectrometry for Intact Protein Separation and Characterization. *Anal. Chem.* **2019**, *91* (1), 935–942. https://doi.org/10.1021/acs.analchem.8b03970.
- (45) Eschelbach, J. W.; Jorgenson, J. W. Improved Protein Recovery in Reversed-Phase Liquid Chromatography by the Use of Ultrahigh Pressures. *Anal. Chem.* **2006**, *78* (5), 1697–1706. https://doi.org/10.1021/ac0518304.
- (46) Liang, Y.; Jin, Y.; Wu, Z.; Tucholski, T.; Brown, K. A.; Zhang, L.; Zhang, Y.; Ge, Y. Bridged Hybrid Monolithic Column Coupled to High-Resolution Mass Spectrometry for Top-Down Proteomics. *Anal. Chem.* **2019**, *91* (3), 1743–1747. https://doi.org/10.1021/acs.analchem.8b05817.
- (47) Hayes, R.; Ahmed, A.; Edge, T.; Zhang, H. Core-Shell Particles: Preparation, Fundamentals and Applications in High Performance Liquid Chromatography. *J. Chromatogr. A* **2014**, *1357*, 36–52. https://doi.org/10.1016/j.chroma.2014.05.010.
- (48) Astefanei, A.; Dapic, I.; Camenzuli, M. Different Stationary Phase Selectivities and Morphologies for Intact Protein Separations. *Chromatographia*. Friedr. Vieweg und Sohn Verlags GmbH May 1, 2017, pp 665–687. https://doi.org/10.1007/s10337-016-3168-z.
- (49) Shen, Y.; Tolić, N.; Piehowski, P. D.; Shukla, A. K.; Kim, S.; Zhao, R.; Qu, Y.; Robinson, E.; Smith, R. D.; Paša-Tolić, L. High-Resolution Ultrahigh-Pressure Long Column Reversed-Phase Liquid Chromatography for Top-down Proteomics. *J. Chromatogr. A* **2017**, *1498*, 99–110. https://doi.org/10.1016/j.chroma.2017.01.008.
- (50) Battellino, T.; Ogata, K.; Spicer, V.; Ishihama, Y.; Krokhin, O. Acetic Acid Ion Pairing Additive for Reversed-Phase HPLC Improves Detection Sensitivity in Bottom-up

- Proteomics Compared to Formic Acid. *J. Proteome Res.* **2023**, *22* (1), 272–278. https://doi.org/10.1021/acs.jproteome.2c00388.
- (51) Tiambeng, T. N.; Roberts, D. S.; Brown, K. A.; Zhu, Y.; Chen, B.; Wu, Z.; Mitchell, S. D.; Guardado-Alvarez, T. M.; Jin, S.; Ge, Y. Nanoproteomics Enables Proteoform-Resolved Analysis of Low-Abundance Proteins in Human Serum. *Nat. Commun.* 2020 111 2020, 11 (1), 1–12. https://doi.org/10.1038/s41467-020-17643-1.
- (52) Larson, E. J.; Zhu, Y.; Wu, Z.; Chen, B.; Zhang, Z.; Zhou, S.; Han, L.; Zhang, Q.; Ge, Y. Rapid Analysis of Reduced Antibody Drug Conjugate by Online LC-MS/MS with Fourier Transform Ion Cyclotron Resonance Mass Spectrometry. *Anal. Chem.* **2020**, acs.analchem.0c03152. https://doi.org/10.1021/acs.analchem.0c03152.
- (53) Astefanei, A.; Dapic, I.; Camenzuli, M. Different Stationary Phase Selectivities and Morphologies for Intact Protein Separations. *Chromatographia* **2017**, *80* (5), 665–687. https://doi.org/10.1007/s10337-016-3168-z.
- (54) Tweeten, K. A.; Tweeten, T. N. Reversed-Phase Chromatography of Proteins on Resin-Based Wide-Pore Packings. *J. Chromatogr. A* **1986**, *359*, 111–119. https://doi.org/10.1016/0021-9673(86)80066-8.
- (55) Teutenberg, T.; Tuerk, J.; Holzhauser, M.; Kiffmeyer, T. K. Evaluation of Column Bleed by Using an Ultraviolet and a Charged Aerosol Detector Coupled to a High-Temperature Liquid Chromatographic System. *J. Chromatogr. A* **2006**, *1119* (1–2), 197–201. https://doi.org/10.1016/j.chroma.2005.12.011.
- (56) Kirkland, J. J.; Truszkowski, F. A.; Dilks, C. H.; Engel, G. S. Superficially Porous Silica Microspheres for Fast High-Performance Liquid Chromatography of Macromolecules. *J. Chromatogr. A* 2000, 890 (1), 3–13. https://doi.org/10.1016/S0021-9673(00)00392-7.
- (57) Schuster, S. A.; Wagner, B. M.; Boyes, B. E.; Kirkland, J. J. Optimized Superficially Porous Particles for Protein Separations. *J. Chromatogr. A* **2013**, *1315*, 118–126. https://doi.org/10.1016/J.CHROMA.2013.09.054.
- (58) Wagner, B. M.; Schuster, S. A.; Boyes, B. E.; Shields, T. J.; Miles, W. L.; Haynes, M. J.; Moran, R. E.; Kirkland, J. J.; Schure, M. R. Superficially Porous Particles with 1000 Å Pores for Large Biomolecule High Performance Liquid Chromatography and Polymer Size Exclusion Chromatography. *J. Chromatogr. A* 2017, 1489, 75–85. https://doi.org/10.1016/j.chroma.2017.01.082.
- (59) Horvath, C. G.; Preiss, B. A.; Lipsky, S. R. Fast Liquid Chromatography: An Investigation of Operating Parameters and the Separation of Nucleotides on Pellicular Ion Exchangers. *Anal. Chem.* **1967**, *39* (12), 1422–1428. https://doi.org/10.1021/ac60256a003.
- (60) Horvath, C.; Lipsy, S. R. Column Design in High Pressure Liquid Chromatography. *J. Chromatogr. Sci.* **1969**, 7 (2), 109–116. https://doi.org/10.1093/chromsci/7.2.109.
- (61) Issaeva, T.; Kourganov, A.; Unger, K. Super-High-Speed Liquid Chromatography of Proteins and Peptides on Non-Porous Micra NPS-RP Packings. *J. Chromatogr. A* **1999**, 846 (1–2), 13–23. https://doi.org/10.1016/S0021-9673(99)00360-X.
- (62) Kirkland, J. J.; Truszkowski, F. A.; Ricker, R. D. Atypical Silica-Based Column Packings

- for High-Performance Liquid Chromatography. *J. Chromatogr. A* **2002**, *965* (1–2), 25–34. https://doi.org/10.1016/S0021-9673(01)01339-5.
- (63) Kalghatigi, K. Micropellicular Stationary Phases For Rapid Protein Analysis By High-Performance Liquid Chromatography. *J. Chromatogr.* **1990**, *499*, 267–278.
- Wang, X.; Barber, W. E.; Carr, P. W. A Practical Approach to Maximizing Peak Capacity by Using Long Columns Packed with Pellicular Stationary Phases for Proteomic Research. *J. Chromatogr. A* **2006**, *1107* (1–2), 139–151. https://doi.org/10.1016/j.chroma.2005.12.050.
- (65) D. Antia, F.; Horváth, C. High-Performance Liquid Chromatography at Elevated Temperatures: Examination of Conditions for the Rapid Separation of Large Molecules. *J. Chromatogr. A* **1988**, *435* (C), 1–15. https://doi.org/10.1016/S0021-9673(01)82158-0.
- (66) Lynch, K. B.; Ren, J.; Beckner, M. A.; He, C.; Liu, S. Monolith Columns for Liquid Chromatographic Separations of Intact Proteins: A Review of Recent Advances and Applications. *Anal. Chim. Acta* **2019**, *1046*, 48–68. https://doi.org/10.1016/j.aca.2018.09.021.
- (67) Eeltink, S.; Wouters, S.; Dores-Sousa, J. L.; Svec, F. Advances in Organic Polymer-Based Monolithic Column Technology for High-Resolution Liquid Chromatography-Mass Spectrometry Profiling of Antibodies, Intact Proteins, Oligonucleotides, and Peptides. *J. Chromatogr. A* **2017**, *1498*, 8–21. https://doi.org/10.1016/j.chroma.2017.01.002.
- (68) Liu, Z.; Ou, J.; Liu, Z.; Liu, J.; Lin, H.; Wang, F.; Zou, H. Separation of Intact Proteins by Using Polyhedral Oligomeric Silsesquioxane Based Hybrid Monolithic Capillary Columns. *J. Chromatogr. A* 2013, 1317, 138–147. https://doi.org/10.1016/j.chroma.2013.09.004.
- (69) Zheng, S.; Yoo, C.; Delmotte, N.; Miller, F. R.; Huber, C. G.; Lubman, D. M. Monolithic Column HPLC Separation of Intact Proteins Analyzed by LC-MALDI Using on-Plate Digestion: An Approach to Integrate Protein Separation and Identification. *Anal. Chem.* 2006, 78 (14), 5198–5204. https://doi.org/10.1021/ac052284h.
- (70) Liu, J.; Ren, L.; Liu, Y.; Li, H.; Liu, Z. Weak Anion Exchange Chromatographic Profiling of Glycoprotein Isoforms on a Polymer Monolithic Capillary. *J. Chromatogr. A* **2012**, 1228, 276–282. https://doi.org/10.1016/j.chroma.2011.08.079.
- (71) Masini, J. C. Separation of Proteins by Cation-Exchange Sequential Injection Chromatography Using a Polymeric Monolithic Column. *Anal. Bioanal. Chem.* **2016**, *408* (5), 1445–1452. https://doi.org/10.1007/s00216-015-9242-9.
- (72) Passamonti, M.; de Roos, C.; Schoenmakers, P. J.; Gargano, A. F. G. Poly(Acrylamide-Co-N,N'-Methylenebisacrylamide) Monoliths for High-Peak-Capacity Hydrophilic-Interaction Chromatography-High-Resolution Mass Spectrometry of Intact Proteins at Low Trifluoroacetic Acid Content. *Anal. Chem.* 2021, 93 (48), 16000–16007. https://doi.org/10.1021/acs.analchem.1c03473.
- (73) Wilson, J. W.; Bilbao, A.; Wang, J.; Liao, Y. C.; Velickovic, D.; Wojcik, R.; Passamonti, M.; Zhao, R.; Gargano, A. F. G.; Gerbasi, V. R.; et al. Online Hydrophilic Interaction

- Chromatography (HILIC) Enhanced Top-Down Mass Spectrometry Characterization of the SARS-CoV-2 Spike Receptor-Binding Domain. *Anal. Chem.* **2022**, *94* (15), 5909–5917. https://doi.org/10.1021/acs.analchem.2c00139.
- (74) Wu, R.; Hu, L.; Wang, F.; Ye, M.; Zou, H. Recent Development of Monolithic Stationary Phases with Emphasis on Microscale Chromatographic Separation. *J. Chromatogr. A* **2008**, *1184* (1–2), 369–392. https://doi.org/10.1016/j.chroma.2007.09.022.
- (75) Detobel, F.; Broeckhoven, K.; Wellens, J.; Wouters, B.; Swart, R.; Ursem, M.; Desmet, G.; Eeltink, S. Parameters Affecting the Separation of Intact Proteins in Gradient-Elution Reversed-Phase Chromatography Using Poly(Styrene-Co-Divinylbenzene) Monolithic Capillary Columns. *J. Chromatogr. A* **2010**, *1217* (18), 3085–3090. https://doi.org/10.1016/j.chroma.2010.03.002.
- (76) De Malsche, W.; De Bruyne, S.; Op De Beek, J.; Sandra, P.; Gardeniers, H.; Desmet, G.; Lynen, F. Capillary Liquid Chromatography Separations Using Non-Porous Pillar Array Columns. *J. Chromatogr. A* **2012**, *1230*, 41–47. https://doi.org/10.1016/j.chroma.2012.01.060.
- (77) Cho, B. G.; Jiang, P.; Goli, M.; Gautam, S.; Mechref, Y. Using Micro Pillar Array Columns (MPAC) for the Analysis of Permethylated Glycans. *Analyst* **2021**, *146* (13), 4374–4383. https://doi.org/10.1039/d1an00643f.
- (78) De Malsche, W.; De Bruyne, S.; Op De Beek, J.; Eeltink, S.; Detobel, F.; Gardeniers, H.; Desmet, G. Separations Using a Porous-Shell Pillar Array Column on a Capillary LC Instrument. *J. Sep. Sci.* **2012**, *35*, 2010–2017.
- (79) Isokawa, M.; Takatsuki, K.; Song, Y.; Shih, K.; Nakanishi, K.; Xie, Z.; Yoon, D. H.; Sekiguchi, T.; Funatsu, T.; Shoji, S.; et al. Liquid Chromatography Chip with Low-Dispersion and Low-Pressure-Drop Turn Structure Utilizing a Distribution-Controlled Pillar Array. *Anal. Chem.* **2016**, *88* (12), 6485–6491. https://doi.org/10.1021/acs.analchem.6b01201.
- (80) Tóth, G.; Panić-Janković, T.; Mitulović, G. Pillar Array Columns for Peptide Separations in Nanoscale Reversed-Phase Chromatography. *J. Chromatogr. A* **2019**, *1603*, 426–432. https://doi.org/10.1016/j.chroma.2019.06.067.
- (81) De Malsche, W.; Op De Beeck, J.; De Bruyne, S.; Gardeniers, H.; Desmet, G. Realization of 1 × 10 6 Theoretical Plates in Liquid Chromatography Using Very Long Pillar Array Columns. *Anal. Chem.* **2012**, *84* (3), 1214–1219. https://doi.org/10.1021/ac203048n.
- (82) Potschka, M. Mechanism of Size-Exclusion Chromatography. I. Role of Convection and Obstructed Diffusion in Size-Exclusion Chromatography. *J. Chromatogr. A* **1993**, *648* (1), 41–69. https://doi.org/10.1016/0021-9673(93)83287-3.
- (83) Cai, W.; Tucholski, T.; Chen, B.; Alpert, A. J.; McIlwain, S.; Kohmoto, T.; Jin, S.; Ge, Y. Top-Down Proteomics of Large Proteins up to 223 KDa Enabled by Serial Size Exclusion Chromatography Strategy. *Anal. Chem.* **2017**, *89* (10), 5467–5475. https://doi.org/10.1021/acs.analchem.7b00380.
- (84) Simpson, D. C.; Ahn, S.; Pasa-Tolic, L.; Bogdanov, B.; Mottaz, H. M.; Vilkov, A. N.;

- Anderson, G. A.; Lipton, M. S.; Smith, R. D. Using Size Exclusion Chromatography-RPLC and RPLC-CIEF as Two-Dimensional Separation Strategies for Protein Profiling. *Electrophoresis* **2006**, *27* (13), 2722–2733. https://doi.org/10.1002/elps.200600037.
- (85) Ge, Y.; Rybakova, I. N.; Xu, Q.; Moss, R. L. Top-down High-Resolution Mass Spectrometry of Cardiac Myosin Binding Protein C Revealed That Truncation Alters Protein Phosphorylation State. *Proc. Natl. Acad. Sci. U. S. A.* **2009**, *106* (31), 12658–12663. https://doi.org/10.1073/pnas.0813369106.
- (86) Jin, Y.; Wei, L.; Cai, W.; Lin, Z.; Wu, Z.; Peng, Y.; Kohmoto, T.; Moss, R. L.; Ge, Y. Complete Characterization of Cardiac Myosin Heavy Chain (223 KDa) Enabled by Size-Exclusion Chromatography and Middle-Down Mass Spectrometry. *Anal. Chem.* **2017**, *89* (9), 4922–4930. https://doi.org/10.1021/acs.analchem.7b00113.
- (87) Tucholski, T.; Knott, S. J.; Chen, B.; Pistono, P.; Lin, Z.; Ge, Y. A Top-down Proteomics Platform Coupling Serial Size Exclusion Chromatography and Fourier Transform Ion Cyclotron Resonance Mass Spectrometry. *Anal. Chem.* **2019**, *91* (6), 3835–3844. https://doi.org/10.1021/acs.analchem.8b04082.
- (88) Tran, J. C.; Doucette, A. A. Multiplexed Size Separation of Intact Proteins in Solution Phase for Mass Spectrometry. *Anal. Chem.* **2009**, *81* (15), 6201–6209. https://doi.org/10.1021/ac900729r.
- (89) Takemori, A.; Butcher, D. S.; Harman, V. M.; Brownridge, P.; Shima, K.; Higo, D.; Ishizaki, J.; Hasegawa, H.; Suzuki, J.; Yamashita, M.; et al. PEPPI-MS: Polyacrylamide-Gel-Based Prefractionation for Analysis of Intact Proteoforms and Protein Complexes by Mass Spectrometry. *J. Proteome Res.* **2020**, *19* (9), 3779–3791. https://doi.org/10.1021/acs.jproteome.0c00303.
- (90) Jooß, K.; McGee, J. P.; Kelleher, N. L. Native Mass Spectrometry at the Convergence of Structural Biology and Compositional Proteomics. *Acc. Chem. Res.* **2022**. https://doi.org/10.1021/acs.accounts.2c00216.
- (91) García, M. C. The Effect of the Mobile Phase Additives on Sensitivity in the Analysis of Peptides and Proteins by High-Performance Liquid Chromatography-Electrospray Mass Spectrometry. *J. Chromatogr. B Anal. Technol. Biomed. Life Sci.* **2005**, *825* (2), 111–123. https://doi.org/10.1016/j.jchromb.2005.03.041.
- (92) Alpert, A. J. High-Performance Hydrophobic-Interaction Chromatography of Proteins on a Series of Poly(Alkyl Aspart-Amide)-Silicas. *J. Chromatogr. A* **1986**, *359*, 85–97. https://doi.org/10.1016/0021-9673(86)80064-4.
- (93) Queiroz, J. A.; Tomaz, C. T.; Cabral, J. M. S. Hydrophobic Interaction Chromatography of Proteins. *J. Biotechnol.* **2001**, *87* (2), 143–159. https://doi.org/10.1016/S0168-1656(01)00237-1.
- (94) Chen, B.; Peng, Y.; Valeja, S. G.; Xiu, L.; Alpert, A. J.; Ge, Y. Online Hydrophobic Interaction Chromatography-Mass Spectrometry for Top-Down Proteomics. *Anal. Chem.* **2016**, *88* (3), 1885–1891. https://doi.org/10.1021/acs.analchem.5b04285.
- (95) Chen, B.; Lin, Z.; Alpert, A. J.; Fu, C.; Zhang, Q.; Pritts, W. A.; Ge, Y. Online

- Hydrophobic Interaction Chromatography-Mass Spectrometry for the Analysis of Intact Monoclonal Antibodies. *Anal. Chem.* **2018**, *90* (12), 7135–7138. https://doi.org/10.1021/acs.analchem.8b01865.
- (96) Mehaffey, M. R.; Xia, Q.; Brodbelt, J. S. Uniting Native Capillary Electrophoresis and Multistage Ultraviolet Photodissociation Mass Spectrometry for Online Separation and Characterization of Escherichia Coli Ribosomal Proteins and Protein Complexes. *Anal. Chem.* **2020**, *92* (22), 15202–15211. https://doi.org/10.1021/acs.analchem.0c03784.
- (97) Shen, X.; Kou, Q.; Guo, R.; Yang, Z.; Chen, D.; Liu, X.; Hong, H.; Sun, L. Native Proteomics in Discovery Mode Using Size-Exclusion Chromatography-Capillary Zone Electrophoresis-Tandem Mass Spectrometry. *Anal. Chem.* **2018**, *90* (17), 10095–10099. https://doi.org/10.1021/acs.analchem.8b02725.
- (98) Jooß, K.; McGee, J. P.; Melani, R. D.; Kelleher, N. L. Standard Procedures for Native CZE-MS of Proteins and Protein Complexes up to 800 KDa. *Electrophoresis* **2021**, *42*, 1050–1059.
- (99) Jorgenson, J. W.; Lukacs, K. D. Capillary Zone Electrophoresis. *Science* (80-.). **1983**, 222 (4621), 266–272.
- (100) Dong, Y.-M.; Chien, K.-Y.; Chen, J.-T.; Wang, T.-C. V.; Yu, J.-S. Site-specific Separation and Detection of Phosphopeptide Isomers with PH-mediated Stacking Capillary Electrophoresis-Electrospray Ionization-Tandem Mass Spectrometry. *Journal of Separation Science*. 2013, pp 1582–1589.
- (101) Lindner, H.; Helliger, W.; Dirschlmayer, A.; Jaquemar, M.; Puschendorf, B. High-Performance Capillary Electrophoresis of Core Histones and Their Acetylated Modified Derivatives. *Biochem. J.* **1992**, *283* (2), 467–471. https://doi.org/10.1042/bj2830467.
- (102) Andrasi, M.; Pajaziti, B.; Sipos, B.; Nagy, C.; Hamidli, N.; Gaspar, A. Determination of Deamidated Isoforms of Human Insulin Using Capillary Electrophoresis. *J. Chromatogr. A* **2020**, *1626*, 461344. https://doi.org/10.1016/j.chroma.2020.461344.
- (103) Shen, X.; Liang, Z.; Xu, T.; Yang, Z.; Wang, Q.; Chen, D.; Pham, L.; Du, W.; Sun, L. Investigating Native Capillary Zone Electrophoresis-Mass Spectrometry on a High-End Quadrupole-Time-of-Flight Mass Spectrometer for the Characterization of Monoclonal Antibodies. *Int. J. Mass Spectrom.* **2021**, *462*, 116541. https://doi.org/10.1016/j.ijms.2021.116541.
- (104) Stolz, A.; Jooß, K.; Höcker, O.; Römer, J.; Schlecht, J.; Neusüß, C. Recent Advances in Capillary Electrophoresis-mass Spectrometry Instrumentation. *Electrophoresis* **2019**, *40*, 79–112.
- (105) Han, M.; Rock, B. M.; Pearson, J. T.; Rock, D. A. Intact Mass Analysis of Monoclonal Antibodies by Capillary Electrophoresis-Mass Spectrometry. *J. Chromatogr. B Anal. Technol. Biomed. Life Sci.* **2016**, *1011*, 24–32. https://doi.org/10.1016/j.jchromb.2015.12.045.
- (106) Zhang, W.; Xiang, Y.; Xu, W. Probing Protein Higher-Order Structures by Native Capillary Electrophoresis-Mass Spectrometry. *TrAC Trends Anal. Chem.* **2022**, *157*,

- 116739. https://doi.org/10.1016/j.trac.2022.116739.
- (107) Fussl, F.; Trappe, A.; Carillo, S.; Jakes, C.; Bones, J. Comparative Elucidation of Cetuximab Heterogeneity on the Intact Protein Level by Cation Exchange Chromatography and Capillary Electrophoresis Coupled to Mass Spectrometry. *Anal. Chem.* **2020**, *92* (7), 5431–5438. https://doi.org/10.1021/acs.analchem.0c00185.
- (108) Mack, S.; Arnold, D.; Bogdan, G.; Bousse, L.; Danan, L.; Dolnik, V.; Ducusin, M.; Gwerder, E.; Herring, C.; Jensen, M.; et al. A Novel Microchip-based Imaged CIEF-MS System for Comprehensive Characterization and Identification of Biopharmaceutical Charge Variants. *Electrophoresis* **2019**, *40*, 3084–3091.
- (109) Wu, Z.; Wang, H.; Wu, J.; Huang, Y.; Zhao, X.; Nguyen, J. B.; Rosconi, M. P.; Pyles, E. A.; Qiu, H.; Li, N. High-Sensitivity and High-Resolution Therapeutic Antibody Charge Variant and Impurity Characterization by Microfluidic Native Capillary Electrophoresis-Mass Spectrometry. *J. Pharm. Biomed. Anal.* **2023**, *223* (October 2022), 115147. https://doi.org/10.1016/j.jpba.2022.115147.
- (110) Baker, E. S.; Burnum-Johnson, K. E.; Ibrahim, Y. M.; Orton, D. J.; Monroe, M. E.; Kelly, R. T.; Moore, R. J.; Zhang, X.; Théberge, R.; Costello, C. E.; et al. Enhancing Bottom-up and Top-down Proteomic Measurements with Ion Mobility Separations. *Proteomics* **2015**, *15*, 276–2776.
- (111) Zinnel, N. F.; Pai, P. J.; Russell, D. H. Ion Mobility-Mass Spectrometry (IM-MS) for Topdown Proteomics: Increased Dynamic Range Affords Increased Sequence Coverage. *Anal. Chem.* **2012**, *84* (7), 3390–3397. https://doi.org/10.1021/ac300193s.
- (112) Nshanian, M.; Lantz, C.; Wongkongkathep, P.; Schrader, T.; Klärner, F. G.; Blümke, A.; Despres, C.; Ehrmann, M.; Smet-Nocca, C.; Bitan, G.; et al. Native Top-Down Mass Spectrometry and Ion Mobility Spectrometry of the Interaction of Tau Protein with a Molecular Tweezer Assembly Modulator. *J. Am. Soc. Mass Spectrom.* **2019**, *30* (1), 16–23. https://doi.org/10.1007/s13361-018-2027-6.
- (113) Shvartsburg, A. A.; Smith, R. D. Fundamentals of Traveling Wave Ion Mobility Spectrometry. *Anal. Chem.* **2008**, *80* (24), 9689–9699. https://doi.org/10.1021/ac8016295.
- (114) Guevremont, R. High-Field Asymmetric Waveform Ion Mobility Spectrometry: A New Tool for Mass Spectrometry. *J. Chromatogr. A* **2004**, *1058* (1–2), 3–19. https://doi.org/10.1016/j.chroma.2004.08.119.
- (115) Fernandez-Lima, F.; Kaplan, D. A.; Suetering, J.; Park, M. A. Gas-Phase Separation Using a Trapped Ion Mobility Spectrometer. *Springer*. https://doi.org/10.1007/s12127-011-0067-8.
- (116) Webb, I. K.; Garimella, S. V. B.; Tolmachev, A. V.; Chen, T. C.; Zhang, X.; Norheim, R. V.; Prost, S. A.; LaMarche, B.; Anderson, G. A.; Ibrahim, Y. M.; et al. Experimental Evaluation and Optimization of Structures for Lossless Ion Manipulations for Ion Mobility Spectrometry with Time-of-Flight Mass Spectrometry. *Anal. Chem.* **2014**, *86* (18), 9169–9176. https://doi.org/10.1021/ac502055e.
- (117) Winter, D. L.; Wilkins, M. R.; Donald, W. A. Differential Ion Mobility-Mass

- Spectrometry for Detailed Analysis of the Proteome. *Trends Biotechnol.* **2019**, *37* (2), 198–213. https://doi.org/10.1016/j.tibtech.2018.07.018.
- (118) Stow, S. M.; Causon, T. J.; Zheng, X.; Kurulugama, R. T.; Mairinger, T.; May, J. C.; Rennie, E. E.; Baker, E. S.; Smith, R. D.; McLean, J. A.; et al. An Interlaboratory Evaluation of Drift Tube Ion Mobility-Mass Spectrometry Collision Cross Section Measurements. *Anal. Chem.* **2017**, *89* (17), 9048–9055. https://doi.org/10.1021/acs.analchem.7b01729.
- (119) Dodds, J. N.; Baker, E. S. Ion Mobility Spectrometry: Fundamental Concepts, Instrumentation, Applications, and the Road Ahead. *J. Am. Soc. Mass Spectrom.* **2019**, *30*, 2185–2195. https://doi.org/10.1007/s13361-019-02288-2.
- (120) Mason, E. A.; Schamp, H. W. Mobility of Gaseous Lons in Weak Electric Fields. *Ann. Phys. (N. Y).* **1958**, *4* (3), 233–270. https://doi.org/10.1016/0003-4916(58)90049-6.
- (121) Ruotolo, B. T.; Robinson, C. V. Aspects of Native Proteins Are Retained in Vacuum. *Curr. Opin. Chem. Biol.* **2006**, *10* (5), 402–408. https://doi.org/10.1016/j.cbpa.2006.08.020.
- (122) Bleiholder, C.; Liu, F. C. Structure Relaxation Approximation (SRA) for Elucidation of Protein Structures from Ion Mobility Measurements. *J. Phys. Chem. B* **2019**, *123* (13), 2756–2769. https://doi.org/10.1021/acs.jpcb.8b11818.
- (123) Dworzanski, J. P.; Kim, M. G.; Peter Snyder, A.; Arnold, N. S.; Meuzelaar, H. L. C. Performance Advances in Ion Mobility Spectrometry through Combination with High Speed Vapor Sampling, Preconcentration and Separation Techniques. *Anal. Chim. Acta* **1994**, *293* (3), 219–235. https://doi.org/10.1016/0003-2670(94)85027-5.
- (124) Meier, F.; Beck, S.; Grassl, N.; Lubeck, M.; Park, M. A.; Raether, O.; Mann, M. Parallel Accumulation-Serial Fragmentation (PASEF): Multiplying Sequencing Speed and Sensitivity by Synchronized Scans in a Trapped Ion Mobility Device. *J. Proteome Res.* **2015**, *14* (12), 5378–5387. https://doi.org/10.1021/acs.jproteome.5b00932.
- (125) D'Atri, V.; Causon, T.; Hernandez-Alba, O.; Mutabazi, A.; Veuthey, J.-L.; Cianferani, S.; Guillarme, D. Adding a New Separation Dimension to MS and LC-MS: What Is the Utility of Ion Mobility Spectrometry? *J. Sep. Sci.* **2018**, *41* (1), 20–67. https://doi.org/10.1002/jssc.201700919.
- (126) Ridgeway, M. E.; Wolff, J. J.; Silveira, J. A.; Lin, C.; Costello, C. E.; Park, M. A. Gated Trapped Ion Mobility Spectrometry Coupled to Fourier Transform Ion Cyclotron Resonance Mass Spectrometry. *Int. J. Ion Mobil. Spectrom.* **2016**, *19* (2–3), 77–85. https://doi.org/10.1007/s12127-016-0197-0.
- (127) Melani, R. D.; Srzentić, K.; Gerbasi, V. R.; McGee, J. P.; Huguet, R.; Fornelli, L.; Kelleher, N. L. Direct Measurement of Light and Heavy Antibody Chains Using Ion Mobility and Middle-down Mass Spectrometry. *MAbs* **2019**, *11* (8), 1351–1357. https://doi.org/10.1080/19420862.2019.1668226.
- (128) Giles, K.; Williams, J. P.; Campuzano, I. Enhancements in Travelling Wave Ion Mobility Resolution. *Rapid Commun. Mass Spectrom.* **2011**, *25* (11), 1559–1566.

- https://doi.org/10.1002/rcm.5013.
- (129) Hopper, J. T. S.; Oldham, N. J. Collision Induced Unfolding of Protein Ions in the Gas Phase Studied by Ion Mobility-Mass Spectrometry: The Effect of Ligand Binding on Conformational Stability. *J. Am. Soc. Mass Spectrom.* **2009**, *20* (10), 1851–1858. https://doi.org/10.1016/j.jasms.2009.06.010.
- (130) Watanabe, Y.; Vasiljevic, S.; Allen, J. D.; Seabright, G. E.; Duyvesteyn, H. M. E.; Doores, K. J.; Crispin, M.; Struwe, W. B. Signature of Antibody Domain Exchange by Native Mass Spectrometry and Collision-Induced Unfolding. *Anal. Chem.* **2018**, *90* (12), 7325–7331. https://doi.org/10.1021/acs.analchem.8b00573.
- (131) Dixit, S. M.; Polasky, D. A.; Ruotolo, B. T. Collision Induced Unfolding of Isolated Proteins in the Gas Phase: Past, Present, and Future. *Curr. Opin. Chem. Biol.* **2018**, *42*, 93–100. https://doi.org/10.1016/j.cbpa.2017.11.010.
- (132) Tian, Y.; Han, L.; Buckner, A. C.; Ruotolo, B. T. Collision Induced Unfolding of Intact Antibodies: Rapid Characterization of Disulfide Bonding Patterns, Glycosylation, and Structures. **2015**. https://doi.org/10.1021/acs.analchem.5b03291.
- (133) Tian, Y.; Lippens, J. L.; Netirojjanakul, C.; Campuzano, I. D. G.; Ruotolo, B. T. Quantitative Collision-Induced Unfolding Differentiates Model Antibody-Drug Conjugates. *Protein Sci.* **2019**, *28* (3), 598–608. https://doi.org/10.1002/pro.3560.
- (134) Gadkari, V. V.; Ramírez, C. R.; Vallejo, D. D.; Kurulugama, R. T.; Fjeldsted, J. C.; Ruotolo, B. T. Enhanced Collision Induced Unfolding and Electron Capture Dissociation of Native-like Protein Ions. *Anal. Chem.* **2020**, *92* (23), 15489–15496. https://doi.org/10.1021/acs.analchem.0c03372.
- (135) Fernandez-Lima, F.; Kaplan, D. A.; Suetering, J.; Park, M. A. Gas-Phase Separation Using a Trapped Ion Mobility Spectrometer. *Int. J. Ion Mobil. Spectrom.* **2011**, *14* (2), 93–98. https://doi.org/10.1007/s12127-011-0067-8.
- (136) Jeanne Dit Fouque, K.; Garabedian, A.; Leng, F.; Tse-Dinh, Y.-C.; Ridgeway, M. E.; Park, M. A.; Fernandez-Lima, F. Trapped Ion Mobility Spectrometry of Native Macromolecular Assemblies. *Anal. Chem.* **2021**, *93* (5), 2933–2941. https://doi.org/10.1021/acs.analchem.0c04556.
- (137) Liu, F. C.; Cropley, T. C.; Ridgeway, M. E.; Park, M. A.; Bleiholder, C. Structural Analysis of the Glycoprotein Complex Avidin by Tandem-Trapped Ion Mobility Spectrometry-Mass Spectrometry (Tandem-TIMS/MS). *Anal. Chem.* **2020**, *92* (6), 4459–4467. https://doi.org/10.1021/acs.analchem.9b05481.
- (138) Meier, F.; Brunner, A. D.; Frank, M.; Ha, A.; Bludau, I.; Voytik, E.; Kaspar-Schoenefeld, S.; Lubeck, M.; Raether, O.; Bache, N.; et al. DiaPASEF: Parallel Accumulation—Serial Fragmentation Combined with Data-Independent Acquisition. *Nat. Methods* **2020**, *17* (12), 1229–1236. https://doi.org/10.1038/s41592-020-00998-0.
- (139) Tose, L. V.; Benigni, P.; Leyva, D.; Sundberg, A.; Ramírez, C. E.; Ridgeway, M. E.; Park, M. A.; Romão, W.; Jaffé, R.; Fernandez-Lima, F. Coupling Trapped Ion Mobility Spectrometry to Mass Spectrometry: Trapped Ion Mobility Spectrometry–Time-of-Flight

- Mass Spectrometry versus Trapped Ion Mobility Spectrometry–Fourier Transform Ion Cyclotron Resonance Mass Spectrometry. *Rapid Commun. Mass Spectrom.* **2018**, *32* (15), 1287–1295. https://doi.org/10.1002/rcm.8165.
- (140) Borotto, N. B.; Osho, K. E.; Richards, T. K.; Graham, K. A. Collision-Induced Unfolding of Native-like Protein Ions Within a Trapped Ion Mobility Spectrometry Device. *J. Am. Soc. Mass Spectrom.* **2022**, *33* (1), 83–89. https://doi.org/10.1021/jasms.1c00273.
- (141) Graham, K. A.; Lawlor, C. F.; Borotto, N. B. Characterizing the Top-down Sequencing of Protein Ions Prior to Mobility Separation in a TimsTOF. *Analyst* **2023**. https://doi.org/10.1039/d2an01682f.
- (142) Liu, F. C.; Kirk, S. R.; Bleiholder, C. On the Structural Denaturation of Biological Analytes in Trapped Ion Mobility Spectrometry-Mass Spectrometry †. *Cite this Anal.* **2016**, *141*, 3722. https://doi.org/10.1039/c5an02399h.
- (143) Larson, E. J.; Roberts, D. S.; Melby, J. A.; Buck, K. M.; Zhu, Y.; Zhou, S.; Han, L.; Zhang, Q.; Ge, Y. High-Throughput Multi-Attribute Analysis of Antibody-Drug Conjugates Enabled by Trapped Ion Mobility Spectrometry and Top-Down Mass Spectrometry. *Anal. Chem.* **2021**, *93* (29), 10013–10021. https://doi.org/10.1021/acs.analchem.1c00150.
- (144) Doucette, A. A.; Tran, J. C.; Wall, M. J.; Fitzsimmons, S. Intact Proteome Fractionation Strategies Compatible with Mass Spectrometry. *Expert Rev. Proteomics* **2011**, *8* (6), 787–800. https://doi.org/10.1586/epr.11.67.
- (145) Pirok, B. W. J.; Stoll, D. R.; Schoenmakers, P. J. Recent Developments in Two-Dimensional Liquid Chromatography: Fundamental Improvements for Practical Applications. **2018**. https://doi.org/10.1021/acs.analchem.8b04841.
- (146) Brown, K. A.; Tucholski, T.; Alpert, A. J.; Eken, C.; Wesemann, L.; Kyrvasilis, A.; Jin, S.; Ge, Y. Top-Down Proteomics of Endogenous Membrane Proteins Enabled by Cloud Point Enrichment and Multidimensional Liquid Chromatography-Mass Spectrometry. *Anal. Chem.* **2020**, *92* (24), 15726–15735. https://doi.org/10.1021/ACS.ANALCHEM.0C02533/SUPPL\_FILE/AC0C02533\_SI\_003. XLSX.
- (147) Xiu, L.; Valeja, S. G.; Alpert, A. J.; Jin, S.; Ge, Y. Effective Protein Separation by Coupling Hydrophobic Interaction and Reverse Phase Chromatography for Top-down Proteomics. *Anal. Chem.* **2014**, *86* (15), 7899–7906. https://doi.org/10.1021/ac501836k.
- (148) Wang, Z.; Ma, H.; Smith, K.; Wu, S. Two-Dimensional Separation Using High-PH and Low-PH Reversed Phase Liquid Chromatography for Top-down Proteomics. *Int. J. Mass Spectrom.* **2018**, *427*, 43–51. https://doi.org/10.1016/j.ijms.2017.09.001.
- (149) Valeja, S. G.; Xiu, L.; Gregorich, Z. R.; Guner, H.; Jin, S.; Ge, Y. Three Dimensional Liquid Chromatography Coupling Ion Exchange Chromatography/Hydrophobic Interaction Chromatography/Reverse Phase Chromatography for Effective Protein Separation in Top-Down Proteomics Santosh. *Anal. Chem.* **2015**, *87* (10), 5363–5371. https://doi.org/10.1021/acs.analchem.5b00657.

- (150) Stoll, D. R.; Shoykhet, K.; Petersson, P.; Buckenmaier, S. Active Solvent Modulation: A Valve-Based Approach to Improve Separation Compatibility in Two-Dimensional Liquid Chromatography. *Anal. Chem.* **2017**, *89* (17), 9260–9267. https://doi.org/10.1021/acs.analchem.7b02046.
- (151) Vonk, R. J.; Gargano, A. F. G. G.; Davydova, E.; Dekker, H. L.; Eeltink, S.; De Koning, L. J.; Schoenmakers, P. J. Comprehensive Two-Dimensional Liquid Chromatography with Stationary-Phase-Assisted Modulation Coupled to High-Resolution Mass Spectrometry Applied to Proteome Analysis of Saccharomyces Cerevisiae. *Anal. Chem.* **2015**, *87* (10), 5387–5394. https://doi.org/10.1021/acs.analchem.5b00708.
- (152) Pursch, M.; Buckenmaier, S. Loop-Based Multiple Heart-Cutting Two-Dimensional Liquid Chromatography for Target Analysis in Complex Matrices. *Anal. Chem.* **2015**, *87* (10), 5310–5317. https://doi.org/10.1021/acs.analchem.5b00492.
- (153) Gargano, A. F. G.; Shaw, J. B.; Zhou, M.; Wilkins, C. S.; Fillmore, T. L.; Moore, R. J.; Somsen, G. W.; Paša-Tolić, L. Increasing the Separation Capacity of Intact Histone Proteoforms Chromatography Coupling Online Weak Cation Exchange-HILIC to Reversed Phase LC UVPD-HRMS. *J. Proteome Res.* **2018**, *17* (11), 3791–3800. https://doi.org/10.1021/acs.jproteome.8b00458.
- (154) Baghdady, Y. Z.; Schug, K. A. Online Comprehensive High PH Reversed Phase × Low PH Reversed Phase Approach for Two-Dimensional Separations of Intact Proteins in Top-Down Proteomics. *Anal. Chem.* **2019**, *91* (17), 11085–11091. https://doi.org/10.1021/ACS.ANALCHEM.9B01665/ASSET/IMAGES/LARGE/AC9B01665\_0004.JPEG.
- (155) Wang, Z.; Yu, D.; Cupp-Sutton, K. A.; Liu, X.; Smith, K.; Wu, S. Development of an Online 2D Ultrahigh-Pressure Nano-LC System for High-PH and Low-PH Reversed Phase Separation in Top-Down Proteomics. *Anal. Chem.* **2020**, *92* (19), 12774–12777. https://doi.org/10.1021/ACS.ANALCHEM.0C03395/SUPPL\_FILE/AC0C03395\_SI\_002. XLSX.
- (156) Cline, E. N.; Alvarez, C.; Duan, J.; Patrie, S. M. Online MSEC2-NRPLC-MS for Improved Sensitivity of Intact Protein Detection of IEF-Separated Nonhuman Primate Cerebrospinal Fluid Proteins. *Anal. Chem.* 2021, 93 (50), 16741–16750. https://doi.org/10.1021/ACS.ANALCHEM.1C00396/ASSET/IMAGES/LARGE/AC1C00 396\_0006.JPEG.
- (157) Moore, A. W.; Jorgenson, J. W. Comprehensive Three-Dimensional Separation of Peptides Using Size Exclusion Chromatography/Reversed Phase Liquid Chromatography/Optically Gated Capillary Zone Electrophoresis. *Anal. Chem.* 1995, 67 (19), 3456–3463. https://doi.org/10.1021/ac00115a014.
- (158) Kong, A. T.; Leprevost, F. V.; Avtonomov, D. M.; Mellacheruvu, D.; Nesvizhskii, A. I. MSFragger: Ultrafast and Comprehensive Peptide Identification in Mass Spectrometry-Based Proteomics. *Nat. Methods* **2017**, *14* (5), 513–520. https://doi.org/10.1038/nmeth.4256.
- (159) Demichev, V.; Messner, C. B.; Vernardis, S. I.; Lilley, K. S.; Ralser, M. DIA-NN: Neural

- Networks and Interference Correction Enable Deep Proteome Coverage in High Throughput. *Nat. Methods* **2020**, *17* (1), 41–44. https://doi.org/10.1038/s41592-019-0638-x.
- (160) Taylor, G. K.; Kim, Y. Bin; Forbes, A. J.; Meng, F.; McCarthy, R.; Kelleher, N. L. Web and Database Software for Identification of Intact Proteins Using "Top down" Mass Spectrometry. *Anal. Chem.* **2003**, *75* (16), 4081–4086. https://doi.org/10.1021/ac0341721.
- (161) Kellie, J. F.; Tran, J. C.; Lee, J. E.; Ahlf, D. R.; Thomas, H. M.; Ntai, I.; Catherman, A. D.; Durbin, K. R.; Zamdborg, L.; Vellaichamy, A.; et al. The Emerging Process of Top Down Mass Spectrometry for Protein Analysis: Biomarkers, Protein-Therapeutics, and Achieving High Throughput. *Mol. Biosyst.* **2010**, *6* (9), 1532–1539. https://doi.org/10.1039/c000896f.
- (162) Fellers, R. T.; Greer, J. B.; Early, B. P.; Yu, X.; Leduc, R. D.; Kelleher, N. L.; Thomas, P. M. ProSight Lite: Graphical Software to Analyze Top-Down Mass Spectrometry Data. *Proteomics* **2015**, *15* (7), 1235–1238. https://doi.org/10.1002/pmic.201570050.ProSight.
- (163) Guner, H.; Close, P. L.; Cai, W.; Zhang, H.; Peng, Y.; Gregorich, Z. R.; Ge, Y. MASH Suite: A User-Friendly and Versatile Software Interface for High-Resolution Mass Spectrometry Data Interpretation and Visualization. *J. Am. Soc. Mass Spectrom.* **2014**, *25* (3), 464–470. https://doi.org/10.1007/s13361-013-0789-4.
- (164) Cai, W.; Guner, H.; Gregorich, Z. R.; Chen, A. J.; Ayaz-Guner, S.; Peng, Y.; Valeja, S. G.; Liu, X.; Ge, Y. MASH Suite Pro: A Comprehensive Software Tool for Top-Down Proteomics. *Mol. Cell. Proteomics* **2016**, *15* (2), 703–714. https://doi.org/10.1074/mcp.O115.054387.
- (165) Wu, Z.; Roberts, D. S.; Melby, J. A.; Wenger, K.; Wetzel, M.; Gu, Y.; Ramanathan, S. G.; Bayne, E. F.; Liu, X.; Sun, R.; et al. MASH Explorer: A Universal Software Environment for Top-Down Proteomics. *J. Proteome Res.* **2020**, *19* (9), 3867–3876. https://doi.org/10.1021/acs.jproteome.0c00469.
- (166) Schaffer, L. V.; Millikin, R. J.; Shortreed, M. R.; Scalf, M.; Smith, L. M. Improving Proteoform Identifications in Complex Systems through Integration of Bottom-Up and Top-Down Data. *J. Proteome Res.* **2020**, *19* (8), 3510–3517. https://doi.org/10.1021/acs.jproteome.0c00332.
- (167) Smith, L. M.; Thomas, P. M.; Shortreed, M. R.; Schaffer, L. V.; Fellers, R. T.; LeDuc, R. D.; Tucholski, T.; Ge, Y.; Agar, J. N.; Anderson, L. C.; et al. A Five-Level Classification System for Proteoform Identifications. *Nat. Methods* **2019**, *16* (10), 939–940. https://doi.org/10.1038/s41592-019-0573-x.
- (168) Zhang, Z.; Marshall, A. G. A Universal Algorithm for Fast and Automated Charge State Deconvolution of Electrospray Mass-to-Charge Ratio Spectra. *J. Am. Soc. Mass Spectrom.* **1998**, *9* (3), 225–233. https://doi.org/10.1016/S1044-0305(97)00284-5.
- (169) Ferrige, A. G.; Seddon, M. J.; Jarvis, S.; Skilling, J.; Aplin, R. Maximum Entropy Deconvolution in Electrospray Mass Spectrometry. *Rapid Commun. Mass Spectrom.* **1991**, *5* (8), 374–377. https://doi.org/10.1002/rcm.1290050810.

- (170) Mcilwain, S. J.; Wu, Z.; Wetzel, M.; Belongia, D.; Jin, Y.; Wenger, K.; Ong, I. M.; Ge, Y. Enhancing Top-Down Proteomics Data Analysis by Combining Deconvolution Results through a Machine Learning Strategy. *J. Am. Soc. Mass Spectrom* **2020**, *31*. https://doi.org/10.1021/jasms.0c00035.
- (171) Marty, M. T.; Baldwin, A. J.; Marklund, E. G.; Hochberg, G. K. A.; Benesch, J. L. P.; Robinson, C. V. Bayesian Deconvolution of Mass and Ion Mobility Spectra: From Binary Interactions to Polydisperse Ensembles. *Anal. Chem* **2015**, *87*, 4370–4376. https://doi.org/10.1021/acs.analchem.5b00140.
- (172) Bern, M.; Caval, T.; Kil, Y. J.; Tang, W.; Becker, C.; Carlson, E.; Kletter, D.; Sen, K. I.; Galy, N.; Hagemans, D.; et al. Parsimonious Charge Deconvolution for Native Mass Spectrometry. *J. Proteome Res.* **2018**, *17* (3), 1216–1226. https://doi.org/10.1021/acs.jproteome.7b00839.
- (173) Reid, D. J.; Diesing, J. M.; Miller, M. A.; Perry, S. M.; Wales, J. A.; Montfort, W. R.; Marty, M. T. MetaUniDec: High-Throughput Deconvolution of Native Mass Spectra MS Data Set MetaUniDec Deconvolution Integration & Extraction. *J. Am. Soc. Mass Spectrom* **2018**, *30*, 118–127. https://doi.org/10.1007/s13361-018-1951-9.
- (174) Jeong, K.; Kim, J.; Gaikwad, M.; Hidayah, S. N.; Heikaus, L.; Schlüter, H.; Kohlbacher, O. FLASHDeconv: Ultrafast, High-Quality Feature Deconvolution for Top-Down Proteomics. *Cell Syst.* **2020**, *10* (2), 213-218.e6. https://doi.org/10.1016/J.CELS.2020.01.003.
- (175) Jeong, K.; Babović, M.; Gorshkov, V.; Kim, J.; Jensen, O. N.; Kohlbacher, O. FLASHIda Enables Intelligent Data Acquisition for Top-down Proteomics to Boost Proteoform Identification Counts. *Nat. Commun.* **2022**, *13* (1). https://doi.org/10.1038/s41467-022-31922-z.
- (176) Park, J.; Piehowski, P. D.; Wilkins, C.; Zhou, M.; Mendoza, J.; Fujimoto, G. M.; Gibbons, B. C.; Shaw, J. B.; Shen, Y.; Shukla, A. K.; et al. Informed-Proteomics: Open-Source Software Package for Top-down Proteomics. *Nat. Methods* **2017**, *14* (9), 909–914. https://doi.org/10.1038/nmeth.4388.
- (177) Sun, R. X.; Luo, L.; Wu, L.; Wang, R. M.; Zeng, W. F.; Chi, H.; Liu, C.; He, S. M. PTop 1.0: A High-Accuracy and High-Efficiency Search Engine for Intact Protein Identification. *Anal. Chem.* 2016, 88 (6), 3082–3090. https://doi.org/10.1021/ACS.ANALCHEM.5B03963/ASSET/IMAGES/LARGE/AC-2015-03963G\_0002.JPEG.
- (178) Liu, X.; Sirotkin, Y.; Shen, Y.; Anderson, G.; Tsai, Y. S.; Ting, Y. S.; Goodlett, D. R.; Smith, R. D.; Bafna, V.; Pevzner, P. A. Protein Identification Using Top-Down. *Mol. Cell. Proteomics* **2012**, *11* (6), 1–13. https://doi.org/10.1074/MCP.M111.008524/ATTACHMENT/3DD4CC4D-1D0B-4BB7-82BB-0D2FA24AA4A2/MMC1.ZIP.
- (179) Kou, Q.; Xun, L.; Liu, X. TopPIC: A Software Tool for Top-down Mass Spectrometry-Based Proteoform Identification and Characterization. *Bioinformatics* **2016**, *32* (22), 3495–3497. https://doi.org/10.1093/bioinformatics/btw398.

- (180) Martin, E. A.; Fulcher, J. M.; Zhou, M.; Monroe, M. E.; Petyuk, V. A. TopPICR: A Companion R Package for Top-Down Proteomics Data Analysis. *J. Proteome Res.* **2023**, 22 (2), 399–409. https://doi.org/10.1021/acs.jproteome.2c00570.
- (181) Jeong, K.; Kim, S.; Bandeira, N. False Discovery Rates in Spectral Identification. *BMC Bioinformatics* **2012**, *13 Suppl 1* (Suppl 16). https://doi.org/10.1186/1471-2105-13-S16-S2.
- (182) Jeong, K.; Kaulich, P. T.; Jung, W.; Kim, J.; Kohlbacher, O. Precursor Deconvolution Error Estimation: The Missing Puzzle Piece in False Discovery Rate in Top-down Proteomics. *Authorea* **2023**, 1–3.
- (183) Cesnik, A. J.; Shortreed, M. R.; Schaffer, L. V.; Knoener, R. A.; Frey, B. L.; Scalf, M.; Solntsev, S. K.; Dai, Y.; Gasch, A. P.; Smith, L. M. Proteoform Suite: Software for Constructing, Quantifying, and Visualizing Proteoform Families. *J. Proteome Res.* **2018**, *17* (1), 568–578. https://doi.org/10.1021/acs.jproteome.7b00685.
- (184) Schaffer, L. V.; Tucholski, T.; Shortreed, M. R.; Ge, Y.; Smith, L. M. Intact-Mass Analysis Facilitating the Identification of Large Human Heart Proteoforms. *Anal. Chem.* **2019**, *91* (17), 10937–10942. https://doi.org/10.1021/acs.analchem.9b02343.
- (185) Wang, X.; Mathieu, M.; Brezski, R. J. IgG Fc Engineering to Modulate Antibody Effector Functions. *Protein Cell* **2018**, *9* (1), 63–73. https://doi.org/10.1007/s13238-017-0473-8.
- (186) Mian, I. S.; Bradwell, A. R.; Olson, A. J. Structure, Function and Properties of Antibody Binding Sites. *J. Mol. Biol.* **1991**, *217* (1), 133–151. https://doi.org/10.1016/0022-2836(91)90617-F.
- (187) Davies, D. R.; Chacko, S. Antibody Structure. *Acc. Chem. Res.* **1993**, *26*, 421–427. https://doi.org/10.1136/jcp.s1-6.1.1.
- (188) Tian, Y.; Hu, D.; Li, Y.; Yang, L. Development of Therapeutic Vaccines for the Treatment of Diseases. *Mol. Biomed.* **2022**, *3* (1), 1–30. https://doi.org/10.1186/s43556-022-00098-9.
- (189) Lyu, X.; Zhao, Q.; Hui, J.; Wang, T.; Lin, M.; Wang, K.; Zhang, J.; Shentu, J.; Dalby, P. A.; Zhang, H.; et al. The Global Landscape of Approved Antibody Therapies. *Antib. Ther.* **2022**, *5* (4), 233–257. https://doi.org/10.1093/abt/tbac021.
- (190) Dumontet, C.; Reichert, J. M.; Senter, P. D.; Lambert, J. M.; Beck, A. Antibody-Drug Conjugates Come of Age in Oncology. *Nat. Rev. Drug Discov.* **2023**. https://doi.org/10.1038/s41573-023-00709-2.
- (191) Runcie, K.; Budman, D. R.; John, V.; Seetharamu, N. Bi-Specific and Tri-Specific Antibodies- the next Big Thing in Solid Tumor Therapeutics. *Mol. Med.* **2018**, *24* (1), 1–15. https://doi.org/10.1186/s10020-018-0051-4.
- (192) Wu, Y.; Yi, M.; Zhu, S.; Wang, H.; Wu, K. Recent Advances and Challenges of Bispecific Antibodies in Solid Tumors. *Exp. Hematol. Oncol.* **2021**, *10* (1), 1–14. https://doi.org/10.1186/s40164-021-00250-1.
- (193) Beckmann, R.; Jensen, K.; Fenn, S.; Speck, J.; Krause, K.; Meier, A.; Röth, M.; Fauser,

- S.; Kimbung, R.; Logan, D. T.; et al. DutaFabs Are Engineered Therapeutic Fab Fragments That Can Bind Two Targets Simultaneously. *Nat. Commun.* **2021**, *12* (1), 1–13. https://doi.org/10.1038/s41467-021-20949-3.
- (194) Beck, A.; Reichert, J. M. Therapeutic Fc-Fusion Proteins and Peptides as Successful Alternatives to Antibodies. *MAbs* **2011**, *3* (5), 415–416. https://doi.org/10.4161/mabs.3.5.17334.
- (195) Ionescu, R.; Vlasak, J.; Price, C.; Kirchmeier, M. Contribution of Variable Domains to the Stability of Humanized IgG1 Monoclonal Antibodies. *J. Pharm. Sci.* **2008**, *97* (4), 1414–1426. https://doi.org/10.1002/jps.
- (196) Zheng, K.; Bantog, C.; Bayer, R. The Impact of Glycosylation on Monoclonal Antibody Conformation and Stability. *MAbs* **2011**, *3* (6). https://doi.org/10.4161/mabs.3.6.17922.
- (197) Ma, H.; Ó'Fágáin, C.; O'Kennedy, R. Antibody Stability: A Key to Performance Analysis, Influences and Improvement. *Biochimie* **2020**, *177*, 213–225. https://doi.org/10.1016/j.biochi.2020.08.019.
- (198) Chen, B.; Lin, Z.; Zhu, Y.; Jin, Y.; Larson, E.; Xu, Q.; Fu, C.; Zhang, Z.; Zhang, Q.; Pritts, W. A.; et al. Middle-Down Multi-Attribute Analysis of Antibody-Drug Conjugates with Electron Transfer Dissociation. *Anal. Chem.* **2019**, *91* (18), 11661–11669. https://doi.org/10.1021/acs.analchem.9b02194.
- (199) Dick, L. W.; Mahon, D.; Qiu, D.; Cheng, K. C. Peptide Mapping of Therapeutic Monoclonal Antibodies: Improvements for Increased Speed and Fewer Artifacts. *J. Chromatogr. B Anal. Technol. Biomed. Life Sci.* **2009**, 877 (3), 230–236. https://doi.org/10.1016/j.jchromb.2008.12.009.
- (200) Stroop, S. D. A Modif Peptide Mapping Strategy for Quantifying Site-specific Deamidation by Electrospray Time-of-Flight Mass Spectrometry. *Rapid Commun. Mass Spectrom.* **2007**, *21*, 830–836.
- (201) Li, X.; Xu, W.; Wang, Y.; Zhao, J.; Liu, Y. H.; Richardson, D.; Li, H.; Shameem, M.; Yang, X. High Throughput Peptide Mapping Method for Analysis of Site Specific Monoclonal Antibody Oxidation. *J. Chromatogr. A* **2016**, *1460*, 51–60. https://doi.org/10.1016/j.chroma.2016.06.085.
- (202) Hara, S.; Rosenfeld, R.; Lu, H. S. Preventing the Generation of Artifacts during Peptide Map Analysis of Recombinant Human Insulin-like Growth Factor-I. *Anal. Biochem.* **1996**, 243 (1), 74–79. https://doi.org/10.1006/abio.1996.0483.
- (203) Kori, Y.; Patel, R.; Neill, A.; Liu, H. A Conventional Procedure to Reduce Asn Deamidation Artifacts during Trypsin Peptide Mapping. *J. Chromatogr. B Anal. Technol. Biomed. Life Sci.* **2016**, *1009–1010*, 107–113. https://doi.org/10.1016/j.jchromb.2015.12.009.
- (204) Sjögren, J.; Olsson, F.; Beck, A. Rapid and Improved Characterization of Therapeutic Antibodies and Antibody Related Products Using IdeS Digestion and Subunit Analysis. *Analyst*. Royal Society of Chemistry June 7, 2016, pp 3114–3125. https://doi.org/10.1039/c6an00071a.

- (205) Srzentić, K.; Fornelli, L.; Tsybin, Y. O.; Loo, J. A.; Seckler, H.; Agar, J. N.; Anderson, L. C.; Bai, D. L.; Beck, A.; Brodbelt, J. S.; et al. Interlaboratory Study for Characterizing Monoclonal Antibodies by Top-Down and Middle-Down Mass Spectrometry. *J. Am. Soc. Mass Spectrom.* **2020**, *31* (9), 1783–1802. https://doi.org/10.1021/jasms.0c00036.
- (206) Yang, R.; Jain, T.; Lynaugh, H.; Nobrega, R. P.; Lu, X.; Boland, T.; Burnina, I.; Sun, T.; Caffry, I.; Brown, M.; et al. Rapid Assessment of Oxidation via Middle-down LCMS Correlates with Methionine Side-Chain Solvent-Accessible Surface Area for 121 Clinical Stage Monoclonal Antibodies. *MAbs* **2017**, *9* (4), 646–653. https://doi.org/10.1080/19420862.2017.1290753.
- (207) Burns, J. A.; Butler, J. C.; Moran, J.; Whitesides, G. M. Selective Reduction of Disulfides by Tris(2-Carboxyethyl)Phosphine. *J. Org. Chem.* **1991**, *56*, 2648–2650. https://doi.org/10.1055/sos-sd-039-00444.
- (208) Konigsberg, W. Reduction of Disulfide Bonds in Proteins with Dithiothreitol. *Methods Enzymol.* **1972**, *25*, 185–188. https://doi.org/10.1016/S0076-6879(72)25015-7.
- (209) Kellie, J. F.; Pannullo, K. E.; Li, Y.; Fraley, K.; Mayer, A.; Sychterz, C. J.; Szapacs, M. E.; Karlinsey, M. Z. Antibody Subunit LC-MS Analysis for Pharmacokinetic and Biotransformation Determination from In-Life Studies for Complex Biotherapeutics. *Anal. Chem.* **2020**, *92* (12), 8268–8277. https://doi.org/10.1021/acs.analchem.0c00520.
- (210) Jin, Y.; Lin, Z.; Xu, Q.; Fu, C.; Zhang, Z.; Zhang, Q.; Pritts, W. A.; Ge, Y. Comprehensive Characterization of Monoclonal Antibody by Fourier Transform Ion Cyclotron Resonance Mass Spectrometry. *MAbs* **2019**, *11* (1), 106–115. https://doi.org/10.1080/19420862.2018.1525253.
- (211) Lodge, J. M.; Schauer, K. L.; Brademan, D. R.; Riley, N. M.; Shishkova, E.; Westphall, M. S.; Coon, J. J. Top-Down Characterization of an Intact Monoclonal Antibody Using Activated Ion Electron Transfer Dissociation. *Anal. Chem.* **2020**, *92* (15), 10246–10251. https://doi.org/10.1021/acs.analchem.0c00705.
- (212) Wei, B.; Lantz, C.; Liu, W.; Viner, R.; Loo, R. R. O.; Campuzano, I. D. G.; Loo, J. A. Added Value of Internal Fragments for Top-Down Mass Spectrometry of Intact Monoclonal Antibodies and Antibody Drug Conjugates. **2023**. https://doi.org/10.1021/acs.analchem.3c01426.
- (213) Rosati, S.; Rose, R. J.; Thompson, N. J.; Van Duijn, E.; Damoc, E.; Denisov, E.; Makarov, A.; Heck, A. J. R. Exploring an Orbitrap Analyzer for the Characterization of Intact Antibodies by Native Mass Spectrometry. *Angew. Chemie Int. Ed.* **2012**, *51* (52), 12992–12996. https://doi.org/10.1002/anie.201206745.
- (214) Tian, Y.; Lippens, J. L.; Netirojjanakul, C.; Campuzano, I. D. G.; Ruotolo, B. T. Quantitative Collision-Induced Unfolding Differentiates Model Antibody–Drug Conjugates. *Protein Sci.* **2019**, *28* (3), 598–608. https://doi.org/10.1002/pro.3560.
- (215) Khongorzul, P.; Ling, C. J.; Khan, F. U.; Ihsan, A. U.; Zhang, J. Antibody-Drug Conjugates: A Comprehensive Review. *Molecular Cancer Research*. American Association for Cancer Research Inc. January 1, 2020, pp 3–19. https://doi.org/10.1158/1541-7786.MCR-19-0582.

- (216) Casi, G.; Neri, D. *Antibody-Drug Conjugates: Basic Concepts, Examples and Future Perspectives*; Elsevier, 2012; Vol. 161, pp 422–428. https://doi.org/10.1016/j.jconrel.2012.01.026.
- (217) Beck, A.; Goetsch, L.; Dumontet, C.; Corvaïa, N. Strategies and Challenges for the next Generation of Antibody-Drug Conjugates. *Nature Reviews Drug Discovery*. Nature Publishing Group May 1, 2017, pp 315–337. https://doi.org/10.1038/nrd.2016.268.
- (218) Diamantis, N.; Banerji, U. Antibody-Drug Conjugates An Emerging Class of Cancer Treatment. *British Journal of Cancer*. Nature Publishing Group February 1, 2016, pp 362–367. https://doi.org/10.1038/bjc.2015.435.
- (219) Tsuchikama, K.; An, Z. Antibody-Drug Conjugates: Recent Advances in Conjugation and Linker Chemistries. *Protein Cell* **2018**, *9* (1), 33–46. https://doi.org/10.1007/s13238-016-0323-0.
- (220) Ducry, L.; Stump, B. Antibody-Drug Conjugates: Linking Cytotoxic Payloads to Monoclonal Antibodies. *Bioconjugate Chemistry*. American Chemical Society January 20, 2010, pp 5–13. https://doi.org/10.1021/bc9002019.
- (221) Ross, P. L.; Wolfe, J. L. Physical and Chemical Stability of Antibody Drug Conjugates: Current Status. *Journal of Pharmaceutical Sciences*. Elsevier B.V. February 1, 2016, pp 391–397. https://doi.org/10.1016/j.xphs.2015.11.037.
- (222) Shaw, S. Y.; Margolies, M. N. A Spontaneous Variant of an Antidigoxin Hybridoma Antibody with Increased Affinity Arises from a Heavy Chain Signal Peptide Mutation. *Mol. Immunol.* **1992**, *29* (4), 525–529. https://doi.org/10.1016/0161-5890(92)90010-U.
- (223) Buecheler, J. W.; Winzer, M.; Weber, C.; Gieseler, H. Oxidation-Induced Destabilization of Model Antibody-Drug Conjugates. *J. Pharm. Sci.* **2019**, *108* (3), 1236–1245. https://doi.org/10.1016/j.xphs.2018.10.039.
- (224) Wright, A.; Tao, M. H.; Kabat, E. A.; Morrison, S. L. Antibody Variable Region Glycosylation: Position Effects on Antigen Binding and Carbohydrate Structure. *EMBO J.* **1991**, *10* (10), 2717–2723. https://doi.org/10.1002/j.1460-2075.1991.tb07819.x.
- (225) Bobály, B.; Fleury-Souverain, S.; Beck, A.; Veuthey, J.-L. L.; Guillarme, D.; Fekete, S. Current Possibilities of Liquid Chromatography for the Characterization of Antibody-Drug Conjugates. *J. Pharm. Biomed. Anal.* **2018**, *147*, 493–505. https://doi.org/10.1016/j.jpba.2017.06.022.
- (226) Fekete, S.; Guillarme, D.; Sandra, P.; Sandra, K. Chromatographic, Electrophoretic, and Mass Spectrometric Methods for the Analytical Characterization of Protein Biopharmaceuticals. *Analytical Chemistry*. American Chemical Society January 5, 2016, pp 480–507. https://doi.org/10.1021/acs.analchem.5b04561.
- (227) Said, N.; Gahoual, R.; Kuhn, L.; Beck, A.; François, Y. N.; Leize-Wagner, E. Structural Characterization of Antibody Drug Conjugate by a Combination of Intact, Middle-up and Bottom-up Techniques Using Sheathless Capillary Electrophoresis Tandem Mass Spectrometry as NanoESI Infusion Platform and Separation Method. *Anal. Chim. Acta* **2016**, *918*, 50–59. https://doi.org/10.1016/j.aca.2016.03.006.

- (228) Chen, T.; Chen, Y.; Stella, C.; Medley, C. D.; Gruenhagen, J. A.; Zhang, K. Antibody-Drug Conjugate Characterization by Chromatographic and Electrophoretic Techniques. *J. Chromatogr. B Anal. Technol. Biomed. Life Sci.* **2016**, *1032*, 39–50. https://doi.org/10.1016/j.jchromb.2016.07.023.
- (229) Janin-Bussat, M.-C. C.; Dillenbourg, M.; Corvaia, N.; Beck, A.; Klinguer-Hamour, C. Characterization of Antibody Drug Conjugate Positional Isomers at Cysteine Residues by Peptide Mapping LC-MS Analysis. *J. Chromatogr. B Anal. Technol. Biomed. Life Sci.* **2015**, *981–982*, 9–13. https://doi.org/10.1016/j.jchromb.2014.12.017.
- (230) He, J.; Su, D.; Ng, C.; Liu, L.; Yu, S. F.; Pillow, T. H.; Del Rosario, G.; Darwish, M.; Lee, B. C.; Ohri, R.; et al. High-Resolution Accurate-Mass Mass Spectrometry Enabling In-Depth Characterization of in Vivo Biotransformations for Intact Antibody-Drug Conjugates. *Anal. Chem.* **2017**, *89* (10), 5476–5483. https://doi.org/10.1021/acs.analchem.7b00408.
- (231) Todoroki, K.; Mizuno, H.; Sugiyama, E.; Toyo'oka, T. Bioanalytical Methods for Therapeutic Monoclonal Antibodies and Antibody–Drug Conjugates: A Review of Recent Advances and Future Perspectives. *Journal of Pharmaceutical and Biomedical Analysis*. Elsevier B.V. February 5, 2020, p 112991. https://doi.org/10.1016/j.jpba.2019.112991.
- (232) Sawyer, W. S.; Srikumar, N.; Carver, J.; Chu, P. Y.; Shen, A.; Xu, A.; Williams, A. J.; Spiess, C.; Wu, C.; Liu, Y.; et al. High-Throughput Antibody Screening from Complex Matrices Using Intact Protein Electrospray Mass Spectrometry. *Proc. Natl. Acad. Sci. U. S. A.* **2020**, *117* (18), 9851–9856. https://doi.org/10.1073/pnas.1917383117.
- (233) Cristobal, A.; Marino, F.; Post, H.; Van Den Toorn, H. W. P.; Mohammed, S.; Heck, A. J. R. Toward an Optimized Workflow for Middle-Down Proteomics. *Anal. Chem.* **2017**, *89* (6), 3318–3325. https://doi.org/10.1021/acs.analchem.6b03756.
- (234) Chevreux, G.; Tilly, N.; Bihoreau, N. Fast Analysis of Recombinant Monoclonal Antibodies Using IdeS Proteolytic Digestion and Electrospray Mass Spectrometry. *Anal. Biochem.* **2011**, *415* (2), 212–214. https://doi.org/10.1016/j.ab.2011.04.030.
- (235) Moelleken, J.; Endesfelder, M.; Gassner, C.; Lingke, S.; Tomaschek, S.; Tyshchuk, O.; Lorenz, S.; Reiff, U.; Mølhøj, M. GingisKHAN<sup>TM</sup> Protease Cleavage Allows a High-Throughput Antibody to Fab Conversion Enabling Direct Functional Assessment during Lead Identification of Human Monoclonal and Bispecific IgG1 Antibodies. *MAbs* **2017**, *9* (7), 1076–1087. https://doi.org/10.1080/19420862.2017.1364325.
- (236) He, L.; Anderson, L. C.; Barnidge, D. R.; Murray, D. L.; Hendrickson, C. L.; Marshall, A. G. Analysis of Monoclonal Antibodies in Human Serum as a Model for Clinical Monoclonal Gammopathy by Use of 21 Tesla FT-ICR Top-Down and Middle-Down MS/MS. https://doi.org/10.1007/s13361-017-1602-6.
- (237) Hernandez-Alba, O.; Houel, S.; Hessmann, S.; Erb, S.; Rabuka, D.; Huguet, R.; Josephs, J.; Beck, A.; Drake, P. M.; Ciaferani, S. A Case Study to Identify the Drug Conjugation Site of a Site-Specific Antibody-Drug Conjugate Using Middle-Down Mass Spectrometry. *J. Mass Spectrom.* **2019**, *30* (11), 2419–2429. https://doi.org/10.1021/JASMS.8B06243;PAGE:STRING:ARTICLE.

- (238) Botzanowski, T.; Erb, S.; Hernandez-Alba, O.; Ehkirch, A.; Colas, O.; Wagner-Rousset, E.; Rabuka, D.; Beck, A.; Drake, P. M.; Cianférani, S. Insights from Native Mass Spectrometry Approaches for Top- and Middle- Level Characterization of Site-Specific Antibody-Drug Conjugates. *MAbs* **2017**, *9* (5), 801–811. https://doi.org/10.1080/19420862.2017.1316914.
- (239) Wagner-Rousset, E.; Colas, O.; François, Y. N.; Heinisch, S.; Guillarme, D.; Cianférani, S.; Beck, A. Drug Loading and Distribution of ADCs After Reduction or IdeS Digestion and Reduction. In *Methods in Molecular Biology*; Humana Press Inc., 2020; Vol. 2078, pp 187–195. https://doi.org/10.1007/978-1-4939-9929-3 12.
- (240) Cai, W.; Guner, H.; Gregorich, Z. R.; Chen, A. J.; Ayaz-Guner, S.; Peng, Y.; Valeja, S. G.; Liu, X.; Ge, Y. MASH Suite pro: A Comprehensive Software Tool for Top-down Proteomics. *Mol. Cell. Proteomics* **2016**, *15* (2), 703–714. https://doi.org/10.1074/mcp.O115.054387.
- (241) Mcilwain, S. J.; Wu, Z.; Wenger, K.; Wetzel, M.; Roberts, D. S.; Bayne, E.; Melby, J. A.; Sun, R.; Liu, X.; Ong, I. M.; et al. *MASH Explorer, A Universal and Comprehensive Software for Top-down Proteomics Empowered by Machine Learning Methods*.
- (242) Loo, J. A.; Edmonds, C. G.; Udseth, H. R.; Smith, R. D. *Effect of Reducing Disulfide-Containing Proteins on Electrospray Ionization Mass Spectra*; Bergman, 1990; Vol. 62.
- (243) Antes, B.; Amon, S.; Rizzi, A.; Wiederkum, S.; Kainer, M.; Szolar, O.; Fido, M.; Kircheis, R.; Nechansky, A. Analysis of Lysine Clipping of a Humanized Lewis-Y Specific IgG Antibody and Its Relation to Fc-Mediated Effector Function. *J. Chromatogr. B Anal. Technol. Biomed. Life Sci.* **2007**, *852* (1–2), 250–256. https://doi.org/10.1016/j.jchromb.2007.01.024.
- (244) Comisarow, M. B.; Marshall, A. G. Theory of Fourier Transform Ion Cyclotron Resonance Mass Spectroscopy. I. Fundamental Equations and Low-Pressure Line Shape ARTICLES YOU MAY BE INTERESTED IN. *J. Chem. Phys* **1976**, *64*, 110. https://doi.org/10.1063/1.431959.
- (245) Wagner-Rousset, E.; Janin-Bussat, M. C.; Colas, O.; Excoffier, M.; Ayoub, D.; Haeuw, J. F.; Rilatt, I.; Perez, M.; Corvaïa, N.; Beck, A. Antibody-Drug Conjugate Model Fast Characterization by LC-MS Following IdeS Proteolytic Digestion. *MAbs* **2014**, *6* (1), 173–184. https://doi.org/10.4161/mabs.26773.
- (246) Agarwal, P.; Bertozzi, C. R. Site-Specific Antibody-Drug Conjugates: The Nexus of Bioorthogonal Chemistry, Protein Engineering, and Drug Development. *Bioconjug. Chem.* **2015**, *26* (2), 176–192. https://doi.org/10.1021/bc5004982.
- (247) Webb, S. Pharma Interest Surges in Antibody Drug Conjugates. *Nat. Biotechnol.* **2011**, *29* (4), 297–298. https://doi.org/10.1038/nbt0411-297.
- (248) Houston, Z. H.; Bunt, J.; Chen, K. S.; Puttick, S.; Howard, C. B.; Fletcher, N. L.; Fuchs, A. V.; Cui, J.; Ju, Y.; Cowin, G.; et al. Understanding the Uptake of Nanomedicines at Different Stages of Brain Cancer Using a Modular Nanocarrier Platform and Precision Bispecific Antibodies. *ACS Cent. Sci.* **2020**, *6* (5), 727–738. https://doi.org/10.1021/acscentsci.9b01299.

- (249) Zheng, K.; Bantog, C.; Bayer, R. The Impact of Glycosylation on Monoclonal Antibody Conformation and Stability. *MAbs* **2011**, *3* (6), 568–576. https://doi.org/10.4161/mabs.3.6.17922.
- (250) Joubert, N.; Beck, A.; Dumontet, C.; Denevault-sabourin, C. Antibody Drug Conjugates: The Last Decade. **2020**, No. April, 1–31.
- (251) Valliere-Douglass, J. F.; McFee, W. A.; Salas-Solano, O. Native Intact Mass Determination of Antibodies Conjugated with Monomethyl Auristatin e and F at Interchain Cysteine Residues. *Anal. Chem.* **2012**, *84* (6), 2843–2849. https://doi.org/10.1021/ac203346c.
- (252) Biacchi, M.; Gahoual, R.; Said, N.; Beck, A.; Leize-Wagner, E.; François, Y. N. Glycoform Separation and Characterization of Cetuximab Variants by Middle-up Off-Line Capillary Zone Electrophoresis-UV/Electrospray Ionization-MS. *Anal. Chem.* **2015**, 87 (12), 6240–6250. https://doi.org/10.1021/acs.analchem.5b00928.
- (253) Watts, E.; Williams, J. D.; Miesbauer, L. J.; Bruncko, M.; Brodbelt, J. S. Correction to Comprehensive Middle-Down Mass Spectrometry Characterization of an Antibody–Drug Conjugate by Combined Ion Activation Methods. *Anal. Chem.* **2020**, *2020* (14), 31. https://doi.org/10.1021/acs.analchem.0c03265.
- (254) Chen, J.; Yin, S.; Wu, Y.; Ouyang, J. Development of a Native Nanoelectrospray Mass Spectrometry Method for Determination of the Drug-to-Antibody Ratio of Antibody-Drug Conjugates. *Anal. Chem.* **2013**, *85* (3), 1699–1704. https://doi.org/10.1021/ac302959p.
- (255) Pacholarz, K. J.; Barran, P. E. Use of a Charge Reducing Agent to Enable Intact Mass Analysis of Cysteine-Linked Antibody-Drug-Conjugates by Native Mass Spectrometry. *EuPA Open Proteomics* **2016**, *11*, 23–27. https://doi.org/10.1016/j.euprot.2016.02.004.
- (256) Bailey, A. O.; Han, G.; Phung, W.; Gazis, P.; Sutton, J.; Josephs, J. L.; Sandoval, W. Charge Variant Native Mass Spectrometry Benefits Mass Precision and Dynamic Range of Monoclonal Antibody Intact Mass Analysis. *MAbs* **2018**, *10* (8), 1214–1225. https://doi.org/10.1080/19420862.2018.1521131.
- (257) Kanu, A. B.; Dwivedi, P.; Tam, M.; Matz, L.; Hill, H. H. Ion Mobility-Mass Spectrometry. *Journal of Mass Spectrometry*. John Wiley & Sons, Ltd January 1, 2008, pp 1–22. https://doi.org/10.1002/jms.1383.
- (258) Debaene, F.; Bœuf, A.; Wagner-Rousset, E.; Colas, O.; Ayoub, D.; Corvaïa, N.; Van Dorsselaer, A.; Beck, A.; Cianférani, S. Innovative Native MS Methodologies for Antibody Drug Conjugate Characterization: High Resolution Native MS and IM-MS for Average DAR and DAR Distribution Assessment. *Anal. Chem.* **2014**, *86* (21), 10674–10683. https://doi.org/10.1021/ac502593n.
- (259) Vallejo, D. D.; Polasky, D. A.; Kurulugama, R. T.; Eschweiler, J. D.; Fjeldsted, J. C.; Ruotolo, B. T. A Modified Drift Tube Ion Mobility-Mass Spectrometer for Charge-Multiplexed Collision-Induced Unfolding. **2019**. https://doi.org/10.1021/acs.analchem.9b00427.
- (260) Michelmann, K.; Silveira, J. A.; Ridgeway, M. E.; Park, M. A. Fundamentals of Trapped

- Ion Mobility Spectrometry. *J. Am. Soc. Mass Spectrom* **2015**, *26*, 14–24. https://doi.org/10.1007/s13361-014-0999-4.
- (261) Rosa Hernandez, D.; Debord, J. D.; Ridgeway, M. E.; Kaplan, D. A.; Park, M. A.; Fernandez-Lima, F. Ion Dynamics in a Trapped Ion Mobility Spectrometer †. **2014**. https://doi.org/10.1039/c3an02174b.
- (262) Morsa, D.; Hanozin, E.; Gabelica, V.; De Pauw, E. Response to Comment on Effective Temperature and Structural Rearrangement in Trapped Ion Mobility Spectrometry. *Anal. Chem.* **2020**, *92* (24), 16334–16337. https://doi.org/10.1021/acs.analchem.0c03937.
- (263) Bleiholder, C.; Liu, F. C.; Chai, M. Comment on Effective Temperature and Structural Rearrangement in Trapped Ion Mobility Spectrometry. **2020**. https://doi.org/10.1021/acs.analchem.0c02052.
- (264) Molano-Arevalo, J. C.; Jeanne Dit Fouque, K.; Pham, K.; Miksovska, J.; Ridgeway, M. E.; Park, M. A.; Fernandez-Lima, F. Characterization of Intramolecular Interactions of Cytochrome c Using Hydrogen-Deuterium Exchange-Trapped Ion Mobility Spectrometry-Mass Spectrometry and Molecular Dynamics. *Anal. Chem.* 2017, 89 (17), 8757–8765. https://doi.org/10.1021/acs.analchem.7b00844.
- (265) Morsa, D.; Hanozin, E.; Eppe, G.; Quinton, L.; Gabelica, V.; De Pauw, E. Effective Temperature and Structural Rearrangement in Trapped Ion Mobility Spectrometry. *Cite This Anal. Chem* **2020**, *92*, 4582. https://doi.org/10.1021/acs.analchem.9b05850.
- (266) Silveira, J. A.; Ridgeway, M. E.; Park, M. A. High Resolution Trapped Ion Mobility Spectrometery of Peptides. *Anal. Chem.* **2014**, *86* (12), 5624–5627. https://doi.org/10.1021/ac501261h.
- (267) Chai, M.; Young, M. N.; Liu, F. C.; Bleiholder, C. A Transferable, Sample-Independent Calibration Procedure for Trapped Ion Mobility Spectrometry (TIMS). *Anal. Chem.* **2018**, 90 (15), 9040–9047. https://doi.org/10.1021/acs.analchem.8b01326.
- (268) Ducry, L. Antibody-Drug Conjugates.
- (269) Gabelica, V.; Shvartsburg, A. A.; Afonso, C.; Barran, P.; Benesch, J. L. P.; Bleiholder, C.; Bowers, M. T.; Bilbao, A.; Bush, M. F.; Campbell, J. L.; et al. Recommendations for Reporting Ion Mobility Mass Spectrometry Measurements. *Mass Spectrom. Rev.* **2019**, *38* (3), 291–320. https://doi.org/10.1002/mas.21585.
- (270) Revercomb, E.; Mason, E. A. Theory of Plasma Chromatography/Gaseous Electrophoresis-A Review.
- (271) Horn, D. M.; Zubarev, R. A.; McLafferty, F. W. Automated Reduction and Interpretation of High Resolution Electrospray Mass Spectra of Large Molecules. *J. Am. Soc. Mass Spectrom.* **2000**, *11* (4), 320–332. https://doi.org/10.1016/S1044-0305(99)00157-9.
- (272) Haler, J. R. N.; Massonnet, P.; Far, J.; de la Rosa, V. R.; Lecomte, P.; Hoogenboom, R.; Jérôme, C.; De Pauw, E. Gas-Phase Dynamics of Collision Induced Unfolding, Collision Induced Dissociation, and Electron Transfer Dissociation-Activated Polymer Ions. *J. Am. Soc. Mass Spectrom.* **2018**. https://doi.org/10.1007/s13361-018-2115-7.

- (273) De Leoz, M. L. A.; Duewer, D. L.; Fung, A.; Liu, L.; Yau, H. K.; Potter, O.; Staples, G. O.; Furuki, K.; Frenkel, R.; Hu, Y.; et al. NIST Interlaboratory Study on Glycosylation Analysis of Monoclonal Antibodies: Comparison of Results from Diverse Analytical Methods. *Mol. Cell. Proteomics* 2020, 19 (1), 11–30. https://doi.org/10.1074/mcp.RA119.001677.
- (274) Kelly, R. T.; Tolmachev, A. V.; Page, J. S.; Tang, K.; Smith, R. D. The Ion Funnel: Theory, Implementations, and Applications. *Mass Spectrom. Rev.* **2009**, *29* (2), n/a-n/a. https://doi.org/10.1002/mas.20232.
- (275) Loo, J. A. Electrospray Ionization Mass Spectrometry: A Technology for Studying Noncovalent Macromolecular Complexes. *Int. J. Mass Spectrom.* **2000**, *200* (1–3), 175–186. https://doi.org/10.1016/S1387-3806(00)00298-0.
- (276) Freeke, J.; Robinson, C. V.; Ruotolo, B. T. Residual Counter Ions Can Stabilise a Large Protein Complex in the Gas Phase. *Int. J. Mass Spectrom.* **2010**, *298* (1–3), 91–98. https://doi.org/10.1016/j.ijms.2009.08.001.
- (277) Pacholarz, K. J.; Porrini, M.; Garlish, R. A.; Burnley, R. J.; Taylor, R. J.; Henry, A. J.; Barran, P. E. Dynamics of Intact Immunoglobulin G Explored by Drift-Tube Ion-Mobility Mass Spectrometry and Molecular Modeling. *Angew. Chemie Int. Ed.* **2014**, *53* (30), 7765–7769. https://doi.org/10.1002/anie.201402863.
- (278) Brekke, O. H.; Michaelsen, T. E.; Sandlie, I. *The Structural Requirements for Complement Activation by IgG: Does It Hinge on the Hinge?*; 1995.
- (279) Campuzano, I. D. G.; Larriba, C.; Bagal, D.; Schnier, P. D. Ion Mobility and Mass Spectrometry Measurements of the Humanized IgGk NIST Monoclonal Antibody. In *Emerging Technologies for Therapeutic Monoclonal Antibody Characterization*; 2015; Vol. 3, pp 75–112.
- (280) Pan, L. Y.; Salas-Solano, O.; Valliere-Douglass, J. F. Conformation and Dynamics of Interchain Cysteine-Linked Antibody-Drug Conjugates as Revealed by Hydrogen/Deuterium Exchange Mass Spectrometry. *Anal. Chem.* **2014**, *86* (5), 2657–2664. https://doi.org/10.1021/ac404003q.
- (281) Xu, K.; Liu, L.; Dere, R.; Mai, E.; Erickson, R.; Hendricks, A.; Lin, K.; Junutula, J. R.; Kaur, S. Characterization of the Drug-to-Antibody Ratio Distribution for Antibody-Drug Conjugates in Plasma/Serum. *Bioanalysis* **2013**, *5* (9), 1057–1071. https://doi.org/10.4155/bio.13.66.
- (282) Marcoux, J.; Champion, T.; Colas, O.; Wagner-Rousset, E.; Corvaïa, N.; Van Dorsselaer, A.; Beck, A.; Cianférani, S. Native Mass Spectrometry and Ion Mobility Characterization of Trastuzumab Emtansine, a Lysine-Linked Antibody Drug Conjugate. *Protein Sci.* **2015**, 24 (8), 1210–1223. https://doi.org/10.1002/pro.2666.
- (283) Hengel, S. M.; Sanderson, R.; Valliere-Douglass, J.; Nicholas, N.; Leiske, C.; Alley, S. C. Measurement of in Vivo Drug Load Distribution of Cysteine-Linked Antibody-Drug Conjugates Using Microscale Liquid Chromatography Mass Spectrometry. *Anal. Chem.* **2014**, *86* (7), 3420–3425. https://doi.org/10.1021/ac403860c.

- (284) Nagy, G.; Attah, I. K.; Conant, C. R.; Liu, W.; Garimella, S. V. B.; Gunawardena, H. P.; Shaw, J. B.; Smith, R. D.; Ibrahim, Y. M. Rapid and Simultaneous Characterization of Drug Conjugation in Heavy and Light Chains of a Monoclonal Antibody Revealed by High-Resolution Ion Mobility Separations in SLIM. *Anal. Chem.* **2020**, *92* (7), 5004–5012. https://doi.org/10.1021/acs.analchem.9b05209.
- (285) Beck, A.; Terral, G.; Debaene, F.; Wagner-Rousset, E.; Marcoux, J.; Janin-Bussat, M.-C.; Colas, O.; Dorsselaer, A. Van; Cianférani, S. Cutting-Edge Mass Spectrometry Methods for the Multi-Level Structural Characterization of Antibody-Drug Conjugates. *Expert Rev. Proteomics* **2016**, *13* (2), 157–183. https://doi.org/10.1586/14789450.2016.1132167.
- (286) Loo, J. A. Studying Noncovalent Protein Complexes by Electrospray Ionization Mass Spectrometry. *Mass Spectrom. Rev.* **1997**, *16* (1), 1–23. https://doi.org/10.1002/(SICI)1098-2787(1997)16:1.
- (287) Sharon, M.; Robinson, C. V. The Role of Mass Spectrometry in Structure Elucidation of Dynamic Protein Complexes. *Annual Review of Biochemistry*. 2007, pp 167–193. https://doi.org/10.1146/annurev.biochem.76.061005.090816.
- (288) Leney, A. C.; Heck, A. J. R. Native Mass Spectrometry: What Is in the Name? *J. Am. Soc. Mass Spectrom.* **2017**, *28* (1), 5–13. https://doi.org/10.1007/S13361-016-1545-3/ASSET/IMAGES/LARGE/JS8B05378 0003.JPEG.
- (289) Keener, J. E.; Zhang, G.; Marty, M. T. Native Mass Spectrometry of Membrane Proteins. *Anal. Chem.* **2021**, *93* (1), 583–597. https://doi.org/10.1021/acs.analchem.0c04342.
- (290) Karch, K. R.; Snyder, D. T.; Harvey, S. R.; Wysocki, V. H. Native Mass Spectrometry: Recent Progress and Remaining Challenges. *Annu. Rev. Biophys.* **2022**, *51*, 157–179. https://doi.org/10.1146/ANNUREV-BIOPHYS-092721-085421.
- (291) Toby, T. K.; Fornelli, L.; Kelleher, N. L. Progress in Top-Down Proteomics and the Analysis of Proteoforms. *Annu. Rev. Anal. Chem.* **2016**, *9* (1), 499–519. https://doi.org/10.1146/annurev-anchem-071015-041550.
- (292) Zhou, M.; Lantz, C.; Brown, K. A.; Ge, Y.; Paša-Tolić, L.; Loo, J. A.; Lermyte, F. Higher-Order Structural Characterisation of Native Proteins and Complexes by Top-down Mass Spectrometry. *Chem. Sci.* **2020**, *11* (48), 12918–12936. https://doi.org/10.1039/d0sc04392c.
- (293) Stiving, A. Q.; Vanaernum, Z. L.; Busch, F.; Harvey, S. R.; Sarni, S. H.; Wysocki, V. H. Surface-Induced Dissociation: An Effective Method for Characterization of Protein Quaternary Structure. *Anal. Chem.* **2019**, *91* (1), 190–209. https://doi.org/10.1021/acs.analchem.8b05071.
- (294) Cleary, S. P.; Thompson, A. M.; Prell, J. S. Fourier Analysis Method for Analyzing Highly Congested Mass Spectra of Ion Populations with Repeated Subunits Sean. *Anal. Chem* **2016**, *88*, 6205–6213. https://doi.org/10.1021/acs.analchem.6b01088.
- (295) Cleary, S. P.; Li, H.; Bagal, D.; Loo, J. A.; Campuzano, I. D. G.; Prell, J. S. Extracting Charge and Mass Information from Highly Congested Mass Spectra Using Fourier-Domain Harmonics. *J. Am. Soc. Mass Spectrom.* **2018**, 31–39.

- https://doi.org/10.1007/s13361-018-2018-7.
- (296) Fellers, R. T.; Greer, J. B.; Early, B. P.; Yu, X.; LeDuc, R. D.; Kelleher, N. L.; Thomas, P. M. ProSight Lite: Graphical Software to Analyze Top-down Mass Spectrometry Data. *Proteomics* **2015**, *15*, 1235–1238.
- (297) Chambers, M. C.; MacLean, B.; Burke, R.; Amodei, D.; Ruderman, D. L.; Neumann, S.; Gatto, L.; Fischer, B.; Pratt, B.; Egertson, J.; et al. A Cross-Platform Toolkit for Mass Spectrometry and Proteomics. *Nature Biotechnology*. 2012, pp 918–920. https://doi.org/10.1038/nbt.2377.
- (298) Liu, X.; Inbar, Y.; Dorrestein, P. C.; Wynne, C.; Edwards, N.; Souda, P.; Whitelegge, J. P.; Bafna, V.; Pevzner, P. A. Deconvolution and Database Search of Complex Tandem Mass Spectra of Intact Proteins: A Combinatorial Approach. *Mol. Cell. Proteomics* 2010, 9 (12), 2772–2782. https://doi.org/10.1074/MCP.M110.002766/ATTACHMENT/EB60E78C-5929-4321-BDE8-5A8C8AD46ED0/MMC1.PDF.
- (299) Yuan, Z. F.; Liu, C.; Wang, H. P.; Sun, R. X.; Fu, Y.; Zhang, J. F.; Wang, L. H.; Chi, H.; Li, Y.; Xiu, L. Y.; et al. PParse: A Method for Accurate Determination of Monoisotopic Peaks in High-Resolution Mass Spectra. *Proteomics* **2012**, *12* (2), 226–235. https://doi.org/10.1002/PMIC.201100081.
- (300) Basharat, A. R.; Ning, X.; Liu, X. EnvCNN: A Convolutional Neural Network Model for Evaluating Isotopic Envelopes in Top-Down Mass-Spectral Deconvolution. *Anal. Chem.* **2020**, *92* (11), 7778–7785. https://doi.org/10.1021/acs.analchem.0c00903.
- (301) Skinner, O. S.; Haverland, N. A.; Fornelli, L.; Melani, R. D.; Do Vale, L. H. F.; Seckler, H. S.; Doubleday, P. F.; Schachner, L. F.; Srzentić, K.; Kelleher, N. L.; et al. Multiplexed Mass Spectrometry of Individual Ions Improves Measurement of Proteoforms and Their Complexes. *Nat. Chem. Biol.* **2018**, *14* (1), 36–41. https://doi.org/10.1038/nchembio.2515.
- (302) Lantz, C.; Zenaidee, M. A.; Wei, B.; Hemminger, Z.; Ogorzalek Loo, R. R.; Loo, J. A. ClipsMS: An Algorithm for Analyzing Internal Fragments Resulting from Top-Down Mass Spectrometry. *J. Proteome Res.* **2021**, *20* (4), 1928–1935. https://doi.org/10.1021/acs.jproteome.0c00952.
- (303) Lantz, C.; Wei, B.; Zhao, B.; Jung, W.; Goring, A. K.; Le, J.; Miller, J.; Loo, R. R. O.; Loo, J. A. Native Top-Down Mass Spectrometry with Collisionally Activated Dissociation Yields Higher-Order Structure Information for Protein Complexes. **2022**. https://doi.org/10.1021/jacs.2c06726.
- (304) Kostelic, M. M.; Marty, M. T. Deconvolving Native and Intact Protein Mass Spectra with UniDec. *Methods Mol. Biol.* **2022**, *2500*, 159–180. https://doi.org/10.1007/978-1-0716-2325-1\_12/FIGURES/4.
- (305) Skinner, O. S.; Haverland, N. A.; Fornelli, L.; Melani, R. D.; Do Vale, L. H. F.; Seckler, H. S.; Doubleday, P. F.; Schachner, L. F.; Srzentić, K.; Kelleher, N. L.; et al. Top-down Characterization of Endogenous Protein Complexes with Native Proteomics. *Nat. Chem. Biol.* **2018**, *14* (1), 36–41. https://doi.org/10.1038/nchembio.2515.

- (306) Wysocki, V. H.; Resing, K. A.; Zhang, Q.; Cheng, G. Mass Spectrometry of Peptides and Proteins. *Methods* **2005**, *35* (3 SPEC.ISS.), 211–222. https://doi.org/10.1016/j.ymeth.2004.08.013.
- (307) Drown, B. S.; Jooß, K.; Melani, R. D.; Lloyd-Jones, C.; Camarillo, J. M.; Kelleher, N. L. Mapping the Proteoform Landscape of Five Human Tissues. *J. Proteome Res.* **2022**, *21* (5), 1299–1310. https://doi.org/10.1021/acs.jproteome.2c00034.
- (308) Toby, T. K.; Fornelli, L.; Kelleher, N. L. Progress in Top-Down Proteomics and the Analysis of Proteoforms. *Annu. Rev. Anal. Chem.* **2016**, *9*, 499–519. https://doi.org/10.1146/annurev-anchem-071015-041550.
- (309) Gilar, M.; Olivova, P.; Daly, A. E.; Gebler, J. C. Orthogonality of Separation in Two-Dimensional Liquid Chromatography. *Anal. Chem.* **2005**, *77* (19), 6426–6434. https://doi.org/10.1021/ac050923i.
- (310) Brown, K. A.; Chen, B.; Guardado-Alvarez, T. M.; Lin, Z.; Hwang, L.; Ayaz-Guner, S.; Jin, S.; Ge, Y. A Photocleavable Surfactant for Top-down Proteomics. *Nat. Methods* 2019 165 2019, 16 (5), 417–420. https://doi.org/10.1038/s41592-019-0391-1.
- (311) Kyte, J.; Doolittle, R. F. A Simple Method for Displaying the Hydropathic Character of a Protein. *J. Mol. Biol.* **1982**, *157* (1), 105–132. https://doi.org/10.1016/0022-2836(82)90515-0.
- (312) Kessner, D.; Chambers, M.; Burke, R.; Agus, D.; Mallick, P. ProteoWizard: Open Source Software for Rapid Proteomics Tools Development. *Bioinformatics* **2008**, *24* (21), 2534–2536. https://doi.org/10.1093/bioinformatics/btn323.
- (313) D, S.; AL, G.; D, L.; A, J.; S, W.; J, H.-C.; M, S.; NT, D.; JH, M.; P, B.; et al. STRING V11: Protein-Protein Association Networks with Increased Coverage, Supporting Functional Discovery in Genome-Wide Experimental Datasets. *Nucleic Acids Res.* **2019**, 47 (D1), D607–D613. https://doi.org/10.1093/NAR/GKY1131.
- (314) Shannon, P.; Markiel, A.; Ozier, O.; Baliga, N. S.; Wang, J. T.; Ramage, D.; Amin, N.; Schwikowski, B.; Ideker, T. Cytoscape: A Software Environment for Integrated Models of Biomolecular Interaction Networks. *Genome Res.* **2003**, *13* (11), 2498–2504. https://doi.org/10.1101/GR.1239303.
- (315) Grushka, E. Chromatographic Peak Capacity and the Factors Influencing It. *Anal. Chem.* **1970**, *42* (11), 1142–1147. https://doi.org/10.1021/ac60293a001.
- (316) Hagel, L. Peak Capacity of Columns for Size-Exclusion Chromatography. *J. Chromatogr. A* **1992**, *591* (1–2), 47–54. https://doi.org/10.1016/0021-9673(92)80221-F.
- (317) Li, X.; Stoll, D. R.; Carr, P. W. Equation for Peak Capacity Estimation in Two-Dimensional Liquid Chromatography. *Anal. Chem.* **2009**, *81* (2), 845–850. https://doi.org/10.1021/ac801772u.
- (318) McCool, E. N.; Xu, T.; Chen, W.; Beller, N. C.; Nolan, S. M.; Hummon, A. B.; Liu, X.; Sun, L. Deep Top-down Proteomics Revealed Significant Proteoform-Level Differences between Metastatic and Nonmetastatic Colorectal Cancer Cells. *Sci. Adv.* **2022**, *8* (51). https://doi.org/10.1126/sciadv.abq6348.

- (319) Melani, R. D.; Gerbasi, V. R.; Anderson, L. C.; Sikora, J. W.; Toby, T. K.; Hutton, J. E.; Butcher, D. S.; Negrão, F.; Seckler, H. S.; Srzentic, K.; et al. The Blood Proteoform Atlas: A Reference Map of Proteoforms in Human Hematopoietic Cells. *Science* (80-.). **2022**, 375 (6579), 411–418. https://doi.org/10.1126/science.aaz5284.
- (320) Zong, S.; Wu, M.; Gu, J.; Liu, T.; Guo, R.; Yang, M. Structure of the Intact 14-Subunit Human Cytochrome c Oxidase. *Cell Res.* **2018**, *28* (10), 1026–1034. https://doi.org/10.1038/s41422-018-0071-1.
- (321) Larson, E. J.; Gregorich, Z. R.; Zhang, Y.; Li, B. H.; Aballo, T. J.; Melby, J. A.; Ge, Y.; Guo, W. Rbm20 Ablation Is Associated with Changes in the Expression of Titin-Interacting and Metabolic Proteins. *Mol. Omi.* 2022. https://doi.org/10.1039/d2mo00115b.
- (322) Aballo, T. J.; Roberts, D. S.; Melby, J. A.; Buck, K. M.; Brown, K. A.; Ge, Y. Ultrafast and Reproducible Proteomics from Small Amounts of Heart Tissue Enabled by Azo and TimsTOF Pro. https://doi.org/10.1021/acs.jproteome.1c00446.
- (323) Spinelli, J. B.; Haigis, M. C. The Multifaceted Contributions of Mitochondria to Cellular Metabolism. *Nat. Cell Biol.* **2018**, *20* (7), 745–754. https://doi.org/10.1038/s41556-018-0124-1.
- (324) Fung, T. S.; Chakrabarti, R.; Higgs, H. N. The Multiple Links between Actin and Mitochondria. *Nat. Rev. Mol. Cell Biol.* **2023**. https://doi.org/10.1038/s41580-023-00613-y.
- (325) Mohammed, S. A.; Ambrosini, S.; Lüscher, T.; Paneni, F.; Costantino, S. Epigenetic Control of Mitochondrial Function in the Vasculature. *Front. Cardiovasc. Med.* **2020**, 7 (March), 1–16. https://doi.org/10.3389/fcvm.2020.00028.
- (326) Santos, J. H. Mitochondria Signaling to the Epigenome: A Novel Role for an Old Organelle. *Free Radic. Biol. Med.* **2021**, *170* (November 2020), 59–69. https://doi.org/10.1016/j.freeradbiomed.2020.11.016.
- (327) Nagai, Y.; Matsuoka, T. aki; Shimo, N.; Miyatsuka, T.; Miyazaki, S.; Tashiro, F.; Miyazaki, J. ichi; Katakami, N.; Shimomura, I. Glucotoxicity-Induced Suppression of Cox6a2 Expression Provokes β-Cell Dysfunction via Augmented ROS Production. *Biochem. Biophys. Res. Commun.* 2021, 556, 134–141. https://doi.org/10.1016/j.bbrc.2021.03.148.
- (328) Sanz-Morello, B.; Pfisterer, U.; Hansen, N. W.; Demharter, S.; Thakur, A.; Fujii, K.; Levitskii, S. A.; Montalant, A.; Korshunova, I.; Mammen, P. P.; et al. Complex IV Subunit Isoform COX6A2 Protects Fast-Spiking Interneurons from Oxidative Stress and Supports Their Function. *EMBO* **2020**, *39* (e105759), 1–21.
- (329) Jiang, M.; Chen, X.; Zhu, M. COX6A2 Deficiency Leads to Cardiac Remodeling in Human Pluripotent Stem Cell-Derived Cardiomyocytes. *Res. Sq.* **2023**.
- (330) Lu, X.; Nobrega, R. P.; Lynaugh, H.; Jain, T.; Barlow, K.; Boland, T.; Sivasubramanian, A.; Vásquez, M.; Xu, Y. Deamidation and Isomerization Liability Analysis of 131 Clinical-Stage Antibodies. *MAbs* **2019**, *11* (1), 45–57. https://doi.org/10.1080/19420862.2018.1548233.

- (331) Lu, X.; Machiesky, L. A.; De Mel, N.; Du, Q.; Xu, W.; Washabaugh, M.; Jiang, X. R.; Wang, J. Characterization of IgG1 Fc Deamidation at Asparagine 325 and Its Impact on Antibody-Dependent Cell-Mediated Cytotoxicity and FcγRIIIa Binding. *Sci. Rep.* **2020**, 10 (1), 1–11. https://doi.org/10.1038/s41598-019-57184-2.
- (332) Papanastasiou, D.; Kounadis, D.; Lekkas, A.; Orfanopoulos, I.; Mpozatzidis, A.; Smyrnakis, A.; Panagiotopoulos, E.; Kosmopoulou, M.; Reinhardt-Szyba, M.; Fort, K.; et al. The Omnitrap Platform: A Versatile Segmented Linear Ion Trap for Multidimensional Multiple-Stage Tandem Mass Spectrometry. *J. Am. Soc. Mass Spectrom* **2022**, *33*, 51. https://doi.org/10.1021/jasms.2c00214.
- (333) Heil, L. R.; Damoc, E.; Arrey, T. N.; Pashkova, A.; Denisov, E.; Peterson, A.; Hsu, C.; Searle, B. C.; Shulman, N.; Riffle, M. Evaluating the Performance of the Astral Mass Analyzer for Quantitative Proteomics Using Data Independent Acquisition. *bioRxiv* 2023.
- (334) Schultheiss, H. P.; Fairweather, D. L.; Caforio, A. L. P.; Escher, F.; Hershberger, R. E.; Lipshultz, S. E.; Liu, P. P.; Matsumori, A.; Mazzanti, A.; McMurray, J.; et al. Dilated Cardiomyopathy. *Nat. Rev. Dis. Prim.* **2019**, *5* (1). https://doi.org/10.1038/s41572-019-0084-1.
- (335) Hershberger, R. E.; Hedges, D. J.; Morales, A. Dilated Cardiomyopathy: The Complexity of a Diverse Genetic Architecture. *Nat. Rev. Cardiol.* 2013 109 **2013**, 10 (9), 531–547. https://doi.org/10.1038/nrcardio.2013.105.
- (336) Herman, D. S.; Lam, L.; Taylor, M. R. G.; Wang, L.; Teekakirikul, P.; Christodoulou, D.; Conner, L.; DePalma, S. R.; McDonough, B.; Sparks, E.; et al. Truncations of Titin Causing Dilated Cardiomyopathy. *N. Engl. J. Med.* **2012**, *366* (7), 619–628. https://doi.org/10.1056/nejmoa1110186.
- (337) Pérez-Serra, A.; Toro, R.; Sarquella-Brugada, G.; de Gonzalo-Calvo, D.; Cesar, S.; Carro, E.; Llorente-Cortes, V.; Iglesias, A.; Brugada, J.; Brugada, R.; et al. Genetic Basis of Dilated Cardiomyopathy. *Int. J. Cardiol.* **2016**, *224*, 461–472. https://doi.org/10.1016/j.ijcard.2016.09.068.
- (338) Wang, C.; Zhang, Y.; Methawasin, M.; Braz, C. U.; Gao-Hu, J.; Yang, B.; Strom, J.; Gohlke, J.; Hacker, T.; Khatib, H.; et al. RBM20S639G Mutation Is a High Genetic Risk Factor for Premature Death through RNA-Protein Condensates. *J. Mol. Cell. Cardiol.* **2022**, *165* (January), 115–129. https://doi.org/10.1016/j.yjmcc.2022.01.004.
- (339) Ihara, K.; Sasano, T.; Hiraoka, Y.; Togo-Ohno, M.; Soejima, Y.; Sawabe, M.; Tsuchiya, M.; Ogawa, H.; Furukawa, T.; Kuroyanagi, H. A Missense Mutation in the RSRSP Stretch of Rbm20 Causes Dilated Cardiomyopathy and Atrial Fibrillation in Mice. *Sci. Rep.* **2020**, *10* (1), 1–14. https://doi.org/10.1038/s41598-020-74800-8.
- (340) Zhang, Y.; Wang, C.; Sun, M.; Jin, Y.; Braz, C. U.; Khatib, H.; Hacker, T. A.; Liss, M.; Gotthardt, M.; Granzier, H.; et al. RBM20 Phosphorylation and Its Role in Nucleocytoplasmic Transport and Cardiac Pathogenesis. *FASEB J.* **2022**, *36* (5), 1–19. https://doi.org/10.1096/fj.202101811RR.
- (341) Haas, J.; Frese, K. S.; Peil, B.; Kloos, W.; Keller, A.; Nietsch, R.; Feng, Z.; Müller, S.; Kayvanpour, E.; Vogel, B.; et al. Atlas of the Clinical Genetics of Human Dilated

- Cardiomyopathy. *Eur. Heart J.* **2015**, *36* (18), 1123–1135. https://doi.org/10.1093/eurheartj/ehu301.
- (342) Kayvanpour, E.; Sedaghat-Hamedani, F.; Gi, W. T.; Tugrul, O. F.; Amr, A.; Haas, J.; Zhu, F.; Ehlermann, P.; Uhlmann, L.; Katus, H. A.; et al. Clinical and Genetic Insights into Non-Compaction: A Meta-Analysis and Systematic Review on 7598 Individuals. *Clin. Res. Cardiol.* **2019**, *108* (11), 1297–1308. https://doi.org/10.1007/s00392-019-01465-3.
- (343) Guo, W.; Schafer, S.; Greaser, M. L.; Radke, M. H.; Liss, M.; Govindarajan, T.; Maatz, H.; Schulz, H.; Li, S.; Parrish, A. M.; et al. RBM20, a Gene for Hereditary Cardiomyopathy, Regulates Titin Splicing. *Nat. Med. 2012 185* **2012**, *18* (5), 766–773. https://doi.org/10.1038/nm.2693.
- (344) Guo, W.; Zhu, C.; Yin, Z.; Wang, Q.; Sun, M.; Cao, H.; Greaser, M. L. Splicing Factor RBM20 Regulates Transcriptional Network of Titin Associated and Calcium Handling Genes in the Heart. *Int. J. Biol. Sci.* **2018**, *14* (4), 369–380. https://doi.org/10.7150/ijbs.24117.
- (345) Hoogenhof, M. M. G. van den; Beqqali, A.; Amin, A. S.; Made, I. van der; Aufiero, S.; Khan, M. A. F.; Schumacher, C. A.; Jansweijer, J. A.; Spaendonck-Zwarts, K. Y. van; Remme, C. A.; et al. RBM20 Mutations Induce an Arrhythmogenic Dilated Cardiomyopathy Related to Disturbed Calcium Handling. *Circulation* **2018**, *138* (13), 1330–1342. https://doi.org/10.1161/CIRCULATIONAHA.117.031947.
- (346) Methawasin, M.; Hutchinson, K. R.; Lee, E.-J.; John E. Smith, I.; Saripalli, C.; Hidalgo, C. G.; Ottenheijm, C. A. C.; Granzier, H. Experimentally Increasing Titin Compliance in a Novel Mouse Model Attenuates the Frank-Starling Mechanism But Has a Beneficial Effect on Diastole. *Circulation* **2014**, *129* (19), 1924–1936. https://doi.org/10.1161/CIRCULATIONAHA.113.005610.
- (347) De Sousa Abreu, R.; Penalva, L. O.; Marcotte, E. M.; Vogel, C. Global Signatures of Protein and MRNA Expression Levels. *Mol. Biosyst.* **2009**, *5* (12), 1512–1526. https://doi.org/10.1039/b908315d.
- (348) Vogel, C.; Marcotte, E. M. Insights into the Regulation of Protein Abundance from Proteomic and Transcriptomic Analyses. *Nat. Rev. Genet.* **2012**, *13* (4), 227–232. https://doi.org/10.1038/nrg3185.
- (349) Maier, T.; Güell, M.; Serrano, L. Correlation of MRNA and Protein in Complex Biological Samples. *FEBS Lett.* **2009**, *583* (24), 3966–3973. https://doi.org/10.1016/j.febslet.2009.10.036.
- (350) Brown, K. A.; Tucholski, T.; Eken, C.; Knott, S.; Zhu, Y.; Jin, S.; Ge, Y. High-Throughput Proteomics Enabled by a Photocleavable Surfactant. *Angew. Chemie* **2020**, *132* (22), 8484–8488. https://doi.org/10.1002/ANGE.201915374.
- (351) Guo, W.; Pleitner, J. M.; Saupe, K. W.; Greaser, M. L. Pathophysiological Defects and Transcriptional Profiling in the RBM20 -/- Rat Model. *PLoS One* **2013**, 8 (12), 1–11. https://doi.org/10.1371/journal.pone.0084281.
- (352) Schneider, J. W.; Oommen, S.; Qureshi, M. Y.; Goetsch, S. C.; Pease, D. R.; Sundsbak, R.

- S.; Guo, W.; Sun, M.; Sun, H.; Kuroyanagi, H.; et al. Dysregulated Ribonucleoprotein Granules Promote Cardiomyopathy in RBM20 Gene-Edited Pigs. *Nat. Med.* **2020**, *26* (11), 1788–1800. https://doi.org/10.1038/s41591-020-1087-x.
- (353) Shah, A. D.; Goode, R. J. A.; Huang, C.; Powell, D. R.; Schittenhelm, R. B. Lfq-Analyst: An Easy-To-Use Interactive Web Platform to Analyze and Visualize Label-Free Proteomics Data Preprocessed with Maxquant. *J. Proteome Res.* **2019**, 204–211. https://doi.org/10.1021/acs.jproteome.9b00496.
- (354) Tyanova, S.; Temu, T.; Sinitcyn, P.; Carlson, A.; Hein, M. Y.; Geiger, T.; Mann, M.; Cox, J. The Perseus Computational Platform for Comprehensive Analysis of (Prote)Omics Data. *Nat. Methods* 2016 139 2016, 13 (9), 731–740. https://doi.org/10.1038/nmeth.3901.
- (355) Szklarczyk, D.; Gable, A. L.; Nastou, K. C.; Lyon, D.; Kirsch, R.; Pyysalo, S.; Doncheva, N. T.; Legeay, M.; Fang, T.; Bork, P.; et al. The STRING Database in 2021: Customizable Protein-Protein Networks, and Functional Characterization of User-Uploaded Gene/Measurement Sets. *Nucleic Acids Res.* **2021**, *49* (D1), D605–D612. https://doi.org/10.1093/nar/gkaa1074.
- (356) Guo, W.; Zhu, C.; Yin, Z.; Zhang, Y.; Wang, C.; Walk, A. S.; Lin, Y. H.; McKinsey, T. A.; Woulfe, K. C.; Ren, J.; et al. The Ryanodine Receptor Stabilizer S107 Ameliorates Contractility of Adult Rbm20 Knockout Rat Cardiomyocytes. *Physiol. Rep.* **2021**, *9* (17), 1–13. https://doi.org/10.14814/phy2.15011.
- (357) Miller, M. K.; Bang, M. L.; Witt, C. C.; Labeit, D.; Trombitas, C.; Watanabe, K.; Granzier, H.; McElhinny, A. S.; Gregorio, C. C.; Labeit, S. The Muscle Ankyrin Repeat Proteins: CARP, Ankrd2/Arpp and DARP as a Family of Titin Filament-Based Stress Response Molecules. *J. Mol. Biol.* **2003**, *333* (5), 951–964. https://doi.org/10.1016/j.jmb.2003.09.012.
- (358) Ling, S. S. M.; Chen, Y. T.; Wang, J.; Richards, A. M.; Liew, O. W. Ankyrin Repeat Domain 1 Protein: A Functionally Pleiotropic Protein with Cardiac Biomarker Potential. *Int. J. Mol. Sci.* **2017**, *18* (7), 1–23. https://doi.org/10.3390/ijms18071362.
- (359) Aihara, Y.; Kurabayashi, M.; Saito, Y.; Ohyama, Y.; Tanaka, T.; Takeda, S. I.; Tomaru, K.; Sekiguchi, K. I.; Arai, M.; Nakamura, T.; et al. Cardiac Ankyrin Repeat Protein Is a Novel Marker of Cardiac Hypertrophy: Role of M-CAT Element within the Promoter. *Hypertension* **2000**, *36* (1), 48–53. https://doi.org/10.1161/01.HYP.36.1.48.
- (360) Zolk, O.; Frohme, M.; Maurer, A.; Kluxen, F. W.; Hentsch, B.; Zubakov, D.; Hoheisel, J. D.; Zucker, I. H.; Pepe, S.; Eschenhagen, T. Cardiac Ankyrin Repeat Protein, a Negative Regulator of Cardiac Gene Expression, Is Augmented in Human Heart Failure. *Biochem. Biophys. Res. Commun.* 2002, 293 (5), 1377–1382. https://doi.org/10.1016/S0006-291X(02)00387-X.
- (361) Jing, J.; He, L.; Sun, A.; Quintana, A.; Ding, Y.; Ma, G.; Tan, P.; Liang, X.; Zheng, X.; Chen, L.; et al. Proteomic Mapping of ER-PM Junctions Identifies STIMATE as a Regulator of Ca 2+ Influx. *Nat. Cell Biol.* **2015**, *17* (10), 1339–1347. https://doi.org/10.1038/ncb3234.
- (362) Sheikh, F.; Raskin, A.; Chu, P. H.; Lange, S.; Domenighetti, A. A.; Zheng, M.; Liang, X.;

- Zhang, T.; Yajima, T.; Gu, Y.; et al. An FHL1-Containing Complex within the Cardiomyocyte Sarcomere Mediates Hypertrophic Biomechanical Stress Responses in Mice. *J. Clin. Invest.* **2008**, *118* (12), 3870–3880. https://doi.org/10.1172/JCI34472.
- (363) Zhong, L.; Chiusa, M.; Cadar, A. G.; Lin, A.; Samaras, S.; Davidson, J. M.; Lim, C. C. Targeted Inhibition of ANKRD1 Disrupts Sarcomeric ERK-GATA4 Signal Transduction and Abrogates Phenylephrine-Induced Cardiomyocyte Hypertrophy. *Cardiovasc. Res.* **2015**, *106* (2), 261–271. https://doi.org/10.1093/cvr/cvv108.
- (364) Hojayev, B.; Rothermel, B. A.; Gillette, T. G.; Hill, J. A. FHL2 Binds Calcineurin and Represses Pathological Cardiac Growth. *Mol. Cell. Biol.* **2012**, *32* (19), 4025–4034. https://doi.org/10.1128/mcb.05948-11.
- (365) Vilà-Brau, A.; De Sousa-Coelho, A. L.; Mayordomo, C.; Haro, D.; Marrero, P. F. Human HMGCS2 Regulates Mitochondrial Fatty Acid Oxidation and FGF21 Expression in HepG2 Cell Line. *J. Biol. Chem.* **2011**, *286* (23), 20423–20430. https://doi.org/10.1074/jbc.M111.235044.
- (366) Zhang, P.; Lu, Y.; Yu, D.; Zhang, D.; Hu, W. TRAP1 Provides Protection Against Myocardial Ischemia-Reperfusion Injury by Ameliorating Mitochondrial Dysfunction. *Cell. Physiol. Biochem.* **2015**, *36* (5), 2072–2082. https://doi.org/10.1159/000430174.
- (367) Lee, S. H.; Lee, S.; Du, J.; Jain, K.; Ding, M.; Kadado, A. J.; Atteya, G.; Jaji, Z.; Tyagi, T.; Kim, W.; et al. Mitochondrial MsrB2 Serves as a Switch and Transducer for Mitophagy. *EMBO Mol. Med.* **2019**, *11* (8), 1–16. https://doi.org/10.15252/emmm.201910409.
- (368) Palikaras, K.; Lionaki, E.; Tavernarakis, N. Mechanisms of Mitophagy in Cellular Homeostasis, Physiology and Pathology. *Nat. Cell Biol.* **2018**, *20* (9), 1013–1022. https://doi.org/10.1038/s41556-018-0176-2.
- (369) Ramaccini, D.; Montoya-Uribe, V.; Aan, F. J.; Modesti, L.; Potes, Y.; Wieckowski, M. R.; Krga, I.; Glibetić, M.; Pinton, P.; Giorgi, C.; et al. Mitochondrial Function and Dysfunction in Dilated Cardiomyopathy. *Front. Cell Dev. Biol.* **2021**, 8 (January), 1–21. https://doi.org/10.3389/fcell.2020.624216.